# Detection of seepage-induced internal instability using acoustic emission

School of Architecture, Building and Civil Engineering
Loughborough University

PhD Thesis

# DETECTION OF SEEPAGE-INDUCED INTERNAL INSTABILITY USING ACOUSTIC EMISSION

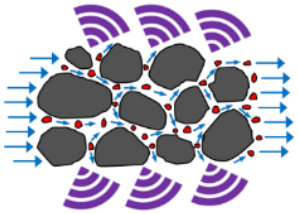

Tiago Jose Biller Teixeira Zuanazzi
(B729171)

November 5th 2021

Supervisors:
Dr Alister Smith
Prof Neil Dixon

# Abstract

Seepage-induced internal erosion is and has for a long time been a matter of concern regarding water-retaining earth structures. Uncertainties about which conditions can be considered hazardous and incomplete knowledge about the involved physical dynamics and the structures themselves illustrate why this is such a difficult problem to solve. As an implication, predicting the occurrence of internal erosion through modelling and implementation of theoretical frameworks, despite being highly sensible and desirable, are still insufficient approaches. Conversely, the ability to directly detect the occurrence of internal erosion in its early stages is a way to hugely minimise the effects of structural damage by providing early warnings and possibly avoiding disaster – as well as producing information for better facing this matter in the future.

Current detection approaches are limited by either inferring its occurrence in already advanced stages (too late for intervention without calamity), implying only fluid seepage (being blind to particle transport, which is critical) or simple susceptibility assessments based on material particle size distributions (which ignores random non-homogeneities and discounts differences between design and construction). A method that specifically detects particle transport by fluid seepage (or internal instability) is lacking but would enable timely interventions.

In this research, acoustic emission (AE) has been investigated for this application. Results from laboratory experiments with a bespoke, purpose designed and built permeameter show that seepage-induced internal erosion processes can detected and monitored using AE. The experimental programme included 22 tests (in two rounds – pre- and post-commissioning of bespoke apparatus) and employed materials used in the construction of earth dams and with varying degrees of estimated internal instability (which varied depending on the different criteria used). These soils were subject to permeating fluid flow and monitored for changes to hydromechanical parameters and the development of internal erosion, from the start of seepage-induced particle movement to piping.

The measurement and interpretation of AE in this context was based on filtering unwanted environmental noise and registering when the signal exceeds a predefined/calibrated threshold (i.e. employing an approach to minimise false alarms). A strong correlation between the occurrence of internal erosion and detectable AE has been found. It was possible to use AE to differentiate between fluid flow with and without particle transport – especially the transition from one to the other, or the onset of internal erosion – as well as observing the evolution of the erosion processes. AE rates tended to increase proportionally to the transport

soil particles, with elevated AE activity occurring during the formation of preferential flow pathways through the soil.

The observations produced in this study show that the use of AE for monitoring the occurrence of seepage-induced internal erosion is feasible, with the necessity of a trained professional to analyse the produce data and account for particularities of individual circumstances. However, the datasets and new understanding produced in this study also indicate that the development of automated interpretation algorithms can be done (e.g. by following the recommendations made in this thesis).

# Acknowledgements

Most importantly, I would like to show my Dr Alister Smith and Prof Neil Dixon my gratitude. They trusted me with the opportunity to develop this research and provided excellent support as my supervisors during the entire process. I hope met their expectations. You taught me a lot and working with you was extremely enjoyable and enriching. Thanks for always being so friendly, helpful, and wise. I consider you great people both professionally and personally.

My sincere thanks also to the gentlemen who so competently and solicitously supported me in my work at the Sir Frank Gibb laboratories: Lewis Darwin, Paul Reeves, Roger Bennett, Jonathan Hales, Zain Khan, Mark Harrod, Nick Rodgers and Dean Sanham. This work would not have been possible without you.

I also wish to thank Berkeley Young for his highly competent support in administrative matters, answering general enquiries of student life and making the environment at the Research Hub so nice and adequate for work. Similarly, but in matters of finance administration, I would like to thank Karishma Joshi.

Thanks also to my fellow researchers and friends Derek, Hellen, Stephen, Riccardo, Pepe, Shima, Roel, Susie, Vincenzo, Meena, Monia, Sid, Luigi, and others, who made this time a whole lot better.

Of course, I should not forget the support given by my family – including the new, extended one – as well as my girlfriend.

The Engineering and Physical Sciences Research Council (EPSRC), the Listening to Infrastructure programme and Loughborough University made this project possible by providing the necessary funding and resources. Their backing and support of such projects promote valuable work that, directly and indirectly, at different time and geographic scales, importantly improve society and its underlying infrastructure.

# Contents

# List of Figures

# List of tables

# Nomenclature

| | |
|---|---|
| ***AE*** | *Acoustic emission* |
| ***i*** | *Hydraulic gradient* |
| $\sigma_v$ | *Vertical stress (kPa)* |
| $\sigma'$ | *Effective stress (kPa)* |
| ***k*** | *Permeability (m/s)* |
| ***n*** | *Porosity* |
| ***Q*** | *Flow rate ($m^3/s$)* |
| ***A*** | *Cross-sectional area of specimen ($m^2$)* |
| ***p*** | *Pressure (kPa)* |
| ***l*** | *Specimen length* |
| ***h*** | *Piezometric head (m)* |
| $\gamma_w$ | *Water density ($kN/m^3$)* |
| $\Delta V$ | *Volume of water collected over time interval ($m^3$)* |
| $\Delta t$ | *Time interval (s)* |
| ***g*** | *Gravitational acceleration (9.807 $m/s^2$)* |
| $E_{tot}$ | *Total hydraulic energy (J)* |
| $E_i$ | *Energy contribution due to hydraulic gradient (J)* |
| $E_v$ | *Energy due to seepage velocity (J)* |
| $E_p$ | *Pressure energy (J)* |
| $E_k$ | *Kinetic energy of seepage per unit volume of soil mass (J)* |
| $E_{Kcrit}$ | *Critical kinetic energy of seepage (J)* |
| ***v*** | *Darcy flow velocity (m/s)* |
| $v_s$ | *Pore seepage velocity (m/s)* |
| $v_c$ | *Critical seepage velocity (m/s)* |
| $M_f$ | *Mass of percolating fluid (kg)* |
| $A_v$ | *Voids effective cross-sectional area ($m^2$)* |
| ***BH*** | *Bottom hydrophone* |
| ***TH*** | *Top hydrophone* |
| ***WG*** | *Waveguide* |
| ***TLC*** | *Top Load cell* |
| ***BLC*** | *Bottom Load cell* |

# List of equations

| | | |
|---|---|---|
| ***Permeability*** | $k = \frac{Q \times l}{A \times h}$ | (ISO TS 17892-11.2004, 2004) |
| ***Flow rate*** | $Q = \frac{\Delta V}{\Delta t}$ | (ISO TS 17892-11.2004, 2004) |
| ***Piezometric head*** | $h = \frac{p}{\Upsilon_w}$ | (ISO TS 17892-11.2004, 2004) |
| ***$M_f$*** | $M_f = n \times 1m^3 \times [99\ 8\ kg/m^3]$ | *(Richards and Reddy, 2014)* |
| ***$E_k$*** | $E_k = \left(\frac{1}{2}\right) \times M_f \times v_s^2$ | *(Richards and Reddy, 2014)* |
| ***$E_{Kcrit}$*** | $E_{Kcrit} = \left(\frac{1}{2}\right) \times M_f \times v_c^2$ | *(Richards and Reddy, 2014)* |
| ***$v_s$*** | $v_s = v \frac{A}{A_v}$ | *(Richards and Reddy, 2014)* |
| ***$A_v$*** | $A_v = n \times A$ | *(Richards and Reddy, 2014)* |
| ***Decibel*** | $dB = 20 \log\left(\frac{P_{rms}}{P_0}\right)$<br>*dB = Sound pressure level; rms = Root mean square value; P0 = reference pressure* | *(Kadam and Nayak, 2016)* |
| ***Amplitude ratio*** | $dB = 20 \log_{10} N$<br>dB=number of decibels<br>N=Amplitude ratio | *(Gelb and Van der Velde, 1968)* |
| ***Characteristic frequency (Biot theory)*** | $f_c = \frac{\eta \emptyset}{2\pi k_0 \rho_f}$<br>*fc=characteristic frequency, ρf =pore fluid density, η=kinematic viscosity, ∅=porosity and k0=permeability.* | *(Dutta and Ode, 1983; Biot, 1956)* |
| ***Sound Intensity*** | $I = p\,u$<br>*I= sound intensity; p = sound pressure; u = particle velocity* | *(Kadam and Nayak, 2016)* |
| ***Critical hydraulic gradient (estimation)*** | $i_{crit} = \frac{G_s - 1}{1+e}$ | (Terzaghi, 1925; Terzaghi and Peck, 1948) |

# 1. Introduction

A long-standing problem with the longevity of water-retaining earth structures is their vulnerability to internal erosion (IE). This process, which can severely compromise the structural integrity of critical infrastructure, has historically been reported in many different settings (e.g. fluvial terraces, stream banks, dams, levees) and in a variety of material configurations. A large range of disturbances, anthropogenic and natural (e.g. changes in hydraulic conditions, trenches, pipelines, topographic modifications), have the capacity to trigger seepage erosion processes and result in unexpected failures (Crosta and Prisco, 1999; Camici et al., 2017; Rönnqvist and Viklander, 2018).

Currently available warning systems have technological limitations or prohibitive costs (or both), which impede the deployment of reliable systems to detect seepage-induced internal erosion in its early stages, or before serious damage has occurred. This phenomenon is largely invisible from the surface of such structures and significant deterioration has likely already occurred when visible signs become present. Technologies for early detection of such processes are urgently needed to enable targeted and timely interventions – this project intends to address this issue.

Fundamentally, seepage erosion consists of water flowing through a porous medium and causing the dislodgement of its particles. The erosion of finer particles from a coarser matrix caused by seepage flow is termed suffusion and is manifested as a combination of detachment, transport, and potential filtration of the finer fraction and can promote a change in particle size distribution, porosity, and hydraulic conductivity of the soil. If the grain-size distribution of a soil is such that the relative particle geometries do not allow the finer particles to fit through the spaces between coarser ones (in a gap-graded, cohesionless soil), this soil is considered internally stable (Moraci et al., 2014; Dallo et al., 2013; Fannin and Slangen, 2014). The term suffosion is used (instead of suffusion) if the seepage flow causes material loss, eventually accompanied by a volume reduction or structural collapse.

There is disagreement about the definition of suffosion containing destructive and non-destructive phenomena – leading or not to some form of collapse of the soil structure - (Fannin and Slangen, 2014) but this research considers that the term encompasses both.

In addition to the grain-size distribution itself, the major variables in the occurrence of seepage-induced internal erosion are effective stress, fluid flow and hydraulic gradient. Intuitively, it can be affirmed that 1) a sufficiently strong [critical] fluid flow is needed to promote particle

transport and 2) a tighter, laden packing of the grains themselves makes particle movement more difficult[1]. The relationship between critical hydraulic gradient[2] and effective stress resulted in the concept of hydromechanical envelope, used to describe a threshold at which the onset of seepage-induced instability occurs in a soil (Ferdos et al., 2018; Moffat and Fannin, 2011, 2006; Li, 2008; Wan and Fell, 2008).

A portion of the energy dissipated during seepage-induced internal erosion is converted to sound. The high-frequency (>10kHz) component of this energy is called acoustic emission (AE) and its monitoring offers the potential to sense particle-scale behaviours that lead to macro-scale responses of soils (Koerner et al., 1981; Smith and Dixon, 2019a). AE is widely used in many industries for non-destructive testing and evaluation of materials and systems (e.g. pipe networks and pressure vessels); however, it is seldom used in geotechnical engineering, despite evidence of the benefits (Smith et al., 2014, 2017), because AE generated by particulate materials is highly complex and difficult to measure and interpret. AE is generated by seepage-induced IE mechanisms through frictional interactions between particles, friction due to fluid flow through the soil, collisions of migrating particles, and collapse of fabric; Figure 1-1 (e.g. suffosion) (Smith et al., 2019a).

This project intended to develop strategies to interpret and quantify seepage-induced internal instability phenomena from AE measurements (currently a research gap,) enabling early detection of IE processes and hence targeted and timely interventions.

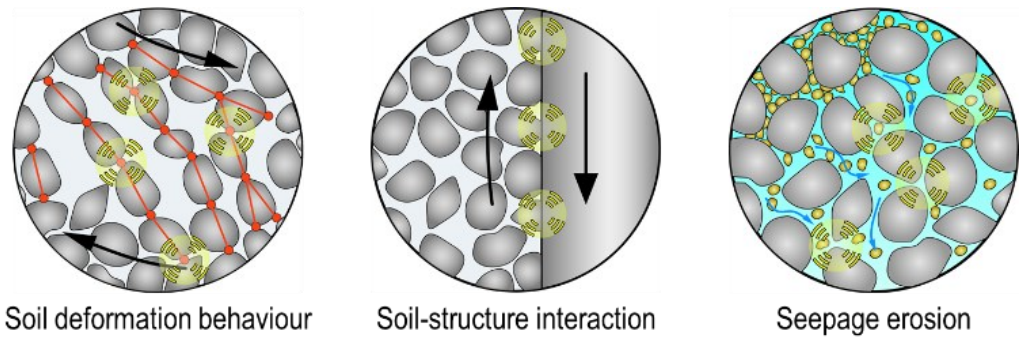


*Figure 1-1. Illustration of three different ways in which AE can be produced in a granular medium: soil deformation, soil/structure interaction and seepage erosion (Smith et al., 2019b).*

[1] The *stress reduction factor* should be considered: the finer fraction of a [gap-graded] soil receives less of the applied mechanical stresses when sufficient numbers of coarse particles are present; only a part of the applied loading is carried by the finer fraction, therefore the effective stress in the finer fraction - susceptible to internal erosion - is lower (Li and Fannin, 2012; Ferdos et al., 2018).

[2] Critical hydraulic conditions governing the onset of internal erosion; the critical gradient should occur when the overburden stress of the grains is equal to the upward flow pressure from the fluid. Skempton & Brogan (1994) observed that particle migration occurred above a critical hydraulic gradient.

## 1.1 Justification of this research

Internal erosion and piping in embankments and their foundations is the main cause of embankment dam failures. Recent developments in the design of filters and transition zones are employed to mitigate internal erosion in new dams. However, many existing dams were constructed before engineers had a sound understanding of filter design, and hence are susceptible to internal erosion.

According to Fell et al. (2003), internal erosion has caused failure of about 1 in every 200 (0.5%) embankment dams: 50% occurring within the embankment fill, 40% in the foundations, and 10% progressing from the embankment to the foundation. Although significant research has focused on improving designs to prevent internal erosion, limited research and development has been undertaken to improve methodologies to detect the onset and evolution of internal erosion in existing dams.

The U.S. Bureau of Reclamation states that the potential for loss of life in dam failure events is significantly dependent on the warning time available to evacuate the population at risk, suggesting that warnings as little one hour ahead of failure can have a significant impact on reducing the number casualties (Fell et al., 2003).

With that in mind, the idea of developing a realistic, effective monitoring system capable of the early-detection of seepage-induced internal erosion, although still not a definite solution, is deemed pertinent and worthwhile as a way to allow for actions to be taken before any severe damage occurs. This project was one such attempt.

## 1.2 Aim and objectives

*Hypothesis:* The central premise of this work is that the processes involved in seepage-induced internal erosion produce AE that could be detected and interpreted.

*Aim:* To advance the application of acoustic emission for detecting seepage-induced internal erosion in water-retaining earth structures.

*Objectives:*

O1. Research the state-of-the-art of the mechanics of seepage-induced internal erosion and the applicability of AE for its detection.

O2. To develop a methodology capable of simulating seepage-induced internal erosion in a controlled manner while detecting AE and measuring hydromechanical parameters.

O3. To enhance understanding of AE generated by seepage-induced internal erosion by analysing the datasets produced in laboratory experiments.

O4. To establish the potential of AE for detecting and interpreting seepage-induced internal erosion and propose strategies for its use in infrastructure monitoring.

These goals were achieved through a sequence of work packages, as illustrated in Figure 1-2.

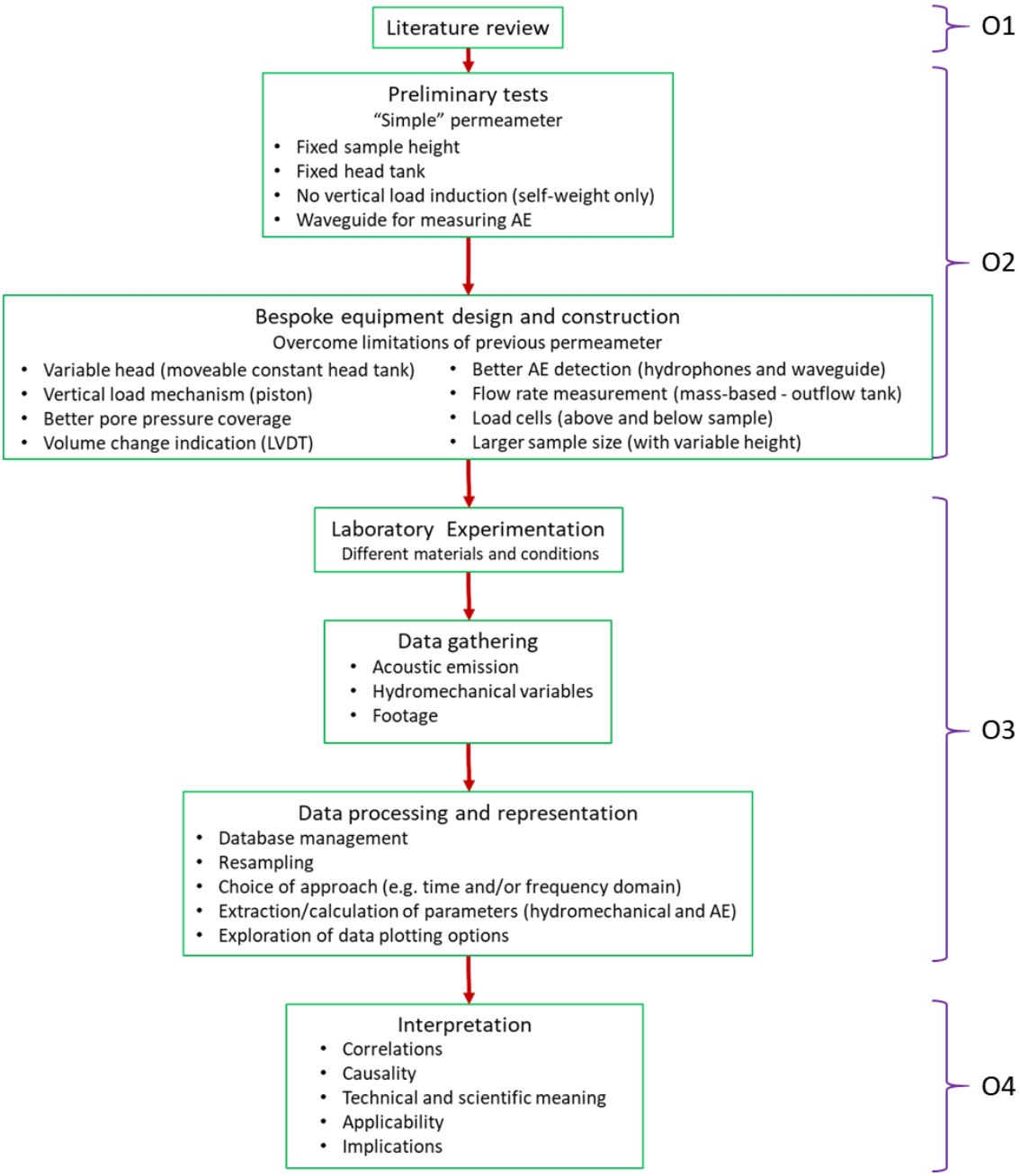


*Figure 1-2. Flow chart with work packages and their correspondence to the achievement of the listed objectives.*

## 1.3 Original contributions to knowledge

Having been based on extensive knowledge found in the available literature, this work has nonetheless offered new contributions that advance this knowledge. A summary of such contributions is listed below and substantiated in the following sections.

- This research has shown that AE can be used to monitor seepage-induced internal erosion.
- Extensive new datasets have been produced for AE measurements from seepage-induced internal erosion.
- An interpretation strategy has been advanced in a way that can be applied to relatively large datasets and allow long-term, continuous monitoring.
- It has been possible to detect seepage-induced internal erosion in its early stages, notably with the differentiation between fluid flow with and without particle transport.
- Hydromechanical variables critical for the onset and development of seepage-induced internal erosion have been interpreted from AE.

## 1.4 Thesis structure

The structure of this thesis intended to show how a) the departure from observing a practical, consequential problem capable of infrastructural damage (i.e. seepage-induced internal erosion) and the knowledge of a methodology (i.e. AE detection and interpretation) successfully applied to analogous/comparable issues (e.g. soil mechanics) led to the b) gathering of research in the matter, c) envisioning how this methodology could be tested for its capacity to address the mentioned issue (i.e. laboratory testing), d) gathering and processing relevant analytical data, and e) interpreting this data and outlining if/how the methodology could be used as intended.

The following chapters partition this progression:

1) Introduction: lays out the aspirations and justifications of this work (a)
2) Literature review: establishes the theoretical basis for its development (b).
3) Materials and methods: defines and justifies the chosen approach (c).
4) Results: displays and describes the acquired data (d).
5) Discussion: interprets the data, produces scientifically based inferences/hypotheses and demonstrates the applicability of the chosen methodology (e).

# 2 Literature review

In this chapter, knowledge about the kind of structures, hazards, influential factors, currently used monitoring techniques and physical concepts relevant for this research is explained.

## 2.1 Embankment Dams

Embankment dams have been in use for at least 5000 years, as testified by ancient remains of mankind's efforts in engineering and construction. Archaeological findings indicate that ancient dam builders made widespread use of soils and gravels, and since only a rather rudimentary understanding of the mechanics of materials or of fluid flow was available, the resulting structures often failed, which persisted for most of history. Hence, embankment dams remained low on the scale of public confidence even until the recent past (U. S. Society on Dams, 2011). Developments in technical knowledge and capabilities dramatically enhanced the level of engineering achievement, such that embankment dams currently exist in excess of 300 meters of height and with volumes of many millions of cubic meters of fill. The considerably widespread adoption of embankment dams can be justified by:

- Possibility of using materials within relatively short haul distances of the construction site,
- Embankment dams being compatible with a variety of foundation conditions, and
- Their substantially lower costs when compared to other dam types.

In parallel, some of the common questions for evaluating whether an existing dam is adequately designed or suitable for a given site are:

- Is the dam subject to overtopping (a severe cause of concern for structural integrity) based on its operational characteristics and the various plausible loading conditions?
- Is structural sliding of the existing or proposed dam and abutment slopes a possible failure mechanism and, if so, can an adequate factor of safety be defined?
- Are the dam and its foundation susceptible to internal or external erosion?

(U. S. Society on Dams, 2011)

Naturally, methodologies and guidelines for the safe construction and monitoring of water-retaining earth structures have been developed over the years (Ferdos, 2016; Martínez-Moreno et al., 2018; Rönnqvist and Viklander, 2018; U. S. Society on Dams, 2011). Occasionally, nonetheless, in practical terms it may be rather challenging to rigorously execute a given project. Remote construction sites, budgetary limitations, material availability and other constraints can cause undesirable compromises and result in uncertainties about specific details of built structures, hindering the ability of current methodologies for estimating

intrinsic instabilities (Moraci et al., 2014; Kenney and Lau, 1985; Marot et al., 2016; USBR, 2015; Shire and O'Sullivan, 2017).

The recent paper by Rasskazov et al. (2018) discusses interesting cases of dam constructions and eventual structural disturbances based on settlements, deformations and pore pressures. During and post construction (and reservoir filling) episodes such as improper material compaction, ground compression, abnormal settlement or core deformation by soaking are shown to promote e.g. creeping deformations or vertical and horizontal displacements (which, aggravatingly, can be differential among different layers or zones). Among the consequences of such processes may be the development of structural weaknesses (beyond intrinsic instabilities of the materials used) that elevate the risk of e.g. internal erosion. Moreover, the 2018 paper mentions that predictive calculations of deformations in the presented cases are often in considerable disagreement with actual measurements. From the above observations, the development of monitoring techniques able to independently identify detrimental processes is urgently needed.

### 2.1.1 Types of embankment dams

Embankment dams can be subdivided into two main categories based on their construction materials: earth fill and rockfill dams. The selection of dam type tends to be determined by factors such as local topography and geology as well as quality and quantity of available materials.

<u>Earthfill dams</u>

Today, as in the past, earthfill dams are the most common type of dam. Their construction usually employs locally available materials and they are designed considering the topographic and foundation conditions at the site (U.S. Department of the Interior, 2012). In this type of dam, the dam body is normally responsible for structural and seepage resistance against failure, often being provided with drains. Figure 2-1, Figure 2-2 and Figure 2-3.

- *Diaphragm Embankments:*
  The bulk of the embankment is made of pervious material (sand, gravel, or rock) and a thin diaphragm of impermeable material is provided to form the water barrier. The diaphragm position may vary from being placed on the upstream face to being in the middle of the fill. The diaphragm or membrane can be a geomembrane, be made of asphaltic concrete, reinforced concrete, metal, or a compacted earthfill. Internal diaphragms are not readily available for inspection or emergency repair (e.g. ruptures, material flaw or settlement of the dam or its foundation).

¶ *Homogeneous Embankments:*

As the name suggests, this type of dam is made of a single kind of material, although the definition admits the use of slope protection. The dam material has to be sufficiently impervious to provide an adequate water barrier. Generally, the shear strength of soils that satisfy this requirement is such that the slopes of the dam must be relatively flat to remain stable. Given enough time, a fully homogeneous section on an impervious foundation, seepage tends to occur on the downstream slope (possibly regardless of the embankment slope and the permeability of the embankment material.

¶ *Zoned Embankments*

Use a combination of materials such as clays, silts, sands, gravels, and rock placed in zones to take advantage of their best properties and mitigate their poorer ones. Zoned earthfill dams typically have a central impervious core flanked by upstream transition zones, downstream filters and drains, and outer zones or shells composed of gravel fill, rockfill, or random fill. Generally, the function of each zone is as follows:

- Shells support and protect the impervious core
- Transition zones, filters, and drains; the upstream pervious zone provides strength for stability (e.g. against rapid drawdown)
- The downstream zone provides strength to support the core and filters.
- The upstream transition zone can offer protection against internal erosion or washout of the core during rapid drawdown and protection against cracking of the core.
- Downstream filters and drains control seepage and leakage and prevent sediment transport through cracks in the core.

(U.S. Department of the Interior, 2012)

<u>Rockfill dams</u>

A rockfill dam can be defined as one that relies on rock as a major structural element, with the term “rock” including angular fragments, produced by quarrying or occurring naturally, as talus and subangular or rounded fragments such as coarse gravel, cobbles, and boulders. The role of water barrier is normally performed by an impervious membrane. This membrane can be made of various materials (e.g. earth, reinforced concrete, steel, asphaltic concrete, geomembrane, and even wood) and can be placed either within the embankment or on the upstream slope (U.S. Department of the Interior, 2012). The main body of such dams consists of a rockfill shell, transition zones, core and facing zones, which serve to minimize leakage

through the embankment. The filter zone serves to prevent loss of soil particles by erosion due to seepage flow through embankment (Narita, 2000). Figure 2-1 and Figure 2-2.

Based on the location of the membrane, rockfill dams can be subdivided in two main types:

¶ *Internal membrane:*

Generally constructed of impervious earth materials, their core is better protected from the effects of weathering and external damage and are more easily adapted to less favourable foundation conditions, especially if the core is centrally located. These can be further subdivided in two types:

- o Central core
- o Sloping/inclined core

¶ Upstream membrane

Also called decked, or with facing, are more readily available for inspection and repair and larger portion of the embankment remains unsaturated, favouring for both static and dynamic stability. The upstream filter zone can also serve as a “crack stopper and the membrane can provide slope protection.

(U.S. Department of the Interior, 2012)

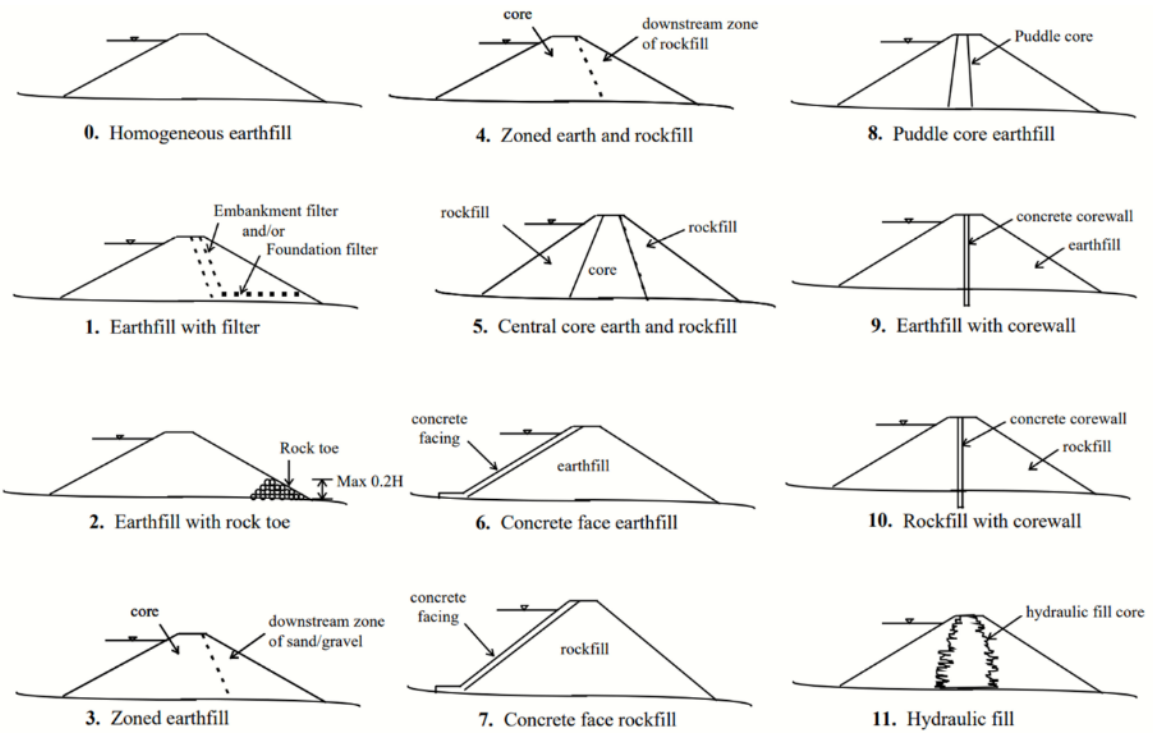


*Figure 2-1. Dam zoning categories (Foster, 1999).*

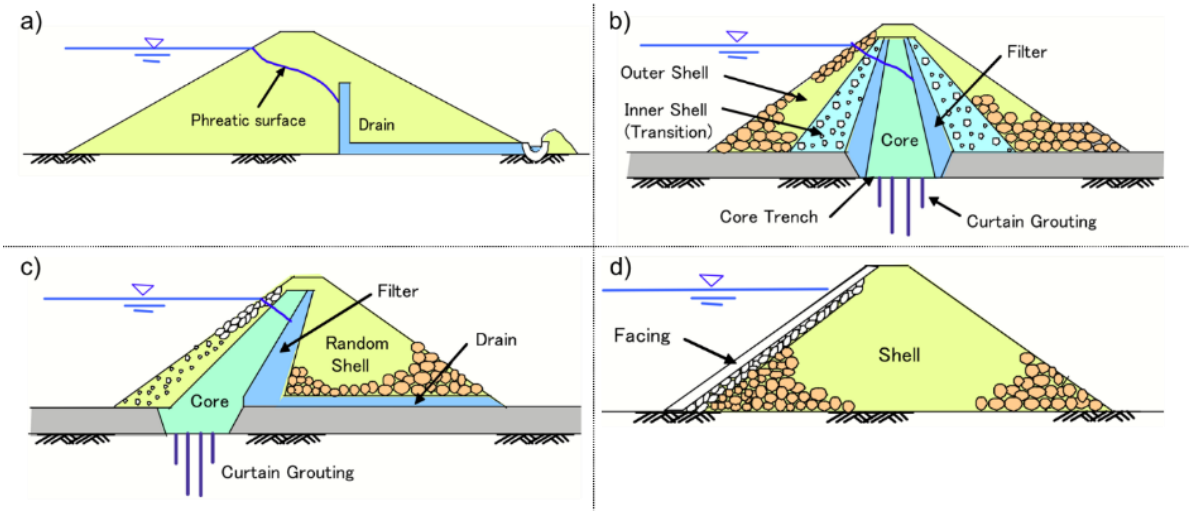


*Figure 2-2.Four generalised types of embankment dams: a) homogeneous earth dam; b) rockfill dam with a centrally located core; c) rockfill dam with an inclined core; d) rockfill dam with a facing (e.g. concrete). (Narita, 2000). Grain-size distributions of some materials used in such structures can be found in Figure 2-3.*

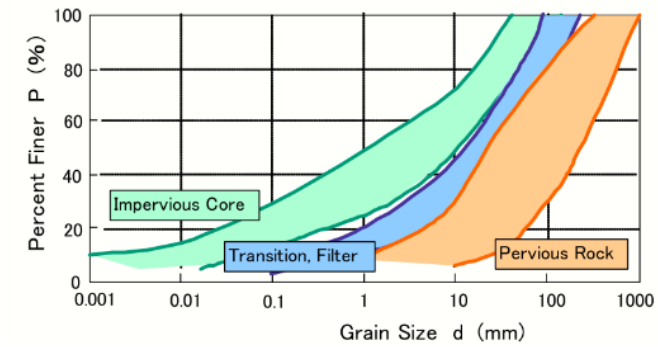


*Figure 2-3. Example of grain-size distributions of materials used in earth embankments (Narita, 2000).*

### 2.1.2 Types of failure in embankment dams

This section summarises some possible causes of damage or failure to earth embankments Figure 2-4. Such issues are largely caused by the interaction between the structure and the fluid being retained as well as by the effects of natural phenomena (weather, earthquakes) or even design or construction flaws.

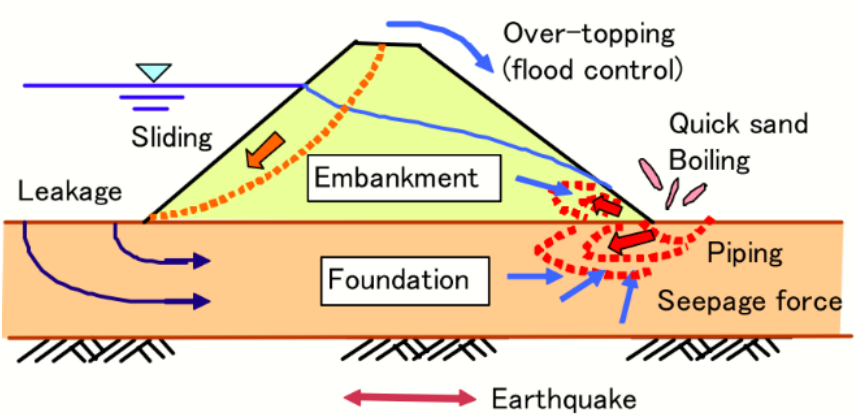


*Figure 2-4. Cross-section of earth embankment with overlapping indications of possible causes of damage. (Narita, 2000). Table 1. Lists such causes.*

*Table 1. Types of damage to embankment dams and their foundations, summarised (Narita, 2000):*

| | |
|---|---|
| Damage to embankment: | - Sliding (by pore-water pressure, earthquake)<br>- Deformation (settlement and lateral deflection)<br>- Leakage<br>- Hydraulic fracture (sand boil, piping, heaving)<br>- Overtopping |
| Damage to foundation: | - Bearing capacity surpass<br>- Settlement<br>- Leakage<br>- Hydraulic fracture<br>- Liquefaction |

*Sliding*: commonly caused by excessive and abrupt increase of pore-water pressure (e.g. built-up during construction, residual due to rapid drawdown of the reservoir) that can cause slope failures.

Seepage Failure (Hydraulic Fracture) When water flows passing through soil in an embankment and foundation, seepage forces act on soil particles due to its viscosity. If seepage forces acting in the soil are large enough as compared to the resisting forces based on the effective earth pressure, erosion by quick sand takes place by washing soil particles away from the surface, and piping successively develops as erosion gradually progresses.

*Table 2. Failure Causes in embankment dams during and after construction (Narita, 2000; Foster et al., 2000; USBR, 2015):*

| | |
|---|---|
| During construction: | - Pore water pressure built-up during construction<br>- Reduction of shear strength due to thixotropic[3] properties<br>- Slope stability |
| After construction: | - Internal erosion<br>- Piping<br>- Hydraulic fracturing<br>- Overtopping<br>- Slope instability<br>- Excess hydrostatic pressure due to rapid draw down<br>- Reduction in shear strength / Weathering, swelling of compacted soil<br>- Differential settlement and cracking<br>- Earthquakes<br>- Liquefaction of foundation |

In Fig.2.4(a), one possible effect of seepage through pervious foundation is hinted at, in which the uplift pressure acting on the impervious foundation causes heaving near the toe of the embankment. Hydraulic fracturing, quick sand and piping, can readily occur around the downstream toe when the hydraulic gradient increases with the concentration of flow lines, and the reduction in effective stresses is inevitable in the ground due to the action of the upward seepage forces, as illustrated in Fig.2.4(b). In an actual dam design, adequate drainage facilities such as filter zones and drains are provided in the interior of the embankment, and piping failures as stated above would not be expected to occur in ordinary situations. One of unusual situations to be considered is the generation of interior cracks in the impervious zone and foundation, which is mainly caused by differential settlements during and after construction, as described in the following.

Differential Settlement, Deformation and Cracking Many types of differential settlement and associated severe deformation such as open cracks appear in both dam body and base foundation, due to compressibility of fill materials and foundation soils and/or their relative rigidity. Fig.2.5 shows several patterns of differential settlement and open cracks which dam engineers often encounter in the field.

[3] Thixotropy: “the continuous decrease of viscosity with time when flow is applied to a sample that has been previously at rest and the subsequent recovery of viscosity in time when the flow is discontinued” (Mewis and Wagner, 2009); time-dependent shear thinning property; property of changing viscosity when depending on applied stress.

Earthquake Damage Embankment failures due to earthquake excitation can be classified into two groups. One isdamages caused by liquefaction or softening of sand foundation and the other is sliding and cracking of embankment body resting on hard foundation. In the former case, high excess pore-water pressure is generated during earthquake by the application of cyclic shear stresses, and large deformation as well as vertical displacement develops in the foundation. These deformations generally lead to catastrophic damages due to overtopping, as shown in Fig.2.6. According to the investigation reports on earthquake damages of actual embankment dams and also to the experimental studies through large scale shaking table tests on the dynamic response of earth and rockfill dams, embankment failures caused by strong excitation are classified into several patterns in their mechanism.

- Differential settlement causes tension cracks on the surface and inner open cracks near the point of sharp change in abutment configuration. Figure 2-5 (a).
- Existence of highly compressible layer of soil in foundation causes local settlement in the embankment, and inner open cracks between them. Figure 2-5 (b).
- Existence of relatively rigid structure causes inner open cracks due to differential settlement and deformation, especially during earthquake. Figure 2-5 (c).
- In a narrow central core, arching may take place in core zone which causes low confining stress and open cracks. Figure 2-5 (d).

Embankment failures due to earthquake excitation can be classified into two groups. One is damages caused by liquefaction or softening of sand foundation and the other is sliding and cracking of embankment body resting on hard foundation. In the former case, high excess pore-water pressure is generated during earthquake by the application of cyclic shear stresses, and large deformation as well as vertical displacement develops in the foundation. These deformations generally lead to catastrophic damages due to overtopping. Figure 2-5 (e).

During construction, shear stress on potential failure surfaces increases. Pore pressure also increases, since soil already in place is loaded as subsequent lifts are placed. A state of limit equilibrium can occur if the shear strength along a plane is reduced by pore pressure increase equating the shear stress required for equilibrium, resulting in sliding failures for both the upstream and downstream slopes. E.g. Phreatic surface in embankment almost remains unchanged when upstream water level goes down rapidly because of low permeability of fill material. Figure 2-5 (f).

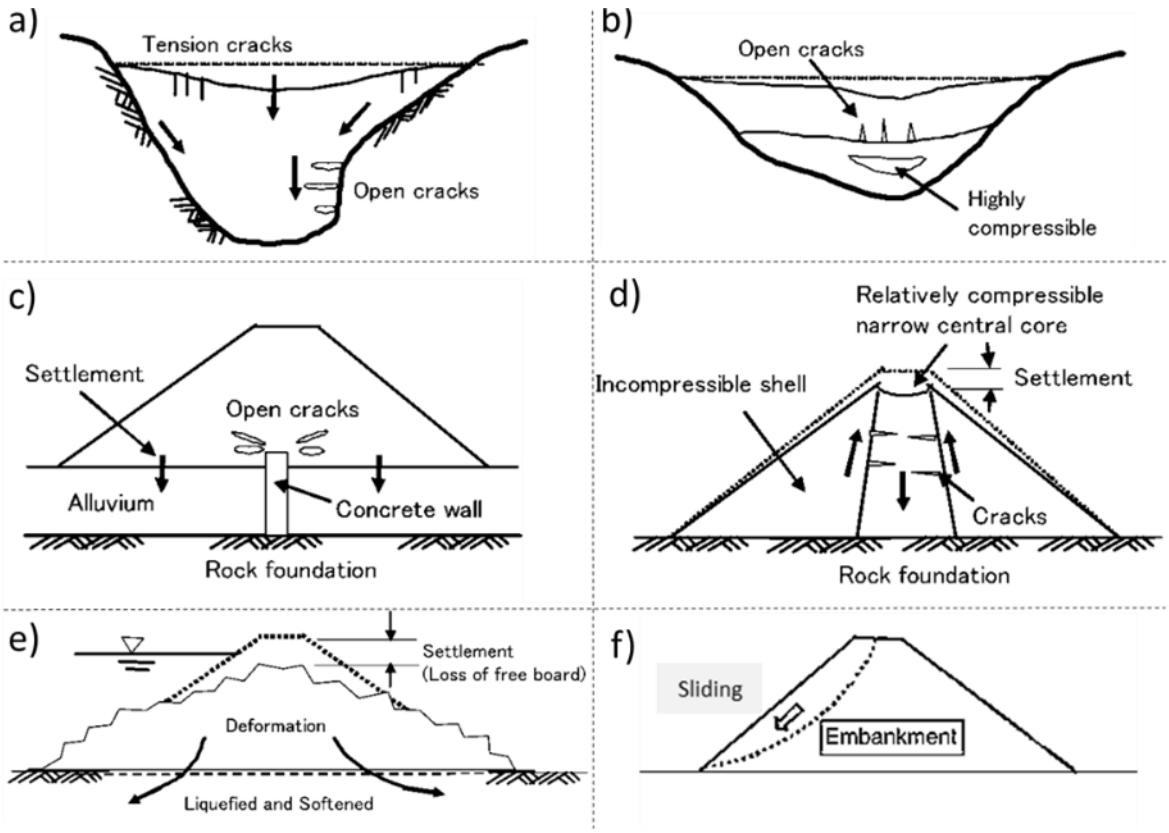


*Figure 2-5. Patterns of differential settlement causing cracks (a, b, c and d), overall shape loss/deformation (e) and sliding (f) due to e.g. shear stress reduction by pore pressure increase. Modified after Narita, 2000; Foster, 1999 and USBR, 2015.*

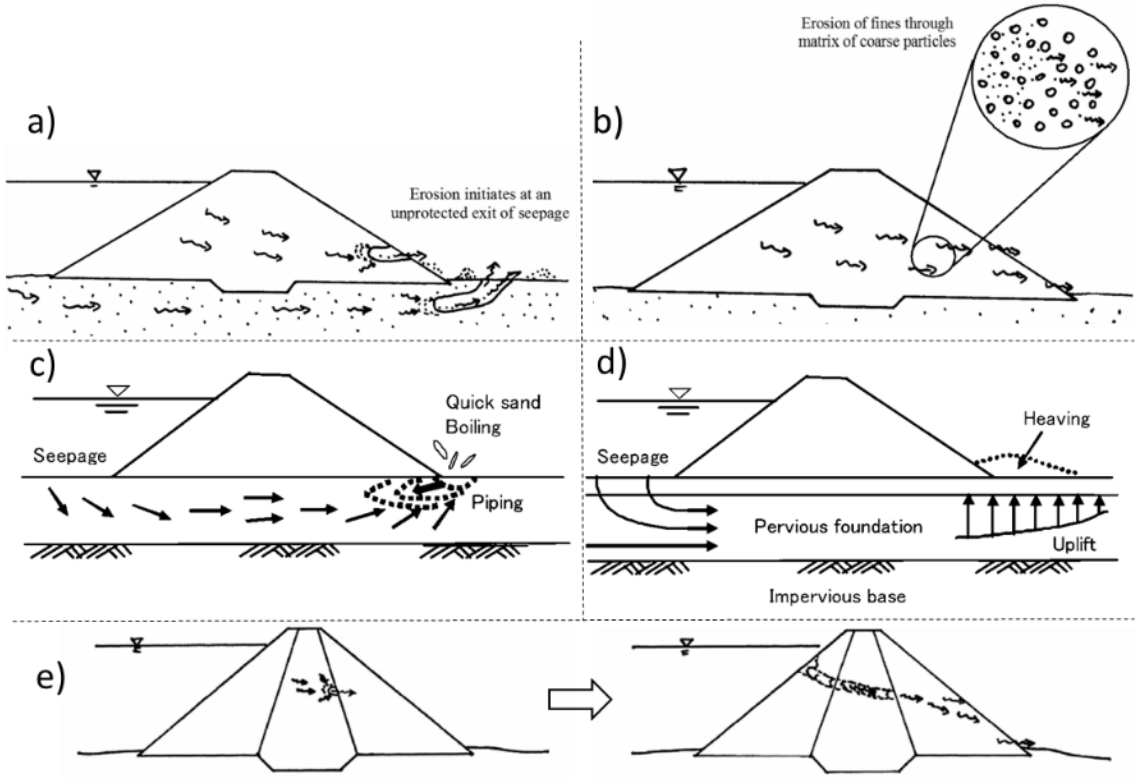


*Figure 2-6. Possible effects of water seepage through embankments: a) backward erosion piping, b) suffusion, c) sand boiling, d) progression of backward erosion (downstream side of core) through embankment. Modified after Narita, 2000; Foster, 1999 and USBR, 2015.*

Backward Erosion Piping: Erosion initiates at an exit point of seepage and progressively erodes back towards the source of water to form a continuous open ‘pipe’. Figure 2-6 (a).

Suffusion: (also called ‘internal instability): A form of mass erosion in which fines are transported by seepage flow through an internally unstable soil, usually one consisting of fine and coarse soil particles, with a deficiency of intermediate sized particles. Figure 2-6 (b).

Hydraulic Fracture: Concentration of flow lines at downstream toe leads to the increase in hydraulic gradient. Upward seepage force causes reduction in effective stresses in foundation, and quicksand and piping take place when counterweight loading is not enough. Hydraulic fracturing, quick sand and piping, can readily occur around the downstream toe when the hydraulic gradient increases with the concentration of flow lines, and the reduction in effective stresses is inevitable in the ground due to the action of the upward seepage forces. Figure 2-6 (c).

In Figure 2-4 one effect of seepage through pervious foundation is demonstrated, in which the uplift pressure acting on the impervious foundation causes heaving near the toe of the embankment. Seepage Through Pervious Foundation: Uplift pressure acts vertically on downstream side, so that counterweight fill or relief well are recommended to prevent heaving and local slide. Figure 2-6 (d).

Internal Erosion through the Embankment Initiated by Backward Erosion. Initiation: Leakage exits on the downstream side of core, and backward erosion initiates; Continuation: Erosion continues into the downstream shell (lack of a filter); Progression: Backward erosion progresses back to the reservoir or flood side; Breach/failure: Breach mechanism forms. (USBR, 2015). Figure 2-6 (e).

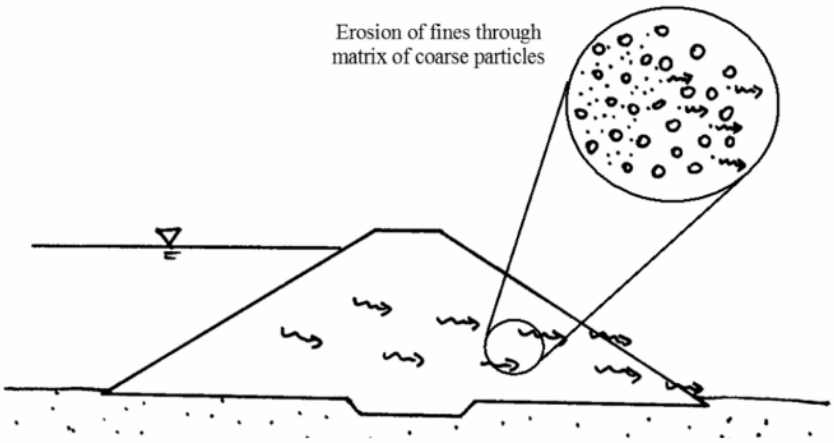


*Figure 2-7. Illustration of suffusion or internal instability in an embankment dam (Foster, 1999).*

Suffusion (Figure 2-7): (also called ‘internal instability) A form of mass erosion in which fines are transported by seepage flow through an internally unstable soil, usually one consisting of fine and coarse soil particles, with a deficiency of intermediate sized particles. This was focused on this thesis.

## 2.2 Instrumentation and monitoring of water-retaining earth structures

As there is a range of methodologies to assess structural damage, stability loss or seepage flow (Uhlemann et al., 2016a; Stark and Choi, 2008; Uhlemann et al., 2016b; Smethurst et al., 2017; Smith, 2015; Rinehart et al., 2012; Wightman et al., 2003; Smith et al., 2014), a comparison of these other techniques is required to investigate the potential benefits of AE, as follows. The works of Smith (2015), Uhlemann et al. (2016b) and more broadly Wightman et al. (2003) add up to a rather comprehensive evaluation of pertinent methods, but given their large variety and for the sake of brevity, here is a selection of the ones deemed more relevant to seepage erosion applications or that exemplify a kind of technique (Table 3):

*Table 3. Summary of methods for infrastructure monitoring.*

| Method | Brief description | Temporal resolution (TR)<br>Local spatial resolution ($SR_L$)<br>Global spatial resolution ($SR_G$) | Use on monitoring water-retaining infrastructures (simplified) | Basic comparison with AE regarding internal erosion |
|---|---|---|---|---|
| *Remote sensing:* | | | | |
| **Ground-penetrating radar** | Emits radio waves, usually in the range 10 MHz to 2.6 GHz (usually polarized), into the ground. When a permittivity boundary (i.e. materials with electrical properties) is found a portion of the energy is reflected [back], which is detected and used to for an image. The effective depth range is defined by the electrical conductivity of the material, the transmitted centre frequency, and the radiated power. (Davis and Annan, 1989; Yeboah-Forson et al., 2014) | TR: Survey dependant (non-real-time, sporadic)<br><br>$SR_L$: Approx. 1/10th of the size of the wavelength of the centre frequency: ~5-10 cm diam. down to ~50 cm depth for a 400 MHz signal.<br><br>$SR_G$: High – can survey entire structure (or large sections). Images subsurface (ca. 0.3 – 30m). | Mapping of the internal structure; Comparing different profiles can reveal the presence of water in the subsurface (e.g. due to seepage) as well as changes to the internal structure (e.g. due to erosion). Produces 2D images that can be combined to form a 3D model. | - Changes in water content (e.g. due to seepage) do not necessarily mean internal erosion.<br>- Changes in internal structure are likely due to already advanced destructive process.<br>- Does not detect suffusion. |
| **Light Detection and Ranging (LIDAR)** | Electromagnetic waves reflected from the surface are used to build a three-dimensional model of the surface. (Heckmann et al., 2012) | TR: Survey dependant, usually by aeroplane (non-real-time, “sporadic”)<br><br>$SR_L$: ~5-30 cm (or lower); variable, dependant e.g. on beam divergence, scanning angle, footprint, frequency.<br><br>$SR_G$: High – Can survey entire structure (or large sections). Limited to surface. | Changes of mapped surface contours (small changes in the topography) used to infer internal changes or larger phenomena (e.g. slope instability). | - Focuses on deformations of the surface.<br>- Limited to surface.<br>- Can only infer subsurface changes (which are likely due to already advanced destructive processes).<br>- Does not detect suffusion. |
| **Synthetic Aperture Radar (SAR) Interferometry** | Electromagnetic waves are emitted from a satellite and their reflection (back-scatter) on earth’s surface is used to produce areal images in which characteristics of the surface (e.g. roughness, composition). SAR uses the motion of the satellite relative to the surveyed landscape to improve spatial resolution. (Rosen et al., 2000; Moreira et al., 2013) | TR: Survey dependant, from Earth-orbiting satellite (non-real-time, “sporadic”)<br><br>$SR_L$: ~10 cm;<br>ultra-wideband ~5 mm; Terahertz SAR <1 mm (experimental).<br><br>$SR_G$: High – Can survey entire structure (or large sections). Limited to surface. | By inferring characteristics of the surface, a number of process can be identified – e.g. piping erosion can gather fines at the surface, creeping can sort the superficial material. | - Limited to surface.<br>- Can only infer subsurface changes (which are likely due to already advanced destructive processes).<br>- Does not detect suffusion. |

| Method | Brief description | Temporal resolution (TR)<br>Local spatial resolution ($SR_L$)<br>Global spatial resolution ($SR_G$) | Use on monitoring water-retaining infrastructures (simplified) | Basic comparison with AE regarding internal erosion |
|---|---|---|---|---|
| **Magnetometry** | A magnetometer is used to measure the direction, strength, or relative change of a magnetic field at a particular location and the data is used to non-intrusively characterize the subsurface as certain minerals produce or respond to magnetism; can monitor mechanical stress in ferromagnetic materials due to its effect on magnetic alignment (microscopic scale). (Witten, 2017; Rosenblum and Brownfield, n.d.; Freidman et al., 2014) | TR: Survey dependant ("sporadic"), although equipment can be (semi-) permanently installed.<br><br>$SR_L$: <1 mm to >1 m; highly variable.<br><br>$SR_G$: High – Can survey entire structure (or large sections). Images subsurface. | The amounts of materials (minerals, objects) that produce or respond to magnetism within the structure, and how they change over time, can be used to presume internal dislocation or sorting of particles (e.g. internal erosion can cause relative accumulations of relevant minerals). | - A magnetic anomaly or change is likely to be detectable only at an advanced stage of the process.<br>- Does not detect suffusion. |
| *Surface placement* | | | | |
| **Differential GPS** | Improvement upon the Global Positioning System (GPS) with improved location accuracy (from ~15 metres to about 1 cm). Uses a network of fixed ground-based reference stations to broadcast the difference between the positions indicated by the GPS satellite system and known fixed positions. (Hobbs, 2008; Marchamalo et al., 2011; Yastika et al., 2019) | TR: Long-term, real-time.<br><br>$SR_L$: ~1 cm<br><br>$SR_G$: Moderate - Individual measuring points; dependant on distribution of installed measurement points. | Changes in the surface shape can be used to infer internal changes or larger phenomena (e.g. slope instability). | - Limited to surface.<br>- Can only infer subsurface changes (which are likely due to already advanced destructive processes).<br>- Does not detect suffusion. |
| **Total station** | Electronic/optical instrument with a theodolite integrated with a rangefinder and a computer to collect data and perform triangulation calculations. Measures both vertical and horizontal angles and the slope distance from the instrument to a chosen point. (Marsella et al., 2020; Lipták, 2011; Artese et al., 2015) | TR: Survey-dependant or real-time (automated, permanent station(s)).<br><br>$SR_L$: ~0.5 mm to 1 cm<br><br>$SR_G$: Moderate - Individual measuring points; dependant on distribution of installed measurement points. | Changes in the surface shape can be used to infer internal changes or larger phenomena (e.g. slope instability). | - Limited to surface.<br>- Can only infer subsurface changes (which are likely due to already advanced destructive processes).<br>- Does not detect suffusion. |
| **Photogrammetry** | Uses photographic images and patterns of electromagnetic radiant imagery for obtaining information about physical objects and the environment. (Nagendran et al., 2019; Bar et al., 2020; James et al., 2019; Colomina and Molina, 2014) | TR: Survey-dependant or real-time (automated, permanent station(s)) if circumstances allow.<br><br>$SR_L$: < 1mm to >1m; dependant on pixel size.<br><br>$SR_G$: High – Can survey entire structure (or large sections), although can also be close-range. | Comparison of different images separated by time might reveal relevant changes to the structure (e.g. settlement, wet spots (colour), cracks, formation of concavities, creep, etc) | - Limited to surface.<br>- Can only infer subsurface changes (which are likely due to already advanced destructive processes).<br>- Does not detect suffusion. |

| Method | Brief description | Temporal resolution (TR)<br>Local spatial resolution ($SR_L$)<br>Global spatial resolution ($SR_G$) | Use on monitoring water-retaining infrastructures (simplified) | Basic comparison with AE regarding internal erosion |
|---|---|---|---|---|
| **Tilt meter** | Detects the rotational component of the movement of the surface where it is installed (not perceiving translational movement). Types include electrolytic tilt meter (spirit level), tilt meter with pendulum, tilt meter with servo accelerometer). (Uhlemann et al., 2016b; Koo and Suh, 2001; Martínez-Rincón et al., 2017) | TR: Long-term, real-time.<br><br>$SR_L$: <1mm<br><br>$SR_G$: Low – limited to individual station(s) | Changes in the surface shape can be used to infer internal changes or larger phenomena (e.g. slope instability). Long-term, real-time. | - Limited to surface.<br>- Can only infer subsurface changes (which are likely due to already advanced destructive processes).<br>- Does not detect suffusion. |
| **Extensometer** | Measures changes in the length of an object (change in the distance between two points). Used for stress-strain measurements and tensile tests. (Hiep and Chung, 2018; Kim and Won, 2003; Lin and Tang, 2005) | TR: Long-term, real-time.<br><br>$SR_L$: <1mm.<br><br>$SR_G$: Low – limited to individual station(s) | Detection of (unidirectional) deformations of the structure by measuring the distance between two arbitrary/relevant points on its surface. | - Limited to surface (although can be integrated to the structure e.g. during its construction).<br>- Can only infer subsurface changes (which are likely due to already advanced destructive processes).<br>- Does not detect suffusion. |
| **Pendulum** | A wire is anchored to the structure under observation with a tensioning weight suspended from the lower end, which is free to move in an oil (to damp oscillations of the wire) tank. Horizontal movements are measured by detecting displacements relative to the wire. (Barzaghi et al., 2018; Chikahisa et al., 2004; Colque Espinoza and Brylawski, 2007; Christie et al., 2019) | TR: Long-term, real-time.<br><br>$SR_L$: <1mm.<br><br>$SR_G$: Low – limited to individual station(s) | Monitoring of horizontal structural movements of large structures such as dams. | - Limited to surface.<br>- Can only infer subsurface changes (which are likely due to already advanced destructive processes).<br>- Does not detect suffusion. |
| **Accelerometer** | Measures proper acceleration, the acceleration (the rate of change of velocity) of a body in its own instantaneous rest frame. (Oskay and Zeghal, 2011; Beemer et al., 2018; Kim et al., 2018; Jayawardana et al., 2016) | TR: Long-term, real-time.<br><br>$SR_L$: <1mm.<br><br>$SR_G$: Low – limited to individual station(s) | Useful for monitoring ground surface movements (i.e. dynamic loads) like earthquakes or by rapid and brittle slope deformations. | - Limited to surface (although can be integrated to the structure e.g. during its construction).<br>- Can only infer subsurface changes (which are likely due to already advanced destructive processes).<br>- Does not detect suffusion. |
| **Seismometer** | Installed on the surface, it detects ground motions (vertical and/or horizontal) that can be used to infer disturbances to the structure. | TR: Long-term, real-time<br><br>$SR_L$: ~50V/m; 500 to 0.00118 Hz<br><br>$SR_G$: Low - limited to individual station(s). | Monitors ground surface movements. | - Limited to surface.<br>- Can only infer subsurface changes (which are likely due to already advanced destructive processes).<br>- Does not detect suffusion. |

| Method | Brief description | Temporal resolution (TR)<br>Local spatial resolution ($SR_L$)<br>Global spatial resolution ($SR_G$) | Use on monitoring water-retaining infrastructures (simplified) | Basic comparison with AE regarding internal erosion |
|---|---|---|---|---|
| **Seismics/Sub-bottom Profiling** | Seismic waves (mechanical perturbations) are induced and, when travelling through a medium and meets acoustic impedance boundaries, some of the energy gets reflected while another portion of it continues through (refracted), with the remainder of the energy being subject to the same process until all of it is dissipated. The two-way travel time (source – reflector – detector) of the waves as well as their velocity are used to reconstruct the pathways taken by the waves and ultimately form an image of the subsurface. (Kwee, 2018; Pehme, 2011; Dondurur, 2018; Yaacob and Mustapa, 2010; Doughty et al., 2014)<br><br>(a)product between wave velocity and density of the medium. Influenced by the mechanical properties. | TR: Survey dependant (non-real-time, "sporadic"), although equipment can be installed at location.<br><br>$SR_L$: <10cm<br><br>$SR_G$: High – Can survey entire structure (or large sections). Images subsurface. | Combining the framework of imaged reflectors (i.e. impedance boundaries) helps construct an image of the subsurface. Changes over time (e.g. changes in the shape and intensity of reflectors, appearance of new ones) can be used to infer changes to the internal structure such as dislocations of the phreatic surface, (re-) deposition of a layer of material, erosion. Produces 2D images that can be combined to form a 3D model. | - Difficulty to establish if inferred phenomenon is active, inactive, or transient.<br>- Change is likely to be detectable only at an advanced stage of the process*.<br>- Does not see water flow.<br>- Does not detect suffusion. |
| **Crack/joint gauges** | Uses the relative movement between fixed positions on different sides of a crack or joint to measure dislocations over time (e.g. crack widening). (Sasaki et al., 2020; Ibrahim et al., 2010; Ju et al., 2019) | TR: Long-term, real-time.<br><br>$SR_L$: <1mm.<br><br>$SR_G$: Low - limited to individual station(s). | Widening/closing of joints used as a proxy to structural deformation/damage. | - Can only infer internal changes to the structure, which are then likely due to already advanced destructive processes*.<br>- Does not detect suffusion. |
| *Subsurface placement* | | | | |
| **Inclinometer** | Probe containing a series of detectors installed either on the ground or in structures (e.g. through a borehole) and, based on spatial orientation changes in each sensor, measures localized displacements with respect to gravity's direction. (Fathi and Golestani, 2017; Dixon et al., 2014; Smith, 2015; Stark and Choi, 2008; Dixon et al., 2010) | TR: Long-term, real-time.<br><br>$SR_L$: <10mm (limited to along/adjacent to borehole).<br><br>$SR_G$: Low - limited to individual station(s). | Deformations along the borehole suggest deep sitting changes to the overall structure (e.g. slope instability). | - Changes to the structure are likely due to already advanced processes*.<br>- Does not detect suffusion.<br>- Impaired by excessive localised bending or twisting of its casing |
| **Borehole extensometer** | A borehole encases extensometers that measure localised unidimensional deformations. (Bayoumi, 2011; Riley, 1969; Liu et al., 2019b; Wang et al., 2014) | TR: Long-term, real-time.<br><br>$SR_L$: <1mm (limited to along/adjacent to borehole).<br><br>$SR_G$: Low to medium - limited to individual station(s) or borehole length. | Deformations along the borehole suggest deep sitting changes to the overall structure (e.g. slope instability). | - Changes to the structure are likely due to already advanced processes*.<br>- Does not detect suffusion. |

| Method | Brief description | Temporal resolution (TR)<br>Local spatial resolution ($SR_L$)<br>Global spatial resolution ($SR_G$) | Use on monitoring water-retaining infrastructures (simplified) | Basic comparison with AE regarding internal erosion |
|---|---|---|---|---|
| **Time domain reflectometry (TDR)** | A coaxial cable installed in a borehole is subject to a voltage pulse and if a change in the characteristic impedance of the cable is encountered by the pulse (due to localised deformation) a reflection occurs (in proportion to the cable deformation) and is detected by a connected oscilloscope. (Lu et al., 2019; Bai et al., 2019; Zhu et al., 2019; Bashan et al., 2018; Curioni et al., 2019) | TR: Long-term, real-time.<br><br>$SR_L$: <1cm (limited to along/adjacent to borehole; worsens with cable length).<br><br>$SR_G$: Low to Medium – limited to station (e.g. borehole) but cable can also be buried along structure. | Deformations along the borehole suggest deep sitting changes to the overall structure, e.g. slope instability. | - Changes to the structure are likely due to already advanced processes*.<br>- Focuses on slope movements.<br>- Does not detect suffusion. |
| **Fibre-optics** | Optical fibres within the sediment have their impedance influenced by minute environmental changes like strain, pressure, displacement, and temperature. E.g. Brillouin Optical Time Domain Reflectometry – BOTDR. (Soga and Schooling, 2016; Gong et al., 2019; Torisu et al., 2019; Zalesky et al., 2014; Kammann et al., 2017) | TR: a) Long-term, real time.<br><br>$SR_L$: <1mm (limited to along/adjacent to cable; worsens with cable length).<br><br>$SR_G$: Medium – can be installed along large parts of structure. | Detection of structural deformation along the fibre as well as changes relative to the fluid within the structure, like pressure and temperature. | - Although can help identifying leakages and/or other risk assessment(s), does not detect suffusion ** |
| **Accelerometer (Shape Accel Array, SAA; borehole array)** | String of micro-electro-mechanical systems (MEMS) sensors. Measures three-dimensional displacements and can be installed vertically inside boreholes to provide deformation vs. depth profiles, or horizontally along the ground surface to provide deformation vs. distance. (Oskay and Zeghal, 2011; Uhlemann et al., 2016a; Liu et al., 2019a; Ni and Gao, 2014; Zhang et al., 2017) | TR: a) Long-term, real time.<br><br>$SR_L$: ~1mm/20m (limited to along/adjacent to borehole; worsens with cable length).<br><br>$SR_G$: Medium – limited to borehole length. | Deformations along the borehole suggest deep sitting changes to the overall structure (e.g. slope instability). | - Changes to the structure are likely due to already advanced processes.<br>- Focuses on slope movements.<br>- Does not detect suffusion. |
| **Settlement sensor** | Used for measuring vertical movements within a structure caused by settlement deformations. E.g. based on fluid displacement/pressure change in tubes through structure. (Ardalan and Jafari, 2012) | TR: a) Long-term, real-time<br><br>$SR_L$: ~0.025% of full scale.<br><br>$SR_G$: Medium – limited to system length. | Settlement (on the built structure and/or on the surrounding "natural" subsurface), which can normally result from construction itself or filling/emptying of reservoir, can produce patterns recognisable as harmful or not, based on broader knowledge/assumptions about such processes and the particular case. | - Changes to the structure are likely due to already advanced processes*.<br>- Does not detect suffusion. |
| **Hydroprofile meter** | Liquid is pushed through a hose and, at predetermined positions, the level of the liquid is measured relative to a reference level, thus determining the vertical position of the hose at these points. (Radzicki, 2016) | TR: a) Long-term, real-time<br><br>$SR_L$: ~1mm<br><br>$SR_G$: Medium – limited to system length. | Used for the linear monitoring of vertical displacements along the length of the structure. | - Changes to the structure are likely due to already advanced processes.<br>- Does not detect suffusion. |
| *Groundwater and pore-water pressure:* | | | | |

| Method | Brief description | Temporal resolution (TR)<br>Local spatial resolution ($SR_L$)<br>Global spatial resolution ($SR_G$) | Use on monitoring water-retaining infrastructures (simplified) | Basic comparison with AE regarding internal erosion |
|---|---|---|---|---|
| **Piezometer** | Probe that detects punctual changes in pore-water pressure, which directly influence the effective stress regime. (Uhlemann et al., 2016b; Borragan and Vazquez, 2014; Fathi and Golestani, 2017; Cita Sari et al., n.d.; Kasireddy et al., 2015; Uhlemann et al., 2016a) | TR: Long-term, real-time (if equipment permanently installed)<br><br>$SR_L$: ~0.1% of measurement range<br><br>$SR_G$: Low to medium – limited to individual probing position but relatively simple to have several positions (and often found in existing structures) | Changes in pore pressure, especially in different points of structure, help detecting related anomalies (e.g. concentrated flow) and/or eventual progression of hydrology in time. | - Although can help identifying leakages and/or assess other risk(s), does not detect suffusion** |
| **Rain gauge** | Used to monitor rainfall/precipitation within an area, which is then used to infer the relative stability of a slope due to predicted changes in pore-water pressures (e.g. tipping bucket). (Moriyama et al., 2016; Zhi et al., 2016; White et al., 2012; Mori, 2007; Chou et al., 2013) | TR: Long-term, real-time (if equipment permanently installed)<br><br>$SR_L$: <1mm; dependant on gauge used.<br><br>$SR_G$: Low to high - limited to individual station(s) but simple and cheap enough to be installed all over structure (and precipitation tends to be rather homogeneous over large areas). | Precipitation patterns associated with knowledge about structure and relevant region (e.g. local geology, stratigraphy) inform models about structural safety (e.g. precipitation levels considered dangerous). | - Helps estimate if measured conditions can overwhelm structural safety limits but not directly measure structural damage, much less internal erosion. |
| **Standpipe** | Simplest instrument for ground water level measurement - a borehole provides direct open access to the water depth, measured e.g. with a level gauge. | TR: Long-term, real-time (if equipment permanently installed)<br><br>$SR_L$: ~1cm<br><br>$SR_G$: Low - limited to individual station(s). | Changes in phreatic surface height, especially in different points of structure, help detecting related anomalies (e.g. concentrated flow) and/or eventual progression of hydrology in time. | - Although can help identifying e.g. leakages, does not detect suffusion** |
| **Soil moisture probe** | Used the relative permittivity of the medium to derive its moisture content. Primarily done through time-domain reflectometry; and capacitance sensors (i.e. employing the medium as a dielectric). (Campora et al., 2019; Kojima et al., 2016; Hardie et al., 2013; Schlaeger et al., 2005) | TR: Long-term, real-time (if equipment permanently installed)<br><br>$SR_L$: 0 to 100% of water content ±3%<br><br>$SR_G$: Low - limited to individual station(s). | Changes in soil moisture help inferring anomalies that could represent danger to the structure. | Although can help identifying e.g. leakages, does not detect suffusion** |
| **Electrical resistivity tomography** | An electric current (which can be affected by moisture content, porosity, discontinuities, mineral composition) is induced through the ground, measured by electrodes, and used to build a resistivity map. (Hellman et al., 2017; Ferdos, 2016; Perrone et al., 2014; Witten, 2017) | TR: Long-term, real-time (if equipment permanently installed, otherwise survey-dependant)<br><br>$SR_L$: ~5% of electrode spacing<br><br>$SR_G$: Medium – limited by number of used electrodes but can be installed along large parts of structure. | Changes in water content or porosity can be detected and used to interpret changes to the internal structure. Produces 2D images that can be combined to form a 3D model. | Although can help identifying leakages and/or other risk assessment(s), does not detect suffusion ** |

| Method | Brief description | Temporal resolution (TR)<br>Local spatial resolution ($SR_L$)<br>Global spatial resolution ($SR_G$) | Use on monitoring water-retaining infrastructures (simplified) | Basic comparison with AE regarding internal erosion |
|---|---|---|---|---|

*Once structural deformation is under way there can be considerable uncertainty about later stages, possibly ranging from slow and smooth to fast and violent. Detecting internal erosion (before structural deformation) with AE would allow for earlier warning and better insights about the active internal mechanisms of the examined structure.

**Although these methods do have the capacity to measure events that happen in correlation with suffusion (i.e. changes in water pressure, temperature and moisture content - all directly or indirectly affected by fluid flow and instrumental for identifying hazardous areas), they do not ascertain if particle movement or erosion is active (Samiec, 2012; Zhu et al., 2008; Smith, 2015) . The use of AE, conversely, supports this ability.

## 2.3 Internal erosion

### 2.3.1 Seepage-induced internal erosion

Fundamentally, seepage erosion consists of water flowing through a granular porous medium (e.g. soil) and causing the dislodgement of the finer particles through the gaps between the coarser ones, or the soil skeleton, with e.g. effective stress, hydraulic gradient and the grain-size distribution being key variables (controlling and/or responding to) its occurrence (Moffat and Fannin, 2006; Slangen and Fannin, 2017b; Hunter and Bowman, 2017b; Wan and Fell, 2008). This process, which can severely compromise the structural integrity of critical infrastructure, has been reported in many different settings (e.g. fluvial terraces, stream banks, dams, levees) and in a variety of material configurations. A large range of disturbances, anthropogenic and natural (e.g. changes in hydraulic conditions, trenches, pipelines, topographic modifications), have the capacity to trigger internal erosion and result in unexpected failures; Figure 2-9 (Crosta and Prisco, 1999; Camici et al., 2017; Rönnqvist and Viklander, 2018). According to Fell et al. (2003), internal erosion has caused failure of about 1 in every 200 (0.5%) embankment dams: 50% occurring within the embankment fill, 40% in the foundations, and 10% progressing from the embankment to the foundation. The considerable number of incidents involving distressed water-retaining earth structures therefore calls for a better understanding of the deterioration mechanisms at play and the development of methodologies for its circumvention.

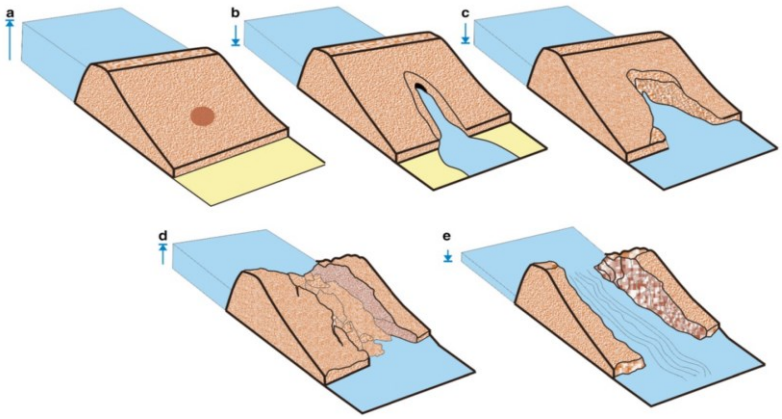


*Figure 2-8. Phases of dam breaching process: a) Wet spot at the downstream slope b Formation and growth of a piping hole c Pipe progression and enlargement d Pipe roof collapse e Final breach profile of the dam. (Okeke and Wang, 2016)*

Approximately two thirds of embankment dam failures happen on the first filling or in the first 5 years of operation (Fell et al., 2003). Internal erosion incidents might occur with a relative slow progression, e.g. after several decades of operation (many of such structures in use date to the early 20$^{th}$ century or earlier), or they might occur relatively rapidly with just a few hours between the first observation of irregularities (e.g. leaks, sinkholes, cavities, slope

deformation) and breach of the dam (Chang et al., 2014; Fell et al., 2003; ICOLD, 2016). See Figure 2-8 and Figure 2-10.

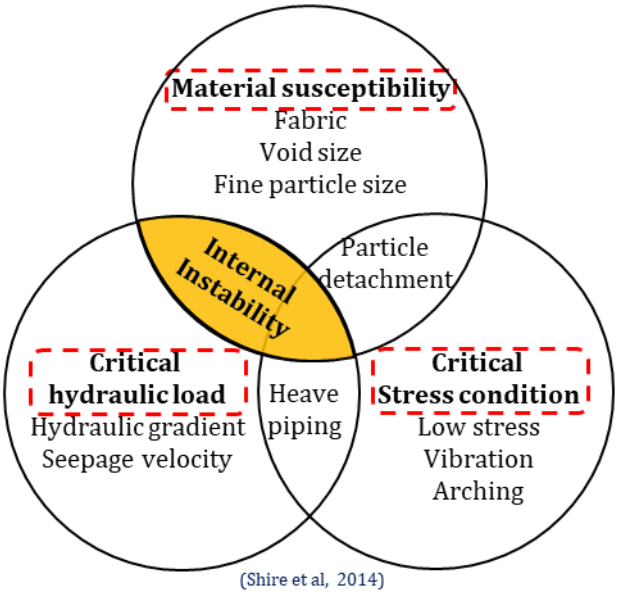


*Figure 2-9. Venn diagram of variables involved in the onset of internal instability (Shire et al., 2014).*

The unpredictability of how fast earth dams might collapse offers a challenge and indicates that detecting the processes responsible for [eventually irreversible] structural damage (e.g. suffusion) in their earlier stages (i.e. before externally visible damage occurs, or when effective remediation is still feasible) is exceptionally important since after these earlier stages the likelihood of a successful solution is very drastically reduced. In other words, the capacity to detect a detrimental process before it caused significant (and repairable) damage is arguably vital for disaster avoidance in the context of substantial water-retaining structures (Kossoff et al., 2014; Foster et al., 2000; Rico et al., 2007; Bolton Seed and Duncan, 1987; de Rubertis, 2018; U.S. Department of the Interior, 2012).

Furthermore, studying for instance the particle distributions, geometries and arrangements vulnerable to internal erosion, idealized, reductive models or other such approaches is in many (or most) cases not useful considering already built structures – these approaches seem more useful as tools for designing new structures. That because, simply by virtue of ordinary structural imperfections, mere discrepancies between their projects and the actual construction, (besides of course when information is not even available; especially in tailings dams) and so on, numerous operational dams and levees cannot have their constitution known in enough detail to evaluate the applicability of such studies, thus implicating in a range of assumptions that in turn increase the risk of mistakes (Kuranchie, 2015; Krutov, 2019; Smalley and Dijkstra, 1991; Marcello et al., 2009; Bolton Seed and Duncan, 1987; Ardalan and Jafari, 2012; Fell et al., 2003; Barzaghi et al., 2018).

Therefore, the development of an approach capable of identifying the occurrence of suffusion regardless of knowing (or successfully conjecturing about) every relevant detail (e.g. the geometry and grain-size distribution of the used materials) of a given earth structure is valuable for its effective monitoring and disaster avoidance.

In one sentence, knowing that damage is under way is better than guessing it.

The U.S. Bureau of Reclamation states that the potential for loss of life in dam failure events is very dependent on the warning time available to evacuate the population at risk, suggesting that warnings as little one hour ahead of failure can have a significant impact on reducing the number casualties (Fell et al., 2003). Current monitoring techniques still do not offer viable early warning systems for the early stages of seepage-induced internal erosion (2.2; Figure 2-10).


*Figure 2-10. Teton Dam in Idaho, USA; 93m high earth zoned embankment. A) Morning of June 5th, 1976: leak from right abutment; B) Mid-morning: leak had enlarged upwards through the dam; C) Mid-day: further enlarged and widened leak under crest. The dam failed during first filling on June 5th, 1976. Except for clear water flows about 400m and 600m downstream of the dam (first seen on June 3rd), and a seep about 50m downstream, no sign of compromising damage had been seen until the morning of June 5th, when a sediment laden leak was observed flowing from the abutment. The leakage and erosion accelerated and by midday the dam had failed. (ICOLD, 2016).*

*Figure 2-11. Teton Dam site at present. This incident resulted in 14 deaths property damage of up to US$1 billion. The dam has not been rebuilt . (ICOLD, 2016).*

### *Suffusion and suffosion*

There is partial agreement amongst the internal erosion research community on the definitions of suffusion and suffosion (Fannin and Slangen, 2014; Ke and Takahashi, 2012; Horikoshi and Takahashi, 2015; Ke and Takahashi, 2014; Rönnqvist and Viklander, 2015). The following definitions are used here:

¶ *Suffusion*: erosion of finer particles from a coarser matrix caused by seepage flow and is manifested as a combination of detachment, transport, and potential filtration of the finer fraction. It can promote a change in particle size distribution, porosity, and hydraulic conductivity of the material.

¶ *Suffosion*: material loss caused by seepage flow and accompanied by a volume reduction or structural collapse[4] (Fannin and Slangen, 2014; Ke and Takahashi, 2014; Rochim et al., 2017; Moffat et al., 2011); Figure 2-12 , Figure 2-14 and Figure 2-15.

*Primary fabric and loose particles:* As a granular material, soil is represented by solid particles forming a solid structure with interconnected pores that contain fluids. Of the particles composing the soil, some have a role at transferring stress and forming force chains through the structure (i.e. the primary fabric), while others are instead loosely placed in the gaps pervading the primary fabric - they are held under their own weight or the weight of other directly adjacent loose particles. Despite scarcely taking part in effective stress transfer, these loose particles do have an effect in the geotechnical properties of the soil, like the bulk density and the hydraulic conductivity; Figure 2-12 and Figure 2-14. Relevantly, favourable conditions allow loose particles to be displaced by suffusion (To et al., 2016; Hunter and Bowman, 2017a; Koerner et al., 1981; Wan and Fell, 2008; Ferdos et al., 2018).

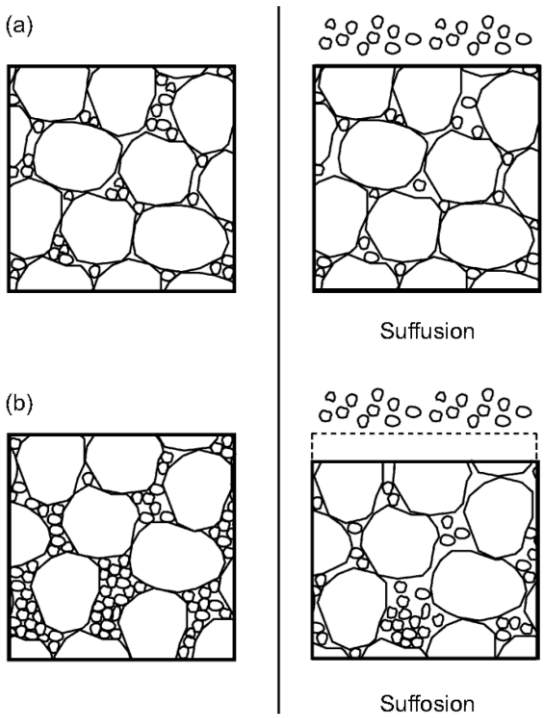


*Figure 2-12. Conceptual visualisation of both a) suffusion and b) suffosion (modified after Fannin and Slangen, 2014).*

[4] There is disagreement about the definition of suffosion containing destructive and non-destructive phenomena (Fannin and Slangen, 2014) but this research considers these as embraced by the term.

Suffusion produces an increase in permeability and possibly initiation of other internal erosion mechanisms as the selective erosion of finer particles from the matrix of coarser particles of an internally unstable soil so that the finer particles are removed through the voids between the larger ones by seepage flow, leaving behind a soil skeleton formed by the coarser particles, as shown in Figure 2-13. (USBR, 2015).

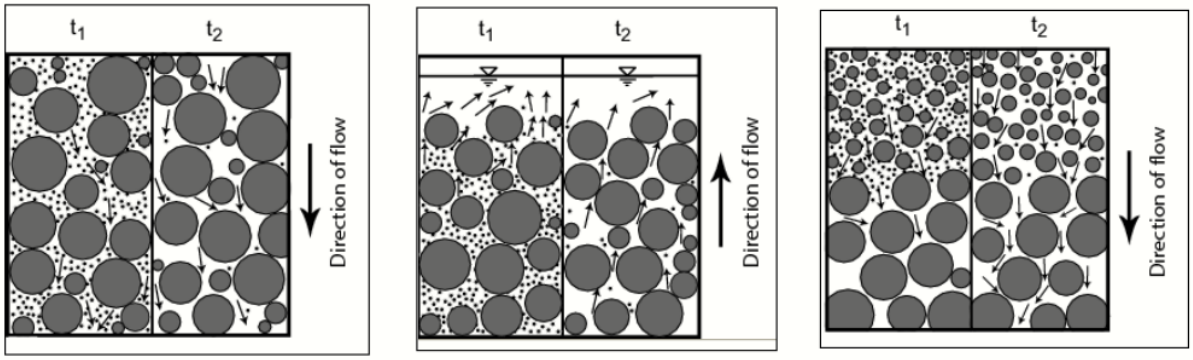


*Figure 2-13. Selective erosion of finer particles from coarser matrix. (USBR, 2015)*

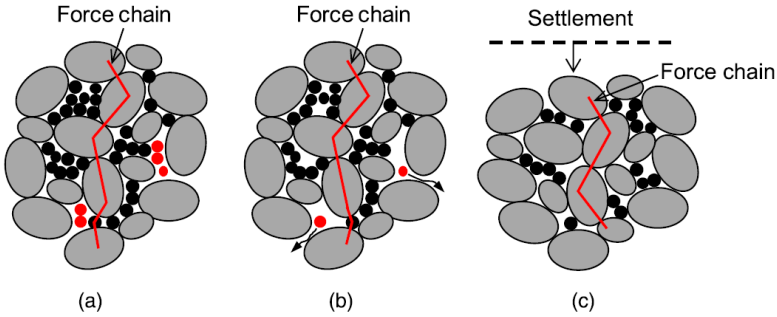


*Figure 2-14. Representation of soil microstructure at: (a) initial state, (b) initiation of internal erosion, (c) significant skeleton deformation (Chang and Zhang, 2013a).*

### 2.3.2 Influential factors

Given the relevance of the phenomena at hand, assessing their likelihood in different cases becomes indispensable. A clear distinction should be made between the potential and the actual onset of suffusion (Langroudi et al., 2015) - a soil might be internally instable (0) but for suffusion to occur certain conditions (e.g. a certain hydraulic gradient, flow velocity, effective stress) still have to be met.

#### *Internal instability*

As explained by Fannin and Slangen in 2014, the first attempt to systematically and empirically analyse internal (or 'inherent') [in]stability was made by the United States Army Corps of

Engineers (USACE, 1953) and sought to define an ideal filter gradation by testing sand and gravel mixtures with a permeameter[5].

The internal stability of a cohesionless soil[6] to seepage erosion can be defined as the susceptibility it has to have its particles displaced by an imposed hydraulic gradient, and is mainly dependant on the grain-size distribution of the soil (Moraci et al., 2014; Dallo et al., 2013; Fannin and Slangen, 2014). The distribution and types of particles in the employed construction materials turn out to be a robust (though not sufficient; good but not flawless) vulnerability predictor. Simply put, materials in which the finer particles can be transported through the gaps between the coarser particles are [internally] unstable or susceptible to seepage erosion. From this geometric criterion it can be found that the grain-size distributions of unstable soils are gap-graded (Fannin et al., 2015; To et al., 2016; Li, 2008; Rosenbrand, 2011; Horikoshi and Takahashi, 2015); Figure 2-12, Figure 2-14 and Figure 2-15. A synthesis of the factors governing internal instability can be seen in Figure 2-9.

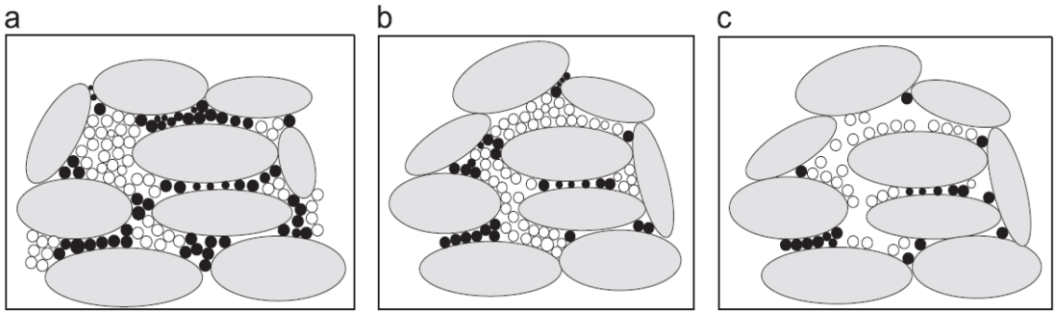


*Figure 2-15. Conceptualization of soil microstructures in which pore spaces that are only partially filled with soil grains are erodible. There can be a supposed relation between the initial content of fine particles and erodibility. Initial fines content in a), b) and c) are respectively 35%, 25% and 15% (Ke and Takahashi, 2014).*

Some of the most prominent methods for geometrically determining internal stability are summarised in Table 4:

*Table 4. Geometric criteria for evaluating soil internal stability (Chang and Zhang, 2013b)*

| | |
|---|---|
| Istomina (1957) | $C_u \leq 10$: internally stable<br>$10 \leq C_u \leq 20$: transitional<br>$C_u \geq 20$: internally unstable |
| Kezdi (1969) | $(d_{15c}/d_{85f})_{max} \leq 4$: internally stable |

[5] This work has since then been substantially enriched by several contributions. Some of the most notable are: Kezdi (1979), Kovács (1981), Sherard (1979), Kenney & Lau (1985, 1986), Burenkova, (1993), Wan & Fell (2008), Skempton & Brogan (1994) and Li & Fannin (2012).

[6] Cohesionless soils: mineral soils that exhibit granular characteristics in which the grains remain separate from each other and do not form clods or hold together in aggregates of particles. They exhibit shear strength that has only a friction component with zero cohesion intercept. Include sand, loamy sand, and possibly sandy loam if the silt-sized particles are non-plastic or non-sticky (Keaton, 2018)

| | |
|---|---|
| Kenney and Lau (1985) | $(H/F)_{min} \geq 1.0$: internally stable |
| Burenkova (1993) | $0.76\log(h'') + 1 < h' < 1.68\log(h'') + 1$: internally stable |
| Wan and Fell (2008) | $30/\log(d_{90}/d_{60}) < 80$, or<br>$30/\log(d_{90}/d_{60}) < 80$ and $15/\log(d_{20}/d_5) > 22$: internally stable |
| Li and Fannin (2008) | For F<15, $(H/F)_{min} \geq 1.0$: internally stable<br>For F>15, $H \geq 15$: internally stable |
| *Cu* = coefficient of uniformity; *H* = mass fraction of particles ranging from *d* to *4d* (assuming that a particle of size *d* can pass through the gaps between particle sizes ≥ *4d*); *F* = mass fraction of particles finer than grain size *d*; $d_{15c}$ = diameter of the 15% mass passing in the coarse part; $d_{85f}$ = diameter of the 85% mass passing in the fine part; $h' = d_{90}/d_{60}$; $h'' = d_{90}/d_{15}$; $d_{90}$, $d_{20}$, $d_{15}$, and $d_5$ = diameters of the 90% , 20%, 15%, and 5% mass passing, respectively. | |

The criteria defined by Burenkova (1993), Kenney and Lau (1985), Kezdi (1969) and Wan and Fell (2008) can be shown in Figure 2-16, Figure 2-17 and Figure 2-18.

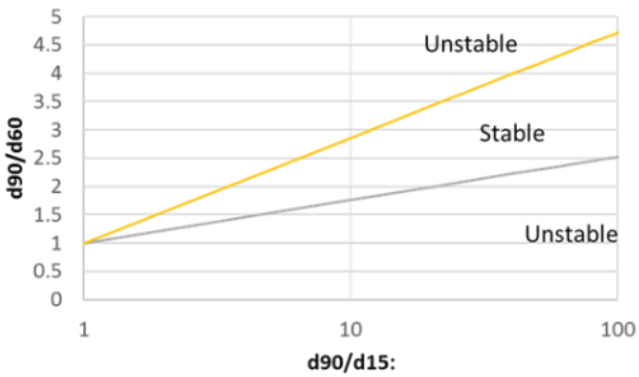


$$0.76\log(d_{90}/d_{15})+1 < d_{90}/d_{60} < 1.86\log(d_{90}/d_{15})+1$$

*Figure 2-16. Plot of the Burenkova (1993) internal stability criterion, where upper and lower limits for the calculated stability area are defined based on the soil gradation. The corresponding formula for its construction is shown below.*

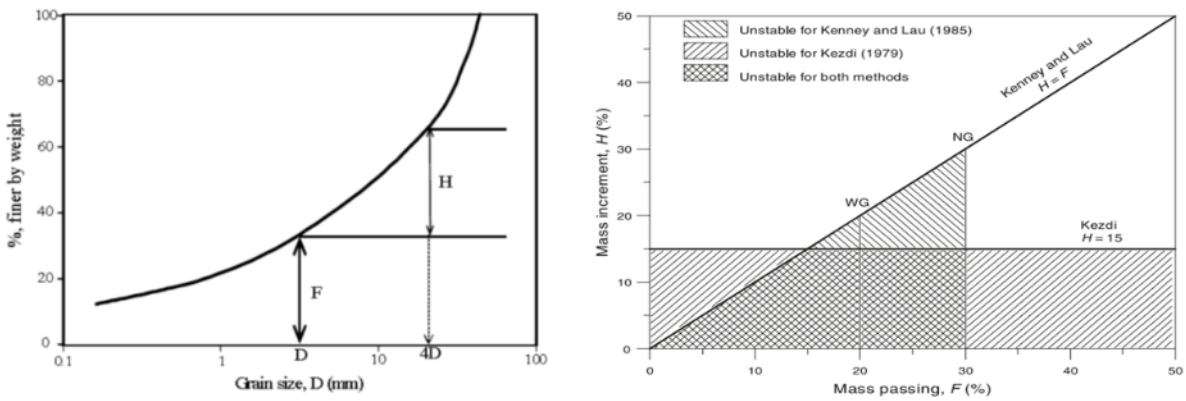


*Figure 2-17. Demonstration of the Kenney and Lau (1985) and Kezdi (1969) stability criteria. The left image shows the definition of the H and F parameters based on the grain size distribution of a given soil. The image to the right shows the instability areas computed by both methods and their overlap. (Li and Fannin, 2008; Li, 2008)*

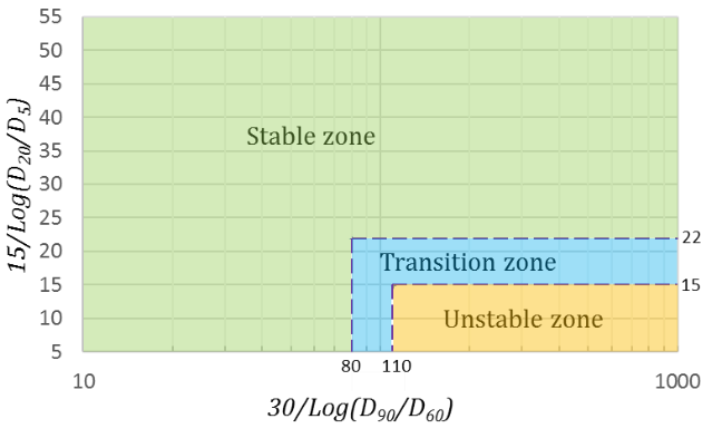


*Figure 2-18. Delineation of stability, transition and instability zones of a soil by Wan and Fell (2008).*

Adoption of the established geometrical criteria in earth structure design, combined with future developments, could lead to significantly reduced occurrences of internal erosion. However, it must be kept in mind that such a prospect also presumes a sound control of the construction process. Earth dams are often constructed using locally available materials, such as quarried rock, gravel, sand, silt or clay. Moreover, even if the materials at disposal do not represent a problem, shortcomings in project implementation might also be the cause of unforeseen structural fragilities and drawbacks (U. S. Society on Dams, 2011).

### *Hydraulic conditions*

The circumstances affecting the behaviour of the fluid itself, in this case water, are very influential to the manifestation of internal erosion - the hydraulic regime and the fluid mechanics within the interested materials strongly control the triggering and the intensity of it. For instance, even if the material properties predict it to be internally unstable, the percolating fluid still needs to have enough energy to mobilise the grains and transport them through the voids in the soil skeleton. In parallel, the intensity of the flow influences the rate and magnitude (i.e. severity) of the process (Li, 2008; Moffat and Fannin, 2006; To et al., 2016; Omofunmi et al., 2017; Rochim et al., 2017; Pride and Berryman, 2003; Sato and Kuwano, 2015; Brown, 2002).

Two important concepts frequently reiterated when studying seepage-related phenomena are those of *hydraulic head* and *hydraulic gradient*. The former, also called piezometric head, can be defined as the measurement of liquid pressure above a given point, measured as the liquid surface elevation, and expressed in units of length. Hydraulic gradient[7] is instead a vector gradient between hydraulic head measurements over a flow path length; for groundwater it

[7] Hydraulic gradient: $i = \frac{dh}{dl} = \frac{(h2-h1)}{length}$, where *i* is the hydraulic gradient (dimensionless), *dh* is the difference between two hydraulic heads (length, usually in m or ft), and *dl* is the flow path length between the two piezometers (also in length units).

can also be termed 'Darcy slope' as it determines the amount of Darcy Flux [8] or discharge. (Mulley, 2004; Chanson, 2004). The way hydraulic gradient relates to the internal instability of a soil based on its particle size distributions, although not fully understood by the research community, is shown in Figure 2-20 and Figure 2-21, where Skempton and Brogan (1994) used laboratory permeameter tests of sand and gravel mixtures to build a stability relationship, postulating that different material gradings become internally unstable when subject to sufficient hydraulic gradients.

Figure 2-20 shows examples from three studies (Nguyen et al., 2017, Moffat et al., 2011 and Israr and Israr, 2018; indicated in the image as A, B and C respectively) where hydraulic gradient variations over time – A) also shows hydraulic conductivity as a dashed line - are seen during internal erosion tests: in A) the authors describe a sudden rise in hydraulic gradient (and drop in hydraulic conductivity; dashed red circle) as likely due to clogging at constrictions by particles transport inside the sample; B) and C show more complex interactions as over the length of the used samples several local hydraulic gradients are measured (as indicated by the diagram in B) and the corresponding onset of instability/suffusion reported.

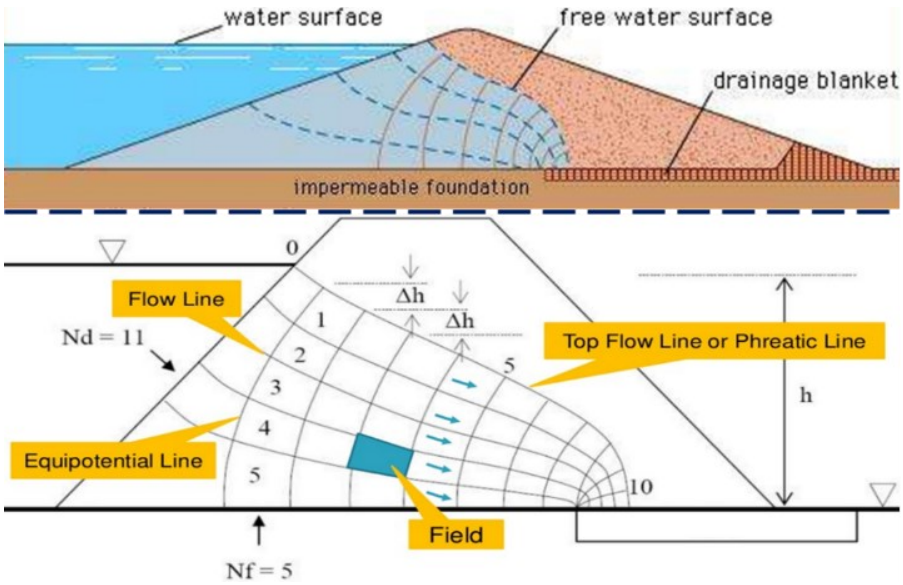


*Figure 2-19. Example of flow net through idealized earth dam (not to scale). Top image describes basic features found in a dam with a drainage blanket/filter but no core (modified after Encyclopædia Brittanica, 1999). Bottom image indicates components used to delineate flow nets: the phreatic line separates the saturated and unsaturated zones, blue arrows indicate flow direction and each field is delimited by the intersection of equipotential and flow lines.. Nd=number of potential drops; Nf=total number of flow channels (after Cedergren, 1989) https://www.slideshare.net/RambabuPalaka/earthen-dam-79855045.*

[8] $Q = \frac{k\ A(p_b - p_a)}{\mu\ L}$; total discharge, $Q$ ($m^3/s$) equals the product of the intrinsic permeability of the medium, $\kappa$ ($m^2$), the cross-sectional area to flow, $A$ ($m^2$), and the total pressure drop $p_b - p_a$ (Pa), divided by the viscosity, $\mu$ (Pa·s) and the length over which the pressure drop occurs $L$ (m).

In order to visualise how water might flow through an earth dam and evaluate the eventual seepage erosion, flow nets can be used. They can be produced by solving the steady groundwater flow equations of a certain permeable body and consist of two sets of lines that always intersect each other perpendicularly. These lines indicate the direction of groundwater flow (flow lines) and the lines of constant head (equipotentials), which show the distribution of potential energy (Cedergren, 1989); Figure 2-19.

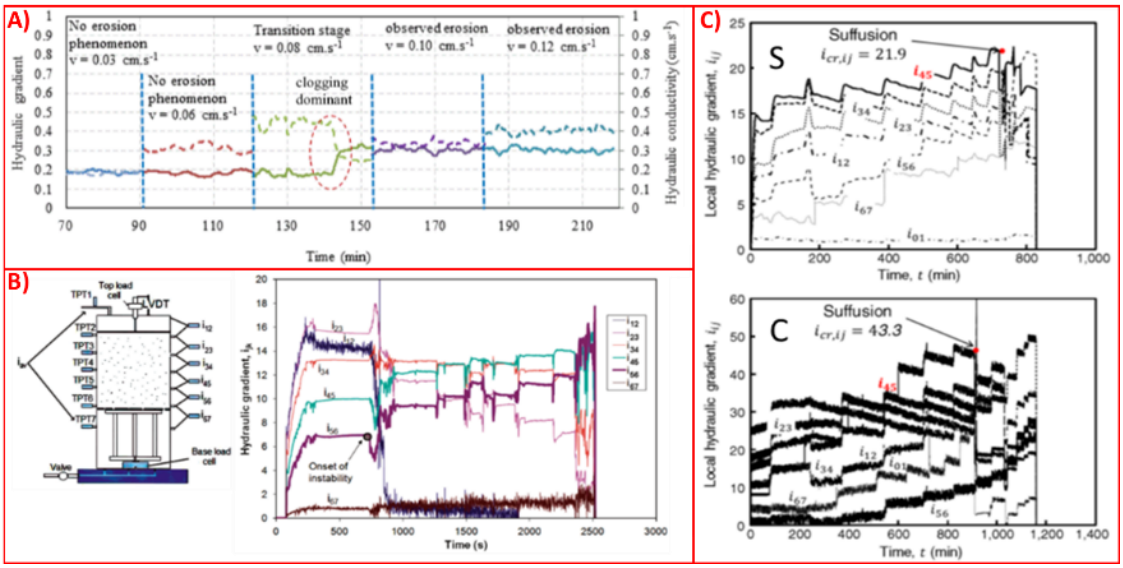


*Figure 2-20. Examples of data highlighting the hydraulic conditions during internal erosion or suffusion experiments, all in the time domain. A) Progression from no erosion to visible erosion read through plots of hydraulic gradient and hydraulic conductivity {dashed line} (Nguyen et al., 2017); B) Hydraulic gradients from several differential pressure sensors vertically distributed along permeameter (as in apparatus diagram to the left) and detail of moment of instability onset (Moffat et al., 2011); C) Results of static [S] and cyclic [C] axial loading tests with multiple sensors used to extract local hydraulic gradients and indication of suffusion initiation is shown (Israr and Israr, 2018).*

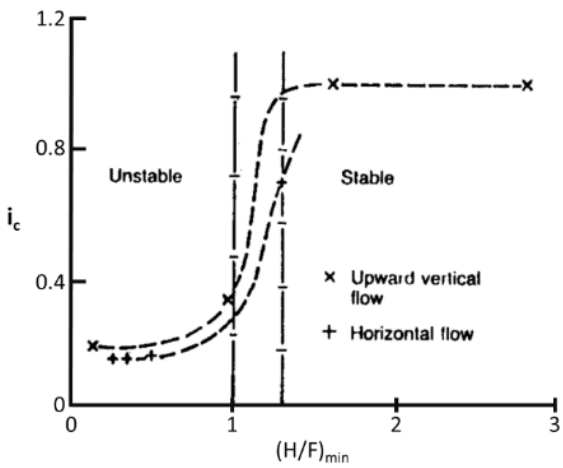


*Figure 2-21. Internal instability of a soil based on its grading ($H/F_{min}$ ratio) and critical hydraulic gradients ($i_c$), including the effect of two different flow orientations (after Skempton and Brogan, 1994)*

### *Effective stress*

Fundamentally, the level of stability of a soil assembly tends to be proportional to the effective stress[9] acting on it. The demonstration that the combined effects of hydraulic gradient and vertical effective stress, govern the initiation of internal instability has been given by Moffat (2005). Moffat (2005) used the effective stress concept of Terzaghi (1925, 1939) for the limiting envelope method to study internal instability for porous materials. This conceptual model was subsequently improved by a number of authors – e.g. Li (2008), Crawford-Flett (2014). One of the latest improvements, by Ferdos et al (2018), proposes the application of the failure envelope[10] concept to the initiation of internal erosion processes in a way that accounts for soil stresses and also flow-induced shear stress; Figure 2-22. Related test results produced by Li (2008) are shown in Figure 2-23, where several soils (their GSD in part (a) of the figure) were subject to increasing hydraulic gradients and effective stresses until the onset of instability and the resulting data was used to construct their corresponding hydromechanical envelopes.

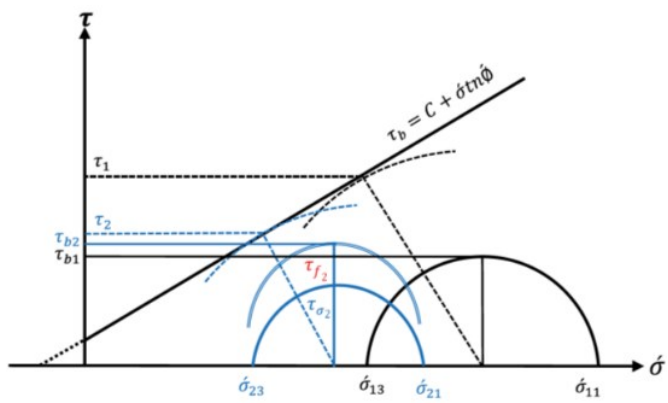


*Figure 2-22. Modified hydromechanical envelope model by Ferdos et al. (2018). Change of in-situ principal stresses in porous media under hydraulic loading and fluid seepage; the undisturbed Mohr-Coulomb circle (black line) shifts to the left due to the hydraulic loading (blue line) and upward due to seepage flow (double blue line). $\tau_1$ and $\tau_2$ are the maximum shear stresses that the specimen can take before instability occurs, $\tau_{b1}$ and $\tau_{b2}$ are the total induced shear stress on the specimen, $\tau_b$ the total in-situ shear stress and $\tau_{fn}$ is the flow-induced shear stress.*

In the paper by Ferdos et al (2018), the authors explain that laboratory experiments were used to develop a new theoretical framework, claiming success in defining a new criterion to determine the initiation of suffusion erosion, where its initiation (due to suffusion) is found to be dependent on in-situ soil stresses. In this method, a continuous slope change of the seepage velocity curve versus time, under constant hydromechanical loading is substantiated as an indicator of erosion initiation. This theoretical concept, based on Mohr-Coulomb's shear

[9] The effective stress (σ') acting on a soil is calculated from the total stress (σ) and pore water pressure (u). $\sigma' = \sigma - u$ ;(Terzaghi, 1925).

[10] In soil mechanics, failure envelopes are used to determine the limiting resistance of a material. They are based on a behaviour that combines various soil parameters where the initiation is governed by reaching the envelope borders. Appendix

failure envelope (where all soil principal stresses, as well as flow-induced shear stress are included), accounts for soil in-situ stress dependency of internal erosion initiation in soils. A semi-empirical constitutive law of internal erosion (with its coefficients extracted experimentally) is produced, being defined as the rate of mass removal due to the application of excessive shear stress higher than the material internal erodibility resistance - both the initiation and the mass removal rate of suffusion are found to be dependent on the soil in-situ stresses (Figure 2-22).

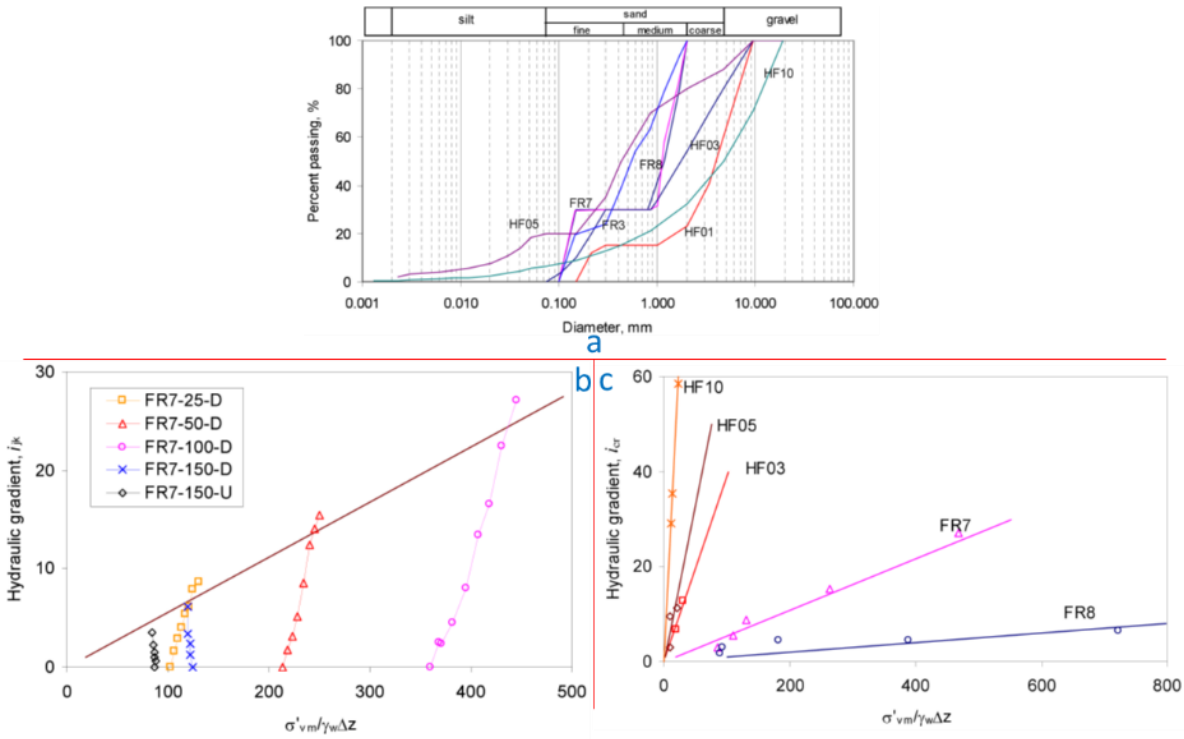


*Figure 2-23. Experimental data showing normalized effective stress and critical hydraulic gradients for several soil gradations (a). The hydromechanical paths for a specific gradation are found at the lower left (b) and a summary of all hydromechanical envelopes is seen at the lower left (c); (Li, 2008).*

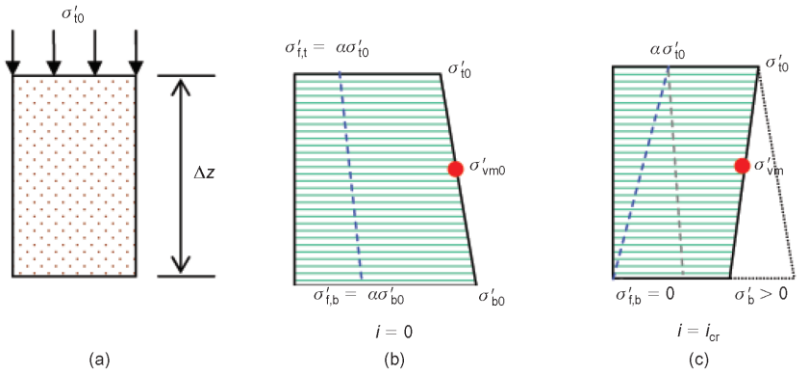


*Figure 2-24. Schematic stress distribution, internally unstable material: (a) element; (b) hydrostatic condition; (c) upward flow (i=icr) (Li and Fannin, 2012).*

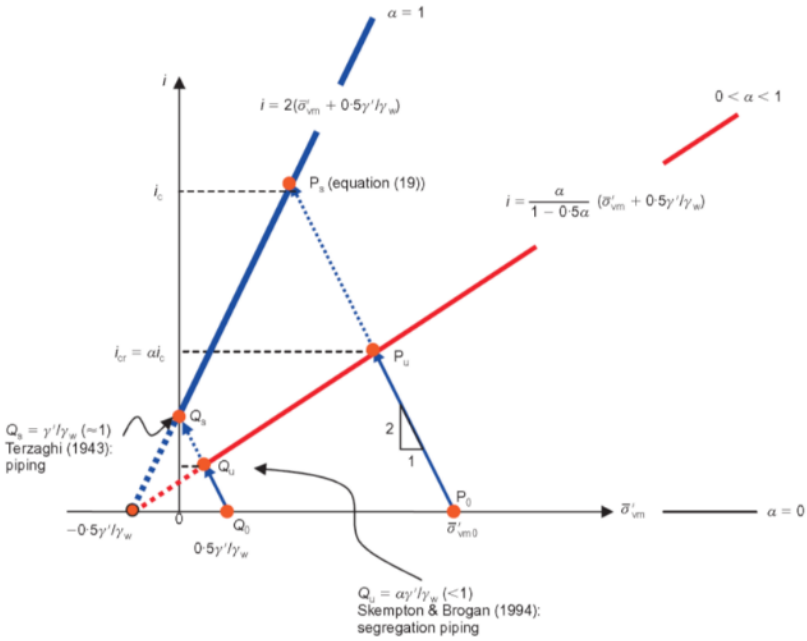


*Figure 2-25. Hydromechanical envelope in the [normalised] mean vertical effective stress domain confronted with hydraulic gradient for one-dimensional upward flow (Li and Fannin, 2012).*

Li and Fannin in 2012 proposed a theoretical envelope for internal instability of cohesionless soils (Figure 2-24 and Figure 2-25). The envelope represents a linear failure criterion that is governed by the proportion of effective stress affecting the finer fraction of soil grains, describing a threshold at which the onset of seepage induced instability occurs in a given soil based on the relation between critical hydraulic gradient and mean vertical effective stress. As upward flow decreases the overall effective stresses, the effective stress acting on the finer fraction[11] ($\sigma'_{f,\ t/b}$; blue dashed line) is eventually reduced to zero at its bottom when the hydraulic gradient becomes critical for internal erosion ($i_{cr}$).

Figure 2-25 conceptualizes the hydromechanical envelope for a) equal effective stress on different soil fractions (α=1) or internally stable material (blue line) and b) stress reduction factor causing effective stress on finer fraction to be lower (0<α<1) or internally unstable material (red line).

An increase in hydraulic gradient (*i*) causes the effective stress to reduce. The paths $Q_0$ => $Q_u/Q_s$ and $P_0$ => $P_u/P_s$ consider respectively just self-weight of the material as load (setting a lower boundary) and higher vertical loads. The difference between $Q_u/P_u$ and $Q_s/P_s$ is that the former corresponds to instability due to migration of the finer fraction (i.e. suffusion) while the latter results from piping by heave.

[11] The effective stress acting on the finer fraction ($\sigma'_{f,\ t/b}$) corresponds to the stress reduction factor, **α; $\sigma'_f = \alpha \cdot \sigma'$**.

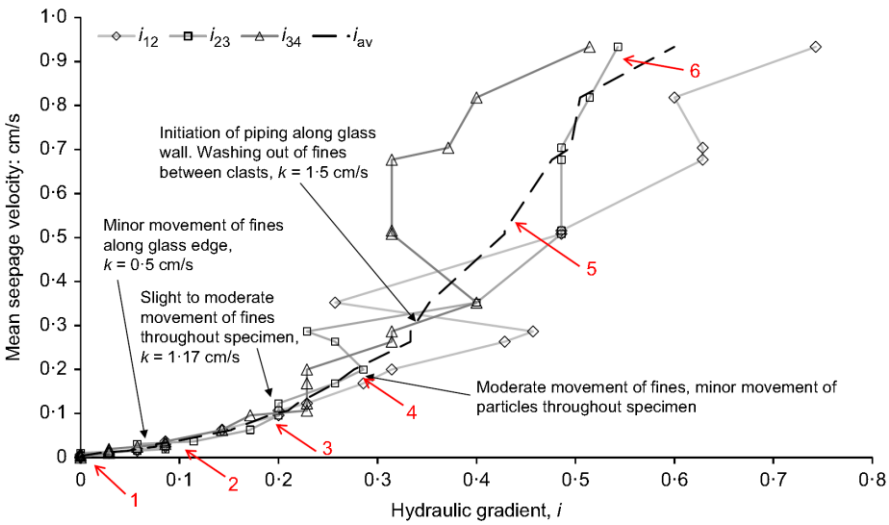


*Figure 2-26. Example of hydraulic gradient plotted against flow velocity as measured in laboratory permeameter tests (Hunter and Bowman, 2017a). The different curves represent the hydraulic gradient between pressure sensors at different positions (greyed lines) as well as the overall averaged hydraulic gradient (black dashed line). The red numbered arrows indicate six phases of movement.*

Figure 2-26 shows a relationship between flow rate and hydraulic gradient obtained from an upward flow laboratory test with an internally unstable soil specimen. In this figure the transition between different stages of seepage erosion is also shown (red arrows). These phases are described as: phase 1: beginning of test; phase 2: minor movement of fines observed along sample boundaries; phase 3: slight movement of fines observed throughout the specimen (typically within open void spaces); phase 4: moderate amount of fines under suffusion, with small movements of the smaller of the coarse fraction; phase 5: piping initiation along device wall; phase 6: advanced piping and wash-out of fines. Note that despite the relationship shown by the average hydraulic gradient being quite smooth and direct, the hydraulic gradient at specific/intermediate portions of the sample have a more complex behaviour, often with a momentary reversal of the relationship.

## 2.4 Acoustic Emission (AE) monitoring

An important delimitation of this research project is that it focuses on a specific approach: the utilization of Acoustic emission (AE). AE can be defined as elastic waves with considerably high frequency (>10kHz) and low amplitude that propagate through materials surrounding their generation source and, in soil, are produced by a suite of mechanisms including inter-particle friction and collisions (Smith, 2015; Dixon et al., 2010).

Koerner et al. (1981) qualitatively demonstrated the applicability of AE for soil monitoring (Figure 2-27) and, following a series of developments that overcame previous obstacles (Table 5), Smith and collaborators (2015) effectively developed a highly accurate system for monitoring and quantifying soil deformation using AE, among other developments. This project

aspires to surpass the state-of-the-art to create new knowledge and advance the understanding of the relationship between AE and internal erosion.

This work distinctively endeavoured at using AE to detect internal erosion in its earlier stages, potentially even before any soil deformation occurs to the load bearing soil skeleton, which would notably enhance the capacity of early warnings and response to associated hazards. The distinct potential of AE for structural monitoring, as already listed by Koerner et al. in 1981, comes from its fairly low equipment, installation and monitoring costs, ability to produce constant and real-time data and, naturally, its capacity to identify internal erosion.

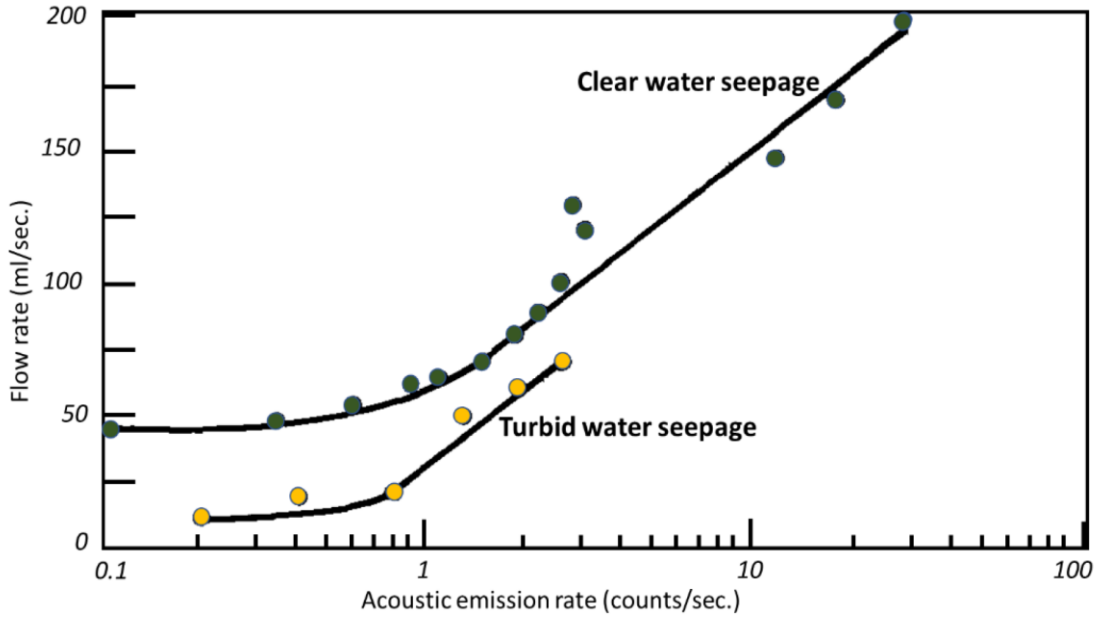


*Figure 2-27. Correlation between AE and flow rate in clear water and turbid water seepage tests. Modified after Koerner et al. (1981).*

*Table 5. Brief summary of previous barriers for using AE and their eventual solutions or improvements (Rouse et al., 1991; Smith, 2015; Koerner et al., 1981; Dixon et al., 2003; Dixon and Spriggs, 2007).*

| Issue | Solution |
|---|---|
| AE attenuation as it travels through soil | Waveguides |
| Background noise | Definition of relevant frequency range and signal filtering |
| Technological limitations (hardware cost, portability, autonomy) | Advent of more powerful, cheaper, and more compact batteries, processors and other equipment |

As mentioned, seepage-induced internal erosion generates characteristic acoustic emission through particle collisions and frictional interactions. Koerner et al. (1981) showed that these emissions can be used to characterize seepage-induced phenomena. Yet, in the observed literature a methodology for using acoustic emission for examining seepage-induced internal erosion as previously described is yet to be developed. Although the best approach for tackling this matter is still being explored, no reason for disregarding AE as a suitable methodology has been found.

Beyond the still standing challenges (e.g. monitoring equipment technicalities, signal complexity, attenuation), the use of AE for investigating the occurrence of seepage-induced internal erosion brings the advantages of being:

- Non-intrusive[12]
- Low cost
- Remotely monitored
- Capable of early detection and warning

### 2.4.1 AE generation and propagation

Sound is essentially a wave phenomenon in which a mechanical disturbance propagates through an elastic medium (e.g. water, air) at a speed characteristic of that medium. As illustrated in Figure 2-28, the movement of a surface (left end) in the horizontal direction against a medium (white-grey-black area) causes a compression of the medium in the region immediately adjacent to the surface, thereby causing an increase in the density of the air in that layer. Because the pressure of the densified layer is greater than the pressure of the undisturbed medium, the added energy propagates away from the moving plane. As the moving plane reverses its direction of movement, an opposite effect occurs - a rarefaction (pressure decrease to a value below that of the undisturbed medium) of the adjacent portion of the medium occurs, which follows the previously generated compression impulse. This succession of compressions and rarefactions constitutes a wave motion- a sound wave is the transfer of energy emitted by a source material or object into the medium as it travels. The plot at the bottom half of the image illustrates the wave properties, which follow the relationship v=f λ. (Raichel, 2006).

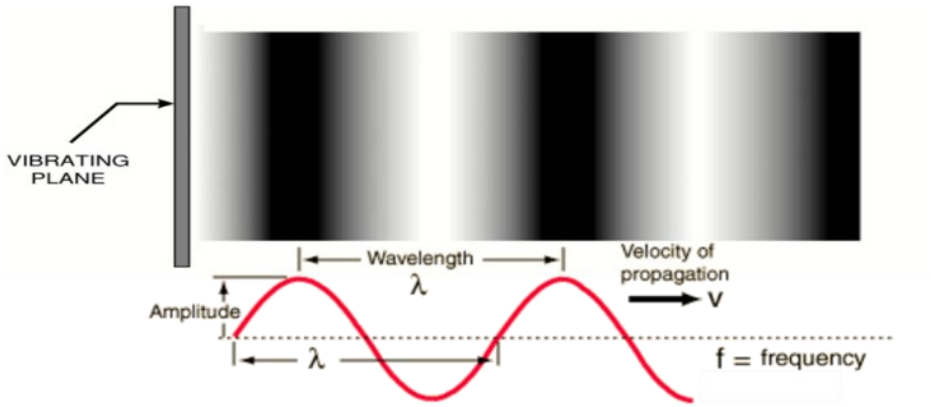


*Figure 2-28. Conceptualization of relative density (darker areas) and rarefaction (lighter areas) of molecules in a given medium subjected to the vibrational impact of a plane wall (grey bar to the left) and propagating to the right side of the image (top half). In the plot at the lower half, the graphic definition of wave properties is shown, with the crests and troughs of the red curve coinciding with points of the wave cycle. Modified after Raichel, (2006).*

[12] Except if waveguides need to be buried in the monitored structure. An alternative to this aspect would be the use of already existing structural elements (e.g. steel pipes, metal bars) as equivalent to waveguides.

This principle can be extrapolated to larger, more complex systems in which the mentioned idealized vibrating plane can be compounded and used to construct the surface of more complex objects, which naturally tends to produce more intricate wave patterns. The principle remains nonetheless applicable despite increased complexity of the vibrating source shape.

Any sort of particle mechanical disturbance in an elasto-plastic medium generates an acoustic response which mainly propagates longitudinally – particle oscillations occur in the direction of the wave motion, resulting in cycles of slight compression and rarefaction of the medium. Waves can also have rotational, torsional or shear components, which are transmitted based on the material properties and are not conveyed by water - such waves are not transmitted in water, but compressional waves are (Raichel, 2006; Kadam and Nayak, 2016; Smith, 2015). In soil, AE is produced by the deformation of soil bodies and soil-structure systems through several mechanisms such as: inter-particle friction; particle contact network rearrangement (e.g. release of contact stresses and stress redistribution); degradation of particle asperities; particle crushing; and friction at the interface between the soil and structural element (Michlmayr et al., 2012; Heather-Smith, 2020; Biller et al., 2019; Smith, 2015). Michlmayr (2013) defined six major source mechanisms for soil generated AE: liquid bridge rupture, crack development, release of force chains, grain friction, grain cementation fracture and the rupture of soil fibres (Figure 2-29). Heather-Smith (2020) compiles a series of mechanisms capable of producing AE in soils, as seen in Table 6.

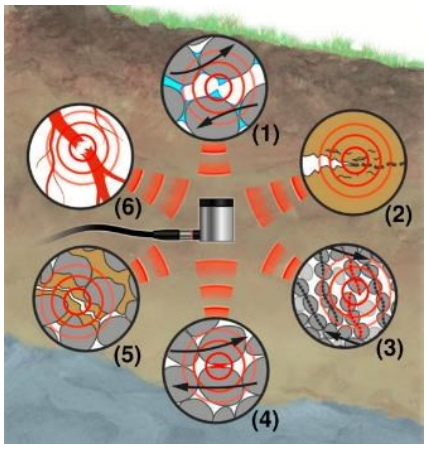


*Figure 2-29. Types of AE generation modes in geological materials (1) liquid bridge rupture, (2) crack development, (3) release of force chains, (4) grain friction, (5) grain cementation fracture, and (6) rupture of soil fibre (Michlmayr et al., 2012).*

Observations such as illustrated in Figure 2 26 (Koerner et al., 1981) indicate that AE also involves particles suspended in the fluid. In fluid seepage through soil (the focus of this thesis), AE is generated through frictional interactions between particles, friction due to fluid flow through the soil, collisions of migrating particles (i.e. by seepage-induced internal erosion mechanisms; Figure 2-30), and collapse of fabric (e.g. suffosion) (Smith et al., 2019) (Smith et al., 2019).

*Table 6. AE generating mechanisms within soils proposed by Heather-Smith, 2020.*

| Ae generating mechanisms | Smith (2015) | Michlmayr (2013) | Rumpf (1962) |
|---|---|---|---|
| **Capillary bridge breakage** | Capillary bridge rupture | Liquid bridge rupture | Capillary bridge breakage |
| **Adhesive bond breakage** | Adhesive bond | Grain cementation fracture | Solid bridges |
| **Grain friction** | Particle-particle interactions | Grain friction | Closed bonds |
| **Force chain rupture** | Force chain rupture | Release of force chains | - |
| **Soil (e.g. Root) fibre rupture** | - | Rupture of soil fibres | - |
| **Crack development (within a soil mass)** | - | Crack development | - |
| **Inter-molecular force Severing** | - | - | Electrostatic force severing |
| **Asperity breakdown** | Degradation of particle asperities | - | - |
| **Soil-structure interactions (all interaction types)** | - | - | - |

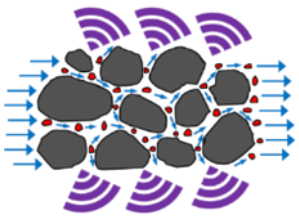

*Figure 2-30. .Schematic of how fluid seepage (blue arrows) through a porous medium can cause the transport of finer particles (red) through the voids of a coarser matrix (grey) and, due to particle collisions and other frictional interactions, produce AE (purple; idealized).*

Essentially, any sort of mechanical disturbance in an elasto-plastic [granular] medium can generate an acoustic response which propagates and principally be of longitudinal nature (i.e. particle oscillations occurring in the direction of the wave motion), resulting in cycles of slight compression and rarefaction of the medium. As mentioned, some wave components (rotational, torsional or shear components) can be through a given elasto-plastic material, but are not conveyed by water, which only transmits the longitudinal component (Raichel, 2006; Kadam and Nayak, 2016; Smith, 2015). The latter is focused in this work, since the studied phenomena are bound to occur in water-saturated conditions.

*Table 7. Influence of soil properties on AE behaviour (Smith, 2015)*

| | Property | Influence on AE behaviour |
|---|---|---|
| Granular soil | Coefficient of uniformity | *Soils with more uniform grading and smaller values of coefficient of uniformity produce greater AE. This is because a greater surface area is achieved over which frictional interactions can occur.* |
| | Particle shape | *Angular particles generate greater magnitude AE than rounded particles.* |
| | Particle size | *Soils with larger particles generate AE with greater magnitude than those with smaller particles; however, smaller particles give rise to a greater number of AE events (due to a greater number of particle-particle interactions per unit volume).* |
| Fine-grained soil | Plasticity index | *The higher the plasticity index the lower the AE response of the soil. This is partly due to the higher clay content (i.e. greater proportion of 'quiet' soil grains) found in high plasticity soils. The influence of clay mineralogy is yet to be investigated.* |
| | Water content | *The higher the water content, and thus lower the inter-particle contact stresses, the lower the AE response.* |
| General factors | Soil structure | *The majority of research has been conducted on remoulded samples and therefore the AE response of samples containing discontinuities (e.g. fissures) has not yet been investigated. It is anticipated that the soil structure has a significant influence on the AE generated, and therefore understanding the influence of soil structure is important when interpretation of AE from undisturbed soil is required.* |
| | Stress history | *Due to the Kaiser effect*, soils have been shown to exhibit greatly increased AE activity when stress levels exceed the pre-stress/ pre-consolidation pressure (Koerner et al., 1981).* |
| *The Kaiser effect is an absence of AE at loads not exceeding the previous maximum load level (e.g. is a clear phenomenon when materials experience repetitive loading). | | |

Considering types of source and transmission, the AE being measured in this research can be subdivided in:

- AE propagating through the water phase and interacting with a waveguide (WG).
- AE propagating through the solid phase (i.e. AE energy propagating from particle to particle and then transmitting into the WG)
- AE generated at the interface with the waveguide from seepage flow and particle movement (i.e. frictional interactions with the waveguide); and
- AE generated by collisions with moving particles suspended in the fluid colliding with the waveguide as they move past.

The properties of a given soil influence the generated AE, which is summarised in Table 7.

When a sound wave interacts with a material or object surface, it may be absorbed, transmitted, reflected, refracted or diffracted form the surface depending on type of the surface Figure 2-31. (Kadam and Nayak, 2016).

Absorption: Materials or surfaces with this capacity convert acoustic energy into heat energy. Sound absorption measures the amount of energy absorbed by the material and expressed as sound absorption coefficient. The coefficient ranges between 0 and 1 where 0 is no absorption and 1 is highest or total absorption. The higher coefficient yields lower reverberation time. The reverberation time is persistence of sound in a space after a sound source has ceased - it is the time lag, in seconds, for the sound to decay by 60 dB after a sound source has been stopped.

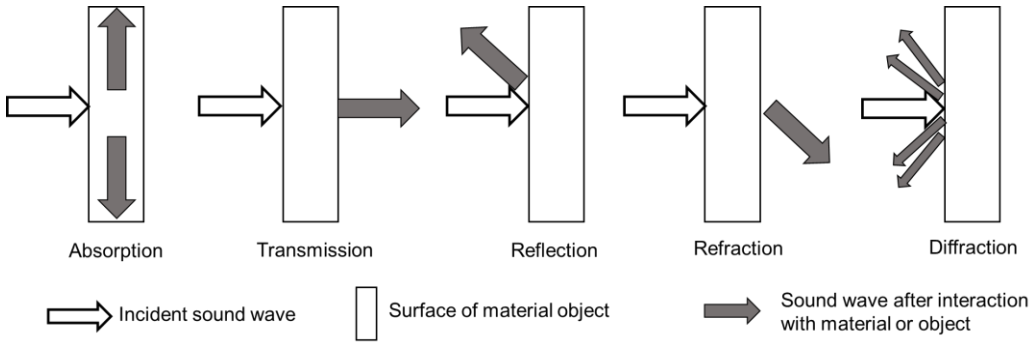


*Figure 2-31. Interactions between sound wave and material or object surface (Kadam and Nayak, 2016)*

Transmission: Occurs when sound waves from the source propagate through a medium without being absorbed or reflected or without any frequency loss.

Reflection: When sound waves impinge a surface, they may reflect [back] with their full or partial energy (full or partial reflection) without altering their properties. The reflection angle of a sound wave from the reflecting surface is equal to the angle of incidence, being defined by a normal to the reflecting plane and the incident and reflected waves (Huygens geometry).

Refraction: Refraction occurs when sound waves transmit through the surface and are bent away from the straight line of travel. It depends on factors such as the speed of sound, angle between sound propagation direction and inhomogeneities or anisotropies of the medium.

Diffraction: Involves a change in the direction of sound waves as it hits a surface. When sound impacts on a partial barrier, some of its energy gets reflected, some propagates without any disturbance and some gets bent over the barrier. (Kadam and Nayak, 2016)

### *Wave types*

If the energy of a wave-type motion passes through a medium, several different types of waves may be generated, depending upon the motion of particles in the medium (Raichel, 2006).

Longitudinal/Compressional waves – Occur when the particles of the medium oscillate along the direction of the wave propagation. Under the influence of this kind of wave the material undergoes compression and decompression cycles. .Figure 2-32

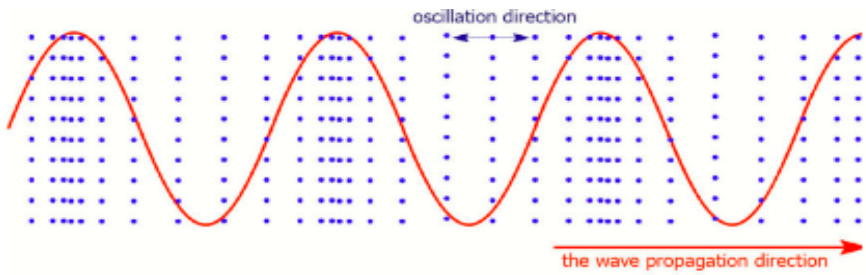


*Figure 2-32. Propagation of longitudinal waves.*

Shear waves – Occur when the particles of the medium vibrate perpendicularly to the direction of wave propagation. Under their influence the material undergoes shear deformation. This type of waves can propagate only in solids or materials that have a high enough shear strength. Figure 2-33

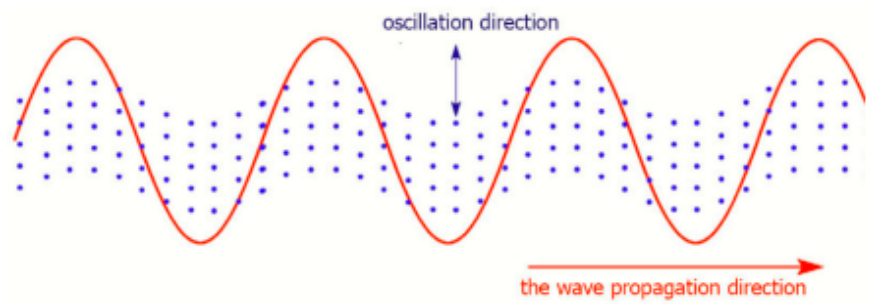


*Figure 2-33. Shear wave propagation.*

Surface waves – are mechanical waves that propagate along the boundary between two media and form in materials with a thickness typically above 1.5 to 2 times the size of the wavelength. Rayleigh, Scholte, and Stoneley waves are types of surface waves. Figure 2-34.

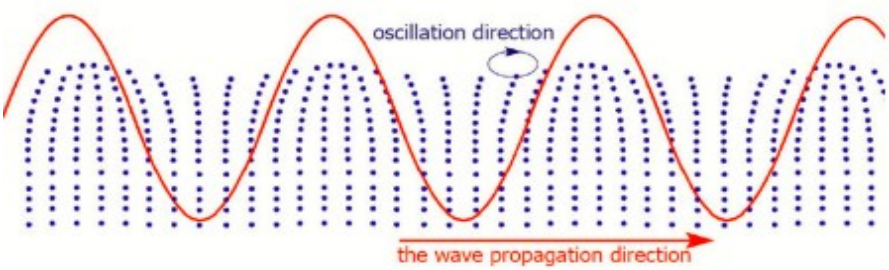


*Figure 2-34. Propagation of surface waves.*

Torsional waves – are waves in which the particles rotate about a common centre direction of propagation, cyclically alternating their rotation direction. They move in a spiralling way that can be considered a vector combination of longitudinal and transverse motions. Figure 2-35.

*Figure 2-35. Representation of how torsional waves propagate (Chaunsali et al., 2016).*

### *Attenuation and material properties*

When acoustic waves propagate through a medium, they tend to lose intensity over distance. Geometric spreading (scattering, divergence effect) and absorption of acoustic energy by the propagation medium itself are the key mechanisms to be considered. In soils, the loss of energy, or dissipation of acoustic energy is greater in loose sediments (Prasad et al., 2004).

The properties of the material being examined for seepage erosion – from its mineral components down to its level of compaction and the effective stress - appear to be the main indicators of the attenuation coefficients to be expected, with e.g. lower density configurations corresponding to elevated attenuation and vice versa. Higher degrees of water saturation have also generated better signal transmission (Prasad et al., 2004; Holmes et al., 2007; Robb et al., 2006; Bardet and Sayed, 1993); Figure 2-36.

Data on generic and specific attenuation values are exemplified in Figure 2-37, Figure 2-38 and Table 8 (Smith, 2015; Koerner et al., 1981). They offer valuable information concerning the feasibility of the aims and objectives here described.

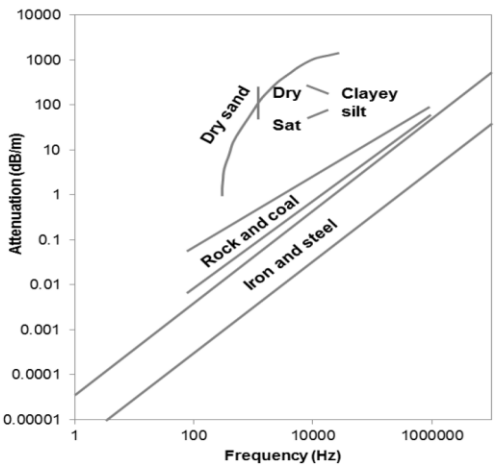


*Figure 2-36. Attenuation coefficients of different materials (Smith, 2015).*

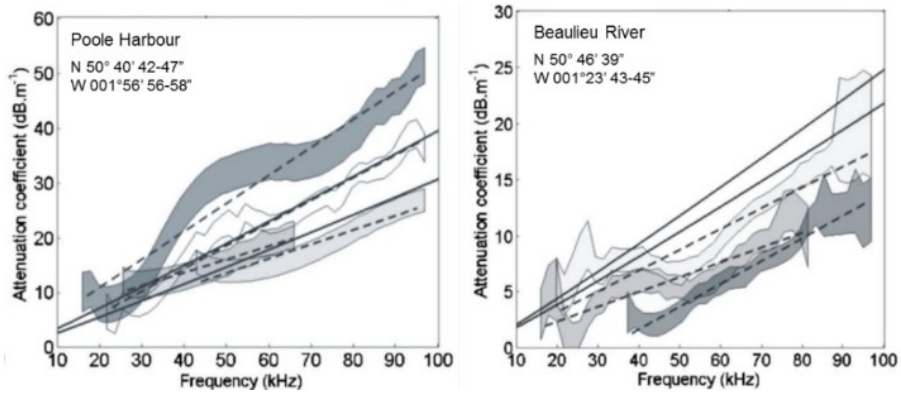


*Figure 2-37. Attenuation coefficients for sediments on southern UK intertidal regions. Shaded regions: attenuation coefficients (different grey shades correspond to different sites within each region); dashed lines: Trendlines of attenuation coefficients[13] for each site; solid lines: limits of phase velocities and absorption coefficients. After Robb et al. (2006).*

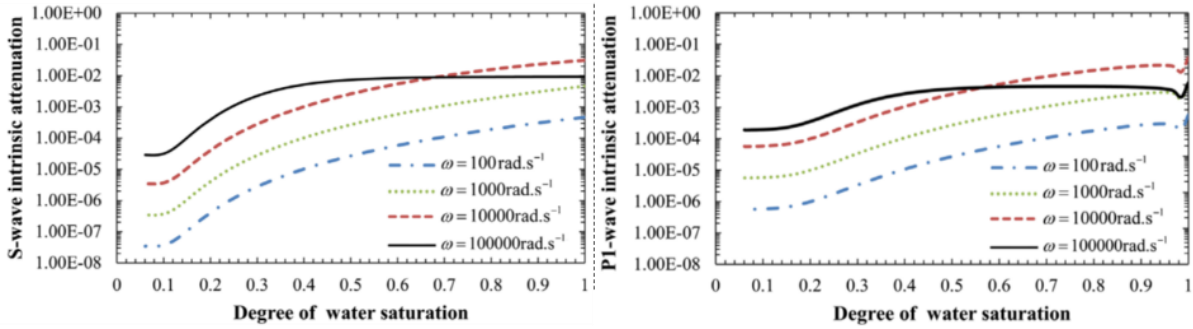


*Figure 2-38. Relationship between water saturation and intrinsic attenuation of Shear (S, left)-and pressure (P1[14], right) waves[15] for different frequencies[16]. (Ghasemzadeh and Abounouri, 2013). Rad/s denotes [angular] frequency; 1 radian per second = approximately 0.159155 Hz.*

The propagation of acoustic waves through soil, especially when in conditions that could result in seepage flow, suggests two main phases: the soil particles and the fluid. For the soil, the stress state of the contacts between solid particles relates to how much of the acoustic emission energy is lost over its propagation path – a particle assembly under high effective stress tends to propagate acoustic waves more efficiently than if in loose conditions. A nuance to these dynamics is that the stress transmission through a volume of soil is not necessarily homogeneous; based on variables such as inter-particle friction, grain-size distribution and particle shapes, the definition of a primary skeleton (or a particulate framework through which the stress burden is predominantly carried) arises. In a gap-graded soil this primary skeleton tends to be mainly formed by the coarser grains.

*Table 8. Gathering of frequency-dependant attenuation coefficients and exponents of frequency (q) for compressional waves in marine sediments. Modified after Robb et al. (2006):*

[13] Weighted means of velocity and weighted least-squares fit to attenuation coefficients.
[14] Equation 46 $\{A_1 + A_2k^2_p + A_3(k^2_p)^2 + A_4(k^2_p)^3 = 0\}$ in Ghasemzadeh and Abounouri (2013) typically has three complex roots (wave numbers), yielding three different compressional wave modes, or P1,P2,and P3. P1 is the wave number that results from the largest wave velocity but the smallest attenuation for the first compressional wave.
[15] Longitudinal or pressure waves: the displacement of the medium is aligned with the wave propagation direction;
Transverse or shear waves: the displacement of the medium is orthogonal to the wave propagation direction.
[16] 1 rad·s$^{-1}$ ≅ 159.155 kHz.

| Frequency (kHz) | Attenuation coefficient (dB $m^{-1}$) | Exponent $q$ | Sediment type | First author and reference |
|---|---|---|---|---|
| 3.5–100.0 | 0.6–74.3 | 0.94–1.1 | *In situ* sand to clay | Hamilton (1972) |
| 15–1500 | - | 1 | Reconstituted silt/clay | McLeroy & DeLoach (1968) |
| 25–100 | 8–60 | Nonlinear | *In situ* sand | Buckingham & Richardson (2002) |
| 0.125–400 | 1–200 | Nonlinear | *In situ* sand | Hampton (1967) |
| 3.5–100 | 1.5–55 | 1 | Compilation of data (sands) | Hamilton (1987) |
| 4–50 | 0.28–3.00 | 1±15% | *In situ* Mud | Wood & Weston (1964) |
| 0.04–0.09 | 0.59 | 1 | *In situ* clayey silt | Bennett (1964) |
| 5–50 | 0.30–1.86 | 1 | *In situ* silty clay | Lewis (1971) |
| 5–50 | - | 1.00–1.26 | *In situ* sand | McCann & McCann (1969) |
| 0.03-500 | $5.6\times10^{-4}$–90 | 1.12 | Compilation of data (muds) | Bowles (2000) |
| 0.05–1.00 | $2.2\times10^{-4}$–$9.5\times10^{-4}$ | 1.25–1.50 | - | Evans & Carey (1992) |
| 20–40 | 0.10–2.48 | 0.6–3.4 | Sand to clayey silt samples | Shumway (1960) |
| 100–1000 | 40–150 | 1.3–2.0 | Silt and clay core samples | Courtney & Mayer (1993) |
| 20–300 | 3–34 | Nonlinear | Glass beads | Hovem & Ingram (1979) |
| 0.2–4.7 | 0–4 | Nonlinear | *In situ* silt | Best et al. (2001) |

Conversely, acoustic wave propagation through a fluid like water is characterized by being fundamentally isotropic, efficient in transmitting compressional waves and continuous especially if the fluid is linked through the pores of the solid phase (Tole, 2005; Aldrich, 2007; Telford et al., 1990; Buckingham, 1997; Bowles, 1997; Li and Pyrak-Nolte, 1998; Hung et al., 2009; Fannin and Slangen, 2014).

Propagation loss (or transmission loss) is highly influential in determining the performance of acoustic systems since it constrains reachable range and the amplitude of the detectable signal - the receiver performance is directly based on the signal-to-noise ratio. (Lurton, 2010). In other words, to better understand how this work could be effectively implemented in real structures (or its feasibility) in the field, the understanding of acoustic wave attenuation is essential (Koerner et al., 1981; Szabo, 1995; Buckingham, 1997), as can be understood from the association with the work of Bowles (1997), Pride and Berryman (2003), Szabo (1995) and others. If attenuation is too strong, suffusion might not be detectable across large enough distances through the soil body, and in a regular sized structure too many detectors or WGs would have to be installed for adequate monitoring, perhaps excessively increasing implementation complexity and costs.

Kibblewhite (1989) reveals that compressional-wave attenuation in porous, granular materials tends to vary as the first power of frequency over the 1 Hz up to 1 MHz frequency range.

<u>Solid/fluid phases and material properties</u>:

Porous media with a solid matrix (elastic) and the pores are occupied by a fluid (viscous) are called poroelastic. A poroelastic medium is characterised by its porosity, permeability and the properties of its constituents, the solid matrix and fluid. The theory of dynamic poroelasticity (now known as Biot theory; attributed to Maurice Anthony Biot, 1905–1985) gives a general description of the mechanical behaviour of poroelastic media and are derived from equations of linear elasticity for the solid matrix, Navier–Stokes equations for the viscous fluid, and Darcy's law for the flow of fluid through the porous matrix. (Berryman, 1981; Biot, 1955, 1956, 1962).

The theory of poroelasticity states three types of elastic waves exist in poroelastic media: a shear or transverse wave, and two types of longitudinal or compressional waves, which Biot called type 1 and type 2 waves. The transverse and type 1 (or fast) longitudinal wave are, respectively, like the transverse and longitudinal waves in an elastic solid. The type 2 (or slow) compressional wave is unique to poroelastic materials.

In Equation 2-1 the definition of a characteristic frequency ($f_c$) is given. This frequency is one below which the type 2 (or slow) compressional wave is highly attenuated and diffused (arguably not actually a wave). Above the characteristic frequency this slow (type 2, compressional) wave propagates and reflects more efficiently, with less attenuation, in effect making its signal detectable.

To account for different frequencies of propagation, it is necessary to know the frequency, the permeability of the rock, the viscosity of the fluid and a coefficient for the inertial drag between skeleton and fluid.

$$f_c = \frac{\eta \emptyset}{2\pi \ k_0 \rho_f}$$

*Equation 2-1. Definition of a characteristic frequency ($f_c$). Where fc=characteristic frequency, $\rho_f$ =pore fluid density, $\eta$=kinematic viscosity, $\emptyset$=porosity and $k_0$=permeability.(Dutta and Ode, 1983; Biot, 1956)*

A correlation is demonstrated between the acoustical and mechanical properties of the studied materials (Buckingham, 1997) - Figure 2-39, Figure 2-40, Figure 2-41 and Figure 2-42.

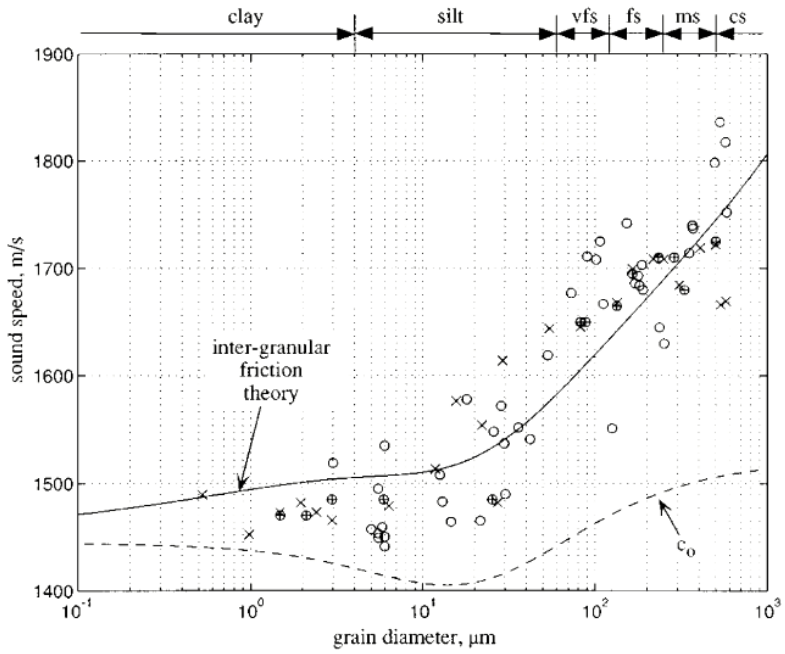


*Figure 2-39. Wave speed versus mean grain diameter. Solid line indicates compressional wave speed (m/s), while dashed line shows compressional wave speed in the absence of intergranular friction (m/s). The point-symbols represent experimental data from different publications. Key for scale on top of plot: Cs=coarse sand; ms=medium sand; fs=fine sand; vfs=very fine sand (Buckingham, 1997).*

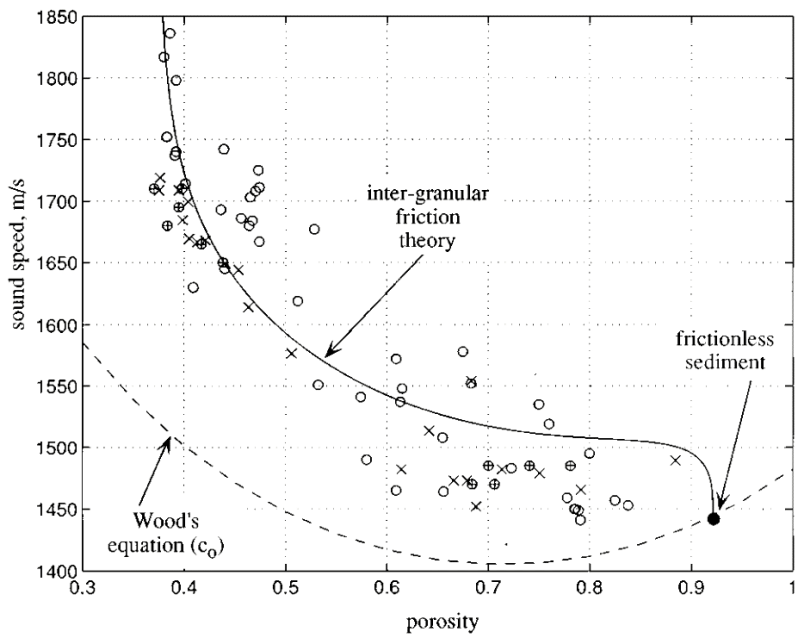


*Figure 2-40. Plot of wave speed as a function of porosity, with the solid line being calculated by Buckingham (1997). The point-symbols represent experimental data from different publications. Dashed line is based on compressional wave speed in absence of intergranular friction ($c_0$) in m/s, Wood's equation (Buckingham, 1997).*

In the context of fully saturated porous media, Buckingham (1997) developed a of sound propagation theory on the basis of a linear wave equation. He took into account the internal losses arising from interparticle contacts and proposes that the energy loss mechanism, which, he mentions, shows a "memory" or hysteresis, is responsible for the acoustic

properties of the studied sediments. In more detail, the wave phase, speed, and attenuation are related to the mechanical properties of the material (i.e. grain size, density, and porosity).

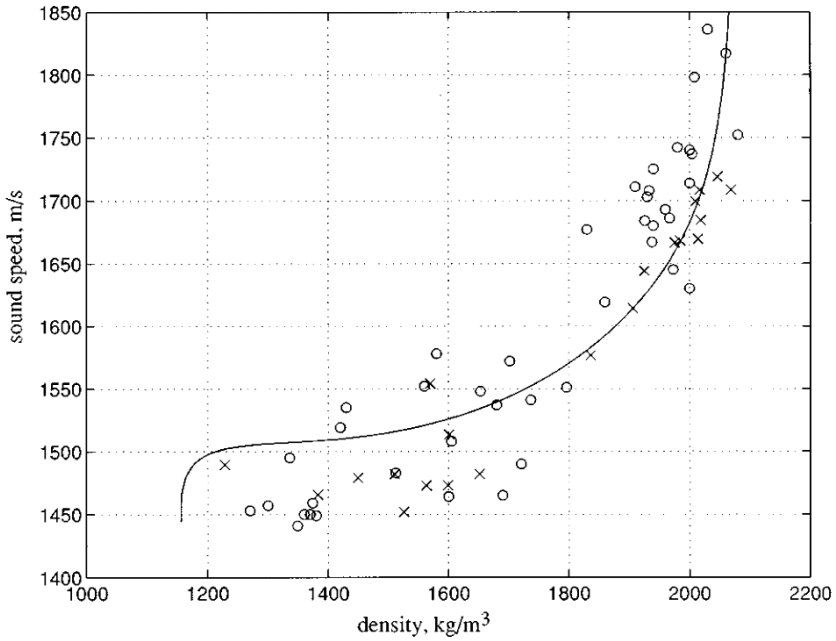


*Figure 2-41. Plot of sound speed as a function of density. with the solid line being calculated by Buckingham (1997) and the point-symbols representing experimental data from different publications (Buckingham, 1997).*

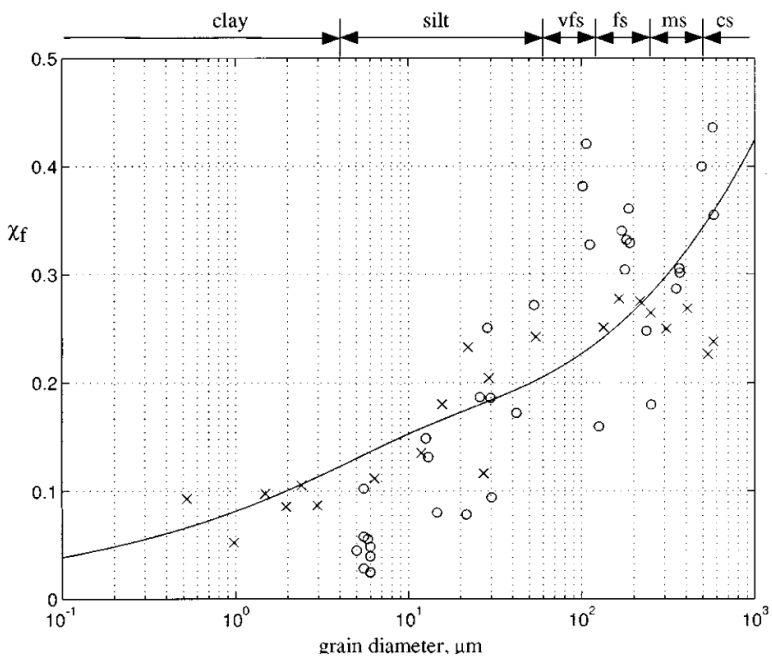


*Figure 2-42. Attenuation coefficient (χf) versus grain size. The solid line being calculated by Buckingham (1997) and the point-symbols represent experimental data from several publications. Key for scale on top of plot: Cs=coarse sand; ms=medium sand; fs=fine sand; vfs=very fine sand (Buckingham, 1997).*

### *Impedance*

Different materials respond differently to the incidence of acoustic waves, depending on the extent to which the medium particles resist mechanical disturbance, or vibrations. This

property is referred to as the characteristic acoustic impedance of the medium in question. This resistance increases in proportion to the density and the sound velocity in the medium - acoustic impedance is defined as the product of medium density and sound velocity in the medium (Tole, 2005).

Regions or interfaces where the values of acoustic impedance change are very important in sound interactions and are called acoustic boundaries Figure 2-43. These boundaries allow for the identification of features of a complex medium. In general, the extent to which an acoustic boundary affects acoustic transmission depends on the magnitude of the difference between the acoustic impedance values across a volume, denoting different material properties like compaction, porosity, hardness/softness, shear strength or state of matter (i.e. liquid, fluid, solid).

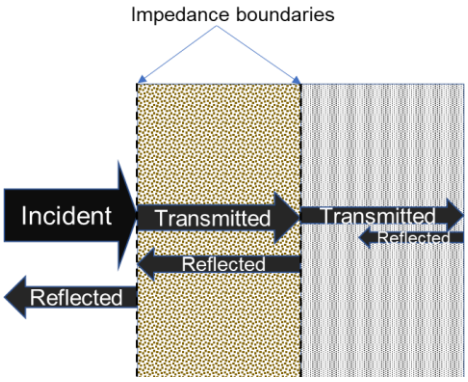


*Figure 2-43. Simplified representation of acoustic energy being partially transmitted and reflected as it meets impedance boundaries (dashed lines) – signal direction, attenuation as it travels through the denoted layers (pattern-filled areas), and other possible interactions such as diffraction and refraction are ignored for simplicity.*

### *Waveguides*

Given its importance, the effect of attenuation should be mitigated, and the utilisation of waveguides is suggested in the field as they are considered relatively simple and reliable implements that provide a low attenuation propagation path for the AE to travel to a sensor (Uhlemann et al., 2016b; Smith et al., 2014; Smith and Dixon, 2014). Figure 2-44 exemplifies how AE propagates in systems involving waveguides. Besides for the observation that soil composition is a central variable, the study by Smith (2015) offers an important base of comparison with more simplified systems; Figure 2-36 indicates attenuation levels for certain material types, while Figure 2-44 shows how they interact in combination (with the waveguide described as ‘pipe’).

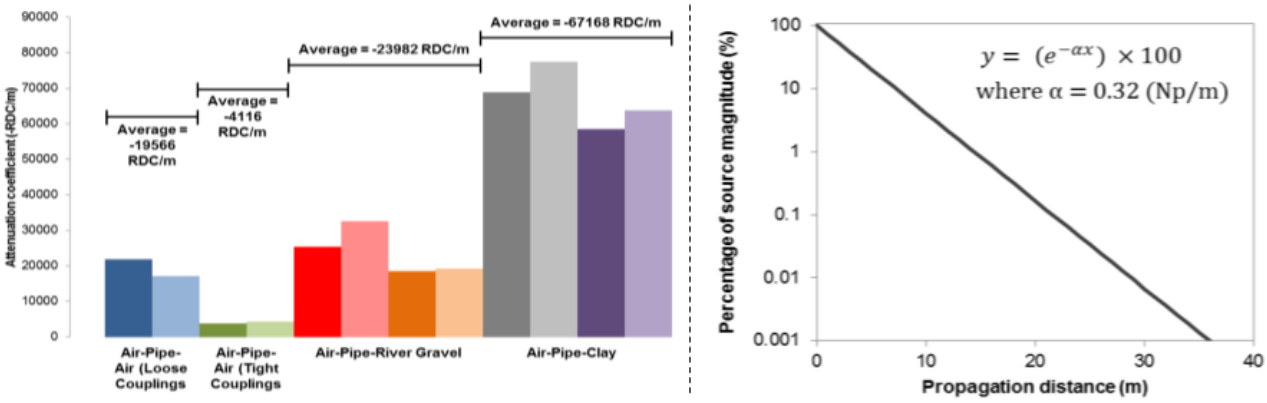


*Figure 2-44. Left: Tri-layer systems attenuation coefficients in ring-down-counts (RDC) per metre; Right: correlation between the percentage of source magnitude and the propagation distance obtained using the attenuation coefficient for air-waveguide-River Gravel system (Smith, 2015).*

From the observations in the sections above it can be seen that the use of a waveguide can be represented as an additional phase, so that the waves propagating through saturated soil should also be communicated and transmitted to and through the waveguide before reaching the AE sensor. The relevance of this insight is that, if the coupling between the soil phases and the waveguide is somehow inefficient due to e.g. a too large impedance change, there might be considerable AE signal loss. Such signal loss would be more dramatic where impedance changes are greater, presumably between the fluid and the waveguide. At any rate, this issue is at the present stage of work under consideration and further analysis and experimentation seems necessary to reach a satisfactory conclusion (Koerner et al., 1981; O'Brien et al., 1996; Moebius et al., 2012).

### 2.4.2 AE measurement

A sensor can be broadly defined as a "device that receives and responds to a signal or stimulus." They must speak the same language as the devices with which they are connected, which is in its nature electrical - a sensor must be able to respond with signals where information is carried by displacement of electrons. This makes it possible to connect a sensor to an electronic system through electrical wires.

A transducer is converter of one type of energy into another (while sensors convert any type of energy into electrical energy). A loudspeaker is one example of a transducer, as it converts an electrical signal into a variable magnetic field and, then, into acoustic waves. Inversely, a loudspeaker can work as a microphone when connected to an input of an amplifier - in this case it acts as an acoustical sensor.

Moreover, transducers might be used as actuators in various systems - an actuator is, in a sense, the opposite to a sensor since it converts electrical signal into energy. For instance, an electric motor is an actuator as it converts electric energy into mechanical action.

Complex sensors can incorporate several transducers (Figure 2-45). For example, a sensor may have a component (a transducer) that converts the energy of a chemical reaction into heat and a second component that converts heat into an electrical signal, which combined form a chemical sensor - a device that produces electrical signal in response to a chemical reagent.

Hence, two types of sensors can be identified: direct and complex. The former converts a stimulus into an electrical signal (or modifies an electrical signal by using an appropriate physical effect), while the latter employs one or more transducers before a [direct] sensor can be employed to generate an electrical output.

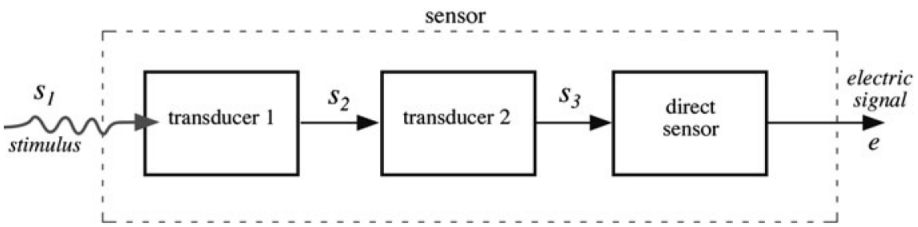


*Figure 2-45. Diagram of how a sensor (area within dashed line) can include several transducers. The last (rightmost) part is a direct sensor producing electrical output (e). $S_1$, $S_2$, and $S_3$ are different types of energy or stimuli (Fraden, 2010).*

An acoustic sensor is a pressure transducer adapted to detecting sound waves. They differ by sensitivity, directional characteristics, frequency bandwidth, dynamic range, sizes, etc, and their designs tend to be suited to the media from which sound waves are sensed (e.g. in air waves or vibrations in solids, the sensor is called a microphone, while for operation in liquids, it is called a hydrophone). The main difference between pressure and acoustic sensors is that latter do not need to measure constant or slowly changing pressures – acoustic sensor operating frequencies usually start at several Hertz up to several mega-Hertz for the ultrasonic applications and even giga-Hertz in a surface acoustic wave device.

Given that acoustic waves are mechanical pressure waves, microphones or hydrophones have the same basic structure as a pressure sensor: a moving diaphragm and a displacement transducer, which converts the deflections of the diaphragm into an electrical signal. Acoustic sensors differ by the designs of these two essential components and may include additional parts like mufflers, focusing reflectors or lenses, etc (Fraden, 2010). Several types of acoustic sensor are described next.

*Sensors*

Resistive Microphones: Resistive pressure converters (pressure to electricity) used to be extensively used in microphones, consisting of a semiconductive powder (commonly graphite) whose bulk resistivity was sensitive to pressure, i.e. possessed piezoresistive properties. Such

a design has a considerably limited dynamic range, poor frequency response, and a high noise baseline.

The main type of such device is a carbon microphone, which consists of a capsule containing carbon granules pressed between two metal plates. A small electric current is induced through the carbon is caused by a voltage applied across the metal plates. The diaphragm (in effect one of the plates), vibrates under the incident sound waves, which applies a varying pressure to the carbon granules and causes them to slightly deform. This causes the contact area between each pair of adjacent granules to change and results in a change of electrical resistance. These resistance changes in turn cause voltage variations across the two plates, and hence in the current flowing through the microphone, producing the electrical signal. Carbon microphones were commonly used in telephones. Currently, the same piezoresistive principle can be employed in the micromachined sensors, where stress sensitive resistors are the integral parts of a silicon diaphragm. (Fraden, 2010).

Condenser Microphones: Also called “capacitive” microphones, basically consist of a parallel-plate capacitor that converts a distance between the plates into electrical voltage (which can be further amplified). It requires a source of electric charge, the magnitude of which directly determines the device sensitivity. Condenser microphones are often made with silicon diaphragms, which serve two purposes: converting acoustic pressure into displacement and acting as a moving plate of a capacitor.

Condenser microphones generally produce a high-quality signal and their sensitivity is mainly due to the quite small mass that must be moved by the incident sound wave. (Fraden, 2010).

Fibre-Optic Microphone: Comprised of a single-mode temperature insensitive Michelson interferometer and a reflective plate diaphragm. The interferometer measures the plate deflection, which is proportional to the acoustic pressure. The sensor is water cooled to provide thermal protection for the optical materials and to stabilize the mechanical properties of the diaphragm.

Generally, two fibres are fused together and cleaved at the minimum tapered region (Figure 2-46) to provide an effect of interference between the incoming and outgoing light beams. The fibres are incorporated into a stainless-steel tube, which is also water cooled. The internal space in the tube is filled with epoxy, while the end of the tube is polished until the optical fibres are observed. Aluminium is selectively deposited to one of the fused fibre core ends to make its surface mirror reflective. This fibre serves as a reference arm of the microphone. The other fibre core is left open and serves as the sensing arm. Temperature insensitivity is obtained by the proximity of the reference and sensing arms of the assembly.

Light from a laser source (a laser diode operating near 1.3 mm wavelength) enters one of the cores and propagates toward the fused end, where it is coupled to the other fibre core. When reaching the end of the core, light in the reference core is reflected from the aluminium mirror toward the input and output sides of the sensor. The portion of light, which goes toward the input is lost and makes no effect on the measurement, while the portion which goes to the output, strikes the detector's surface. That portion of light that travels to the right in the sensing core exits the fibre and strikes the copper diaphragm. Part of the light is reflected from the diaphragm back toward the sensing fibre and propagates to the output end, along with the reference light. Depending on the position of the diaphragm, the phase of the reflected light varies, thus becoming different from the phase of the reference light.

While traveling together to the output detector, the reference and sensing lights interfere with one another, resulting in the light intensity modulation. Therefore, the microphone converts the diaphragm displacement into a light intensity. Theoretically, the signal-to-noise ratio in such a sensor is obtainable on the order of 70–80 dB, thus resulting in an average minimum detectable diaphragm displacement of 1 Å ($10^{-10}$ m). (Fraden, 2010).

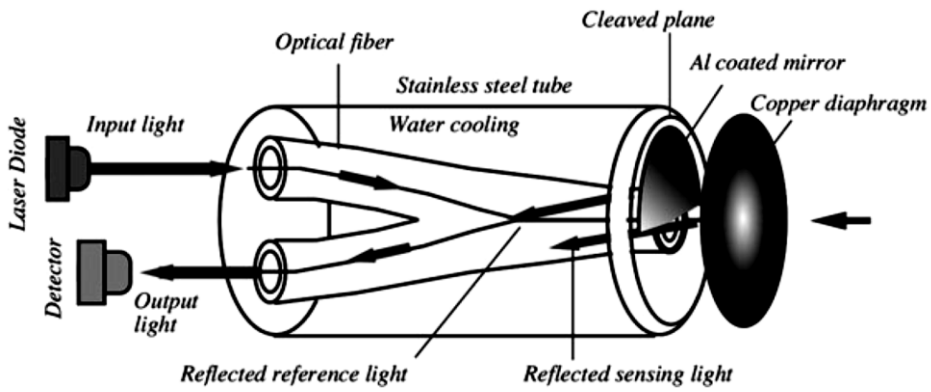


*Figure 2-46. Fibre optic interferometric microphone movement of copper diaphragm is converted into light intensity in the detector (Fraden, 2010)*

Piezoelectric[17] Microphones: Typically consist of a piezoelectric ceramic disk with two electrodes deposited on the opposite sides. Since the output electrical impedance of such a microphone is very large, a high input impedance amplifier is required (Figure 2-47).

Such piezoelectric transducers have the advantage of not being confined to use in air and can be bonded to a solid or immersed in a non-conducting liquid so as to pick up sound signals in any of these media. They can also be used at ultrasonic frequencies, with some types being capable of use in the high MHz region. All piezoelectric transducers require a crystalline material in which the ions of the crystal are displaced in an asymmetrical way when the crystal

[17] The piezoelectric effect is generation of electric charge by a crystalline material upon subjecting it to stress. The effect exists in natural crystals, such as quartz (SiO2), and poled (artificially polarized) human-made ceramics and some polymers, such as PVDF.

is strained. The linearity can vary considerably with the type of material that is used, and from sample to sample. The sensitivity of modern piezoelectric materials to vibration is such that the impact of the sound wave on the crystal alone is enough to provide an adequate output. Most microphones of this type are made as pressure-operated types because one side of the crystal is normally used for securing the assembly to its casing.

The piezoelectric microphone has a very high impedance level and a much higher output than other types of acoustic sensors. The impedance level is of the order of several megohms, as distinct from a few ohms for a moving coil type. At this very high impedance level, electrostatic pick-up of hum is almost impossible to avoid, along with the problems of the loading and filtering effect of the microphone cable. (Fraden, 2010).

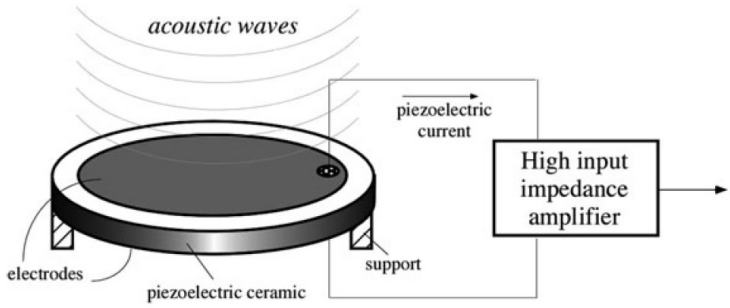


*Figure 2-47. Schematic of piezoelectric microphone (Fraden, 2010).*

Electret Microphones: An electret is a permanently electrically polarized crystalline dielectric material. An electret microphone is an electrostatic transducer consisting of a metallized electret diaphragm and backplate separated from the diaphragm by an air gap. Electret microphones are high impedance sensors and require high input impedance interface electronics.

An upper metallization (application of a metal coating to a surface) and a metal backplate are connected through a resistor voltage across which can be amplified and used as an output signal. Since the electret is permanently electrically polarized dielectric, charge density on its surface is constant and sets in the air gap an electric field. When acoustic waves meet the diaphragm, it deflects, reducing the air gap in between. (Fraden, 2010).

Dynamic Microphones: Dynamic microphones work via electromagnetic induction. They are robust, relatively inexpensive, and resistant to moisture. Moving-coil microphones use the same dynamic principle as in a loudspeaker, only reversed (Figure 2-48a). A small movable induction coil, positioned in the magnetic field of a permanent magnet, is attached to the diaphragm. When sound enters through the windscreen of the microphone (not shown in the

figure), the sound wave moves the diaphragm. When the diaphragm vibrates, the coil moves in the magnetic field, producing a varying voltage across the coil terminals. This is a result of electromagnetic induction. A variable magnetic field then induces voltage in a coil. Thus, movement of the coil inside a permanent magnet generates the induced voltage and a subsequent current in direct relationship with the rate of changing the magnetic field.

Ribbon microphones, a second type of dynamic microphones, use a thin, usually corrugated metal ribbon suspended in a magnetic field (Figure 2-48b). The ribbon is electrically connected to the microphone's output, and its vibration within the magnetic field generates the electrical signal. Ribbon microphones are similar to moving coil microphones in the sense that both produce sound by means of magnetic induction. Basic ribbon microphones detect sound in a bidirectional (also called figure-eight) pattern because the ribbon, which is open to sound both front and back, responds to the pressure gradient rather than the sound pressure. Though the symmetrical front and rear pickup can be a nuisance in normal stereo recording, the high side rejection can be used to advantage is some applications, especially where a background noise rejection is required. (Fraden, 2010).

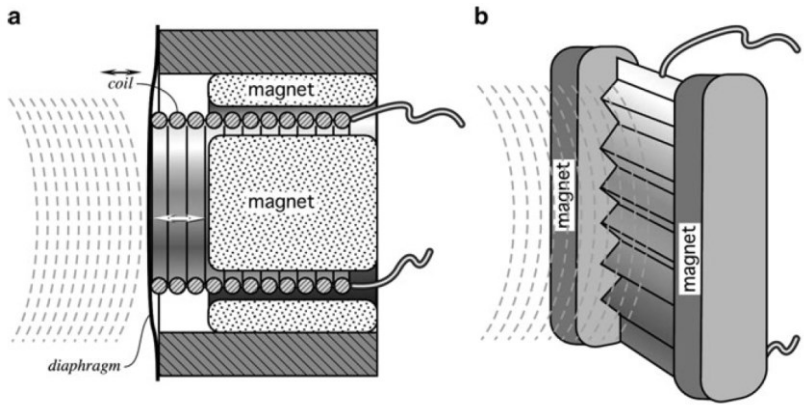


*Figure 2-48. Dynamic microphones: moving coil (a) and ribbon (b) (Fraden, 2010).*

<u>Solid-State Acoustic Detectors:</u> Their operation is centred on the elastic motions in solid parts of the sensor. The atoms of the solid are forced to vibrate by an excitation device (normally piezoelectric), causing the neighbouring atoms to produce a restoring force tending to bring the displaced atoms back to their original positions. In such acoustic sensors, vibratory characteristics, such as phase velocity and/or attenuation coefficient, are affected by the stimulus. Since mechanical stress (vibration) induces an electrical response and electric stimulus causes stress in the piezoelectric crystal – it goes both ways -, the sensor usually has two piezoelectric transducers at both ends: one at the transmitting end for generation of acoustic waves and the other at the receiving end for conversion of acoustic waves into electrical signal. (Fraden, 2010).

*Data acquisition*

As might be expected, a sensor does not function in isolation; it is practically always a part of a larger system that might incorporate many other components. It can be placed at the input of a device to perceive the outside effects and to signal the system about variations in the outside stimuli. It can also be an internal part of a device that monitors the state of the device itself (e.g. to assure proper performance). The input signals (stimuli) to a sensor can have practically any conceivable physical or chemical nature (e.g., light, temperature, pressure, vibration, displacement, position, velocity, ion concentration, etc).

Furthermore, a sensor is always a part of a data acquisition system and control device - such a system might itself be a part of a larger control system that includes various feedback mechanisms. Figure 2-49 illustrates the positioning of sensors in a larger system. Data are collected from the object (target of detection and measurement) by a number of sensors (1, 2, 3, 4 and 5 in Figure 2-49). Some of these sensors (2, 3, and 4) are positioned directly on or inside the object, while sensor 1 perceives the object without direct physical contact. A different purpose is fitted by sensor 5, which monitors internal conditions of the data acquisition system itself.

Some sensors (1 and 3 in this example) cannot be directly connected to electronic circuits (e.g. inappropriate output signal formats), making the use of interface devices (signal conditioners) necessary. Here, sensors 1, 2, 3, and 5 are passive (they generate electric signals without energy consumption from the electronic circuits), while sensor 4 is active, meaning it requires an operating signal (provided by an excitation circuit; this signal may be modified based on the converted information).

Electrical signals from the sensors may be sent to a multiplexer (a switch or a gate), which serves to connect sensors one at a time to an analog-to-digital converter (A/D or ADC) if a sensor produces an analog signal), or directly to a computer if a sensor produces signals in a digital format. It may as well send control signals to an actuator, which acts on the object.

A system like the one in Figure 2-49 may contain some peripheral devices (e.g. a data recorder, a display, an alarm, etc.) as well as a number of components such as filters, sample-and-hold circuits, amplifiers, and so forth (not shown in this block diagram example).

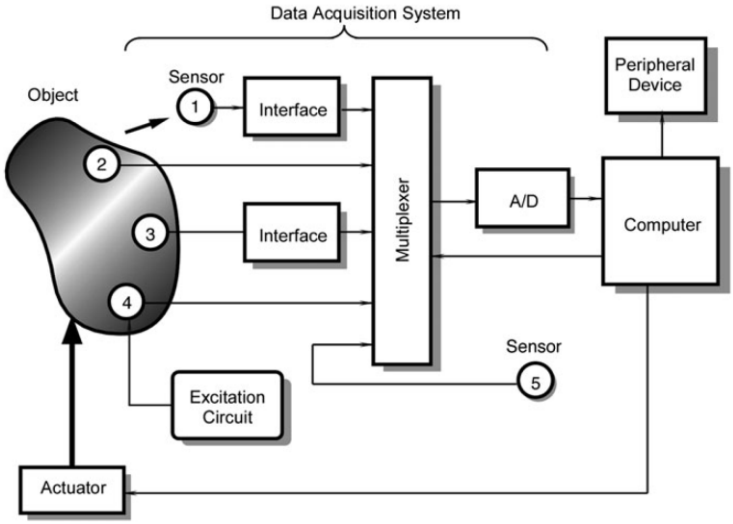


*Figure 2-49. Block diagram of a data acquisition and control device. 1, 2, 3, 4 and 5 represent sensors: sensor 1 is noncontact, sensors 2 and 3 are passive, sensor 4 is active, and sensor 5 is internal to a data acquisition system (Fraden, 2010).*

## *Signal processing*

Vibrations detected by the sensors are transformed into a voltage signal that is normally amplified before being transmitted to an acquisition board, which then converts it into a digital format. Display, data processing and analysis of this signal is commonly done using a computer. The time and frequency domains are relevant ways to approach the problem of processing electrical signals produced by physical data. These ways of looking at a problem are interchangeable: that is, no information is lost in changing from one domain to another (Hewlett Packard, 1981; King, 2009; Kadam and Nayak, 2016; Tohyama and Koike, 1998; Lurton, 2010; Raichel, 2006).

Time Domain:

The time domain is arguably the most traditional way of observing signals. It is a record of what happened to a certain parameter over time. Figure 2-50 illustrates this concept with a time-domain view of displacement where a simple spring-mass system attached to a pen writes on a piece of paper moving past the pen at a constant rate.

In this example (Figure 2-50) the Force can be equivalent to the phenomenon being investigated, the Spring-Mass-Pen to a rudimentary amplifier-transducer, and the paper where the data is recorded. Such a direct recording scheme can of course be used, but it tends to be more practical to convert the parameter of interest into an electrical signal as is allows for more precise, efficient and versatile data acquisition and recording.

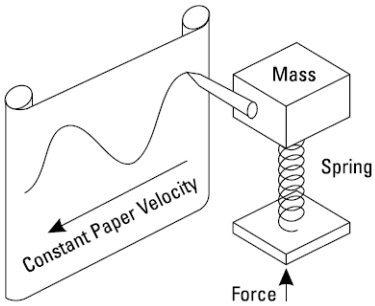


*Figure 2-50. Simple concept of recording in the time domain – the applied force (bottom) causes a mass with an attached pen to move and, as the pen touches a roll of paper moving at a certain speed, a representation of the movement of the mass in time is drawn on the paper (Hewlett Packard, 1981).*

Frequency Domain

The Frequency Domain is the analytic space in signals (or mathematical functions) are conveyed in terms of frequency, rather than time. Frequency-domain plots show how much of the signal lies within each given frequency band over a range of frequencies. Over a century ago Baron Jean Baptiste Fourier showed that that any waveform that exists in the real world can be decomposed into sine waves. In this process, a signal is sampled over a time period and divided into its frequency components, which are single sinusoidal oscillations at distinct frequencies, each with their own amplitude and phase. Figure 2-51. The FFT (Fast Fourier Transformation) is an optimized algorithm for the implementation of the "Discrete Fourier Transformation" (DFT), which is in turn the Fourier Transform of a discrete-time signal.

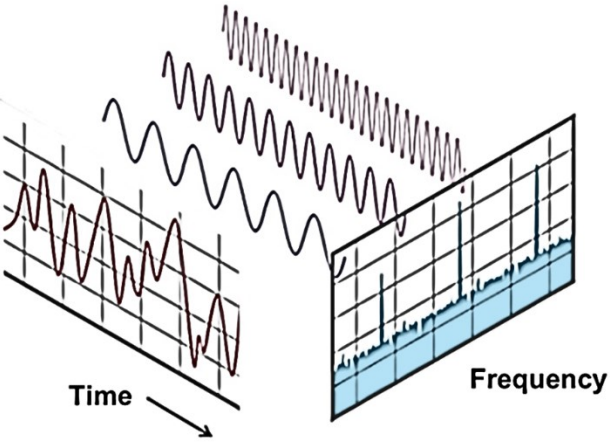


*Figure 2-51. Illustration of Fourier Transform, where the relationship between the time and frequency domains (red and blue plots respectively) is shown after having decomposed the original signal (red plot) into a series of sine waves - each sine wave with a particular frequency and amplitude seen on the blue plot as individual peaks (Hewlett Packard, 1981).*

In one type of analysis of a transient acoustic emission signal (the one focused on this thesis), a threshold is set separating acoustic events (signal) from environmental and equipment noise (Figure 2-52) - an AE event is thus considered to start when the signal amplitude exceeds an assigned threshold. AE events may then consist of many signal oscillatory cycles (considering the fact that mechanical generation processes typically generate full wave packages). Having

determined the significant events, more information can be extracted, e.g.: the event amplitude is the maximum amplitude reached during an AE event; the event duration is the time difference between the first and the last threshold crossing; the rise time is the time difference from the first threshold crossing to the event amplitude. Integrating of the square of the signal deviation from its average has as outcome a measure of the wave energy captured by the sensor (Michlmayr et al., 2012).

The use of zero-crossing or ring-down counts (RDC) is based on the assumption that the count rate increases with increasing AE source strength (Figure 2-52). Practically, this method is simple to use because it compares relative magnitudes among test results. The relationship between seepage flow rate and count rate may be affected by the user-set threshold level (Hung et al., 2009; Smith et al., 2014). It has also been shown to be proportional to AE energy (Dixon et al., 2015a; Smith and Dixon, 2019c). Compared to recording the full waveform, the use of RDC as a simple AE parameter offers benefits that are valuable in a field-based system, such as simplifying data processing and requiring dramatically lower computing power and data storage capacity.

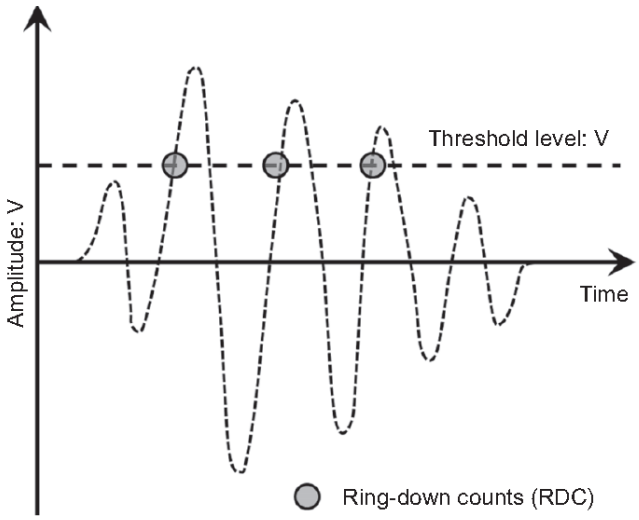


*Figure 2-52. Concept of AE detection removal of noise based on amplitude (voltage) threshold (Smith et al., 2014)*

If the complete transient waveform of individual AE events is recorded, further analysis is possible by, e.g., transforming it into the frequency domain. Michlmayr et al. (2012) report that that the frequency content of a signal is often subjected to natural [inevitable] band-pass filtering because of the frequency dependent sensitivity of many piezoelectric AE sensors. Nonetheless, the frequency content of a signal can allow for the identification of sources of elastic waves, despite limitations like sensor intrinsic bias, sensor-signal interaction (reflection of elastic waves, mode conversion, etc.).

Detecting and interpreting the complex AE signal produced by the displacement of soil particles by water seepage is specially challenging. Besides the already discussed, the knowhow from other disciplines or for addressing distinct problems can be very helpful.

Naturally, the application of data processing techniques (Table 9) is inherent to achieving the intended - pattern recognition, signal filtering and other concepts like Hidden Markov models (Heck et al., 2018) are among the considered tools and approaches. The potential of the information extractable from AE is not yet fully known, but assuming that different processes and materials have different AE signatures, at this time it is deemed plausible that information about the characteristics of specific seepage-induced internal erosion events can be produced.

*Table 9. Examples of signal processing methods (Smith, 1999; Tohyama and Koike, 1998).*

| **Method** | **Brief description** |
|---|---|
| Fourier Transform | Complex function of a real variable (frequency) that operates by sine wave decomposition. It works by sampling a signal over a period of time and dividing it into its frequency components. Figure 2-51. |
| Bilinear transform | Mathematical technique of confrontal mapping, where one complex plane is algebraically distorted or warped into another complex plane. |
| Laplace transform | Complex function of a complex variable that converts integral and differential equations into algebraic equations - it takes a function of a real variable (e.g. time) to a function of a complex variable (frequency). |
| Wavelet decomposition | Mathematical method that deconstructs a signal into its constituent wavelets, or any wavelength shape with zero mean amplitude |
| Z-transform | Converts a discrete-time signal (sequence of real or complex numbers) into a complex frequency domain representation |
| Görtzel algorithm | Applies a single real-valued coefficient at each iteration when analysing one selectable frequency component from a discrete signal, using real-valued arithmetic for real-valued input sequences. |
| Empirical mode decomposition | Type of method based on empirical observations instead of mathematical principles that identify and separate representative modes within a signal |

*AE parameter quantification*

With the capacity to detect an acoustic signal, it follows that this signal must be quantified to be interpreted. As explained, different sensors/transducers have a particular type of output that is intrinsic to its operational mechanism – mostly voltage in the case of electrical devices.

One way of studying a series of electric pulses (e.g. sensor output) is to directly register their amplitudes over time, and essentially use that as a parameter to be processed and analysed. In acoustics though, considering the nature of the phenomenon (i.e. pressure waves), it can be interesting to know.

Decibel: the decibel (symbol: dB) is a relative unit of measurement corresponding to one tenth of a bel. It is a considerably simple and convenient way to measure the volume (loudness) of sound in terms of the sound pressure. More specifically, the dB is used to express the ratio of one value of a power or field quantity to another, on a logarithmic scale, the logarithmic quantity being called the power level or field level, respectively. Two signals whose levels differ by one decibel have a power ratio of $10^{1/10}$ (approximately 1.25893) and an amplitude (field quantity) ratio of $10^{1/20}$ (1.12202)

$$dB = 20 \log\left(\frac{P_{rms}}{P_0}\right)$$

*Where: dB = Sound pressure level; rms = Root mean square value; $P_0$ = reference pressure.*

It was created by Alexander Graham Bell and is based on the logarithmic quality of how humans to sense sound pressure. In other practical terms, it serves to resolve small/weak signals in the presence of disproportionally larger/stronger ones (Hewlett Packard, 1981; Sessler, 1991; Kadam and Nayak, 2016).

Sound intensity: refers to the transfer of the sound wave energy that is a product of sound pressure and particle velocity and is associated with the sound power and surface area surrounding a given source (Kadam and Nayak, 2016).

$$I = p\,u$$

*Where I = sound intensity; p = sound pressure; u = particle velocity.*

The basic outline here used to define which experimental approach should be used is the way other researchers faced similar issues. The systematic investigation of internal instability in soils is thought to have originated in 1953 by the United States Army Corps of Engineers with the usage of a permeameter, and since then a series of studies solidified this methodology, as explained by Fannin and Slangen (2014). Interestingly to this research, suffusion - specifically or in parallel to other phenomena like changes in hydraulic conductivity or strength - has also been repeatedly examined with permeameters (Kovács, 1981; Chapuis et al., 1996; Moffat et al., 2011; Ke and Takahashi, 2012; Hunter and Bowman, 2017b; Slangen and Fannin, 2017a).

Figure 2-53 illustrates a simplified system where water seepage through e.g. an earth dam would generate acoustic emission that could then be detected by the appropriate sensors. Besides demonstrating an anticipated experiment to be performed in this research, it exemplifies a configuration for the detection system. In the (probable) event of having detectors just on the surface of the structure being insufficient, waveguides are suggested as a way of providing a low attenuation path for AE to travel to the surface. Additionally, based on efficacy and practicality, the achievement of adequate sensitivity could also rely on having instrumentation (e.g. hydrophones) present deep within the targeted structure. Both can be symbolized by the dark dashed lines in the figure.

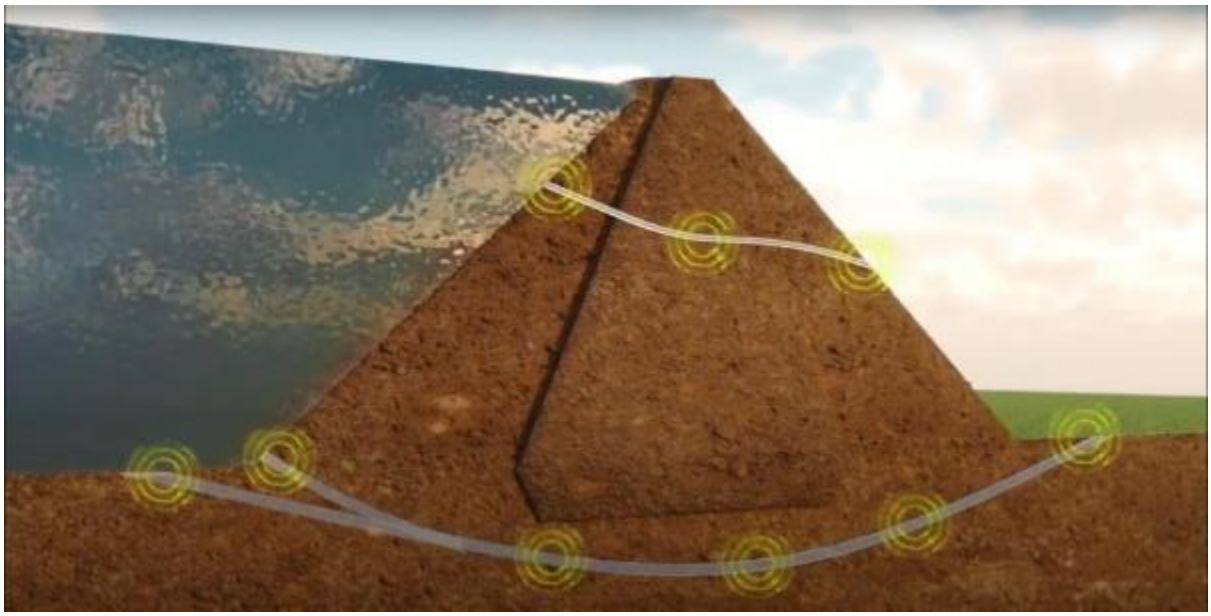

*Figure 2-53. Idealized representation of water-retaining earth structure with the occurrence of seepage, the ensuing generation of acoustic emission and the corresponding AE detectors (https://www.lboro.ac.uk/enterprise/talking-infrastructure/).*

### 2.4.3 AE interpretation

Beyond measuring and processing AE data, making it meaningful for robust observations and responses (e.g. warn about possible disasters, inform about especial necessity of maintenance, evaluate [normal] structural performance, see if negative trends are developing) is necessary for making it relevant and worthwhile. Hence, having systematic ways or frameworks for doing so is necessary to be able to extend the gained knowledge to all applicable contexts.

*Frameworks*

Perhaps the most influential publication in this regard, Koerner et al. (1981) presents very practical while firmly scientific approach(es) to interpret AE from a range of geotechnically important topics.

Simply put, in his 1981 paper Koerner uses already stablished knowledge about a given issue (e.g. dam and embankment stability, soil settlement and deformation and seepage) and AE measurements in the time domain to identify useful correlations, as is clarified in the following examples.

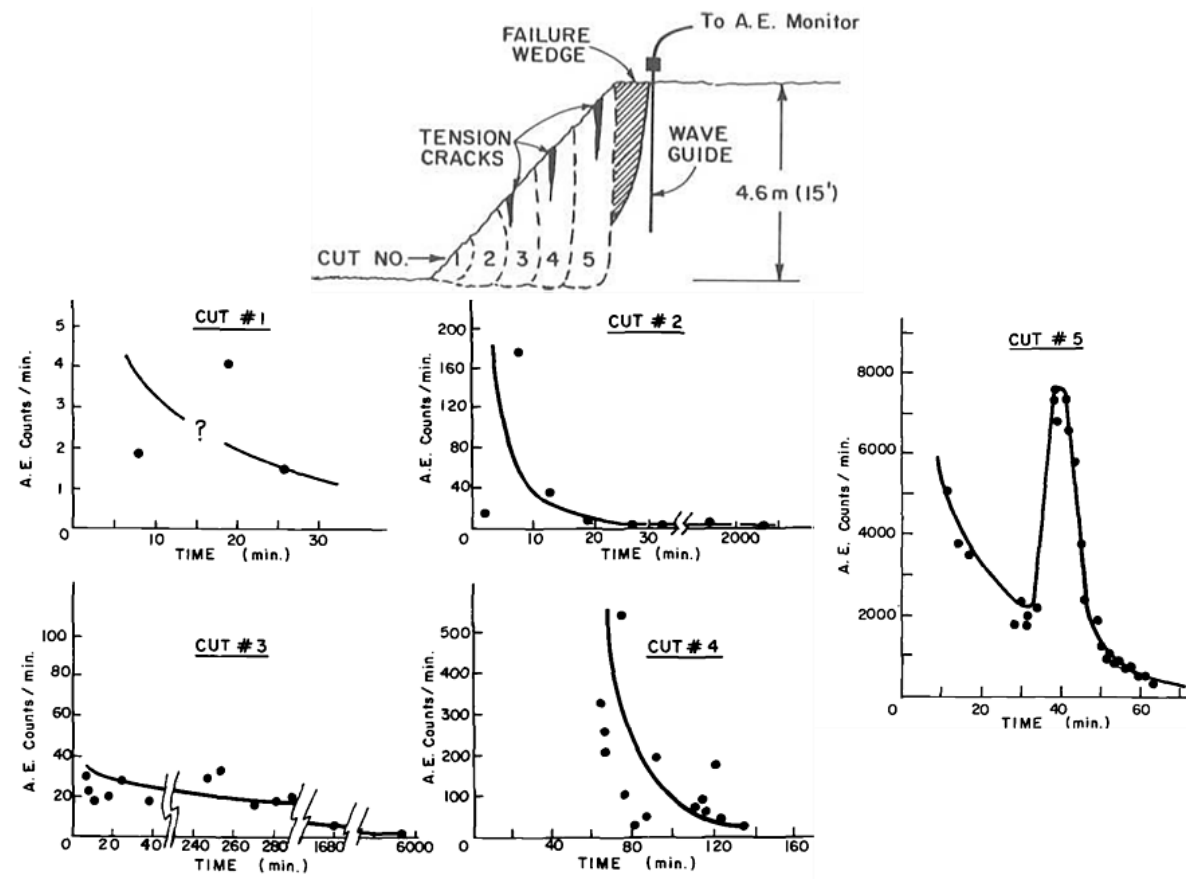


*Figure 2-54. Top diagram shows cuts (1, 2, 3, 4 and 5) done on embankment, with indications of tension cracks and a failure wedge as well as the position of AE waveguide. Below, plots show acoustic emission response over time for the (Koerner et al., 1981).*

Figure 2-54 describes a case in which an embankment was brought to failure by progressive cutting (de-stabilizing) of its slope. In the shown embankment cross-section, the numbered cuts – from toe extending into the slope – had a length of 18 metres (on embankment axis) and were made over a 21-day period. The data shown in the AE plots comes from a 13mm diameter waveguide vertically driven from the top of the slope down through the embankment. The AE response of cuts 1-4 generally shows a high initial rate with a seemingly exponential decay with time until stability its reached. AE rates tended to increase with each successive cut. On cut 5 though the AE rate started by following the same trend but ca. 30 minutes in it is noted to acutely increase and then by minute 40 decrease again (re-assuming the previous trend), which was observed to coincide with a large section of soil detaching from the slope and sliding down.

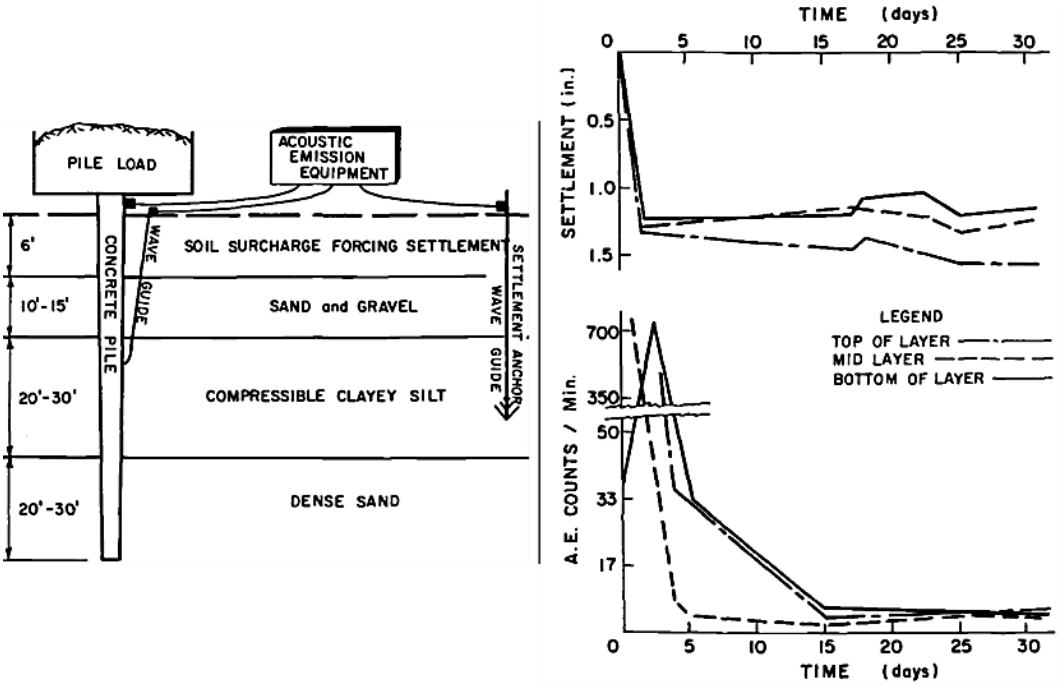


*Figure 2-55. The plots on the upper and lower right respectively show time versus settlement and time versus AE rate of vertical consolidation of a site described on the left side of the figure. In this site description (left) the shown soil profile is subject to a surcharge mobilizing vertical consolidation. The associated AE instrumentation is also indicated. (Koerner et al., 1981)*

The left side of Figure 2-55 depicts a test in which a surcharge fill was placed on a bearing pile to observe soil consolidation, in what constitutes a full-scale negative skin friction, or down drag, test where AE generation was monitored. The piles and settlement anchors were used as AE waveguides. On the right side of the image the test results are displayed, with a considerably robust correlation between the settlement (upper half) and AE Lower half) - the dissipation of the AE response after 5 to 15 days is in agreement with theoretical computations using standard consolidation theory. The reason for the mid layer AE response reaching equilibrium in a shorter time than the adjacent ones is described in the paper as not known.

The upper half of Figure 2-56 illustrates a case in which water seepage had been observed in a dam (ca. 3.6m high and 370m long). A series of borings was then made along the axis of the dam to perform flow rate tests. The boreholes had a plastic casing that could not conduct acoustic emissions (thus not usable as waveguides), so, to be able to measure AE at the bottom of the boreholes (where seepage seemed to be occurring), heavy steel wires were inserted down the boreholes. On the lower half of the image the plotted data shows that the section between borings 3 and 4 (62 m or 200ft long) is seemingly the most active seepage region of the dam, which finds a quite strong correlation with the corresponding AE. The authors mention that the mechanism causing the emissions is not known but point to the flow of the seepage against and around the casing as a likely explanation. They also comment that these results are quite encouraging for the use of the AE technique in monitoring for seepage.

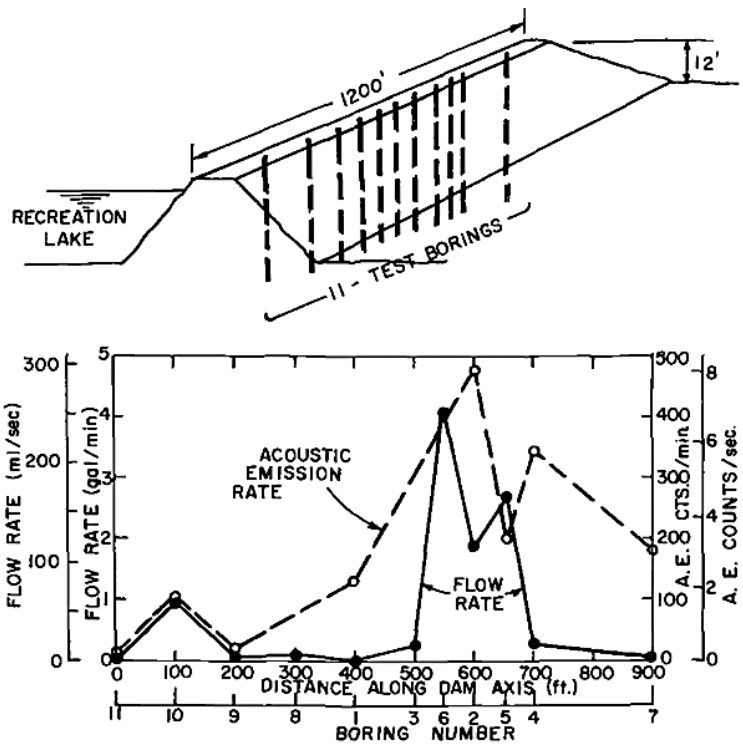


*Figure 2-56. The illustration on top represents a ca. 3.6m high dam (ca. 370m long) with a series of vertical borings that, due to the occurrence of seepage, were used to measure flow rates accommodate AE instrumentation. The produced data – seepage flow rates and AE counts for each borehole location and their relative position along the dam axis – can be seen in the lower half of the figure (Koerner et al., 1981).*

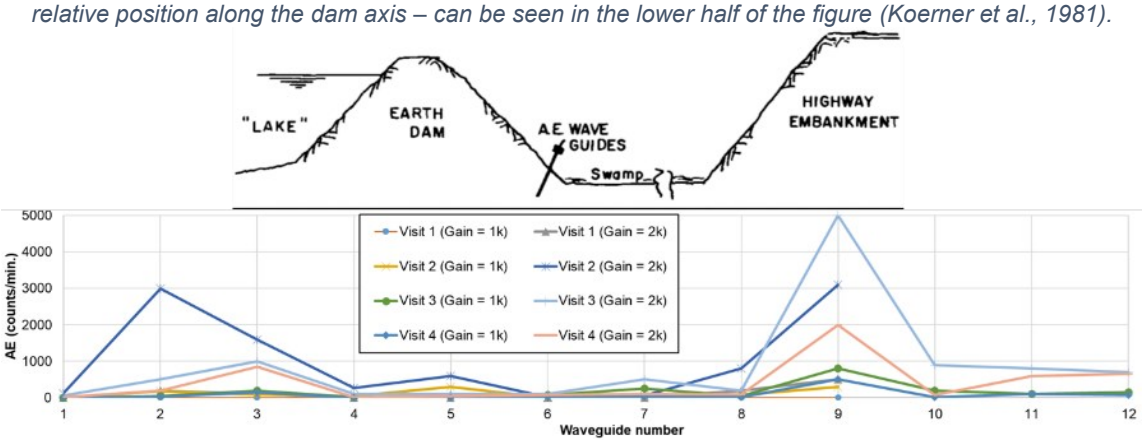


*Figure 2-57. Top half of figure shows profile view of site investigated for seepage. AE waveguides were installed at downstream toe. In each of the four visits when data was gathered the AE system recorded at two gain/amplification settings (1k and 2k) - bottom half of figure. (Koerner et al., 1981).*

The upper half of Figure 2-57 shows the profile view of a reservoir ("Lake") retained by a ca. 7.5m high earth dam where seepage was thought to be happening. Visible signs of seepage would probably have been found on the downstream toe of the dam, but it was under water due to the presence of a shallow swamp. Seepage investigation was done to inform how to proceed with grouting as possible remediation. Twelve AE waveguides (12 mm diameter steel rods) were driven into the toe of the slope at selected points, resulting in the information plotted at the bottom half of Figure 2-57. The data was collected in four different visits to the site over

a period of about 2 months and shows the areas of greatest AE activity, indicating where grouting should be done if judged necessary.

As a summary of the paper by Koerner (1981) the final statements can be drawn:

a) Soil masses that do not generate AE are probably not deforming and are therefore stable.
b) Soil masses that generate moderate levels of AE are deforming slightly and are to be considered marginally stable.
c) Soil masses that generate high levels of AE are deforming substantially and are to be considered unstable.
d) Soil masses that generate very high levels of AE are undergoing large deformations and can be considered to be in a failure state.

<u>Slope displacement</u>

In about the past 60 years AE research in geotechnical engineering has focused on quantifying relationships between acoustics and soil strength and deformation behaviour. The overall purpose of this pursuit has been to create the capacity of evaluating field performance of geotechnical infrastructure assets.

The work done by Smith, Dixon and colleagues (Smith et al., 2014, 2019a; Smith and Dixon, 2019c; Smith et al., 2019b; Smith and Dixon, 2019a) has summarized and elevated the employment of AE for geotechnical purposes to a higher standard – Smith and Dixon in 2018 mention that until then the interpretation of the AE generated by particulate materials had been qualitative and strived to advance it into the quantitative realm, which would enable the early warning of serviceability, limit state failures in the field, enhance element and physical model tests in the laboratory.

Based on the abovementioned (2.4.1) principle that in soil AE is generated by inter-particle friction (e.g. particle sliding and rolling friction, contact network rearrangement, degradation at particle asperities) and consequently the detection of AE is an indication of deformation (Koerner et al., 1981; Michlmayr et al., 2012), the study of AE behaviour in soils demonstrates that:

¶ Deforming soil produces detectable AE.
¶ AE characteristics follow the soil properties (e.g. AE from fine-grained soils is influenced by moisture content and plasticity, soil with large angular particles produce higher magnitude AE.
¶ AE magnitude relates to the stress state of the soil (e.g. AE events with greater magnitude are generated by deforming soil with high inter-particle contact stresses).

(Smith et al., 2014)

Despite the fact that several authors have used AE monitoring to assess slope stability (e.g. Beard, 1961; Cadman & Goodman, 1967; Chichibu et al., 1989; Naemura et al., 1990; Nakajima et al., 1991; Rouse et al., 1991; Fujiwara et al., 1999; Dixon et al., 2003, 2014) the work described in this section is thought to demonstrate this application in a particularly concise and straightforward way.

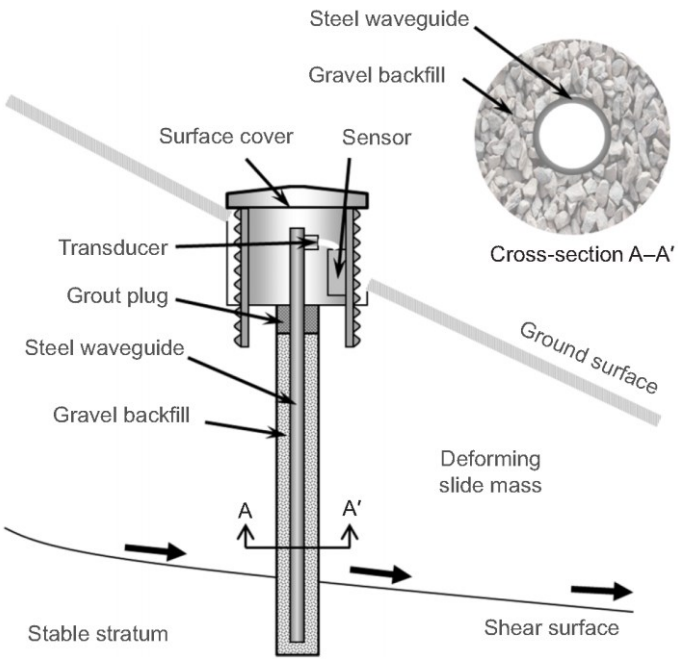


*Figure 2-58. Schematic of active waveguide installed through a slope with an ALARMS sensor placed at ground surface. The detail on the upper right corner shows how the gravel backfill is put in contact with the waveguide (Smith et al., 2014).*

Field work conducted by Dixon et al. (2003) demonstrated that AE monitoring with the use of waveguides is capable of detecting pre-failure deformations earlier than conventional techniques (e.g. inclinometers). The *Slope ALARMS* AE measurement system [18] (Smith, 2015; Dixon and Spriggs, 2007; Dixon et al., 2010) represented in Figure 2-58 was successfully used to quantify slope movements and produce the data observed in Figure 2-59 and Figure 2-60. It uses a 30 kHz resonant frequency transducer coupled to a waveguide at the ground surface and converts the AE into electric signals, which are then amplified and filtered (in order to preserve signals between 20 to 30kHz, so removing low-frequency environmental noise).

[18] https://www.slopealarms.com/

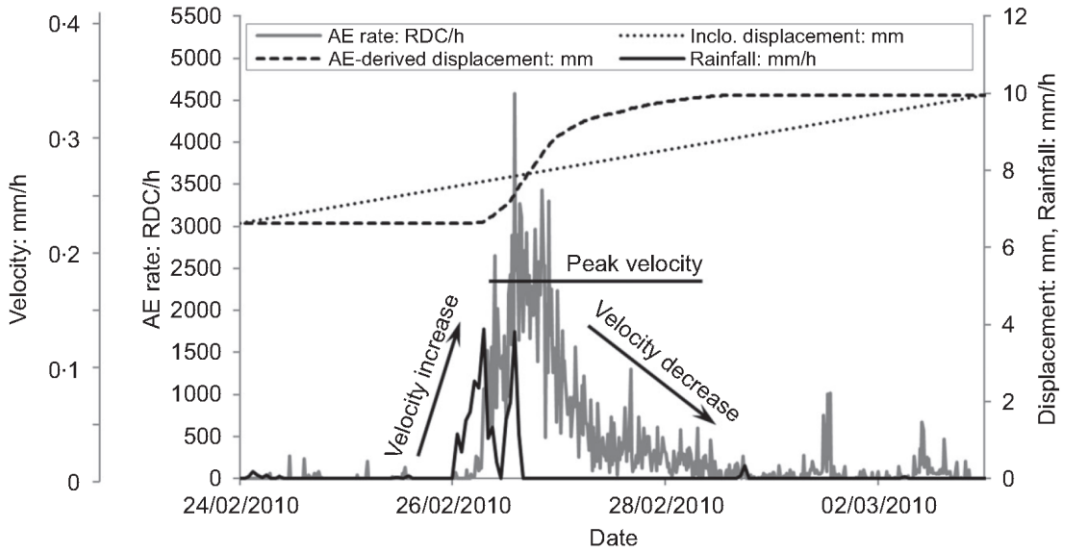


*Figure 2-59. Combined plot of AE rate/hour, AE derived velocity, inclinometer-measured displacement, AE-derived displacement, and rainfall over time of a reactivated slope deformation event (Smith et al., 2014).*

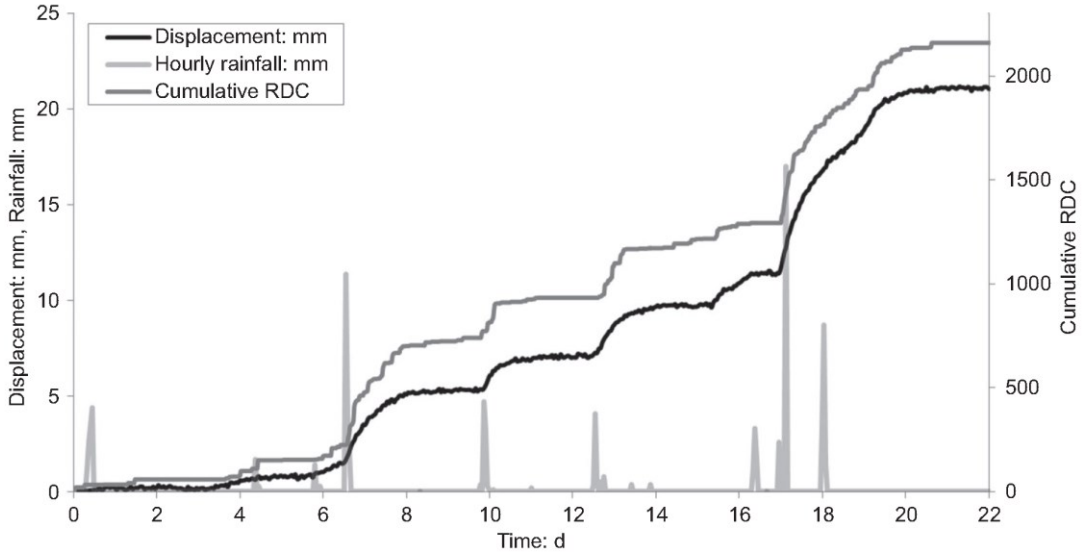


*Figure 2-60. Resultant measured displacement–time, cumulative RDC–time and hourly rainfall–time (Smith et al., 2014)*

The plot shown in Figure 2-59 shows that AE detection can be used to quite precisely infer the displacement of a slope – here notably relatable to an increase in rainfall, very likely to have triggered the movement. Figure 2-60 shows several subsequent such slope movements and further substantiates that slope movements (at the millimetric scale) produce a rather clear detectable acoustic signal. Having in mind the used instrumentation (Figure 2-58), a rise in the rate of slope deformation produces an increasing number of particle–particle/particle–waveguide interactions, resulting in a series of AE events that end up propagating along the waveguide and bring the signal to a sensor at the ground surface.

The observed AE rates are proportional to the velocity of slope movement and depend on several variables related to the AE measurement system, such as:

- Sensor sensitivity.
- Depth to the shear surface – directly related to signal attenuation in its transmission from the shear zone by the waveguide.
- Other waveguide properties (e.g. tube geometry, backfill properties)

Shearing

For a few decades already, laboratory studies on the AE behaviour of soils (e.g. Koerner et al., 1976, 1978, 1981, 1984; Tanimoto & Nakamura, 1981; Mitchell & Romeril, 1984; Tanimoto & Tanaka, 1986; Garga & Chichibu, 1990; Shiotani & Ohtsu, 1999) led to a few qualitative conclusions:

- Well-graded soils generate more AE than uniformly graded soils.
- Angular particles generate more AE than rounded particles.
- AE amplitude increases with particle size.
- Higher imposed stresses generate greater AE activity.
- AE activity increases with imposed strain rate.
- Soils exhibit greatly increased AE activity when stress levels exceed the pre-stress/pre-consolidation pressure due to the Kaiser effect (Lavrov, 2003).
- AE activity increases with strain when densely packed arrangements of grains are sheared until the transition from contractive to dilative behaviour, whereupon the AE activity remains relatively constant.

Based on that and on the idea that stresses applied at the boundary of a soil mass are transmitted to the soil skeleton and cause normal and tangential forces to develop at particle contacts (Cundall & Strack, 1979; Senetakis et al., 2013) and that the distribution and evolution of inter-particle forces at particle contacts strongly controls the mechanical behaviour of particulate systems (Wan & Guo, 2004), Smith and Dixon in 2018 used triaxial tests to investigate the evolution of AE in the stress–strain response of dense sands at a range of effective confining stresses and strain rates under drained conditions (Figure 2-61). Testing 50mm in diameter and 100mm tall specimens, with shearing performed in a strain-controlled way - application of a constant rate of axial displacement – results such as seen in Figure 2-62, Figure 2-64 and Figure 2-65 were produced (Smith and Dixon, 2019a).

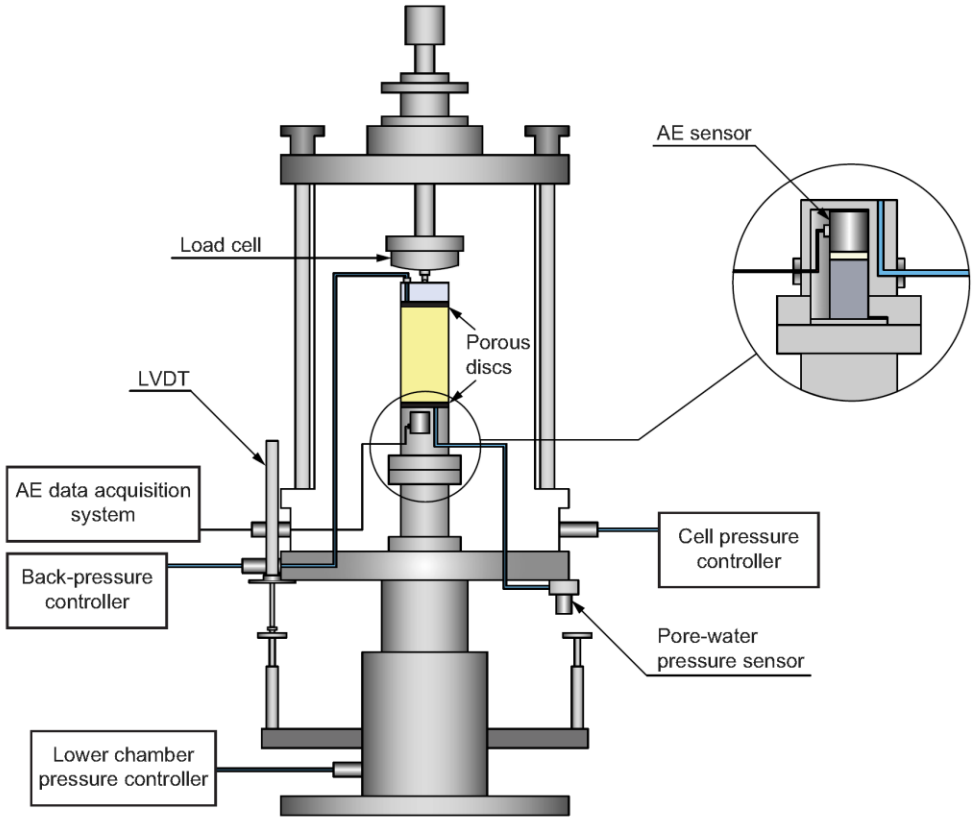


*Figure 2-61. Illustration of triaxial cell with LVDT, linear variable differential transformer and adapted to AE detection – the base pedestal (detail) is equipped for AE and pore-water pressure measurement. (Smith and Dixon, 2019b)*

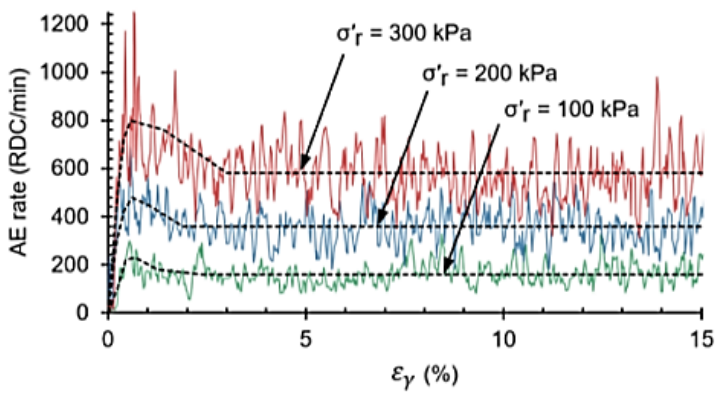


*Figure 2-62. AE rate versus shear strain ($\varepsilon_\gamma$) from triaxial tests at different radial effective stresses (Smith et al., 2019a).*

In the example of Figure 2-62 it is seen that, as effective confining pressure increases, a proportional increase in AE rates is produced, as well as a larger range of shear strain being reached before observing constant AE rates. The authors mention that AE rates increase in proportion to the confining pressure because of the development of greater inter-particle contact stresses, which requires more work to displace particles relative to each other (Smith and Dixon, 2019a).

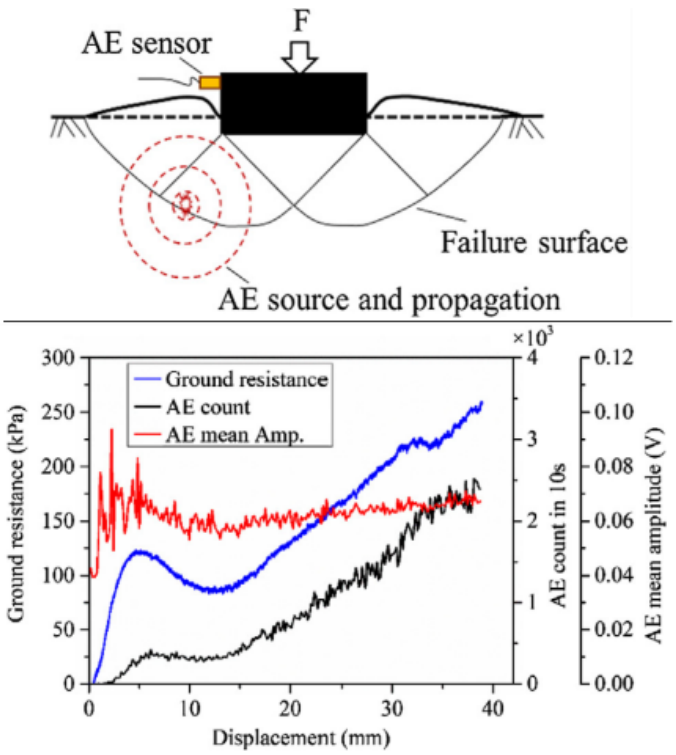


*Figure 2-63. Top half: simplified test arrangement (force applied by loading frame represented by vertical arrow, F) and typical subsurface failure pattern, with generalised AE source point. Lower half: AE rate, mean amplitude and ground resistance [to downward movement] as a function of footing displacement in dense ground (Mao et al., 2019).*

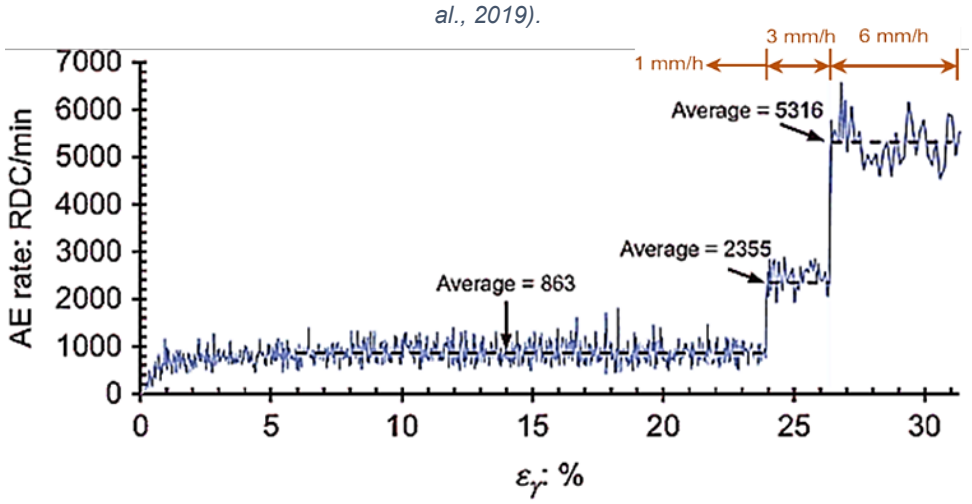


*Figure 2-64. Plot of AE rate (RDC/min) against shear strain ($\varepsilon_\gamma$) from a drained triaxial shearing test at an effective confining pressure of 300 kPa. The displacement rates used in the different test phases (corresponding to the AE "steps") are shown in the upper right corner (Smith and Dixon, 2019b)*

Applying AE to the failure process of shallow foundations, Mao et al. (2019) performed experiments to model this process on sandy ground. Their loading tests were conducted in a conventional motor loading frame assembly and yielded results showing that, as the downward displacement by the loading frame progresses, the AE rate trend correlates quite well with the ground resistance curve. In further detail, the interpreted failure represented as a peak in ground resistance (displacement at ca. 5mm) is seen in the AE (particularly its mean amplitude) also as a quite pronounced peak (Figure 2-63). These observations are key since

they shows that the AE not only can track how the soil counteracts the loading force (effectively being able to infer it) but that it can also identify phase changes or nonlinearities, i.e. failure as opposed to plastic deformation.

In Figure 2-64 results of a test with stepped increases in axial displacement rate, imposed during post-peak conditions, is seen. This test intended to investigate the AE response to accelerating deformation behaviour and demonstrated that AE rates are proportional to the rate of shear strain (Smith and Dixon, 2019a). In other words, AE generation in granular soils is proportional to the imposed stress level and strain rate, which agrees with previous findings (e.g. Koerner et al., 1981; Tanimoto & Nakamura, 1981).

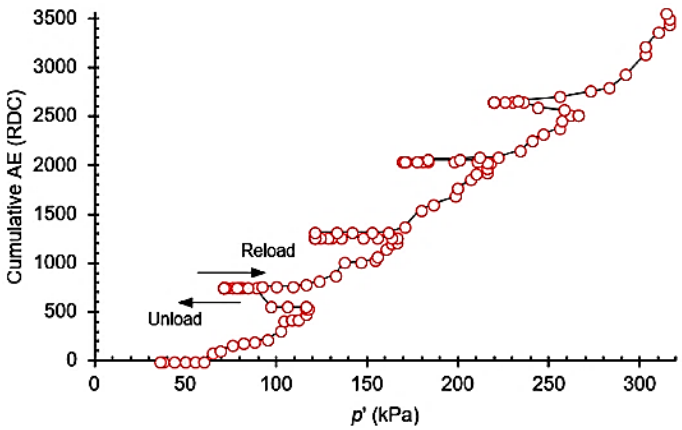


*Figure 2-65. Plot of measured cumulative AE RDC against mean effective stress (p') for isotropic load–unload–reload cycles (Smith et al., 2019a)*

A demonstration of the effect of cyclic loading and unloading is seen on Figure 2-65. The observation that each time a reduction of effective stress (unload) occurs the AE generation practically stops, remains so while effective stress is increased (reload) and just starts rising again once the previously maximum effective stress is reached, clearly shows an instance of the Kaiser effect. Adding to previous research that had shown how particulate materials experience the Kaiser effect in compression (e.g. Koerner et al., 1984; Dixon et al., 1996), the 2018 study by Smith and Dixon extended this knowledge by showing its existence also in shearing (Smith and Dixon, 2019a).

## 2.5 Literature review conclusions

The following points summarise the key findings from the literature review that are most relevant for guiding the development of this thesis. They denote the knowledge base (research questions - “known knowns”) and the knowledge gaps (“known unknowns”) central to this work.

State-of-the-art:

- Seepage-induced internal erosion is a serious problem, source of critical damage in a substantial percentage of failures in water-retaining earth structures.
- Internal erosion and the related particle movement:
    - Cannot be fully predicted,
    - Can evolve at different rates, including irregularly/non-linearly,
    - Can lead to different outcomes (e.g. structural deformation, failure),
    - Can occur in different portions/positions of a given structure,
    - May be influenced by a series of factors external to the structure itself (e.g. weather, freeze-thaw cycles, reservoir levels, mineral dissolution/precipitation).
- The occurrence of internal erosion is associated with:
    - Soil internal stability (geometric criteria)
    - Hydromechanical conditions (Effective stress, hydraulic gradient, flow rate)
- There is still no reliable way to detect seepage-induced internal erosion currently available.
    - It is possible to infer the presence of fluid in a structure (e.g. electrical resistivity) or observe [advanced] external signals of its occurrence. However, current techniques still cannot detect its onset and the critical difference between seepage flow that does and does not transport particles.
- AE is generated by soil dynamics/particle movement.
    - Detectability and interpretation aside, AE generation is intrinsic to the occurrence of internal erosion since a portion of the [kinetic] energy involved is, essentially, inevitably converted into acoustic waves.

Research questions:

- Can the AE generated by seepage-induced internal erosion (specifically particle transport) be detected independently/separately from the AE generated by other phenomena (e.g. fluid[only] seepage, larger scale soil movement, environmental noise)?
- Is AE detection a viable strategy for infrastructure monitoring regarding seepage-induced internal erosion, including interpreting its onset and progression phases?
- Is there one (or more) hydromechanical parameter(s) directly promoting to the onset of internal erosion (i.e. a parameter that not only represents a susceptibility interval but directly incites particle movement)?
- How do hydromechanical behaviours influence AE generation?
- How can AE be deployed to detect and monitor seepage erosion in the field?

Research has demonstrated that AE can monitor energy dissipation inside soil bodies and soil/structure systems. Early work by Koerner showed promise in the use of AE for seepage monitoring. However, further work is required to enhance understanding of AE generated by seepage erosion before a monitoring system for dam monitoring is possible.

This literature review served to inform the development of the methodology described in the following chapter. The key points are:

- Laboratory testing with a permeameter is a robust way to examine the occurrence of seepage-induced internal erosion in a practical, realistic, and controlled manner.
- The physical and technical principles regarding the generation, propagation and detection of AE are significantly well understood and applicable to infrastructure monitoring.
- AE shows considerable advantages when compared to other monitoring methods.
- AE RDC is a suitable way to compute the acoustic signal produced by internal erosion.

# 3 Materials and methods

## 3.1 Introduction

The core of this methodology was the creation of a system for the physical modelling of water seepage through different soil gradations, with the capacity to systematically modify hydromechanical conditions (vertical stress, head), measure changes in the soil over time (pore pressure, volume change, hydraulic gradient, flow rate, visual inspection) and measure/monitor the associated AE response.

The main experimental approaches considered for this pursuit were laboratory testing and scale modelling (i.e. reduced scale earth dams). The reasons why permeameter tests were here chosen are as follows:

- Variables involved in seepage erosion can be controlled in a rather straightforward manner
- The installation of sensors, detectors and gauges is relatively simple and can be customised as well as made modular
- It is relatively inexpensive and simple to prepare and execute several consecutive tests
- Tests can be performed in a rather repeatable way
- Other authors studying internal erosion have successfully employed such equipment (Slangen and Fannin, 2017a; Moffat and Fannin, 2006; Taylor et al., 2017; Zhou et al., 2018; Tomlinson and Vaid, 2000; Hunter and Bowman, 2017a; Li, 2008; Nguyen et al., 2017; Rönnqvist et al., 2017; Ouyang and Takahashi, 2016; Yang et al., 2019)
- Scale modelling would for each test require the construction of a new model, including the installation of equipment, drastically increasing the amount of time, effort and resources needed to perform several tests and thus reducing the number of workable tests
- Once in possession of the equipment, it becomes part of the assets of the institution (i.e. The School of Architecture, Building and Civil Engineering at Loughborough University) and can be used by future researchers and students. Having designed and built the apparatus in-house also adds to the know-how and expertise of the ones directly and indirectly involved in the project and, in a broader sense, the institution itself.

Given the experimental character of the chosen approach, studying the phenomena at hand entails the capacity to simulate them in a controlled environment. As no standard, apposite test equipment is readily available a test apparatus has been designed and built - although a number of equivalent test devices have been used in comparable studies (Indraratna et al.,

2018; Wan, 2006; Rochim et al., 2017; Hung et al., 2009; Sibille et al., 2015a; Hunter and Bowman, 2017a; Moffat and Fannin, 2006), these devices are normally commissioned for each study and, perhaps more importantly, there is still no agreed standard, especially considering the particularities of each project. Being based on a permeameter (ISO TS 17892-11.2004, 2004; Moffat and Fannin, 2006), the design aspires to control vertical load and hydraulic head (or the hydraulic load and the stress condition) given their role in the occurrence or internal erosion in susceptible soils (Figure 2-9) as well as measuring relevant hydromechanical parameters (i.e. vertical compression, pore pressures, [effective] vertical load, outflow rate) and AE.

Preliminary experiments were performed with a simple permeameter, which demonstrated the potential of the approach but had several limitations. This led to the design and construction of a new permeameter with an improved set of characteristics. This new device was then used for subjecting a selection of soils used in civil engineering and with different estimated degrees of internal instability to seepage-induced internal erosion.

This chapter describes the preliminary experiments with a simple permeameter, the design and development of the new, large permeameter, the experimental programme, test soils, instrumentation and the AE measurement system.

### 3.1.1 Preliminary tests (simpler permeameter)

Initial laboratory work was performed to probe the study of internal erosion using AE. The device used in the initial tests is illustrated in Figure 3-1. It was a Perspex tube with ports for two pressure transducers, two manometers and one for the insertion of a steel-tube waveguide in contact with a piezoceramic acoustic transducer on the outside. It could apply vertical (up- or downward) flow at a fixed head to a sample under self-weight. Details of the tested samples can be found in Figure 3-2 and Figure 3-3. Water pressure variation in these preliminary test results was controlled by varying the hydraulic head, which was done by changing the height of the permeameter with a hydraulic lift table (Figure 3-4), as the water tank had a fixed position.

The operation of the permeameter illustrated in can be described in Figure 3-1 as follows:

1) Flow was induced by applying a constant hydraulic head.
2) Pressure was measured by manometers and pressure transducers at two different heights along the specimen.
3) Water flow and eventual particle movement generate AE.
4) AE was transmitted through a WG and measured by a sensor external to the specimen.

5) The signal was amplified, pre-filtered by a data acquisition software and stored for further analysis.

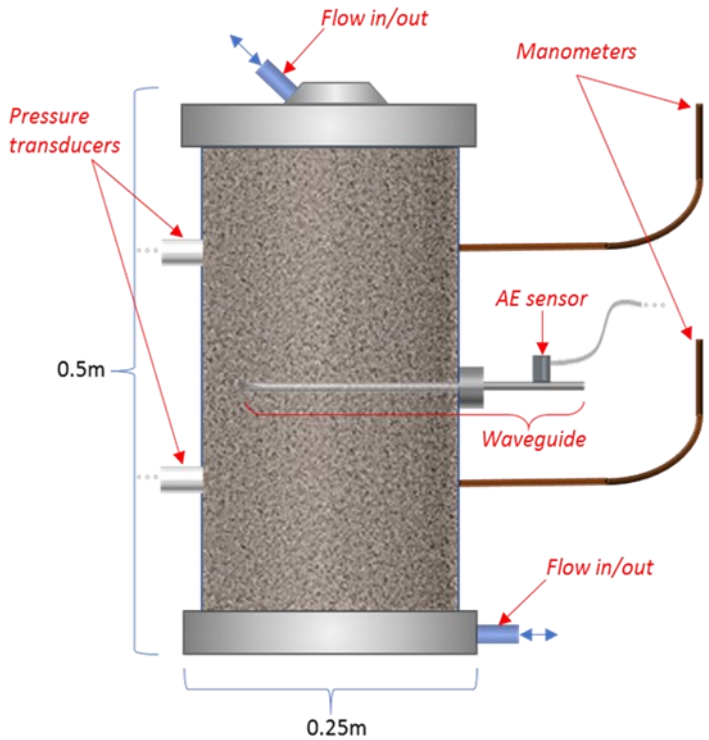


*Figure 3-1. Schematic of permeameter used in initial experiments.*

The data produced by this equipment (see Results chapter) was quite useful, especially regarding AE, but had shortcomings when it came to the control and measurement of hydromechanical parameters. A description of the main shortcomings is seen below:

- The fixed position of the constant-head tank did not allow for head control, including not being able to start a test at a neutral head.
- The lack of application and measurement of stress (beyond self-weight) excluded effective stress as a variable to be considered, one regarded by the available literature as pertinent to the studied processes.
- Incapacity of measuring volume change (vertical displacement), which can reveal important changes to the sample.
- No systematised measurement of flow rate, an intrinsically important component concerning seepage-erosion.

Also, the observation of the produced acoustic signal in parallel to visually observing the erosional process led to the idea of using other forms of AE detection in addition to the waveguide-based system, as is explained in the following sections. Despite the mentioned limitations, these preliminary results were very promising regarding the detection of AE from internal erosion and served as further motivation for pursuing this methodology.

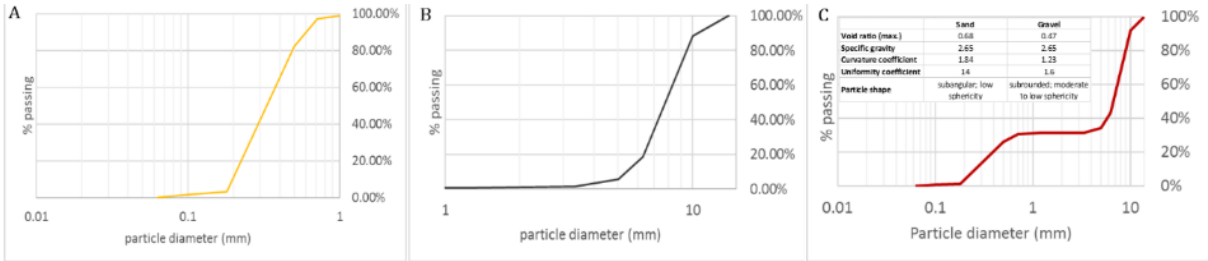


*Figure 3-2. Grain size distribution curves of materials used in initial laboratory tests. A) sand; B) gravel; C) sand and gravel mixture.*

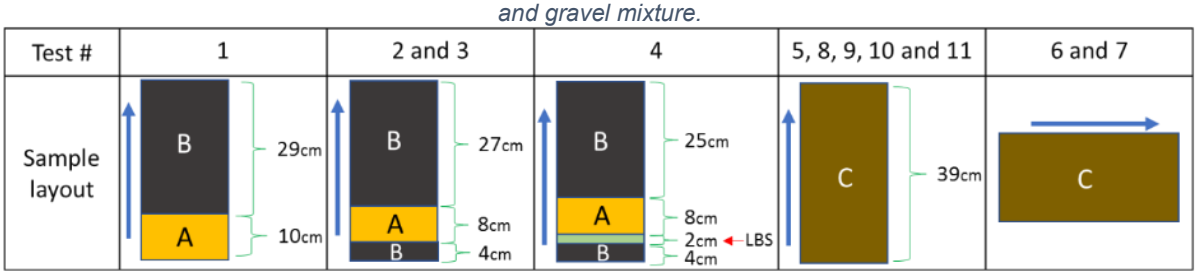


*Figure 3-3. Disposition of soils (A, B and C; Figure 3-2) within permeameter during initial tests. Blue arrows indicate flow direction. In test 4 the 2cm Leighton Buzzard Sand (LBS) layer had a nearly uniform grain diameter of 1mm.*

*Figure 3-4. Exemplar of lift table used in experiments for varying permeameter height.*

### 3.1.2 Implications of preliminary tests

#### *3.1.2.1 Particle size distributions*

An observation about the soils tested in the initial experimental phase is that their grain sizes and permeability were considerably high, besides being gap-graded in a way that makes them especially internally unstable for the applied hydraulic gradients. But, despite the considerable straightforwardness of initiating internal erosion and detecting the corresponding AE (leaving aside its complex interpretation), subsequent tests meant to use materials closer to the limits of internal stability conditions (i.e. near their margin of internal stability) and that better represent the soils used in the construction of earth embankments and dams.

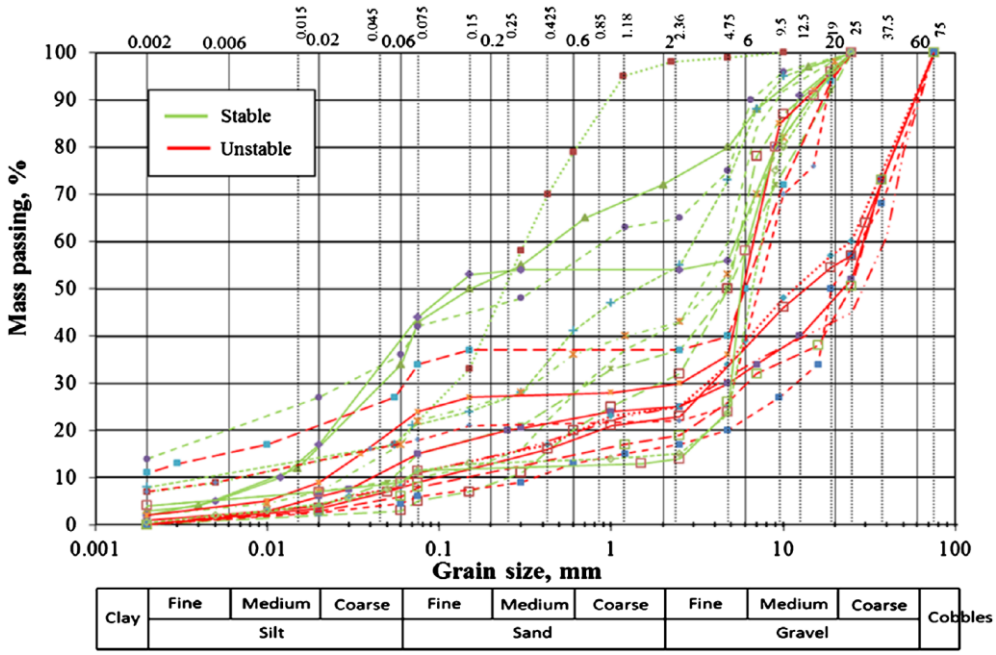


*Figure 3-5. Soil gradations tested by Wan and Fell and UNSW to study internal erosion in the context of embankment dams (Rönnqvist and Viklander, 2014).*

Compilations of soils used in embankment dams made by Rönnqvist and Viklander, (2014), Wan and Fell (2008) and the U. S. Society on Dams (2011) served as guidelines for choosing the materials to be tested here in subsequent experiments (Figure 3-5), with focus on finer gradations due to their lower permeability and practicality when working at a laboratory scale (i.e. ease of producing sufficient hydraulic gradients in a permeameter with moderate dimensions and with lower hydraulic head). The methodologies for estimating internal stability presented in the literature review (particularly the ones by Burenkova (1993), Kenney and Lau (1985) and Wan and Fell (2008)) were used for estimating the internal stability of such soils, which was preferred at a boundary stability condition as to better control the onset and progression of internal erosion.

#### *3.1.2.2 Equipment*

A series of features, or the capacity to control them, have been noted as lacking for a more adequate study of the matter at hand. Such features and justifications for their implementation are listed below:

*Reliable measurement of AE:* there was doubt about the use of a WG linked to an AE sensor as early tests hint that only direct particle collisions with the WG seem to be detected – large impedance difference between water-soil mixture and metal rod/tube of the WG was thought to be an issue. Hydrophones were thought to be better suited to detect longitudinal waves transmitted by the water in the saturated medium, which in principle alters the kind of waves possibly detected but gives prospective advantages regarding sensitivity and signal loss (Koerner et al., 1981; O'Brien et al., 1996; Moebius et al., 2012).

*Effective stress (σ') and volume change gauge*: effective stress is a key condition for the proneness of a soil to internal erosion and needs to be controlled and measured (Moffat and Fannin, 2006; Ke and Takahashi, 2014; Ferdos et al., 2018).

*Volume change:* An LVDT was used for measuring vertical displacement as suffosion and particle re-accommodation occurs during testing.

*Hydraulic head control*: although non-trivial hydraulic gradients could be applied, the range and control of the imposed head are still limited. The hydraulic gradient is also a crucial variable for internal erosion. A pressure pump or vertically movable water tank are possible solutions (Chang and Zhang, 2013a; Sibille et al., 2015b; Moffat and Herrera, 2015).

*Flow measurement:* values such as permeability and flow rate are strongly linked to internal erosion and need to be collected. Weighing of the outflow in time using a tank and logging scale (Figure 3-6, Figure 3-9) seems to be a simple and reliable solution (Sibille et al., 2015b; Marot et al., 2016; Rochim et al., 2017).

*Larger number of pressure transducers:* better spatial distribution of sensors could help identify location of activity (e.g. onset of erosion, clogging) within the soil sample (Moffat and Fannin, 2006; Moffat, 2005; Moffat et al., 2011).

## 3.2 Design and construction of new test apparatus

The device was composed of a permeameter cell mounted in a reaction frame, an axial loading system, an adjustable height constant head tank for imposing unidirectional water flow and an outflow tank for quantifying mass loss and fluid flow. Its basic functions can be described as:

1) Controlling the experimental conditions deemed most important for the onset and progression of the phenomena in question.
   a) vertical stress
   b) hydraulic head/gradient
2) Measuring the relevant variables
   a) AE – use of hydrophone(s) as well as a WG.
   b) Pore pressures – series of pressure transducers across the sample
   c) Vertical stress – load cells above and below sample
   d) Vertical compression – LVDT
   e) Flow rates – outflow tank computing effluent mass increments over time

The design choices were based on designs by other authors (Moffat and Fannin, 2006), expected costs, ease of construction and, of course, understanding of the studied processes. These are explained as follows:

*Permeameter*: adequate for inducing fluid flow through a soil with standardized procedures (ISO TS 17892-11.2004, 2004) for calculating different parameters in a way that could be straightforwardly adapted to this modified version. A permeameter with a rigid wall, despite not being able to control [lateral] confining pressure (as in a triaxial cell) and having issues like boundary effects and wall friction, facilitated the installation of ports for different sensors, sample preparation, and simplified the overall design, especially considering the intended sample sizes. The size of the chamber reserved for the soil samples considered the soil gradations to be tested and intended to reduce effects such as arching and wall friction (Take and Valsangkar, 2001; Lovisa et al., 2014; Ke and Takahashi, 2014), while also allowing for a more gradual and realistic development of internal erosion – a longer sample length also allows for particle transport and formation of eventual preferential pathways to be clearer and observed in a more detailed, step-by-step way.

*Acoustic sensors*: the use of a waveguide, had already been successfully implemented for the detection of soil movements/deformation (Smith and Dixon, 2019b; Dixon et al., 2015a; Smith, 2015; Smith and Dixon, 2014) and, based on the initial tests showed useful also for the detection of internal erosion, at least for processes directly affecting/interacting with the waveguide itself. Hydrophones were conversely chosen by their capacity to detect AE occurring in a volume of material (i.e. not directly in contact with the sensor) by detecting the compressional acoustic component transmitted by the permeating fluid. Hydrophones positioned above and below the sample may offer the benefit of calculating sound attenuation through the specimen or other such comparative correlations between their detections. The AE signal from the waveguide and the hydrophones can also be compared and lead to useful inferences.

*Load cells*: the likelihood of wall friction hindering the transmission of stress across the sample, one load cell above and another below the specimen (confined by the perforated plates) serve to linearly interpolate their measurements and construct a stress gradient. The intercept of this gradient and the pore pressure measured at the position of any given pressure transducer allows for an estimation of effective stresses at different points in the soil length.

*Pressure transducers*: a series of 7 pressure transducers at a vertical distance of 10cm from one another (with an alternating horizontal offset of 10cm to avoid the formation of a fragility/fracture zone) makes hydraulic gradient(s) calculation possible. It offers the option of having hydraulic gradients with different lengths and involving/excluding portions of the sample. These can of course also be used to obtain the pore pressure at different locations.

*Perforated (confining) plates*: the orifices of the plates for confining the soil sample had a chosen diameter of 3mm because of the targeted soil gradations, allowing the passage of the

finer (passive of suffusion) fraction while containing the coarser fraction. The distribution of orifices was designed to be spatially homogeneous.

*Vertical stress system*: the use of weights and a lever for application of vertical stress was chosen for being a simple way to apply considerable load (~ 5x the used weight) in an almost perfectly constant manner – the use of mechanical actuator(s) was discarded because it would add financial cost as well as possibly presenting issues such as vibration, inconstant force (especially over long periods of time), need of calibration and so on. A rail-bearings system was used to assure stress application to be vertical and avoid the likely change in angle between lever arm and vertical loading shaft (if ≠ from 90°) to become an issue.

*Outflow tank*: measurement of flow rate using an outflow tank and its change in mass over time (cyclically being emptied by a hydraulic pump) was chosen due to its much lower cost in comparison with an [electronic] flow meter of equivalent sensitivity/precision.

*Head tank*: a constant-head tank with variable height (regulated by a winch) was deemed suitable due to its low cost and simplicity, despite the applicable head being limited by how high the water supply connected and, mainly, the winch system could be installed.

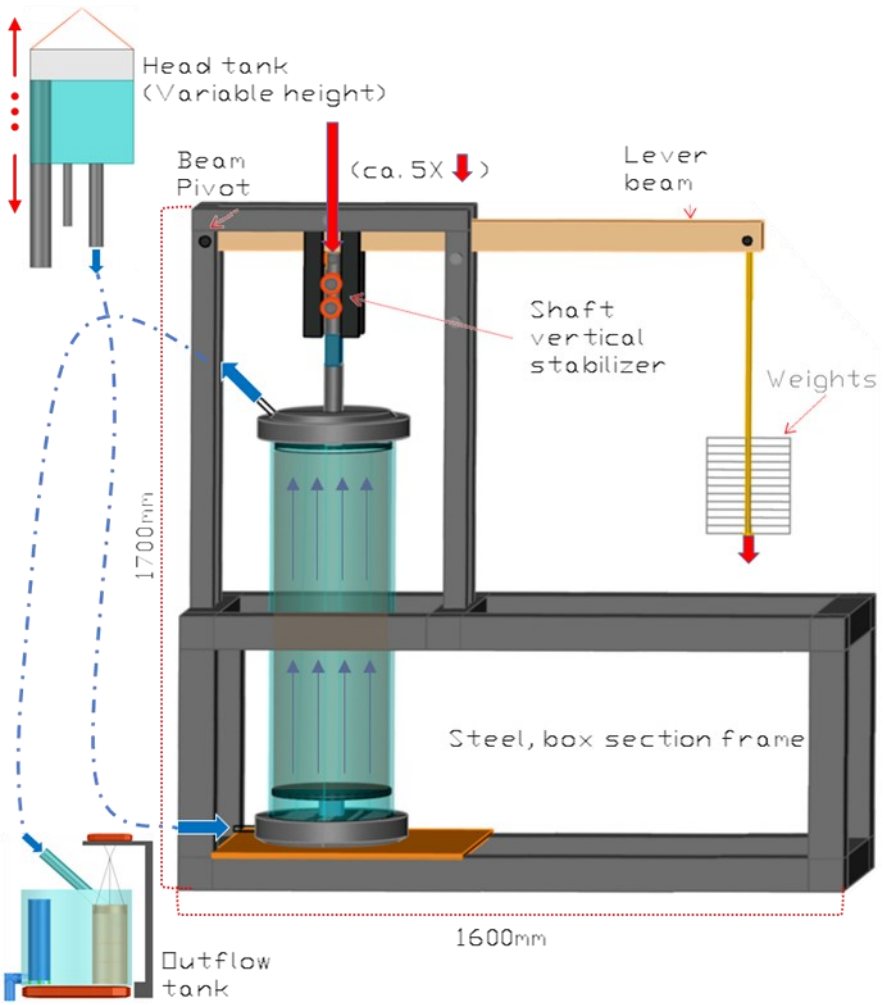


*Figure 3-6. Annotated Illustration of test rig.*

### 3.2.1 Permeameter

The central element of the test rig is a considerably large permeameter cell (Figure 3-7), an Acrylic tube 1000mm long, with 280mm internal diameter and a wall thickness of 10mm, positioned vertically and closed at both ends by two caps with ports for water in-/outflow. Inside the tube are two perforated plates (covered by a geotextile, depending on the material being tested) responsible for containing the soil sample while allowing the flow of water. The upper plate functions as a piston by being attached to a vertical shaft that goes through the upper cap and was connected to a weight-based vertical loading system. Extensions (inter-attachable steel cylinders, each 100mm long, 45mm ∅) can be added between the bottom cap and the base perforated plate (load cell in between) to vary sample size.

Regarding measuring devices, load cells are located above and below each perforated plate, pressure transducers are connected to the Acrylic tube and AE sensors, a hydrophone and a WG, are located inside the large tube through its wall.

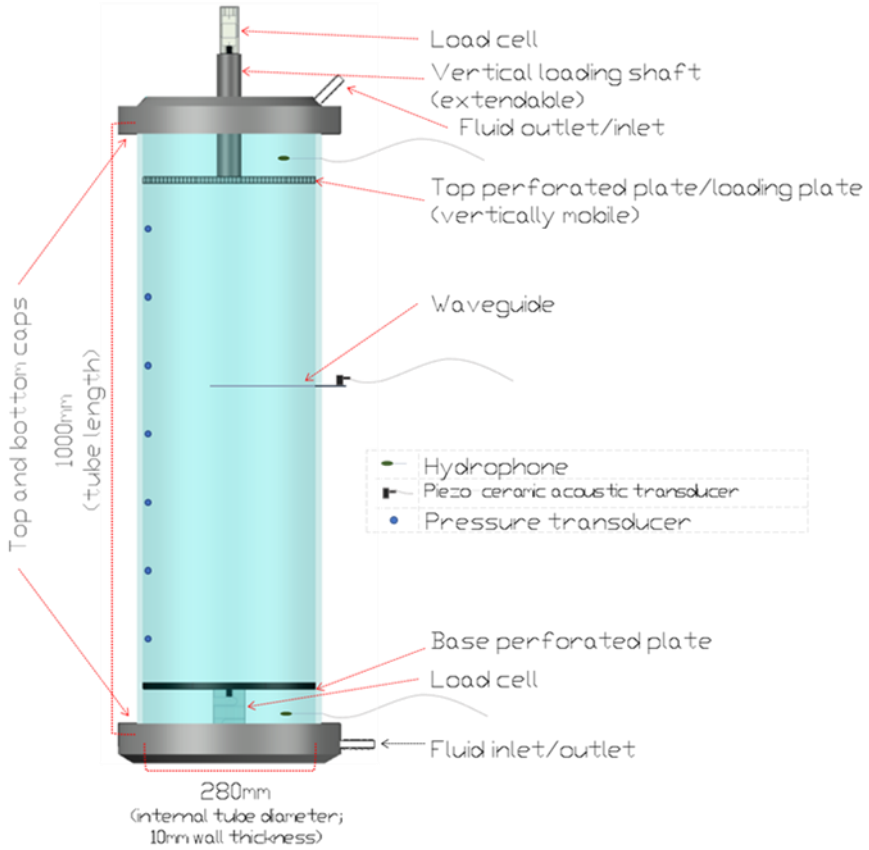


*Figure 3-7. Detail of permeameter cell outlining the sensors and gauges and their approximate position.*

Although the test rig was designed to accommodate samples up to 905mm tall (280mm diameter), different configurations are possible. For instance, 400mm of extensions/spacers can be added between the bottom cap and the BLC, effectively making the used sample height ca. 500mm (Figure 3-8; Figure 3-12). In this case, the pressure transducer positions within the sample relative to the bottom perforated plate (i.e. their distance from the bottom perforated plate) are:

| Pressure transducer positions relative to bottom perforated plate (distances from plate) with 400mm of spacers between bottom cap and BLC: | | | |
|---|---|---|---|
| Pr. tr. 1 | Pr. tr. 2 | Pr. tr. 3 | Pr. tr. 4 |
| 385mm | 285mm | 185mm | 85mm |

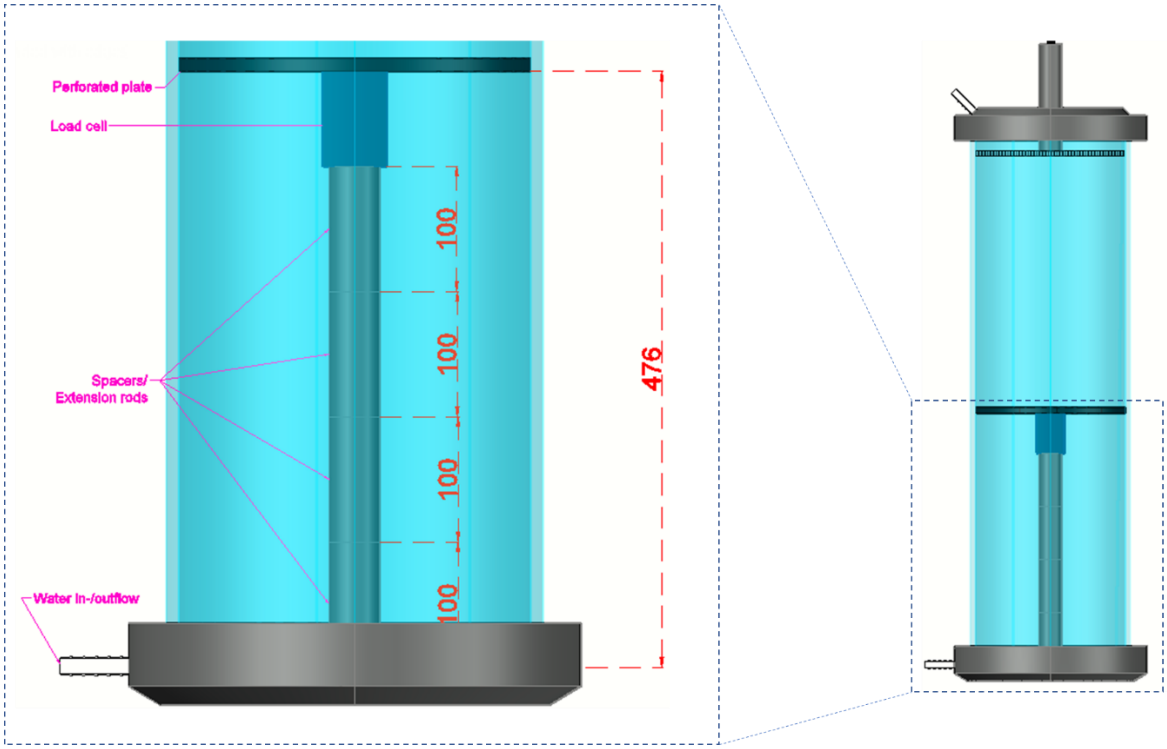


*Figure 3-8. Detail of permeameter configuration in which the bottom plate and top LC are elevated by adding spacers or extension rods.*

| | | | |
|---|---|---|---|
| Pressure transducers |  (with de-airing block) | 7 X<br>Vertically distributed<br>(every 100mm) | • Pore fluid pressures<br>• Hydraulic gradients |
| Load cells |  | 2 X<br>Above vertical loading shaft and below bottom perforated plate. | • Vertical stress<br>• Stress gradient |
| LVDT |  | 1 X<br>Attached to vertical loading shaft; in contact with top cap. | • Volume change/deformation |
| Logging scale(s) |  | 1 X<br>Under outflow tank | • Mass-based effluent flow rates |
| AE sensors – Piezo-ceramic transducer |  | 1 X<br>Attached to waveguide inserted in sediment sample<br>(external to permeameter cell) | • Acoustic emission |
| AE sensors – Hydrophones |  | 2 X<br>Above and below top and bottom perforated plates, respectively.<br>Inside permeameter but external to sediment sample. | • Acoustic emission |

*Figure 3-9. Summary of sensors and gauges used in the test rig, with a brief description of how many of each, where they are placed and their purpose.*

Technical specifications of used instruments can be found in the Appendix.

#### 3.2.1.1 Caps

The acrylic tube was closed on each end by caps (one on top and another at the bottom) that are the interface between the material being tested and the external environment. Both of them have ports for allowing the unidirectional flow of water through the cell – the direction of flow can be controlled by making one of the caps flow inlet as the other serves as outlet/drain (e.g. [external] inflow from the bottom and discharge at the top induces upward flow). Both caps have been manufactured by CNC (computer numerical control) machining of solid aluminium blocks at the Wolfson School of Mechanical, Electrical and Manufacturing Engineering of Loughborough University. The drawings used for their production can be seen in the Appendix.

#### 3.2.1.2 Internal plates

The soil specimen to be tested was contained above and below by two perforated plates, which have been manufactured by CNC machining of solid aluminium disks at the Wolfson School of Loughborough University. They are responsible for containing the soil specimen while allowing for unimpeded seepage. Drawings of the perforated plates can be found in the Appendix.

Depending on the particle-size distribution of materials being tested, a mesh (wireframe, geosynthetic) was put between the perforated plate(s) and the tested sample to either contain or allow the removal/erosion of soil fractions (e.g. the finer grains) being subjected to seepage-induced erosion.

Additionally, five steel cylindric rod segments with a height of 100mm and a diameter of 45mm have been manufactured to be used as extensions/spacers between the bottom cap and the bottom perforated plate (with the bottom load cell between these), allowing the height of the tested specimen to be arbitrarily reduced by between 100m and 500mm, in 100mm steps. These spacers are attachable to each other by threaded bolts and orifices along their central axis.

### 3.2.2 Vertical loading system

The permeameter device is placed within a box-section/square-tube steel frame integral to the vertical loading system (Figure 3-10, Figure 3-12). The vertical loading employs a class 2 lever, or the resistance (targeted stress point) between the effort (load/weight) and the fulcrum/pivot (Uicker et al., 2010; Usher, 1929) with a ~5x leverage. The vertical shaft responsible for transferring the force from the lever to the top perforated/confining plate has its vertical movement guided by stabilisers that act like rails keeping vertical movement/force of the shaft (Figure 3-11). Contact between lever and vertical shaft is made by a bearing that

is attached to the top of the shaft – the role of the bearing is also to avoid a horizontal force component, since if the lever moves vertically their contact point (on the lever beam) may change.

Application and increase of vertical stress to the specimen is done by simply adding weights (e.g. common plate weights) to the assigned position on the lever beam. Although the specific applied stress can be calculated based on the geometry of the system, this load can be verified by a load cell positioned within the vertical shaft - which can be useful if availability of weights (or accuracy/consistency of their [presumed] mass) is suboptimal.

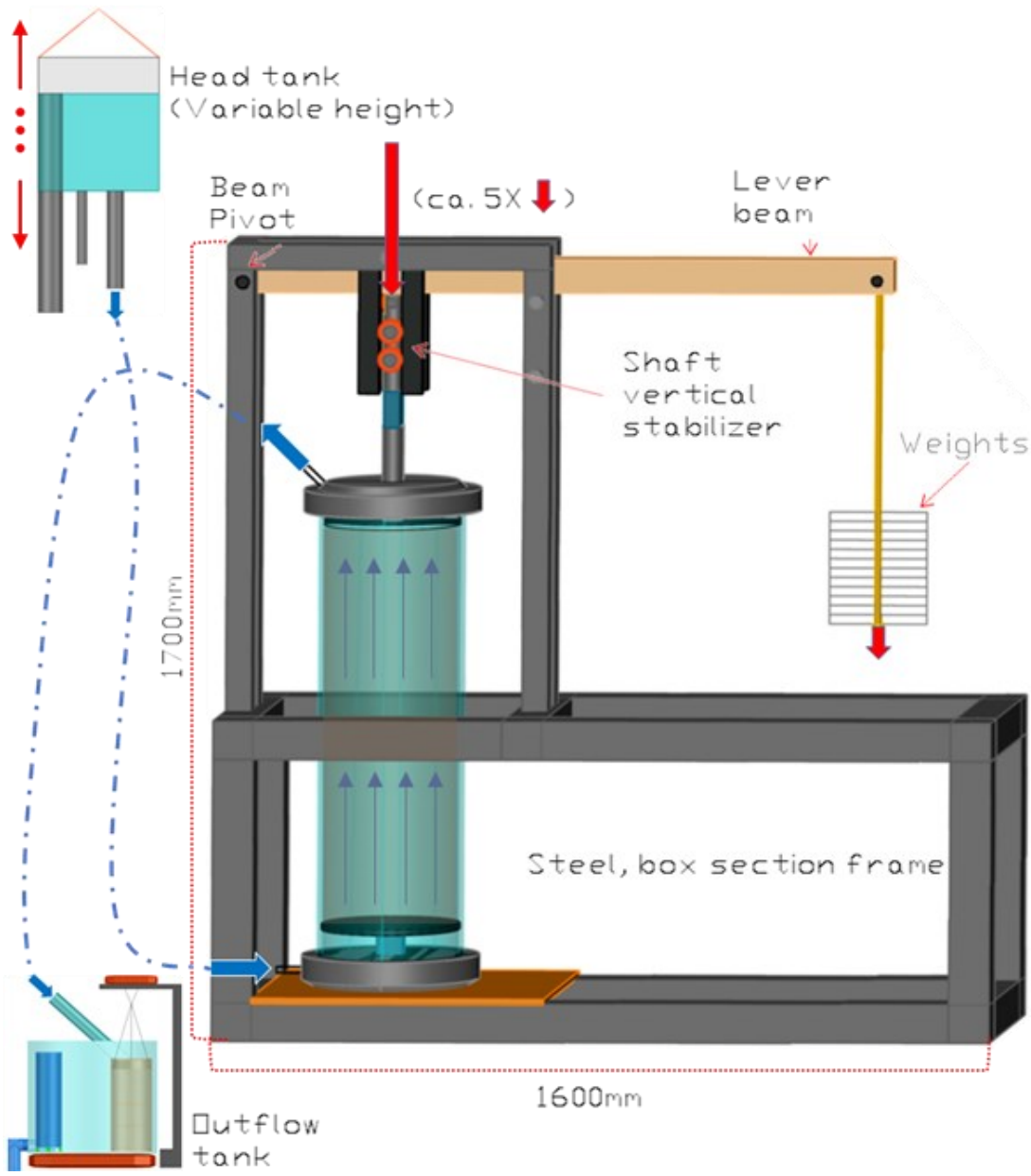


*Figure 3-10. Illustration of bespoke permeameter apparatus and its key constituent parts.*

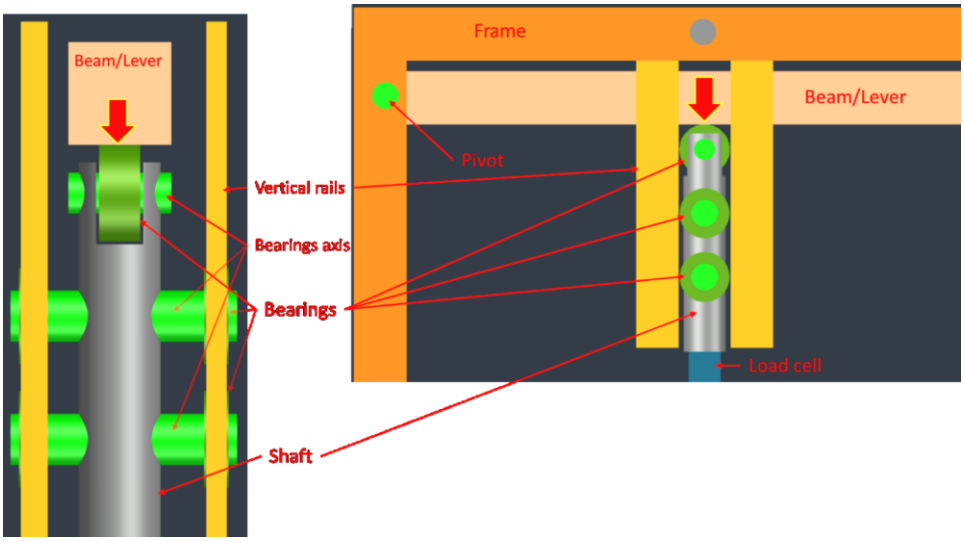


*Figure 3-11. Illustration of vertical stabilisation system from perpendicular horizontal viewpoints. Shaft transfers the force from the lever/beam to the top perforated/confining plate. Vertical movement/force of the shaft has its orientation assured by rails avoiding horizontal shifting or tilting. The lever/beam lays on a bearing integrated to the top of the vertical shaft. Specific dimensions have been slightly changed during construction.*

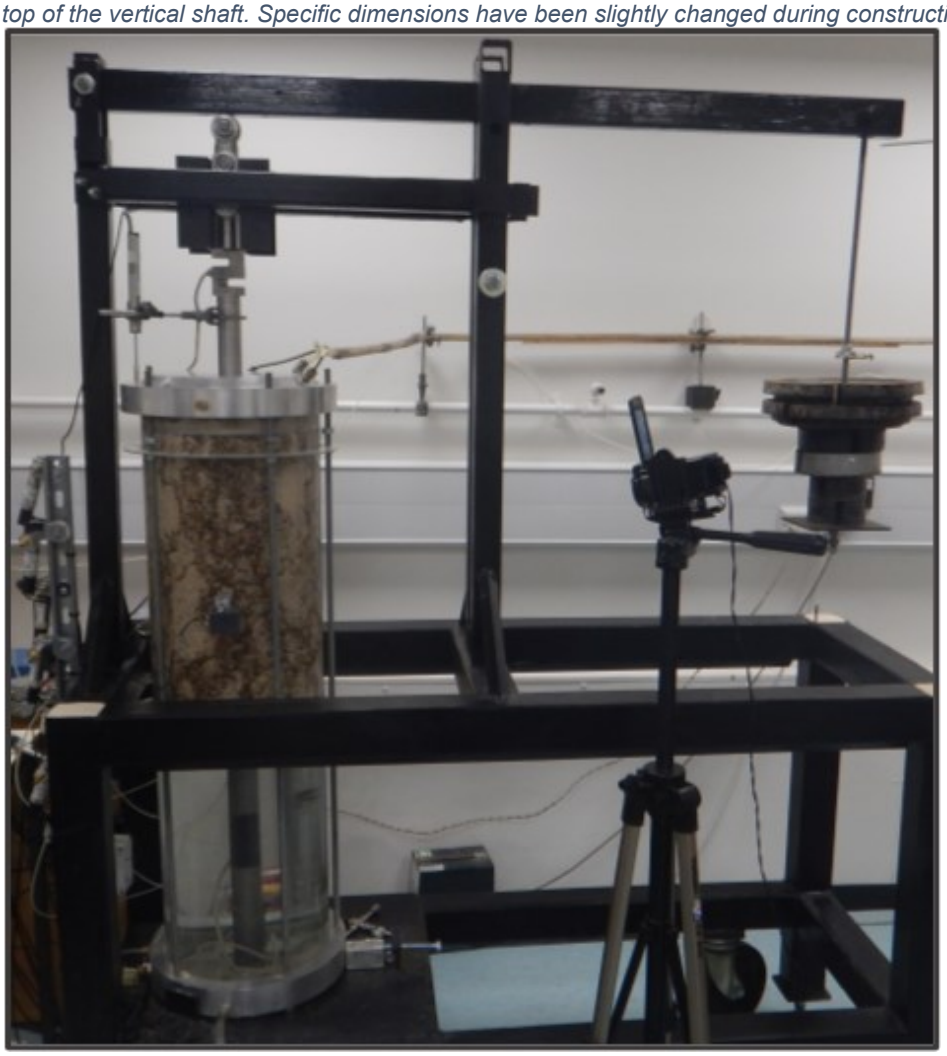

*Figure 3-12. Photograph of test rig during an experiment.*

### 3.2.3 AE sensors

A piezo-ceramic acoustic transducer was used attached to a WG inserted in the soil through the permeameter wall. From preliminary tests it seemed that only a fraction of the internal erosion-related events was detected by this instrument, that is the soil interactions occurring either in direct contact with the WG (i.e. collisions or friction between the soil particles and the WG) or quite close to it (cm).

It was thought that, besides direct contact with the WG (including friction from movement of the soil mass), sound waves in the saturated soil could only be transmitted by the soil fabric or by the [pore] water. The former, depending on e.g. soil compaction, fabric and composition, typically has a relatively high attenuation coefficient (perhaps not enough sound energy for detection reaches the WG), while the latter could have an impedance difference too high to effectively transmit the AE - the impedance difference between the water and the WG itself would deter the sound transmission between them.

Regarding a way of addressing this issue, a hydrophone was thought to be better suited to detect longitudinal waves transmitted by the water in the saturated medium, which in principle alters the kind of waves possibly detected but might be advantageous for improving sensitivity and signal clarity (Koerner et al., 1981; O'Brien et al., 1996; Moebius et al., 2012; Oelze et al., 2002).

The Broadband Measurement Hydrophone AS-1 by Aquarian Scientific was acquired (Figure 3-13). It should be noted though that the hydrophones employed in this study are arguably not of the best available quality (in terms of sensibility, signal reliability, noise minimization; despite being quite acceptable) and have been designed for use in a different context (i.e. open water), so, for reasons such as these, the results of this study are quite passive of improvement and do not express the full potential of using acoustic emission for detecting seepage-induced internal erosion.

Naturally, the use of different AE sensors and the potentially different signal acquired by each of them does not characterize an a priori issue. In effect, they might be complementary or serve as alternatives based on the constraints of a certain situation. For instance, although the signal from the piezoceramic transducer + waveguide was apparently limited to processes occurring in close proximity or direct contact with the WG, it largely represents the very practical and useful approach of using buried infrastructural elements (pipes, shafts, sheet piles) for AE detection in real structures. The data from hydrophones in the other hand represents the approach that would be taken in the case of effectively non-intrusive monitoring of a given asset within its water-saturated volume. Laboratory and field experiments should provide the information needed to better assess how and when to use each of these.

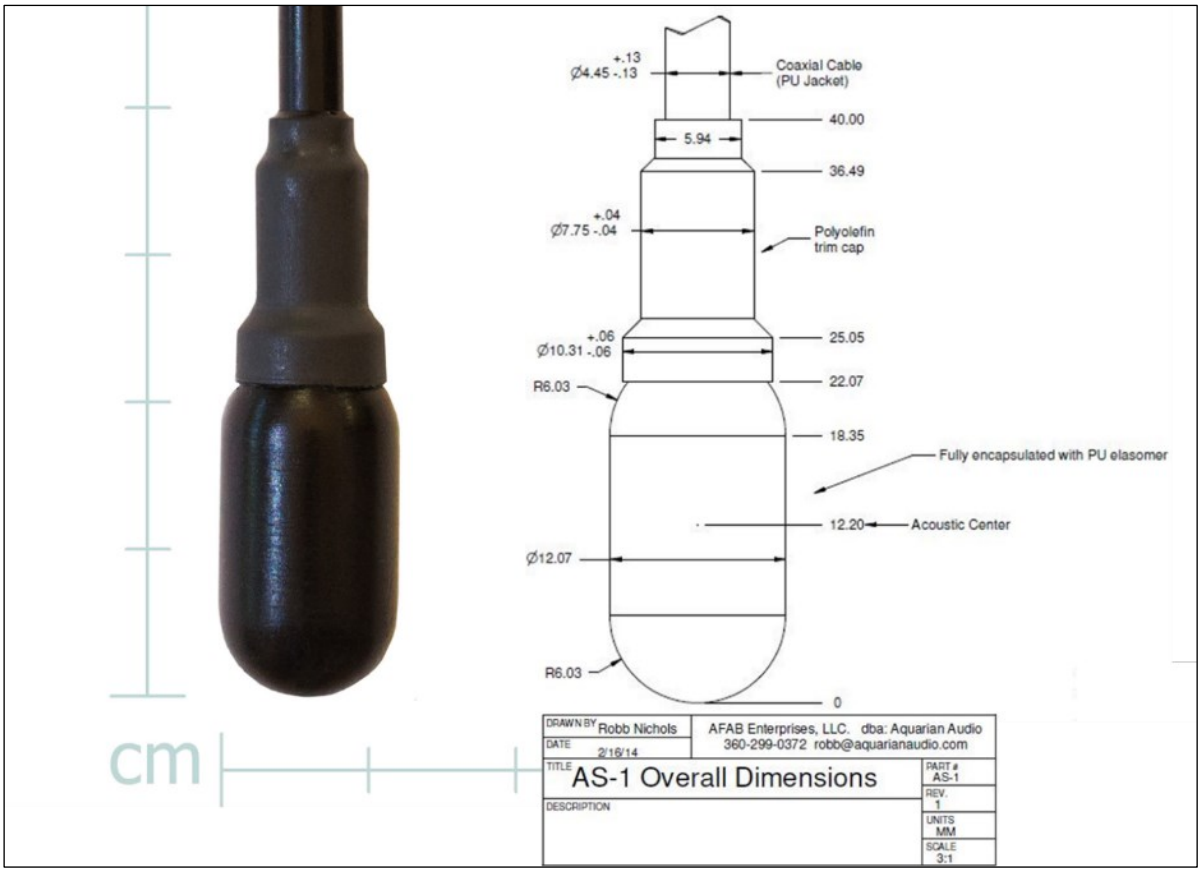


*Figure 3-13. Photo and diagram with dimensions of AS-I Hydrophone.*

The data acquisition system is described in Figure 3-14 and Figure 3-15.


*Figure 3-14. Schematic of AE data acquisition process.*

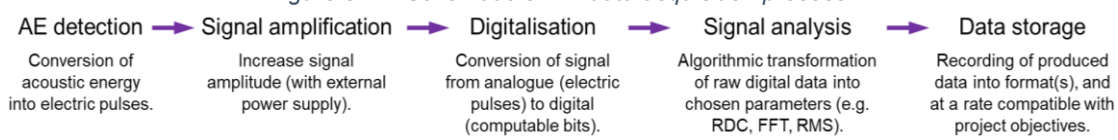


*Figure 3-15. Workflow of AE data collection.*

### 3.2.4 Head tank

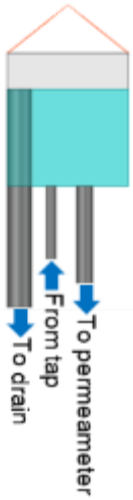


*Figure 3-16. Schematic of head tank indicating fluid directions for keeping constant head.*

The function of the head tank (Figure 3-10) is to keep a constant hydraulic head, which is achieved by having an elevated drain tube within the tank that forbids the water level to go above its height while water is constantly being fed from the tap/mains/building water supply at a rate sufficient to maintain the tank continuously full. A third tube directs the water to the permeameter (Figure 3-16). The entire head tank assembly is vertically movable as is hangs from a winch capable of lifting/lowering the system.

### 3.2.5 Outflow tank

The outflow tank is essentially a reservoir filler by effluent of the permeameter that has its varying mass logged by a scale/balance on which the tank sits (Figure 3-10). Flow rate is calculated by measuring mass change over time. The tank is repeatedly emptied every time the water level reaches a set height. Emptying of the tank was done with a hydraulic pump electronically activated by float sensors at the chosen maximum water level.

## 3.3 Test procedure

### 3.3.1 Sample preparation

The preparation of samples was based on the following procedure described by Moffat and Fannin in 2006, which was considered adequate with minor adaptations, e.g. less emphasis on removing air from the sample (as in real conditions air is likely to be in the fluid due to e.g. biologic activity, temperature-/pressure-driven fluid solubility changes, air entrapment with change of phreatic surface). The following points regarding the definition of a test procedure have been considered:

- Practicality: the procedure must consider simplicity and ease of implementation.
- Reproducibility: it must be easily repeatable and allow for experimental consistency.
- Coherence: the employed methodologies have to be aligned with the character of the research being developed

Note on Arching: despite the reassurance given by papers that observe wall friction (Lovisa et al., 2014; Take and Valsangkar, 2001) – the cell diameter (280mm ID) was large enough to amply minimize this effect - it was possible that the interaction between soil grains and the permeameter wall (e.g. scratching, soil grains "digging into" the acrylic) result in a less efficient and possibly inacceptable stress transmission through the sample. This seems to only be verifiable by experimentation and the information extracted from the load cells as well as visual observation (including post-test inspection of the Perspex tube) served as assessment tools.

Procedure:

The procedure adopted was based on that developed by Moffat and Fannin (2006) for a large permeameter study of internal stability in cohesionless soils, as well as by Li (2008) for a study of seepage induced instability in widely graded soils. Both these studies were able to generate and characterise internal instability using the sample preparation and measurement approaches adopted.

1) Specimen Reconstitution

Making sure that the sample was properly loaded into the permeameter cell was of course essential for assuring reliability of the test results and the understanding of the conditions that originate the AE. Here, the purpose of the specimen reconstitution technique was to replicate a saturated homogeneous specimen and the procedure was described below:

- Saturated homogeneous specimens are produced by the method of slurry deposition.
- A series of layers (ca. 5cm each) are gradually added to the test cell and manually compacted by gentle tapping on its top.
- A thin film of standing water is kept throughout.
- Sample homogeneity is initially qualitatively assessed by visual observation and later gauged by measuring the fluid pressure distribution).

The test of samples formed by layers of different materials (to model e.g. the interface between different layers of an earth dam) was also examined and the corresponding sample preparation method was analogous to the above mentioned, with each different stratum and their transition(s) simply being formed by the gradual addition of soil.

The size of the test sample was of variable height by varying the position of the lower perforated plate with modular attachments between it and the bottom cap – further specimen variation of about ± 100mm was possible by controlling the initial position of the top perforated plate, lever arm, vertical load shaft assembly .The specimen diameter was fixed at 280mm.

2) Consolidation

Once the soil specimen has been added to the permeameter, a phase of consolidation to achieve the conditions stipulated for each test takes place as described below:

- The initial specimen length was measured.
- Vertical, axial stress loading was imposed on the soil specimen in the permeameter cell in drained conditions.
    - Double drainage through the top and bottom caps allowing pore pressure dissipation.
    - This loading was applied in a gradual, controlled manner to avoid internal instability due to transient hydraulic gradients.
    - Stress was applied at the top of the specimen in increments, which was maintained at each increment until overall hydraulic gradient reached zero – in practice, the increase in vertical stress was induced by adding more weights to the system and the stress translated to the sample (as well as the eventual loss due to e.g. wall friction; in kPa) was measured by the load cells above and below the perforated plates.
- At end of consolidation the specimen length was measured again, with the measurement of its variation in height aided by an LVDT.

### 3.3.2 Hydraulic conditions, seepage flow

Reviewed authors tend to use systems based on automated pumps, actuators, pressurized containers or the equivalent to control the seepage flow through their samples and induce different hydraulic gradients (Sibille et al., 2015a; Moffat and Fannin, 2006; Zhou et al., 2018; Tomlinson and Vaid, 2000). Nonetheless, for practicality, simplicity, experimental robustness (reduction of possible experimental setup artefacts) and presumed realism, the experiments here described vary the induced hydraulic gradient and seepage flow by the use of a constant-head water tank that can have its height changed; in other words, the hydraulic head was the controlled variable.

Other experimental arrangements from the available literature (as well as the test rig used in the earlier experimental phase at the 1st year of this PhD project, which just had one fixed position for its head tank) are limited by having a minimum applicable pressure/hydraulic

gradient, which might either exclude phenomena occurring at hydraulic regimes below the minimum applicable one or produce unrealistic effects during testing. To that point, the head tank used here has the capacity of being positioned at a height low enough relative to the permeameter to permit the initial hydraulic gradient to be effectively null (at least when set for upward flow, as having the fluid outlet at the bottom of the permeameter would cause virtually inevitable flow) and then have its height varied at will - although it was predicted to be continually increased.

Following the consolidation phase, the seepage flow and hydraulic gradient induction phase of tests are outlined as follows:

- With the sample under water saturation, it was carefully connected by opening the relative tap/valve to the filled head tank positioned at its minimum height – by this point there was still no water flow though the test cell.
    - For upward flow the head tank was connected to the bottom cap flow port, with the opposite for downward flow.
- The input of [tap] water to the tank was turned on (to assure that the head tank was kept full once flow through the tested specimen begins).
- Unidirectional seepage flow is imposed.
    - The outflow is opened.

      For upward flow, the top outlet valve was responsible for fluid discharge from the permeameter - this was the targeted modality for the programmed tests, subject to change depending on new information or ideas e.g. from outcomes of previous tests.
    - The head tank was gradually elevated in a series of increments (between 0.5 and 10cm)
        - The arbitrary default rate was 10mm/h, which was continually revised.
        - Defining the height increments and the time interval between them was intrinsic to the tested sample characteristics (e.g. hydraulic conductivity, erosion susceptibility and their change over time due to clogging, mass loss or other effects).

      The idea was to start from a condition of internally stable soil and induce internal instability by increasing the hydraulic gradient, which was verified by visual inspection and by observing the measured hydraulic gradients.
- The termination of an experiment was in principle based on:
    - Reaching a condition of equilibrium after the successful initiation and evolution of internal erosion.

- Seepage erosion failing to be initiated despite forcing the controllable variables.
- Reaching test apparatus limitations.

Although the critical hydraulic gradient for a given experiment was estimated, its quantification demanded knowing variables that are in practice difficult to gauge (e.g. stress reduction factor (α); Li and Fannin, 2012). Therefore, the intention here was to provoke the onset of instability in a marginally stable soil by varying the hydraulic head at a constant vertical stress. This approach should then be able to identify the critical hydraulic gradient (Figure 3-19).

### 3.3.3 Vertical load

From the available literature on laboratory testing of seepage-induced internal erosion, it was observed that the effective stresses imposed on soil specimens tend to be from 0 to 300kPa (most being below 100kPa) and, if different loads are used, they are amplified in steps of ca. 20 to 50kPa (Moffat and Fannin, 2006; Hunter and Bowman, 2017; Israr and Indraratna, 2018; Slangen and Fannin, 2017; Fonseca et al., 2014; Slangen, 2015).

In this study, the maximum targeted vertical stress was ca. 130kPa (translated into an effective stress of ca. 100kPa for a hydraulic head of 3m). Nonetheless, higher vertical stresses can be applied if need be (Figure 3-17).

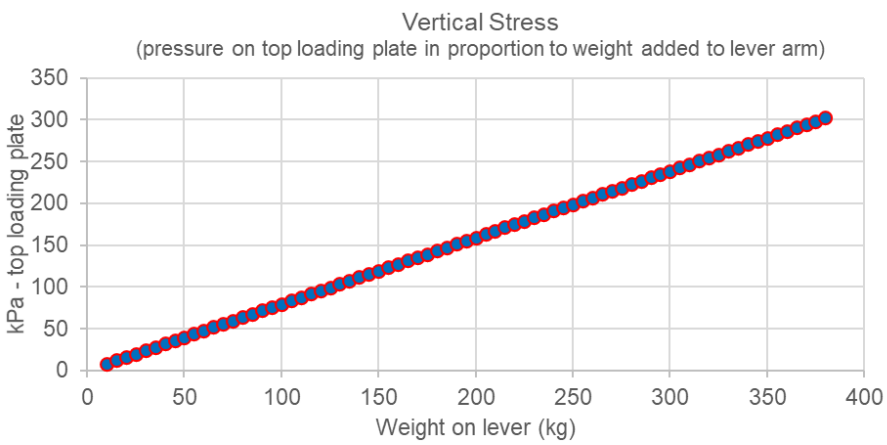


*Figure 3-17. Vertical stress applicable on specimen by varying the weight put on lever system (0 to 350 kPa).*

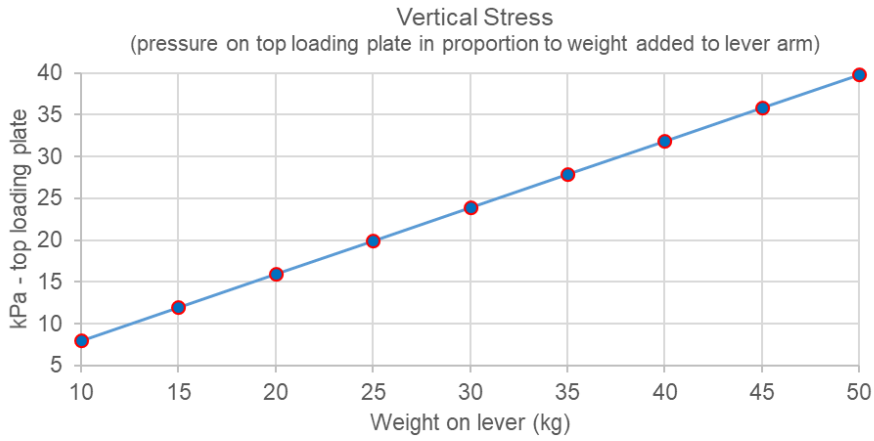


*Figure 3-18. Vertical stress applicable on specimen by varying the weight put on lever system (5 to 40 kPa).*

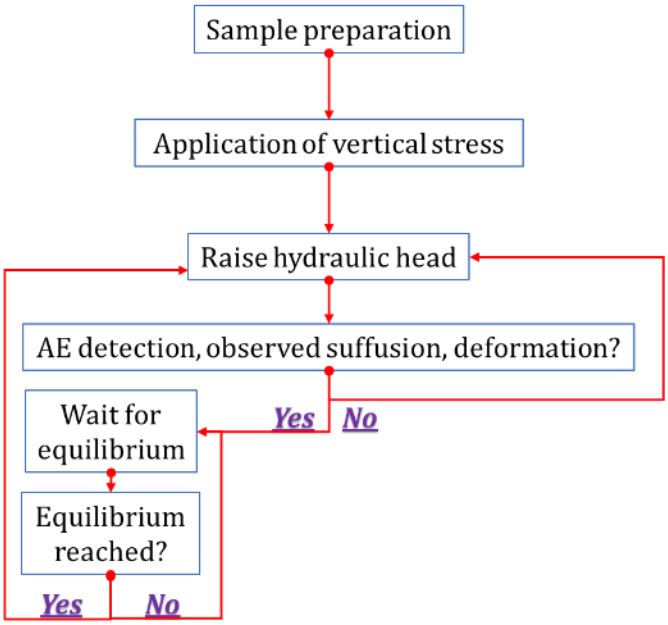


*Figure 3-19. Simplified flowchart of how permeameter tests are to be carried out.*

Experiments are to have a constant vertical stress applied throughout, with each test iteration for a given soil having an increment of approximately 50 kPa and the first applied load being 30kPa (Figure 3-18).

Note on test configuration: although the test rig was designed to accommodate samples up to 905mm tall (280mm diameter), this test program used about the upper half of its capacity – 400mm of extensions/spacers were added between the bottom cap and the BLC, effectively making the used sample height ca. 500mm (Figure 3-12). Two of the reasons for this are a) practicality (faster/easier sample preparation) and b) better water flow dissipation before it reaches the sample (the “water only” volume helps avoid preferential flow artifacts). Consequently, the pressure transducer positions within the sample relative to the bottom perforated plate (i.e. their distance from the bottom perforated plate) are:

| Pressure transducer positions relative to bottom perforated plate (distances from plate) with 400mm of spacers between bottom cap and BLC: | | | |
|---|---|---|---|
| Pr. tr. 1 | Pr. tr. 2 | Pr. tr. 3 | Pr. tr. 4 |
| 385mm | 285mm | 185mm | 85mm |

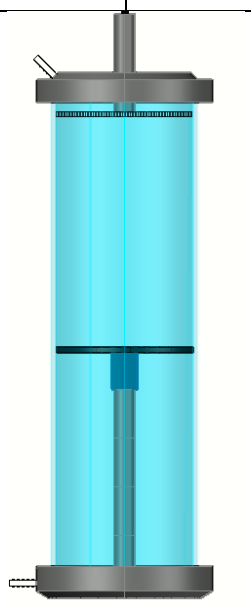

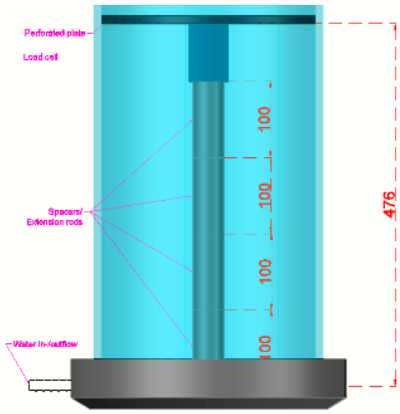


Table 10 summarises the key particularities of the permeameter tests described in the Results section. This description shows the external hydromechanical conditions changed/chosen between tests (i.e. head and stress). The results section shows the effect of such conditions over time as water seepage through the different soils progresses.

*Table 10. Characteristics of tests with the different soils.*
*Key for test names: S#(P)T# = **S**oil # (**P**reliminary) **T**est #.*

| Test | Hydraulic head (cm) | Vertical stress (~ kPa) | Sample size (~ height x diameter; cm) | Initial condition |
|---|---|---|---|---|
| S1PT1 | 100 | (self-weight) | 40 x 16 | Uncompacted |
| S1PT2 | 100 | (self-weight) | 40 x 16 | Uncompacted |
| S1PT3 | 100-130 | (self-weight) | 40 x 16 | Uncompacted |
| S1PT4 | 100 | (self-weight) | 40 x 16 | Uncompacted |
| S1PT5 | 100-130 | (self-weight) | 40 x 16 | Uncompacted |
| S1PT6 | 100 | (self-weight) | 40 x 16 | Uncompacted |
| S1PT7 | 100 | (self-weight) | 40 x 16 | Uncompacted |
| S1PT8 | 100 | (self-weight) | 40 x 16 | Uncompacted |
| S1PT9 | 100 | (self-weight) | 40 x 16 | Uncompacted |
| S1PT10 | 100 | (self-weight) | 40 x 16 | Uncompacted |
| S1PT11 | 100 | (self-weight) | 40 x 16 | Uncompacted |
| S1T1 | 0-50 | 30 | 50 x 28 | Compacted |
| S2T1 | 0-50 | 30 | 50 x 28 | Compacted |
| S2T2 | 0-50 | 30 | 50 x 28 | Compacted |
| S3T1 | 0-50 | 30 | 50 x 28 | Compacted |
| S4T1 | 0-50 | 30 | 50 x 28 | Compacted |
| S4T2 | 0-50 | 30 | 50 x 28 | Compacted |
| S4T3 | 0-50 | 45 | 50 x 28 | Compacted |
| S4T4 | 0-50 | 55 | 50 x 28 | Compacted |
| S4T5 | 0-100 | 30 | 50 x 28 | Compacted |
| S5T1 | 0-50 | 30 | 50 x 28 | Compacted |
| S6T1 | 0-50 | 30 | 50 x 28 | Compacted |

## 3.4 Test program

### 3.4.1 Test soils

The targeted soils (based on materials mentioned on Rönnqvist and Viklander, 2015) have been chosen for being representative of real structures and for having calculated as marginally stable based on different geometric criteria (or for having estimated internal stabilities that find disagreement between different criteria). Calculation of internal instability of these soils used the methods of Burenkova (1993), Kenney and Lau (1986) and Kezdi (1979) (Rönnqvist and Viklander, 2015; Kenney and Lau, 1985; Israr and Israr, 2018). The soil gradations were reproduced by mixing different materials, which have been purchased from *Minerals Marketing Limited*, stored and (re-)characterized according to the BS1377(2) procedures and with the guidance of Mr Lewis Darwin (Geotechnics Technician) at the Sir Frank Gibb laboratory facilities.

The [base] soils that were mixed to form the targeted grain-size distributions (Figure 3-20) have been individually characterized and the corresponding summary can be found in Figure 3-21 and Figure 3-22.

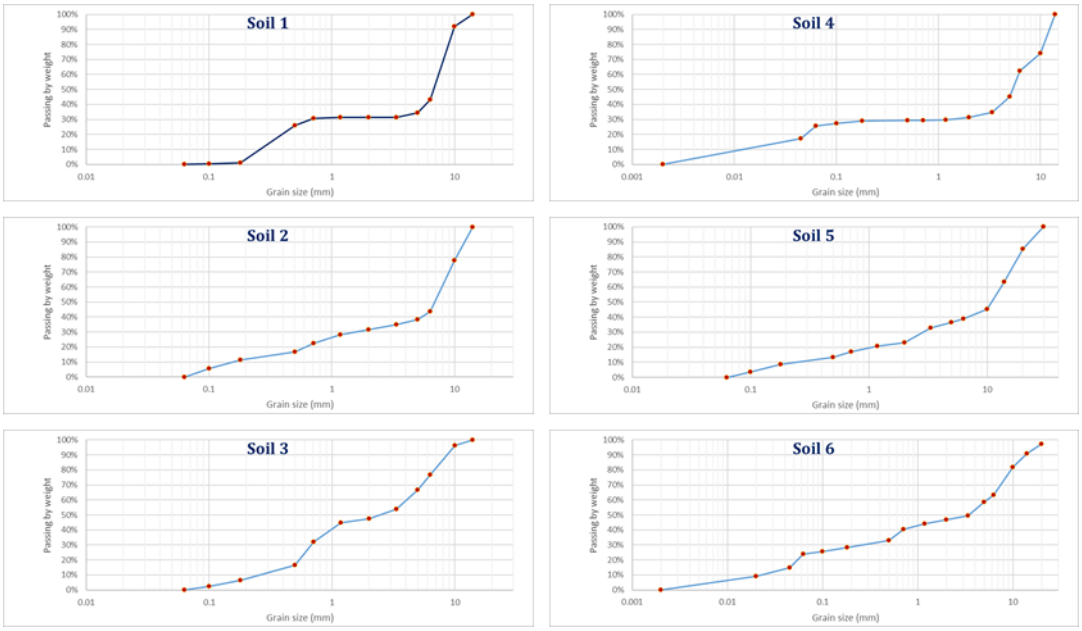


*Figure 3-20. Grain-size distributions of the soils targeted in the upcoming laboratory experiments with the newly constructed permeameter apparatus.*

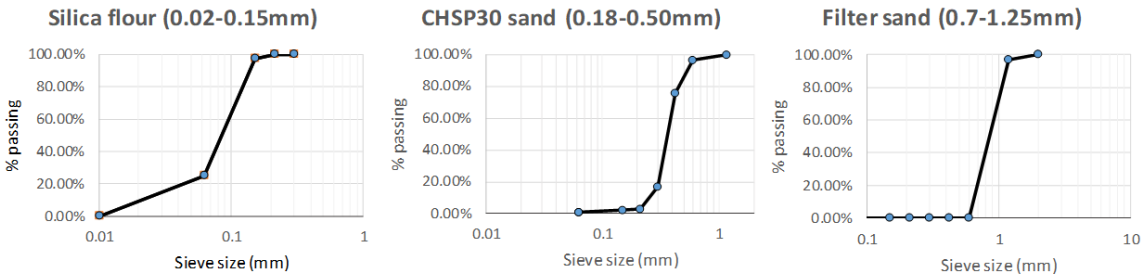


| | | | | | | | | |
|---|---|---|---|---|---|---|---|---|
| Specific gravity | | 2.58786 | Specific gravity | | 2.57133 | Specific gravity | | 2.62734 |
| Density | Loose | 1273.91 | Density | Loose | 1564.62 | Density | Loose | 1478.52 |
| | Compact | 1608.77 | | Compact | 1779.23 | | Compact | 1677.62 |
| Void ratio | Max. | 1.03142 | Void ratio | Max. | 0.64342 | Void ratio | Max. | 0.77702 |
| | Min. | 0.60859 | | Min. | 0.44519 | | Min. | 0.56611 |
| Uniformity coeff. (Cu) | | 3.36891 | Uniformity coeff. (Cu) | | 1.52505 | Uniformity coeff. (Cu) | | 8.28521 |
| Curvature coeff (Cc) | | 1.45313 | Curvature coeff (Cc) | | 1.06998 | Curvature coeff (Cc) | | 2.07105 |

*Figure 3-21. Characterization of soils to be mixed to form chosen GSDs (1 of 2). Density in kg/m$^3$.*

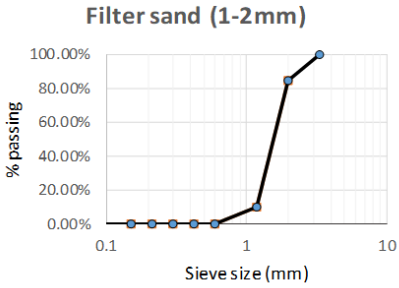


| | | |
|---|---|---|
| Specific gravity | | 2.63012 |
| Density | Loose | 1439.7 |
| | Compact | 1657.91 |
| Void ratio | Max. | 0.82685 |
| | Min. | 0.58641 |
| Uniformity coeff. (Cu) | | 16.5655 |
| Curvature coeff (Cc) | | 4.1384 |

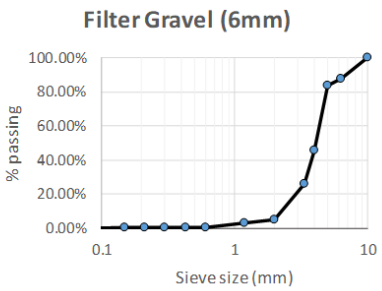


| | | |
|---|---|---|
| Specific gravity | | 2.64673 |
| Density | Loose | 1432.82 |
| | Compact | 1640.14 |
| Void ratio | Max. | 0.84722 |
| | Min. | 0.61372 |
| Uniformity coeff. (Cu) | | 14.1528 |
| Curvature coeff (Cc) | | 3.53167 |

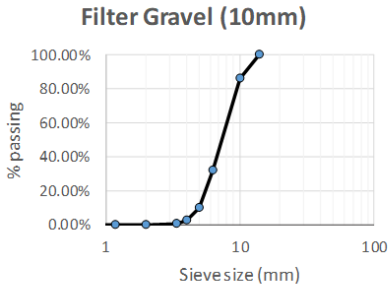


| | | |
|---|---|---|
| Specific gravity | | 2.59231 |
| Density | Loose | 1483.7 |
| | Compact | 1668.74 |
| Void ratio | Max. | 0.74719 |
| | Min. | 0.55345 |
| Uniformity coeff. (Cu) | | 5.17911 |
| Curvature coeff (Cc) | | 1.29505 |

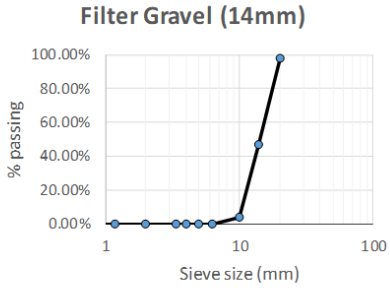


| | | |
|---|---|---|
| Specific gravity | | 2.60813 |
| Density | Loose | 1445.14 |
| | Compact | 1661.3 |
| Void ratio | Max. | 0.80476 |
| | Min. | 0.56994 |
| Uniformity coeff. (Cu) | | 41.4116 |
| Curvature coeff (Cc) | | 10.3444 |

*Figure 3-22. Characterization of soils to be mixed to form chosen GSDs (2 of 2).*

| | *Material A* | *Material B* | *Material C* | *Material D* | *Material E* | *Material F* | *Material G* |
|---|---|---|---|---|---|---|---|
| | Silica flour (0.02-0.15mm) | CHSP30 sand (0.18-0.5mm) | Filter sand (0.7-1.25mm) | Filter sand 1.0-(2.0mm) | Filter gravel (6mm) | Filter gravel (10mm) | Filter gravel (14mm) |
| Coefficient of uniformity, $C_u$ | 3.36 | 1.52 | 8.28 | 16.56 | 14.15 | 5.17 | 41.41 |
| Coefficient of curvature, $C_c$ | 1.45 | 1.06 | 2.07 | 4.13 | 3.53 | 1.29 | 10.34 |
| Minimum void ratio, $e_{min}$ | 0.6 | 0.44 | 0.56 | 0.58 | 0.61 | 0.55 | 0.57 |
| Maximum void ratio, $e_{max}$ | 1.03 | 0.64 | 0.77 | 0.82 | 0.84 | 0.74 | 0.80 |
| Specific gravity $G_s$ | 2.58 | 2.57 | 2.62 | 2.63 | 2.64 | 2.59 | 2.61 |

*Figure 3-23. Characteristics of base materials used to produce targeted soils.*

| | Soil2 | | Soil 3 | | Soil 4 | | Soil 5 | | Soil 6 | |
|---|---|---|---|---|---|---|---|---|---|---|
| | | *Mass (kg)* | | *Mass (kg)* | | *Mass (kg)* | | *Mass (kg)* | | *Mass (kg)* |
| Material A | 11.31% | 6.8 | 6.70% | 4 | 29.20% | 17.5 | 8.50% | 5.1 | 28.42% | 17.1 |
| Material B | 11.31% | 6.8 | 25.70% | 15.4 | 0.30% | 0.2 | 8.50% | 5.1 | 11.93% | 7.2 |
| Material C | 8.99% | 5.4 | 15.30% | 9.2 | 1.90% | 1.1 | 6.10% | 3.7 | 6.42% | 3.9 |
| Material D | 3.33% | 2 | 6.30% | 3.8 | 3.40% | 2.1 | 9.80% | 5.9 | 2.75% | 1.7 |
| Material E | 8.99% | 5.4 | 23% | 13.8 | 27.50% | 16.5 | 12% | 7.2 | 13.76% | 8.3 |
| Material F | 56.07% | 33.7 | 23% | 13.8 | 37.70% | 22.6 | 18.50% | 11 | 27.52% | 16.5 |
| Material G | --- | --- | --- | --- | --- | --- | 36.60% | 22 | 9.17% | 4.6 |
| Total: | | 60.1 | | 60 | | 60 | | 60 | | 60 |

*Figure 3-24. Description of soil mixtures used to produce the different targeted soils.*

### 3.4.1.1 Calculated soil properties

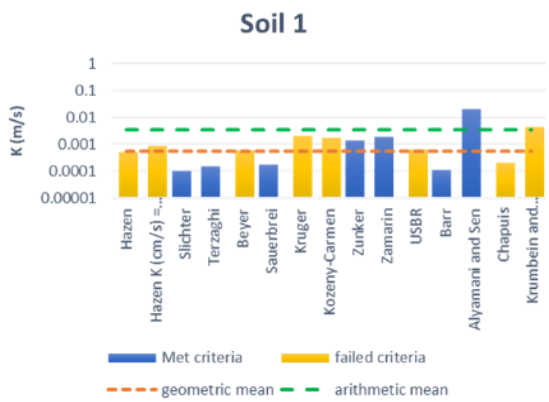


| | | | |
|---|---|---|---|
| d10 | 0.296 | Uniformity Coef. | 25.62 |
| d17 | 0.386 | n computed | 0.26 |
| d20 | 0.424 | g (cm/s²) | 980.00 |
| d50 | 6.814 | r (g/cm³) | 0.9981 |
| d60 | 7.575 | m (g/cm s) | 0.0098 |
| $d_{geometric\ mean}$ | 2.878 | rg/m (1/cm s) | 9.9327E+04 |
| de (Kruger) | 0.998 | tau (Sauerbrei) | 1.053 |
| de (Kozeny) | 0.817 | $d5_f$ | -2.112 |
| de (Zunker) | 0.873 | $d16_f$ | -1.424 |
| de (Zamarin) | 0.935 | $d50_f$ | 2.766 |
| Io (Alyameni) | -1.334 | $d84_f$ | 3.233 |
| | | $d95_f$ | 3.528 |
| | | $\sigma_\phi$ | 2.019 |

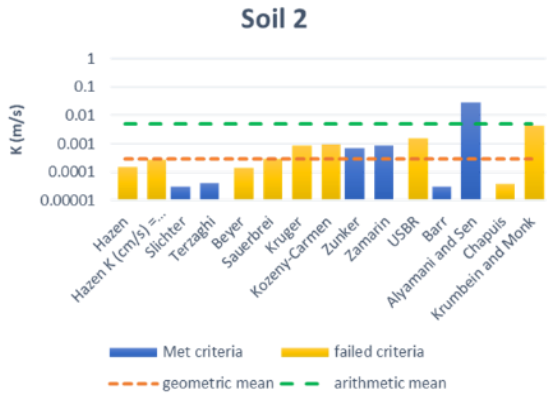


| | | | |
|---|---|---|---|
| d10 | 0.162 | Uniformity Coef. | 49.73 |
| d17 | 0.505 | n computed | 0.26 |
| d20 | 0.618 | g (cm/s²) | 980.00 |
| d50 | 6.978 | r (g/cm³) | 0.9981 |
| d60 | 8.076 | m (g/cm s) | 0.0098 |
| $d_{geometric\ mean}$ | 3.273 | rg/m (1/cm s) | 9.9327E+04 |
| de (Kruger) | 0.658 | tau (Sauerbrei) | 1.053 |
| de (Kozeny) | 0.605 | $d5_f$ | -3.382 |
| de (Zunker) | 0.622 | $d16_f$ | -1.148 |
| de (Zamarin) | 0.640 | $d50_f$ | 2.801 |
| Io (Alyameni) | -1.542 | $d84_f$ | 3.479 |
| | | $d95_f$ | 3.713 |
| | | $\sigma_\phi$ | 2.232 |

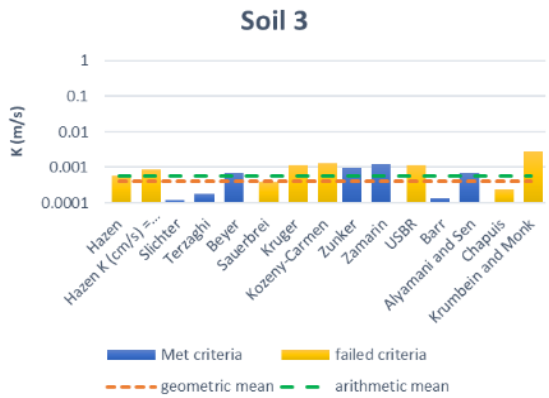


| | | | |
|---|---|---|---|
| d10 | 0.292 | Uniformity Coef. | 14.18 |
| d17 | 0.505 | n computed | 0.27 |
| d20 | 0.546 | g (cm/s²) | 980.00 |
| d50 | 2.540 | r (g/cm³) | 0.9981 |
| d60 | 4.142 | m (g/cm s) | 0.0098 |
| $d_{geometric\ mean}$ | 2.104 | rg/m (1/cm s) | 9.9327E+04 |
| de (Kruger) | 0.716 | tau (Sauerbrei) | 1.053 |
| de (Kozeny) | 0.647 | $d5_f$ | -2.731 |
| de (Zunker) | 0.669 | $d16_f$ | -1.061 |
| de (Zamarin) | 0.693 | $d50_f$ | 1.344 |
| Io (Alyameni) | -0.270 | $d84_f$ | 2.938 |
| | | $d95_f$ | 3.290 |
| | | $\sigma_\phi$ | 1.912 |

*Figure 3-25. Estimated hydraulic conductivities and other parameters based on the GSD of the soils targeted for tests (1 to 3; Figure 3-20). Values defined in Table 11 and Table 12.*

In Figure 3-25 and Figure 3-26 some properties the soils to be tested (Figure 3-20) have been estimated.

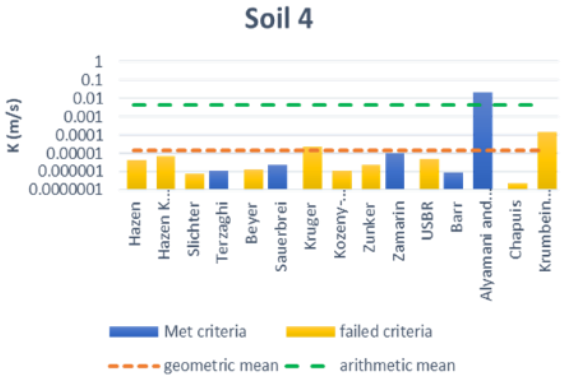


| | | | |
|---|---|---|---|
| d10 | 0.027 | Uniformity Coef. | 226.40 |
| d17 | 0.045 | n computed | 0.26 |
| d20 | 0.051 | g (cm/s²) | 980.00 |
| d50 | 5.371 | r (g/cm³) | 0.9981 |
| d60 | 6.128 | m (g/cm s) | 0.0098 |
| $d_{geometric\ mean}$ | 1.375 | rg/m (1/cm s) | 9.9327E+04 |
| de (Kruger) | 0.107 | tau (Sauerbrei) | 1.053 |
| de (Kozeny) | 0.021 | $d5_f$ | -6.104 |
| de (Zunker) | 0.035 | $d16_f$ | -4.570 |
| de (Zamarin) | 0.069 | $d50_f$ | 2.423 |
| Io (Alyameni) | -1.309 | $d84_f$ | 3.525 |
| | | $d95_f$ | 3.725 |
| | | $\sigma_\phi$ | 3.513 |

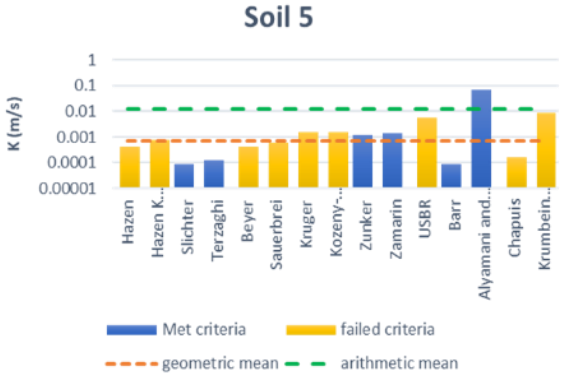


| | | | |
|---|---|---|---|
| d10 | 0.276 | Uniformity Coef. | 48.02 |
| d17 | 0.706 | n computed | 0.26 |
| d20 | 1.086 | g (cm/s²) | 980.00 |
| d50 | 11.067 | r (g/cm³) | 0.9981 |
| d60 | 13.253 | m (g/cm s) | 0.0098 |
| $d_{geometric\ mean}$ | 5.199 | rg/m (1/cm s) | 9.9327E+04 |
| de (Kruger) | 0.872 | tau (Sauerbrei) | 1.053 |
| de (Kozeny) | 0.798 | $d5_f$ | -3.035 |
| de (Zunker) | 0.823 | $d16_f$ | -0.625 |
| de (Zamarin) | 0.848 | $d50_f$ | 3.465 |
| Io (Alyameni) | -2.422 | $d84_f$ | 4.295 |
| | | $d95_f$ | 4.732 |
| | | $\sigma_\phi$ | 2.407 |

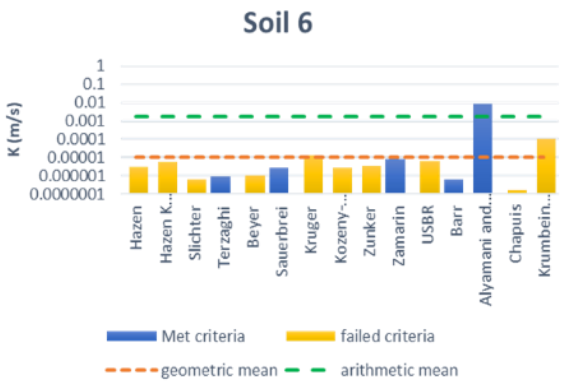


| | | | |
|---|---|---|---|
| d10 | 0.024 | Uniformity Coef. | 225.85 |
| d17 | 0.050 | n computed | 0.26 |
| d20 | 0.055 | g (cm/s²) | 980.00 |
| d50 | 3.433 | r (g/cm³) | 0.9981 |
| d60 | 5.364 | m (g/cm s) | 0.0098 |
| $d_{geometric\ mean}$ | 1.216 | rg/m (1/cm s) | 9.9327E+04 |
| de (Kruger) | 0.080 | tau (Sauerbrei) | 1.053 |
| de (Kozeny) | 0.033 | $d5_f$ | -6.404 |
| de (Zunker) | 0.045 | $d16_f$ | -4.393 |
| de (Zamarin) | 0.062 | $d50_f$ | 1.778 |
| Io (Alyameni) | -0.828 | $d84_f$ | 3.463 |
| | | $d95_f$ | 4.162 |
| | | $\sigma_\phi$ | 3.565 |

*Figure 3-26. Estimated hydraulic conductivities and other parameters based on the GSD of the soils targeted for tests (4 to 6; Figure 3-20). Values defined in Table 11 and Table 12.*

Values calculated with help of the HydrogeoSieveXL program (Devlin, 2015).

Adopting the equation form presented in Vukovic and Soro (1992),

$$K = \frac{\rho\ g}{\mu} N\ \varphi(n) d_e^2$$

the following values and equations are substituted into the appropriate terms to evaluate the models listed in the table below. The values of $d_e$ to be entered should be in cm units. The values of $K$ calculated have the units cm/s, except for the Alyamani and Sen model. $K$=hydraulic conductivity, $\rho$=temperature-dependent water density (g mL$^{-1}$), $g$=gravitational constant (cm s$^{-2}$), $\mu$ =temperature-dependent dynamic viscosity of water (g cm$^{-1}$s$^{-1}$), $N$ is a case-specific constant regarded as a 'shape factor', $\varphi$(n)=function of porosity, and $d_e$ is an effective grain size or function of the grain size distribution.

*Table 11. References, formulae and conditions used for calculating what is displayed in Figure 3-25 and Figure 3-26 (1 of 2).*

| Source | N | $\varphi(n)$ | $d_e$ | Applicable Conditions |
|---|---|---|---|---|
| Hazen simplified (Freeze and Cherry, 1979) | $10\frac{\mu}{\rho g}$ | 1 | $d_{10}$ | uniformly graded sand, $n$ = 0.375 $T$ = 10 °C |
| Hazen (1892)[a] | $6 \times 10^{-4}$ | $[1+10(n-0.26)]$ | $d_{10}$ | 0.01 cm < $d_{10}$ < 0.3 cm $U$ < 5 |
| Slichter (1898)[a] | $1 \times 10^{-2}$ | $n^{3.287}$ | $d_{10}$ | 0.01 cm < $d_{10}$ < 0.5 cm |
| Terzaghi (1925)[a] | $10.7 \times 10^{-3}$ smooth grains $6.1 \times 10^{-3}$ coarse grains | $\left(\frac{n-0.13}{\sqrt[3]{1-n}}\right)^2$ | $d_{10}$ | sandy soil, coarse sand |
| Beyer (1964)[a] | $5.2 \times 10^{-4}\log\frac{500}{U}$ | 1 | $d_{10}$ | 0.006 cm < $d_{10}$ <0.06 cm 1 < $U$ < 20 |
| Sauerbrei (1932)[a] (Vuković and Soro, 1992) | $(3.75 \times 10^{-5}) \times \tau$ $\tau \cong 1.093 \times 10^{-4}T^2 + 2.102 \times 10^{-2}T + 0.5889$ | $\frac{n^3}{(1-n)^2}$ | $d_{10}$ | sand and sandy clay $d_{17}$ < 0.05 cm |
| Krüger (1919)[a] | $4.35 \times 10^{-4}$ | $\frac{n}{(1-n)^2}$ | $\frac{1}{\sum_{i=1}^{n}\frac{\Delta w_i}{d_i}}$ | medium sand $U$ > 5 $T$ = 0 °C |
| Kozeny-Carmen (1953)[a] | $8.3 \times 10^{-3}$ | $\frac{n^3}{(1-n)^2}$ | $d_{10}$ or $\frac{1}{\frac{3}{2}\frac{\Delta w_1}{d_1}+\sum_{i=2}^{n}\Delta g_i\frac{d_i^g+d_i^d}{2d_i^g d_i^d}}$ $d_1=\frac{1}{\frac{1}{2}\left(\frac{1}{d_i^g}+\frac{1}{d_i^d}\right)}$ | Coarse sand |
| Zunker (1930)[a] | $0.7 \times 10^{-3}$ for nonuniform, clayey, angular grains $1.2 \times 10^{-3}$ for nonuniform $1.4 \times 10^{-3}$ for uniform, coarse grains $2.4 \times 10^{-3}$ for uniform sand, well rounded grains | $\frac{n}{(1-n)}$ | $\frac{1}{\sum_{i=1}^{n}\Delta g_i\frac{d_i^g-d_i^d}{d_i^g d_i^d ln\left(\frac{d_i^g}{d_i^d}\right)}}$ | no fractions finer than $d$ = 0.0025 mm |
| Zamarin (1928)[a] | $8.65 \times 10^{-3}$ | $\frac{n^3}{(1-n)^2}C_n$ $C_n=(1.275-1.5n)^2$ | $\frac{1}{\sum_{i=1}^{n}\Delta g_i\frac{\ln\left(\frac{d_i^g}{d_i^d}\right)}{d_i^g-d_i^d}}$ | Large grained sands with no fractions having $d$ < 0.00025 mm |

*Table 12. References, formulae and conditions used for calculating what is displayed in Figure 3-25 and Figure 3-26 (2 of 2).*

| | | | | |
|---|---|---|---|---|
| USBR (United States Bureau of Reclamation) (Bialas, 1966)[a] | $(4.8 \times 10^{-4})(10^{0.3})$ | 1.0 | $d_{20}^{1.15}$ | Medium grained sands with $U < 5$; derived for $T = 15$ °C |
| Barr (2001) | $\frac{1}{(36)5C_s^2}$ <br> $C_s^2 = 1$ for spherical grains <br> $C_s^2 = 1.35$ for angular grains | $\frac{n^3}{(1-n)^2}$ | $d_{10}$ | unspecified |
| Alyamani and Sen (1993) | 1300 | 1.0 | $[I_o + 0.025(d_{50} - d_{10})]$ | unspecified |
| Chapuis (2004) | $\frac{\mu}{\rho g}$ | $10^{1.291\xi - 0.6435}$ <br> $\xi = \frac{n}{1-n}$ | $d_{10}^{\left(\frac{10^{(0.5504-0.2937\xi)}}{2}\right)}$ | $0.3 < n < 0.7$ <br> $0.10 < d_{10} < 2.0$ mm <br> $2 < U < 12$ <br> $d_{10}/d_5 < 1.4$ |
| Krumbein and Monk (1942) | $7.501 \times 10^{-6}$ | $e^{(-1.31 \times \sigma_\emptyset)}$ <br> $\sigma_\emptyset = \frac{d_{84\emptyset} - d_{16\emptyset}}{4} - \frac{d_{95\emptyset} - d_{5\emptyset}}{6.6}$ | $2^{\left(\frac{d_{16\emptyset} + d_{50\emptyset} + d_{84\emptyset}}{3}\right)}$ | natural sands with lognormal grain size distribution |

* indicates formulas were taken from Vuković and Soro, (1992)
$N$ = constant dependent on characteristics of the porous medium
$\varphi(n)$ = function of porosity
$T$ = water temp. (°C)
$g = 980$ cm s$^{-2}$
$\rho = 3.1 \times 10^{-8}\,T^3 - 7.0 \times 10^{-6}\,T^2 + 4.19 \times 10^{-5}T + 0.99985$
$\mu = -7.0 \times 10^{-8}\,T^3 + 1.002 \times 10^{-5}\,T^2 - 5.7 \times 10^{-4}T + 0.0178$
$\tau = 1.093 \times 10^{-4}\,T^2 + 2.102 \times 10^{-2}\,T + 0.5889$
$n$ = porosity as fraction of aquifer volume
$d_i^g$ = the maximum grain diameter in fraction $i$
$d_i^d$ = the minimum grain diameter in fraction $i$
$d_{10}$ = grain size (cm) corresponding to 10% by weight passing through the sieves
$d_{20}$ = grain size (cm) corresponding to 20% by weight passing through the sieves
$d_{50}$ = grain size (cm) corresponding to 50% by weight passing through the sieves
$d_{60}$ = grain size (cm) corresponding to 60% by weight passing through the sieves
$U = d_{60}/d_{10}$
$\Delta g_i$ = the fraction of mass that passes between sieves $i$ and $i+1$ where $i$ is the smaller sieve
$\Delta w_i$ = fraction of total weight of sample with fraction identifier '$i$'
$d_i$ = mean grain diameter of the fraction $i$
$d_{i\phi}$ = mean grain diameter of the fraction $i$ in phi units ($\phi = \log_2 (d_e/d_o)$, $d_e$ in mm, $d_o = 1$ mm)
$I_o$ = x-intercept (grain size) of a percent grain retention curve plotted on arithmetic axes and focussing on data below 50% retained

### 3.4.1.2 Estimated internal stability.

| Soil GSD | Calculated internal stability (geometric) | | | | |
|---|---|---|---|---|---|
| | Kenney & Lau | Rönnqvist et al | Kezdi (1979) | Istomina (1957) | Burenkova (1993) |
| Soil 1 | 0.096 | 0.096 | 9.812 | 25.623 | unstable |
| Soil 2 | 0.475 | 0.475 | 1.594 | 49.729 | unstable |
| Soil 3 | 0.516 | 0.516 | 2.891 | 14.185 | stable |
| Soil 4 | 0.069 | 0.069 | 59.057 | 226.399 | unstable |
| Soil 5 | 0.685 | 0.685 | 1.986 | 48.019 | unstable |
| Soil 6 | 0.198 | 0.198 | 5.048 | 0.046 | unstable |

*Figure 3-27. Estimated internal instability of soil gradations. Green indicates stable, red unstable and yellow in a transition between stable and unstable, as defined by authors.*

Definition of criteria: Kenney & Lau, 1985: H/F <1 = unstable; Rönnqvist et al (2017): H/F <0.68 = unstable; (H = mass fraction of particles ranging from d to 4d; F = mass fraction of particles finer than grain size d); Kezdi (1979): D'15/d'85>4 = unstable; Istomina (1957): ≤10=stable; 10 to 20=transit.; ≥20=unstable; Burenkova (1993): defined by placement of gradation on plot below:

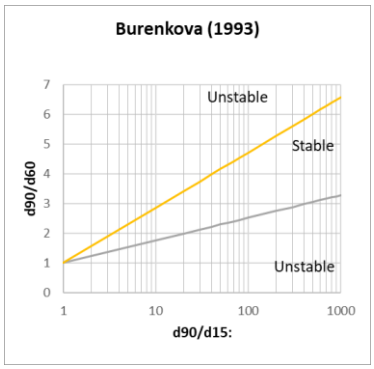


### 3.4.1.3 Remarks

*i.* AE quantification relative to hydromechanics and internal erosion: technical issues traced back to the preamplifiers caused the AE amplitude quantification to be uncertain, especially regarding the hydrophones. This means that the relative AE changes throughout a given test was considered.

*ii.* AE from different sensors: The WG (piezoceramic transducer) detects AE differently from the hydrophones. The hydrophones respond in a frequency-dependant fashion (i.e. signal with frequencies outside of the pre-set detection range (10-100kHz) are, as expected, not detected) while the waveguide detects virtually any direct collisional or frictional interactions with itself - if e.g. soil particles directly impact or graze against the WG, this was detected, more or less independently of the frequencies produced.

*iii.* Wall friction: The Perspex tube forming the permeameter wall seems to offer enough friction against a given soil sample to avoid the full force of the load (weights → lever → vertical loading shaft →top perforated plate → top of soil sample) from reaching the entire sample equally. This effect can of course vary

over time - e.g. the wall friction might simply retard the dissipation of stress through the sample, fluid flow [intensity] or erosion itself could influence wall friction, etc.

*iv.* Sample base/lower plate position: Although the test rig was designed to accommodate samples up to 905mm tall (280mm diameter), this test program used about the upper half of its capacity – 400mm of extensions/spacers were added between the bottom cap and the BLC, effectively making the used sample height ca. 500mm (Figure 3-12). Two of the reasons for this are a) practicality (faster/easier sample preparation) and b) better water flow dissipation before it reaches the sample (the "water only" volume helps avoid preferential flow artifacts). Consequently, the pressure transducer positions within the sample relative to the bottom perforated plate (i.e. their distance from the bottom perforated plate) are:

| Pressure transducer positions relative to bottom perforated plate (distances from plate) with 400mm of spacers between bottom cap and BLC: | | | |
|---|---|---|---|
| Pr. tr. 1 | Pr. tr. 2 | Pr. tr. 3 | Pr. tr. 4 |
| 385mm | 285mm | 185mm | 85mm |

*v.* Variations in [hardware] noise: The level of noise produced by the AE data acquisition hardware occasionally oscillated sufficiently to interfere with the RDC (ring-down counts). When this occurred the RDC thresholds were as soon as possible adjusted accordingly. Overall, the ensuing data distortions were either reduced to negligibility or pointed out in the description of results. The cause for such issues could not be exactly identified but seemed to lie in the functioning of the preamplifiers – the voltage outputs may have varied as, during the considerably long tests, some element of their circuitry (or equivalent) fluctuated in e.g. temperature.

*vi.* Moving averages were used to smoothen some of the plotted curves. This tended to skew the curves on the time axis. So, for instance, oscillations of a time-domain RDC curve might be skewed to slightly earlier times than the events they in fact represent.

*vii.* Effective stress calculation: As only two load cells are used in the test rig (above and below the sample), the values from the load cells have been linearly interpolated in order to estimate the effective stress at selected positions between them.

- Later observation of the produced data showed that:
  - During the loading phase of a given test the stress measured on the BLC was lower than that of the TLC.

- Á After the loading phase, the load perceived by the Top load cell was rather constant when compared to the BLC. In other words, the effective stress variations displayed during a test are much more influenced by the measurements of the BLC than by those of the Top Load cell.

*viii.* Effective stress and pore pressure: Knowing that vertical stress and pore pressure vary over the height of the sample (i.e. the water column and the amount of soil above a position was different at different heights, influencing the effective stress), the effective stress at the position of Pressure Transducer "3" (3rd from the top, ; Figure 3-7) has been chosen as the one used in the plots – this position was deemed as relatively neutral to the boundary conditions of the sample, especially its top, where e.g. in upward flow the ejection of eroded material and sudden drop in permeability were less influential.

Each test can be separated in two phases:

a) Sample consolidation: Once the soil specimen was in the permeameter cell the vertical stress mechanism was loaded with a predefined mass (leveraged by ~5x). The system was then left to equilibrate (potential dissipation of pore overpressure, dissipation of wall friction, soil compaction)
b) Variation of head tank height

## 3.5 Summary

This chapter clarified the experimental phase of this research, justifying the choices made, apparatus details and laying out the procedures to be followed.

Preliminary tests led to the development of a bespoke permeameter based on the work by Moffat and Fannin (2006). This new apparatus was able to accommodate a large sample (ca. 500/900mm tall by 280mm diameter), control vertical stress, vary hydraulic head, measure key hydromechanical variables, quantify fluid flow, induce and observe seepage-induced internal erosion is soils prone to it and, crucially, detect AE from the incurring soil dynamics.

A programme of 11 experiments (each approx. 4 days in duration) was performed on 6 soils with marginal degrees of estimated internal stability. The soil gradations for the tests were selected based on their representability of materials used in real assets and by having been used in studies by other authors. In each test with the bespoke apparatus a range of hydraulic heads and vertical stresses was applied to the samples. The intention was provoking internal instability in a gradual and controlled manner as well as allowing the eventual erosional process to evolve, all while recording hydromechanical parameters and AE.

The applied vertical stresses (Table 10) are at about the range of what has been applied in comparable published studies (Liang et al., 2017; Moffat et al., 2011; Moffat and Fannin, 2011; Chen et al., 2016). The purpose of the vertical stress was mainly keeping the soil skeleton at a roughly fixed configuration and have the fluid flow essentially just directly influence the non-load-bearing fines present in the gaps/pores between the [larger] fraction composing the soil skeleton.

# 4 Results

## 4.1 Introduction

This chapter details the results obtained from the experimental programme. A preliminary round of tests was performed with a simpler, less complex permeameter device which were then used to help develop a more sophisticated test apparatus and produce more comprehensive results. The first of the following sections will focus on the preliminary tests and will be followed by the tests with the bespoke, newly designed, large permeameter.

### 4.1.1 Preliminary tests

Initial laboratory work was performed to study of internal erosion AE using the permeameter apparatus described in the Materials and Methods section (3.2). Given the focus on AE generated by suffusion, the primary intent was ascertaining that the corresponding acoustic signal could be measured while sufficiently filtering background noise and excluding the AE produced by water flow without particle movement. The differentiation between seepage flow and seepage erosion (i.e. with particle movement) was done visually. Although some turbidity due to fine particles in suspension could be observed (particularly in the first moments of open water flow; from fines initially covering the coarser grains), the considered signal excluded its occurrence (largely because the energy generated by the movement of fines is too small to be detected), targeting the transport of the sand grains.

The evolution of the internal erosion process (roughly equivalent to the RDC increments) related to hydraulic gradient changes as the specimen material reorganized and hydraulic conductivity was affected. The displayed water pressures (Figure 4-1) were calibrated so that 1kPa equals 0.1m (±0.05m) of head. At the beginning of a test run, a sudden pressure elevation was observed when the taps regulating flow were opened, but the pressure would rapidly be dissipated and reach equilibrium with the flow.

In observing the frequency spectra of the performed tests, notable differences are in the frequencies and their corresponding amplitudes. Generally, it can be noted that:

- Amplitude ratio peaks vary in order of magnitude (approximately 0.03 in test 1, 0.0012 in tests 3, 6 and 7, 0.0025 in test 2, up to 0.1 in test 8).
- The frequencies with more significant amplitude ratios vary among tests, although, roughly:

  - tests with mixed/homogenized sediment (tests 5 through 11; Figure 4-3 and Figure 4-4) tend to have more prominent amplitude ratios between 20 and 50kHz (with signal demarcation also varying) and,
  - tests with layered soils (1 through 4; Figure 4-2) have more varied spectra.
- Some of the amplitude ratio peaks (e.g. tests 7, 8 and 11) seem to obscure the rest of the produced signal due to scale effects, or the vertical accentuation of higher amplitude frequencies comes at the cost of lower amplitude ones. This could be addressed by using e.g. a logarithmic scale, but brief attempts to do so visually homogenized the full spectrum in a way that signal clarity became less satisfactory. A better form of data visualisation will be pursued. Alternatively, if such peaks are recognized to be overrepresented or not meaningful for the purposes of this research, better signal filtering can serve as solution.
- Changes in hydraulic gradient seem to roughly correlate with RDC variations, with a time lag in between.
- As the material reorganizes within the sample and erosion evolves, RDC variations seemingly decoupled from the measured hydraulic gradient are produced. This agrees with expectations and offers credibility to the experiment.

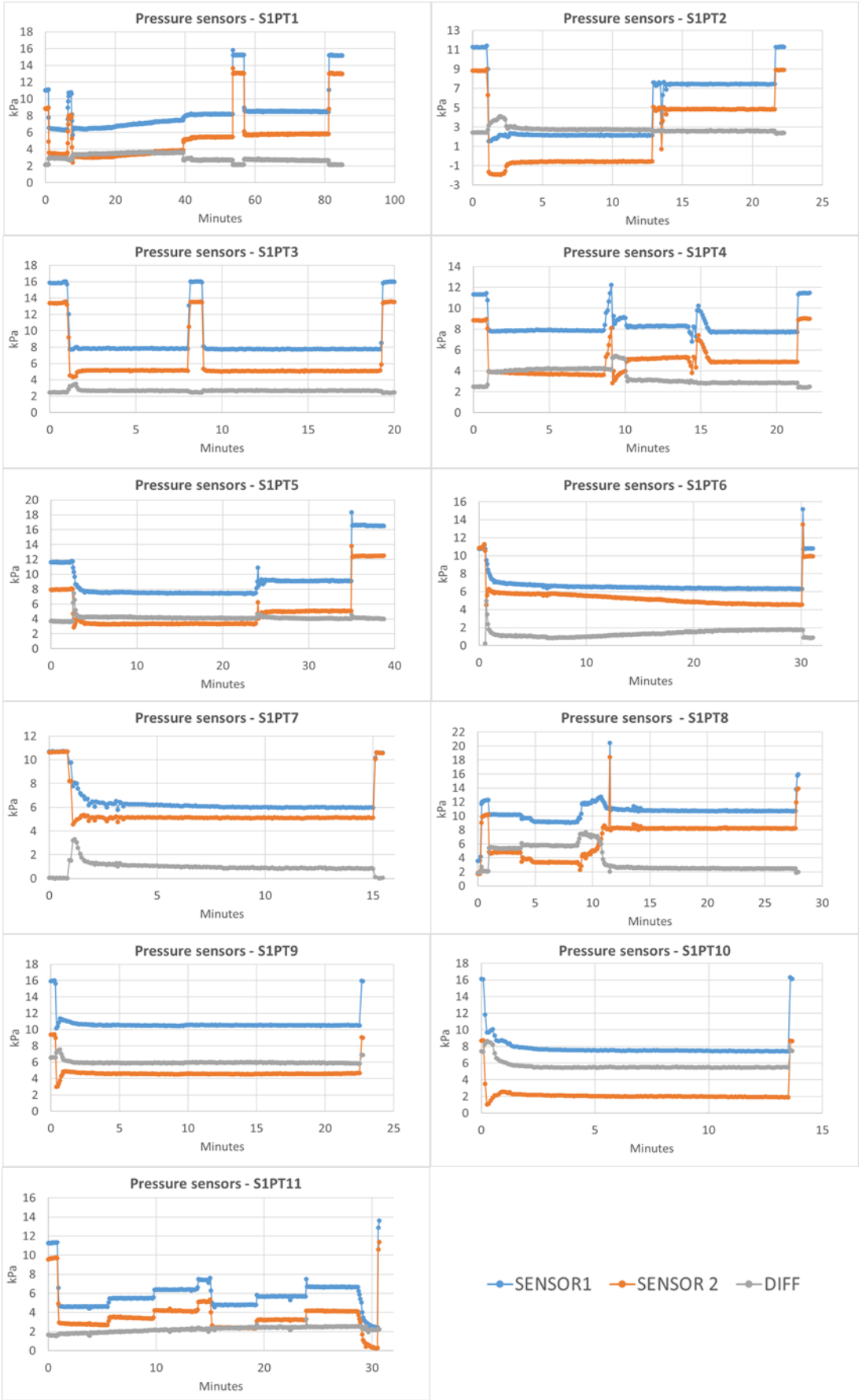


*Figure 4-1. Pressure sensor data of performed experiments. Blue and orange lines represent data from lower and upper transducers respectively and grey lines show the pressure difference.*

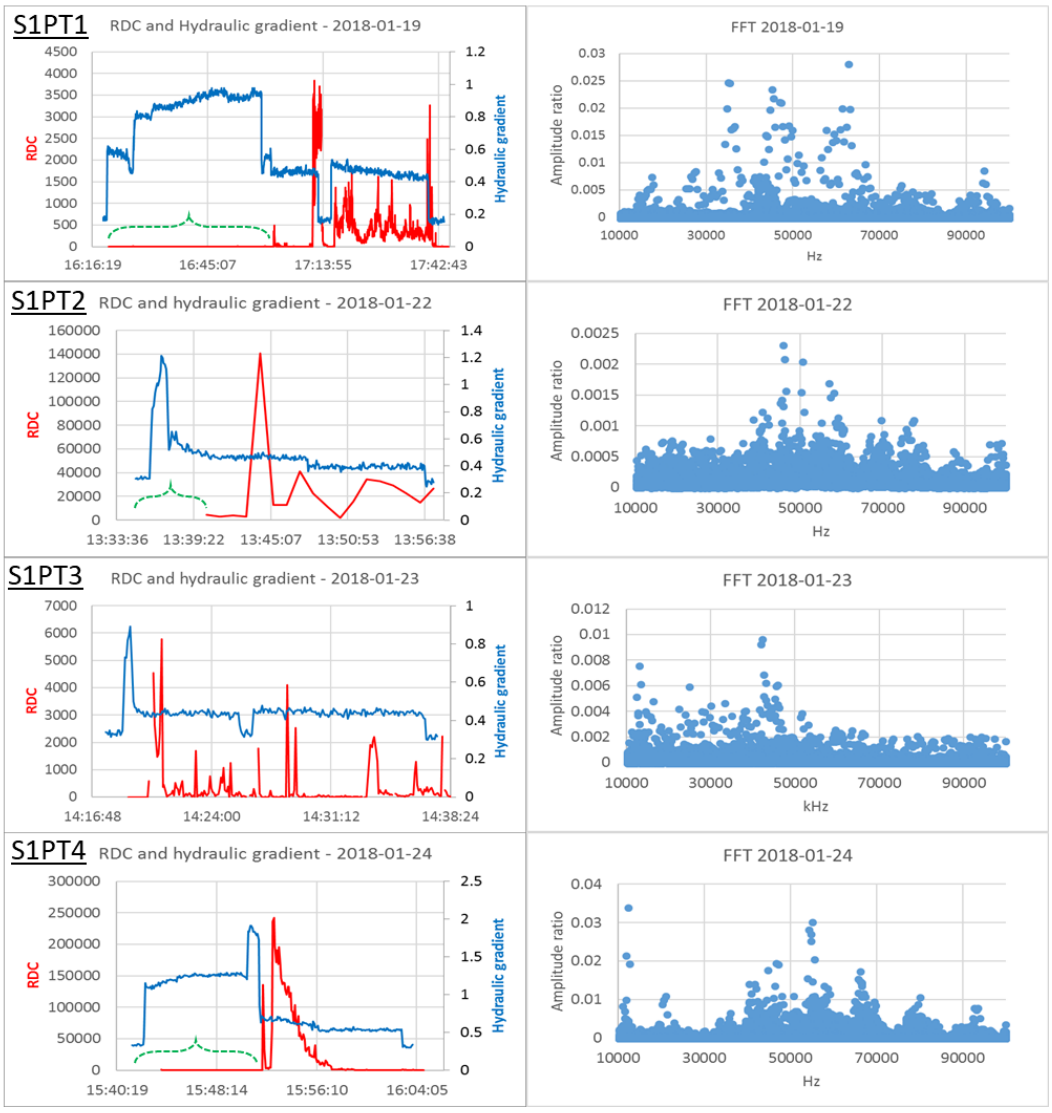


*Figure 4-2. Results of initial permeameter tests performed in January 2018. Right plots represent the frequency domain amplitude ratio of individual experiments while plots at the left show the variation in time of RDC increments (red) and hydraulic gradients calculated from pressure transducers (blue). Dashed green braces show regions where RDC data failed to be registered.*

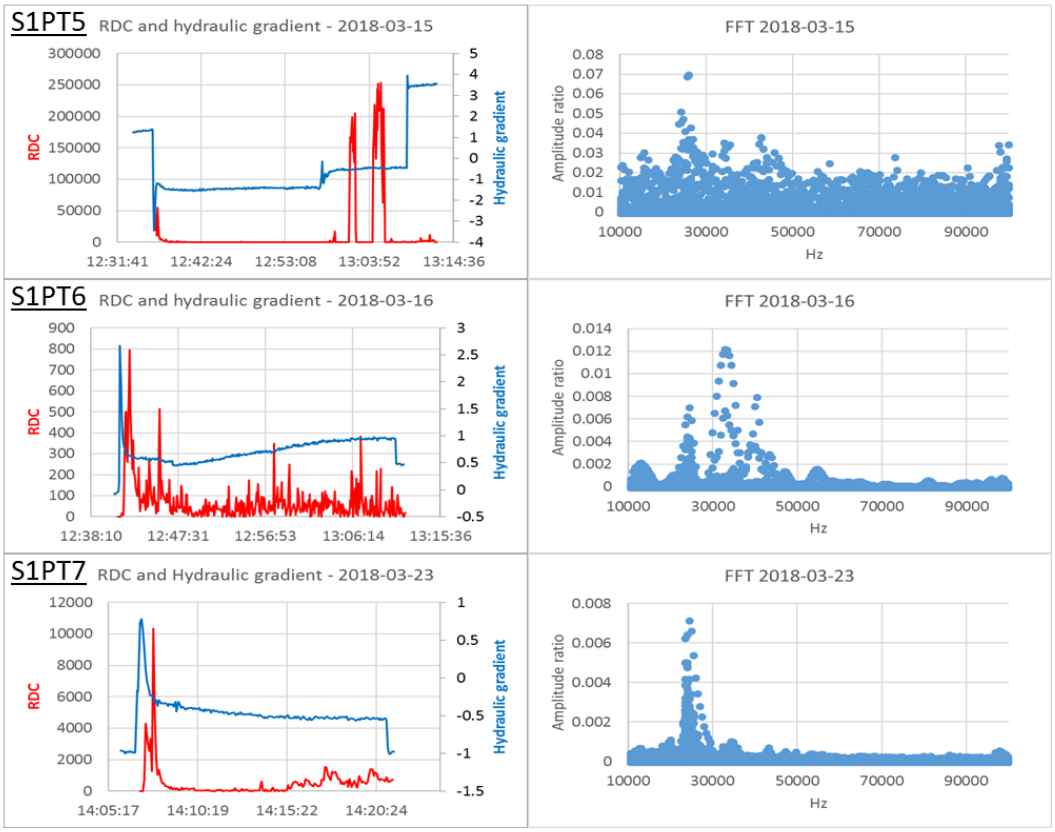


*Figure 4-3. Results of initial permeameter tests performed in March 2018. Right plots represent the frequency domain amplitude ratio of individual experiments while plots at the left show the variation in time of RDC increments (red) and hydraulic gradients calculated from pressure transducers (blue).*

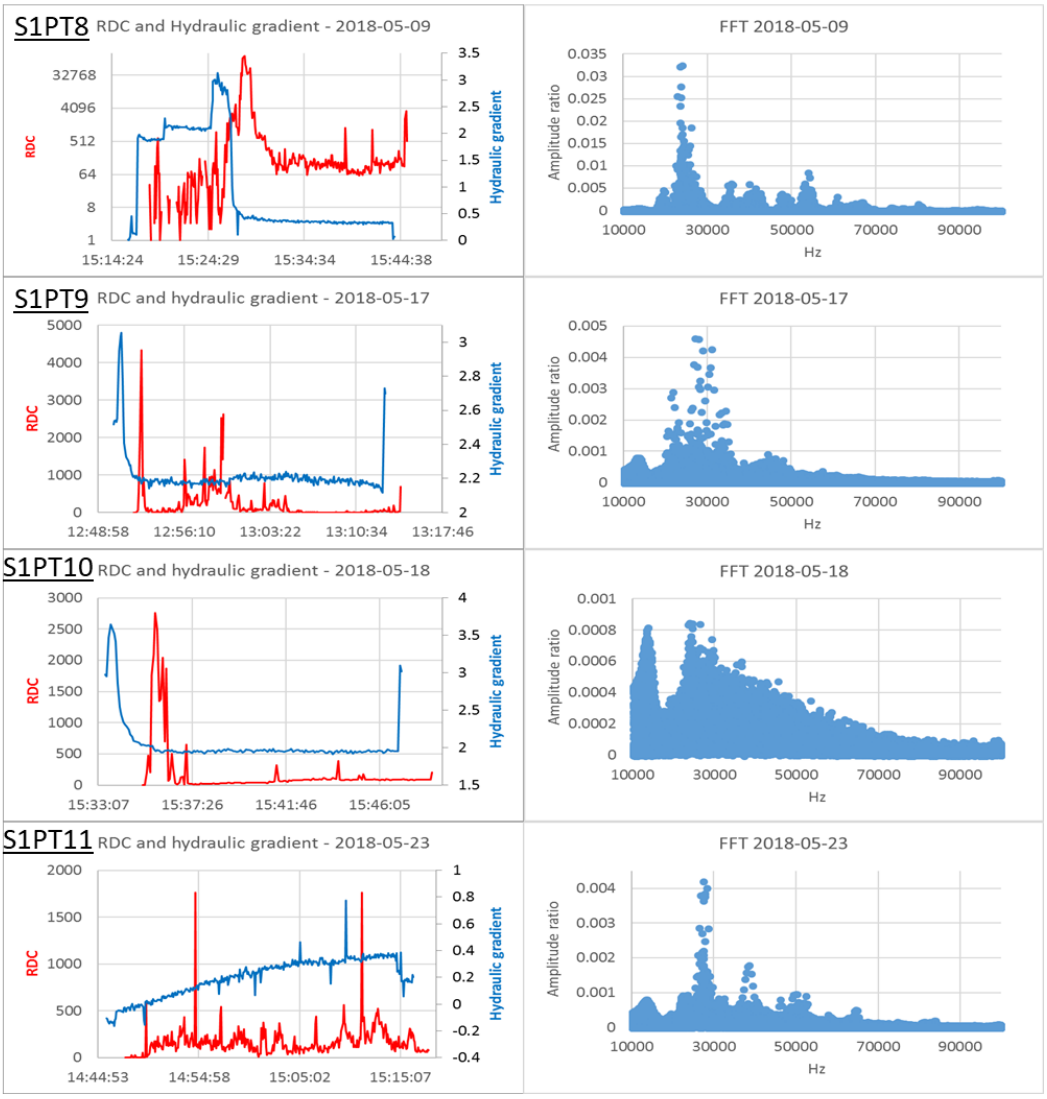


*Figure 4-4. Results of initial permeameter tests performed in May 2018. Right plots represent the frequency domain amplitude ratio of individual experiments while plots at the left show the variation in time of RDC increments (red) and hydraulic gradients calculated from pressure transducers (blue). Note that test #8 has a base 2 Log RDC axis scale for better visualisation.*

### 4.1.2 Large permeameter experiments

Observation of the tests with the more advanced permeameter is separated in consolidation and post-consolidation phases, or respectively, a phase in which the addition of vertical stress is the controlled/manipulated variable and another in which this variable is the variation of hydraulic head (under constant vertical stress). Data has been laid out in the time domain as this allows visualisation of the progression of the studied phenomena. The two main sets of observations regard hydromechanical parameters and AE. The tests will be presented in order of the examined soils, including successive tests with a soil gradation. Results of test with Soil 1 are in the Appendix since this test faced technical issues. Data of the individual load cells, permeability, values recorded by individual pressure transducers during tests as well as estimated critical hydraulic gradients and calibration values for different sensors can also be found in the Appendix.

### *S2T1*

Test done between 09.10.2019 and 16.10.2019. During this test a few technical matters had to be addressed – electronics and connectors were re-checked for e.g. noise levels and the AE sensor thresholds re-set. The response was:

a) The electronic components were checked, and the coaxial connector of the top hydrophone was re-fitted. The AE signal remained comparable to how it was before.

b) Random voltage spikes coming from both hydrophones while the system is static (no flow, no suffusion, no obvious processes producing detectable AE) were not conclusively recognized as noise or actual physical events occurring inside the permeameter – this impacted the selection of RDC thresholds, as setting them thresholds below these random spikes could produce noisy data (assuming these spikes are noise), while having thresholds above these spikes could mean neglecting data (if these spikes are from indeed real, relevant physical phenomena). So, the chosen solution was to be able to define two different thresholds, one above and the other below these spikes. This was done and sensors ai0 and ai1 (bottom and top hydrophones) could then produce RDC from two independent voltage thresholds, which after the test could be chosen based on the assessed signal quality. Two more data gaps occurred (light-yellow areas indicated in Figure 4-6) due to issues with the data storage system.

**S2T1 Consolidation phase**

In Figure 4-5 and Table 13 the seepage phase of test S2T1 is shown. In the hydromechanical parameters (Figure 4-5a), the LVDT and $\sigma'$ curves formed upward steps, corresponding to vertical stress increases. The hydraulic gradient ($i$) peaked twice as vertical stress rises induced excess pore pressure that then dissipated. From ca. min. 180 onwards, compression (LVDT) slightly increases, $\sigma'$ decreases (seemingly due to more stress being transferred to the bottom LC, partially overcoming wall friction), and $i$, in a series of steps, also increases.

In the AE during this consolidation phase (Figure 4-5b), the BH and WG recorded an upward slope almost simultaneously (ca. min. 75-78; slightly earlier in the BH) followed by an equivalent rise on the TH shortly after (ca. min. 83). By ca. min. 100 all three RDC trends return to baseline values. This occurs sequentially: BH followed by WG and then TH, respectively at min. 91, 95 and 103.

In the second load increase step (min. 109), the WG and the BH peak with a ca. 10 min. offset while the TH did not show a significant signal. At ca. min. 150-160, coinciding with the start of the 3rd step of vertical load rise, all three AE sensors peak and then proceed to drop coinciding with the end of the vertical load increase.

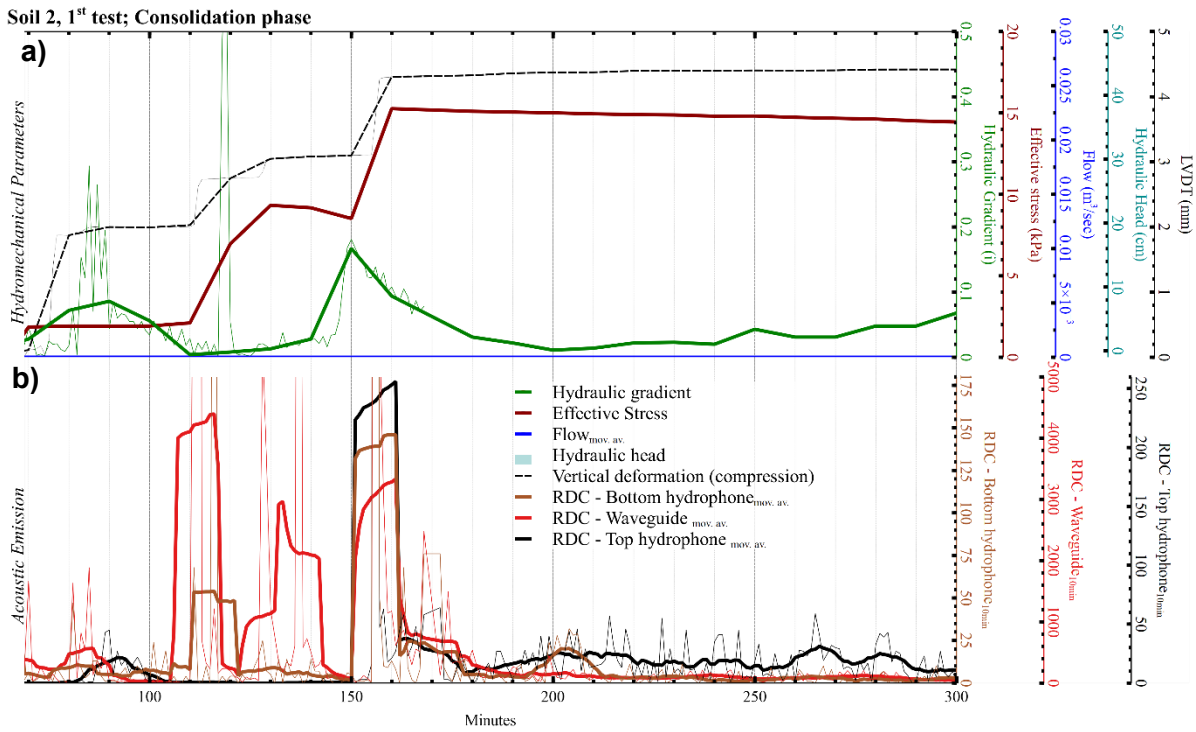


*Figure 4-5. Combined plot of the measured hydromechanical parameters (a) and AE (b) of S2T1 (consolidation phase) in the time domain. Each parameter has an independent vertical axis with the same colour of the plotted curve (e.g. the blue line represents flow rate and corresponds to the blue vertical axis). The LVDT data indicates compression of the sample – a reduction of volume is reflected as an increased LVDT value (in millimetres). Thin lines represent raw data of variables shown with the same colour in thicker lines, which are moving averages.*

*Table 13. Summary of main general trends observed over time during the consolidation phase of test S2T1. Key to symbols in Table 35.*

S2T1 – Consolidation phase

| Time (minutes) | σ' | *i* | LVDT (compression) | BH | WG | TH |
|---|---|---|---|---|---|---|
| **0-110** | ↗ | Λ | ↗ | Λ | Λ | Λ |
| **110-150** | ↗ | ↗ | ↗ | ∿ | Λ | — |
| **150-170** | ↗ | ↘ | ↗ | Λ | Λ | Λ |
| **170-300** | — | — | — | ∿ | ↘ | ∿ |

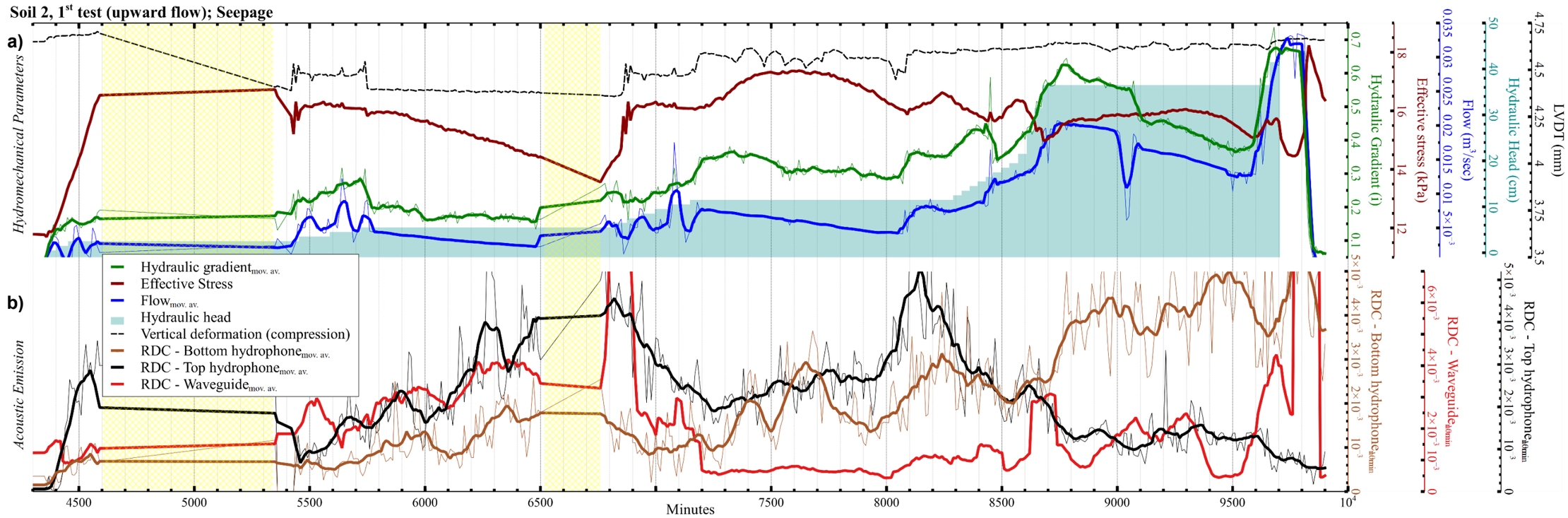


*Figure 4-6. Combined plot of the measured hydromechanical parameters (a) and AE (b) of S2T1 (post consolidation phase) in the time domain. Each parameter has an independent vertical axis with the same colour of the plotted curve (e.g. the blue line represents flow rate and corresponds to the blue vertical axis). The LVDT data indicates compression of the sample – a reduction of volume is reflected as an increased LVDT value (in millimetres). The light-yellow crossed areas represent data gaps due to data recording issues. Thin lines represent raw data of variables shown with the same colour in thicker lines, which are moving averages.*

*Table 14. Summary of main general trends observed over time during the seepage test (post-consolidation) phase of test S2T1. Key to symbols in Table 35.*

S2T1 – Seepage test (post-consolidation)

| Time (minutes) | Hydraulic head | σ' | Q | i | LVDT (compression) | BH | WG | TH |
|---|---|---|---|---|---|---|---|---|
| 4300-4600 | ↗ | ↗ | ↗ | ↗ | ↗ | ↗ | ↗ | ↗ |
| 5400-5700 | ↗ | ∿ | ↗ | ↗ | ∿ | ∿ | Λ | ↗ |
| 5700-5800 | ↗ | ↘ | ↘ | ↘ | ↘ | ↗ | ↗ | ∿ |
| 5800-6450 | — | ↘ | ↘ | ↘ | — | ↗ | ↗ | ↗ |
| 6800-7200 | ↗ | ∿ | ↗ | ↗ | ∿ | ↘ | ↘ | ↘ |
| 7200-8000 | — | ⌒ | ↘ | ↘ | ∿ | ∿ | — | ↗ |
| 8000-8250 | — | ↗ | ↗ | ↗ | ↗ | ↗ | ↗ | Λ |
| 8250-8700 | ↗ | ↘ | ↗ | ↗ | — | ∿ | ∿ | ↘ |
| 8700-9500 | — | ⌒ | ↘ | ↘ | ∿ | ↗ | ∿ | ∿ |
| 9500-9700 | ↗ | ∿ | ↗ | ↗ | ∿ | ↘ | ↗ | ↘ |
| 9700-9900 | ↘ | ↗ | ↘ | ↘ | ∿ | ↗ | ↗ | ↘ |

**S2T1 Seepage test (post-consolidation)**

Figure 4-6 and Table 14 show the data from the post-consolidation phase of this test. During the first sequence of Head increase (of 4), between min. 4350 and 4455 all the hydromechanical parameters showed rises in values, apart from the compression (LVDT), which remained constant.

On the AE plots (Figure 4-6b), the three sensors showed increases once the head tank was raised (the TH being the most significant one – the rise at ca. min 4400 corresponded to the observation of seepage-induced particle movement, or early-stage internal erosion).

At min. 4453 head elevation began, during which the LVDT and *σ'* show a relatively constant but jagged behaviour. The hydraulic gradient showed an increase during this head rise sequence (from ca. 0.19 to 0.3) and, although a smoother trend, it also showed minor oscillations that correlate to the observations in the LVDT. *Q* showed an irregular increase. Once the head rise stopped, both *i* and *Q* started decreasing.

On the AE, the behaviour of the sensors was comparable to the first head rise sequence: the WG initially rose, dropped and rose once again while both hydrophones continually rise (again at different rates, the TH being more accentuated). After the head tank stopped being lifted, the AE of all three sensors went on a rather long (>1000 minutes) RDC increase. This increase was oscillatory and irregular.

On the hydromechanical sensors, after this second head rise sequence and until the following data gap (min. 6500), the LVDT stayed constant while *σ'* and *Q* steadily dropped. The *i* curve in turn dropped. Shortly after the data gap, a 3rd (of 4) head rise sequence began. In this head rise sequence the LVDT, hydraulic head, *Q* and *σ'* show a similar pattern to the one observed in the previous head rise sequence.

During this second head rise sequence the AE of the WG showed a peak, despite an overall downward trend. The TH showed a different behaviour in this head rise sequence when compared to the two previous ones: once this 3rd head rise sequence began, the RDC of the TH continually dropped. The BH behaved in part similarly to that of the TH, in that it also started dropping with the head rise, but about halfway through the head rise sequence it rose. After this 3rd head rise sequence, the LVDT entered a series of similar "arches" (min. 7148 and 7830) and then flattened, while the *σ'* curve formed one long arch. Between min. 7148 and 7590 *i* also formed an arch and then roughly stabilized with a slight downward slope. Between min. 7230 and 8020 *Q* steadily dropped.

On the AE, the WG dropped to its minimum over the whole test at min. 7200 (shortly after the head rise) and remained so until ca. min. 8500, with minor oscillations. At min. 7250 the TH

reverted from a downward trend to an upward one that at about min. 7950 got accentuated until it peaked (ca. min 8150, the highest TH RDC peak in the test). The BH had a more oscillatory behaviour after the 3rd head rise sequence, with an overall upward trend that peaked at ca. min. 8250.

Starting at min. 8010 (note: with no external manipulation), the LVDT dropped - increase in sample volume, or height -, reaching a local minimum at min. 8040. At minute 8020 both *Q* and *i* started increasing. The *σ',* the last of the hydromechanical parameters to change during this event, at min. 8090 started increasing and peaked at min. 8240.

The last head rise sequence started at min. 8289, during which the LVDT varied slightly. The *σ'* dropped, until at min. 8450 reverted to a rise that peak at min. 8570, which coincides with an increase in the rate of head increase – at min. 8608 the head tank went from being risen in 1cm steps to 5cm ones. With a stop of head rise *σ'* began rising. *Q* and *i* oscillated but showed an overall increase, with two main deviations (min. 8400 and 8510), from then on following near- parallel trends. With a constant head (min. 8675), *σ'* showed an "arch" that lasted until min. 9590, *Q* and *i* decreased (with an oscillation at ca. min 9050) and the LVDT formed a series of roughly rectangular steps.

On the AE, the RDC of the hydrophones during this last head rise sequence (1cm head rise steps, until min. 8532) was characterized by a downward slope. Once the 5cm head rise steps began, both the BH and the TH showed an uptick. At ca. min. 8700 however the RDC of the hydrophones diverged – the TH continued dropping while the BH rose. At ca. min. 8800 both hydrophones roughly stabilised, each slightly sloping in their previous directions. The WG locally peaked at min. 8650, and then trended upwards, with a trough at ca. min 9400 - 9600.

At min. 9550, *i* and *Q* markedly sloped upwards (peaking at ca. min. 9760). At min. 9600 *σ'* increased but ceased with this last head rise. The LVDT plateaued from this last head rise onwards. At min. 9705 the head tank was lowered. Between then and minute 9760, *i* and *Q* continued their upward trend, but then (after a ca. 60 min. lag between the drop of the head tank and the peak in these parameters) markedly dropped. The *σ'* troughed at min. 9760, and then peaked (to its highest value during this test) at min. 9830 before dropping until data collection ceased.

On the AE, at ca. min. 9600 the downward trend the TH was on accentuated. At ca. min 9650 the BH reached a local trough that was replaced by a steep rise and peak (ca. min 9750) corresponding to the drop of the head tank. The WG at ca. min. 9550 steeply rose (corresponding to the rise seen on *i* and *Q*), reaching its maximum RDC of the test at ca. min. 9850) before a final equally steep drop.

### *S2T2*

Test done between 29.11.2019 and 04.12.2019. During this test, a leakage found in a sediment trap integral to the laboratory plumbing. This issue occurred by the end of the consolidation phase and was immediately fixed. Since this phase of the test did not include fluid flow (or discharge) and the problem was downstream of the entire experiment, it did not influence the test outcomes. This was an upward flow test.

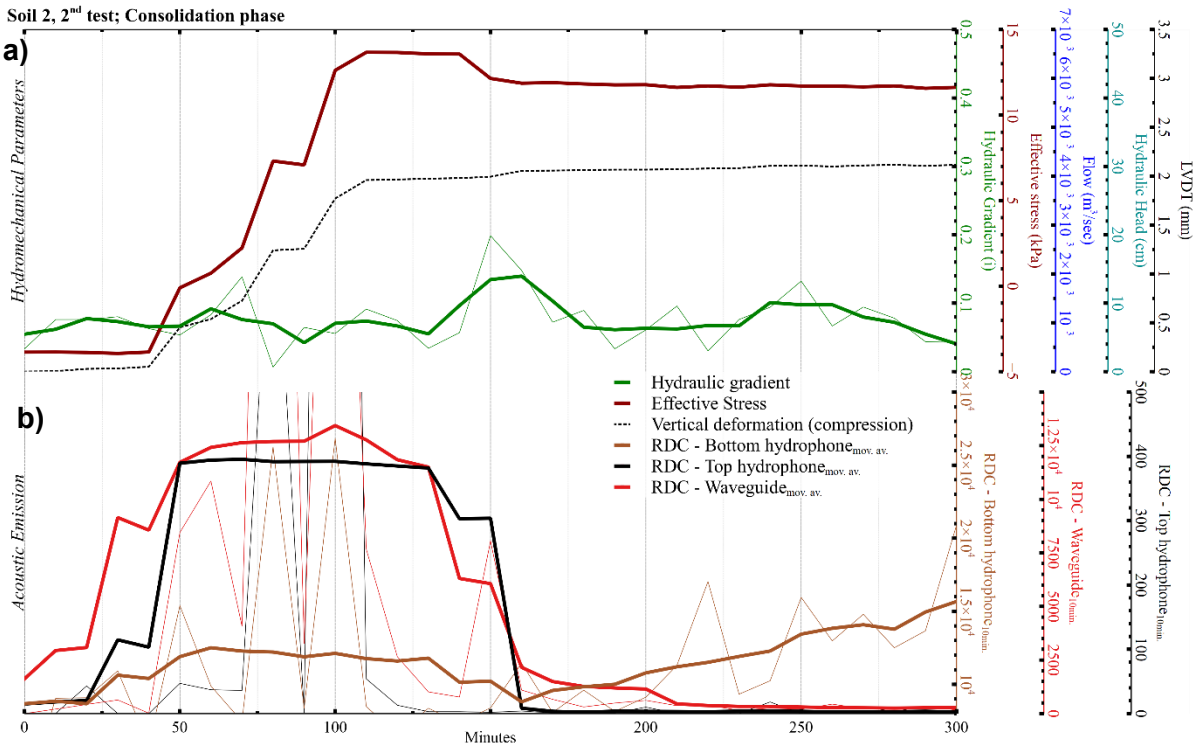


*Figure 4-7. Combined plot of the measured hydromechanical parameters (a) and AE (b) of S2T2 (consolidation phase) in the time domain. Each parameter has an independent vertical axis with the same colour of the plotted curve (e.g. the blue line represents flow rate and corresponds to the blue vertical axis). The LVDT data indicates compression of the sample – a reduction of volume is reflected as an increased LVDT value (in millimetres). Thin lines represent raw data of variables shown with the same colour in thicker lines, which are moving averages.*

*Table 15. Summary of main general trends observed over time during the consolidation phase of test S2T2. Key to symbols in Table 35.*

S2T2 – Consolidation phase

| Time (minutes) | σ' | *i* | LVDT (compression) | BH | WG | TH |
|---|---|---|---|---|---|---|
| **0-100** | ↗ | — | ↗ | ∧ | ∧ | ∧ |
| **100-900** | — | — | ↗ | ↗ | — | — |
| **900-1100** | — | — | ↗ | ↘ | — | — |

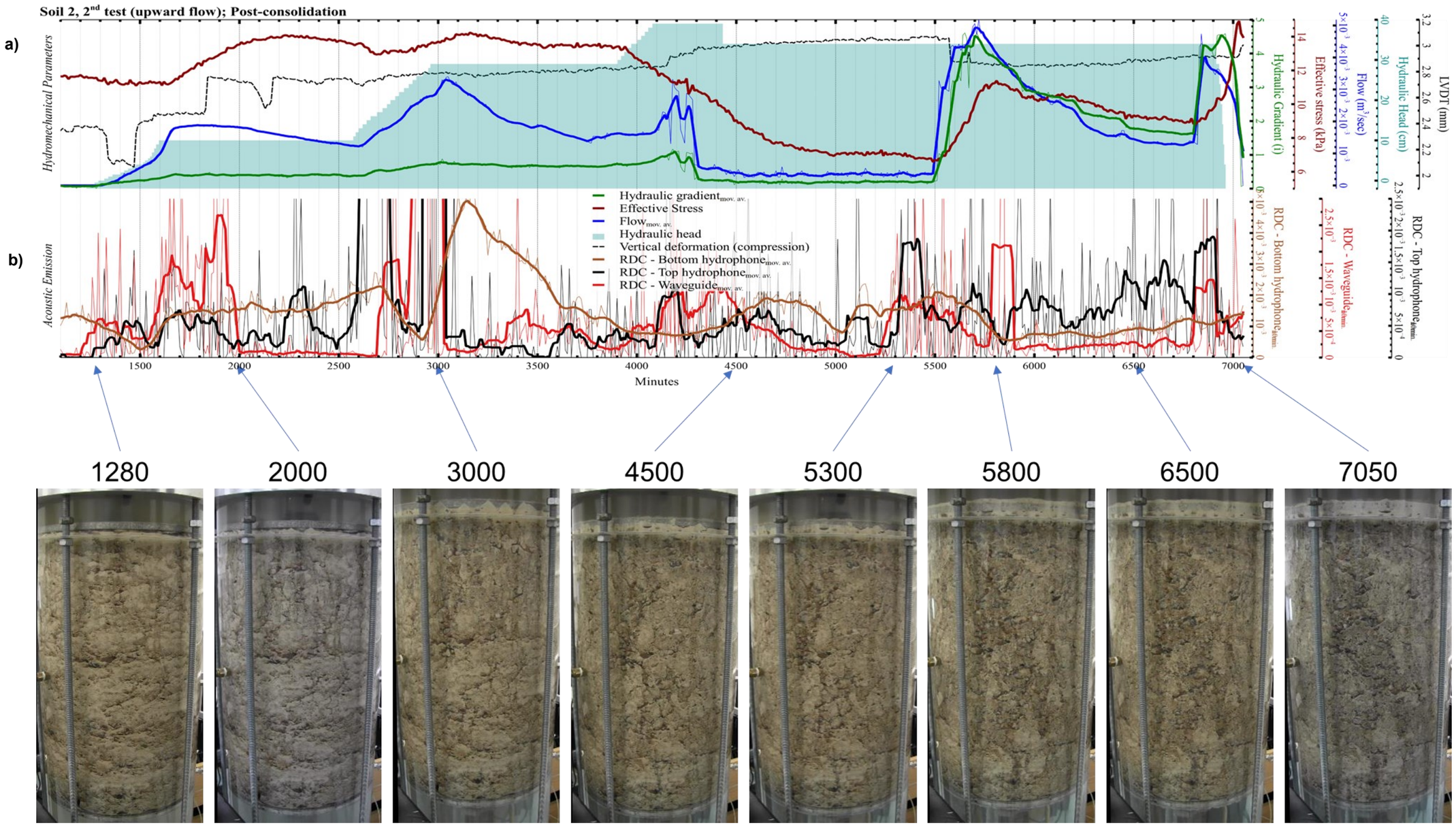


*Figure 4-8. Combined plot of the measured hydromechanical parameters (a) and AE (b) of S2T2 (post consolidation phase) in the time domain. Each parameter has an independent vertical axis with the same colour of the plotted curve (e.g. the blue line represents flow rate and corresponds to the blue vertical axis). The LVDT data indicates compression of the sample – a reduction of volume is reflected as an increased LVDT value (in millimetres). Thin lines represent raw data of variables shown with the same colour in thicker lines, which are moving averages. Picture series below shows soil specimen at different points during the test (elapsed minutes indicated above each image).*

**S2T2 Consolidation phase**

Figure 4-7and Table 16 show the hydromechanical parameters during the consolidation phase of S2T2. The two notable variables are the LVDT and *σ'*, both rising in steps corresponding to the addition of weight to the vertical loading system (min. 45, 60, 65 and 100). At minute 150, after the loading had already ended, the *σ'* slightly increased and the LVDT slightly dropped. The LVDT showed a progressive compression of the sample, albeit somewhat irregularly.

Figure 4-7b and shows the AE of the consolidation phase of S2T2. Here, the RDC of the three sensors rose and peaked in correspondence to vertical loading – note that the moving average process does tend to broaden the curves, making it appear that events occurred earlier than what happened in reality, but this is an artifact verifiable by observing the raw data curves (thin lines). At ca. min 150 the AE of all sensors dropped to baseline. The BH then proceeded to have a continuous rise throughout the rest of the plot. This rise in the RDC of the BH correlated to the settling of fines in suspension at the water volume below the soil sample, at the bottom of which the BH is located – particles in suspension slowly precipitated, most likely directly impacting the BH and causing this RDC signal. At ca. min 750 BH starts dropping (consistent with the settling of fines in suspension).

**S2T2 Seepage test (post-consolidation)**

In the first head rise sequence (Figure 4-8), *Q* and *i* started rising in proportion to the head rise steps. The LVDT between min 1300 and 1500 showed a drop and then returned to the slight upward trend it was on. Throughout this head rise sequence the *σ'* kept slightly trending downward. With the halting of head rise, *i* stabilised, *Q* trended downward and *σ'* went up and formed an arch. After min. 1800 the LVDT stepped up and plateaued, being interrupted by a trough at ca. min. 2150.

On the AE, the WG and TH rose corresponding to the rise in head, with a time offset (ca. 50 minutes, first the WG than the TH). Particle movement (or early-stage internal erosion) was noted at ca. min. 1270. The BH kept the downward trend it was on. At ca. min 1500 the WG and BH formed a trough, that ~50 min. later was also seen on the TH. From this point on (corresponding to the change in rate of head tank rise from 0.5cm to 1cm steps) all three AE sensors showed a marked RDC rise. With the head constant (min. 1600 on), the TH followed an irregular path, with a series of peaks (ca. min 1600, 1700, 2100 and 2300), the BH roughly stabilised and at ca. min 2400 sloped upward and the WG rose until at ca. min. 2000 dropped and stayed so.

*Table 16. Summary of main general trends observed over time during the seepage test (post-consolidation) phase of test S2T2. Key to symbols in Table 35.*

S2T2 – Seepage test (post-consolidation)

| Time (minutes) | Hydraulic head | σ' | Q | i | LVDT (compression) | BH | WG | TH |
|---|---|---|---|---|---|---|---|---|
| 1100-1700 | ↗ | ↘ | ↗ | ↗ | ∿ | ∿ | ↗ | ↗ |
| 1700-2600 | — | ↗ | ↘ | — | ∿ | ↗ | ↘ | ∿ |
| 2600-3000 | ↗ | ↗ | ↗ | ↗ | ↗ | Λ | Λ | Λ |
| 3000-3900 | — | ↘ | ↘ | — | ↗ | ↘ | ∿ | ∿ |
| 3900-4200 | ↗ | ↘ | ↗ | ↗ | ↗ | ∿ | ↗ | ↗ |
| 4200-4500 | — | ↘ | ↘ | ↘ | ↗ | ↗ | ↗ | ↗ |
| 4500-5300 | — | ↘ | — | — | ↗ | ∿ | ∿ | ↘ |
| 5300-5700 | — | ↗ | ↗ | ↗ | ↘ | Λ | ↘ | Λ |
| 5700-6700 | — | ↘ | ↘ | ↘ | ↗ | ↗ | ∿ | ↗ |
| 6700-6900 | — | ↗ | ↗ | ↗ | — | ∿ | Λ | Λ |
| 6900-7100 | ↘ | ↗ | ↘ | ↘ | ↗ | ↗ | ↗ | ↘ |

At the 2nd head rise sequence (ca. min. 2570 - 2950), *i* and *Q* rose (though at different proportions). The LVDT and *σ'* increased. With the head constant *i* stayed constant and *Q* substantially dropped, while the LVDT trended upward and *σ'* roughly formed an arch.

On the AE, this 2nd head rise sequence was seen in the BH as a drop (min. 2700 – 2900) that gave place to a rise when the head got constant. This BH rise peaked at ca. min 3150 (shortly after *Q* and while *σ'* peaked) and was followed by a long (ca. 1000 min.) downward slope. At min 2700 the WG spiked (peaking at ca. min. 2780 and 2970) and, once the head rise stopped, dropped and entered an irregular oscillatory phase. The TH behaved similarly to the WG, but in advance – practically at the same time as the head tank rise began, the TH spiked (peaks at min. 2670 and 2980, with a trough in between). When the head was made constant the TH produced irregular (though likely meaningful) oscillations.

The 3rd head rise sequence (min. 3903 – 4078) began with the *σ'* entering a downward slope that became less steep by minute 5000 and lasted until ca. min. 5500. *Q* and *i* began rising at ca. min. 4050 (ca. 150 min. after the head rise began) and peaked ca. 150 minutes after the head tank lift ended (ca. min. 4200). *Q* and *i* then notably dropped and stayed so until around min. 5500. The LVDT kept its slight upward trend, with a step up at ca. min. 4150.

At ca. min 5500, *σ'*, *Q* and *i* show a substantial rise (for *Q* and *i* of the largest magnitude throughout the test, and for *σ'* just second to the seen in the consolidation phase). By about min. 5700 for *Q* and *i* and 5800 for *σ'*, they entered a downward slope that by min. 6850 give place to still another steep rise. Then, consecutively at ca. min. 6850, 6960 and 7030, *Q, i and σ'* began a drop that lasted until data recording ended at min. 7050.

On the AE, during this 3rd head rise sequence the BH stayed nearly constant throughout the head rise and, after the head rise ended, sloped upwards and formed with to two rough arches. From ca. min. 5800 onwards the BH undulated trending upward. On the WG, the 3rd head rise began an upward trend that accentuated shortly after the head stabilised(min. 4100), troughed at ca. min 4200 (correspondence to a movement of *Q* and *i*) and from min. 4450 on sloped downward. At ca. min 5250 WG locally peaked and sloped down, spiking at ca. min. 5850, and then roughly stabilised until a spike at ca. min. 6850. With the lowering of the head tank (min. 6915 - 6962) it rose until the end of the test.

Once this 3rd head rise ceased, the TH showed a local spike that by min. 4200 subsided and became relatively irregular (approximating the observed after the previous head rises). By min 5300 the TH spiked (shortly after a spike on the WG and ca. 100 min. before a notable rise on *Q* and *i*) and then got more irregular, with a slight and rough upward trend. At ca. min 6800 – 6900 the TH increased and, with the head lowering, sloped downward. An erosional pipe or preferential flow pathway was recognised at ca. min. 5250.

### *S3T1*

Test performed between 25.10.2019 and 30.10.2019. While calibrating the s test the signal from the hydrophones was put in question due to the amount of noise being generated. After investigating the matter, the connector of the bottom hydrophone was re-done. This improved the signal but still did not eliminate the problem, which was nonetheless considered sufficient to proceed with the test. Also, it should be noted that this test was terminated somewhat differently from the others, with the water supply (tap) being closed and the head tank kept at a constant height and left to passively drain (through the sample). This was an upward flow test.

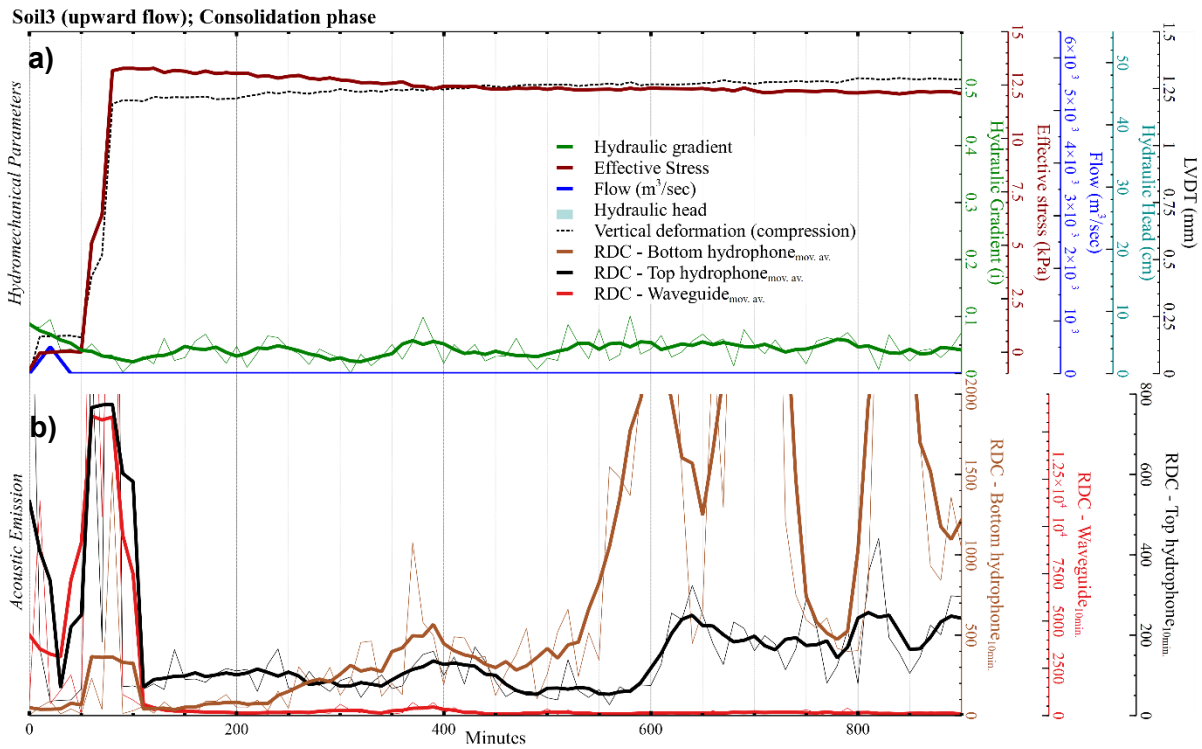


*Figure 4-9. Combined plot of the measured hydromechanical parameters (a) and AE (b) of S3T1 (consolidation phase) in the time domain. Each parameter has an independent vertical axis with the same colour of the plotted curve (e.g. the blue line represents flow rate and corresponds to the blue vertical axis). The LVDT data indicates compression of the sample – a reduction of volume is reflected as an increased LVDT value (in millimetres). Thin lines represent raw data of variables shown with the same colour in thicker lines, which are moving averages.*

*Table 17. Summary of main general trends observed over time during the consolidation phase of test S3T1. Key to symbols in Table 35.*

S3T1 – Consolidation phase

| Time (minutes) | σ' | *i* | LVDT (compression) | BH | WG | TH |
|---|---|---|---|---|---|---|
| **0-100** | ↗ | — | ↗ | ∧ | ∧ | ∧ |
| **100-500** | ↘ | — | ↗ | ↗ | ∿ | ∿ |
| **500-900** | — | — | ↗ | ↗ | — | ↗ |

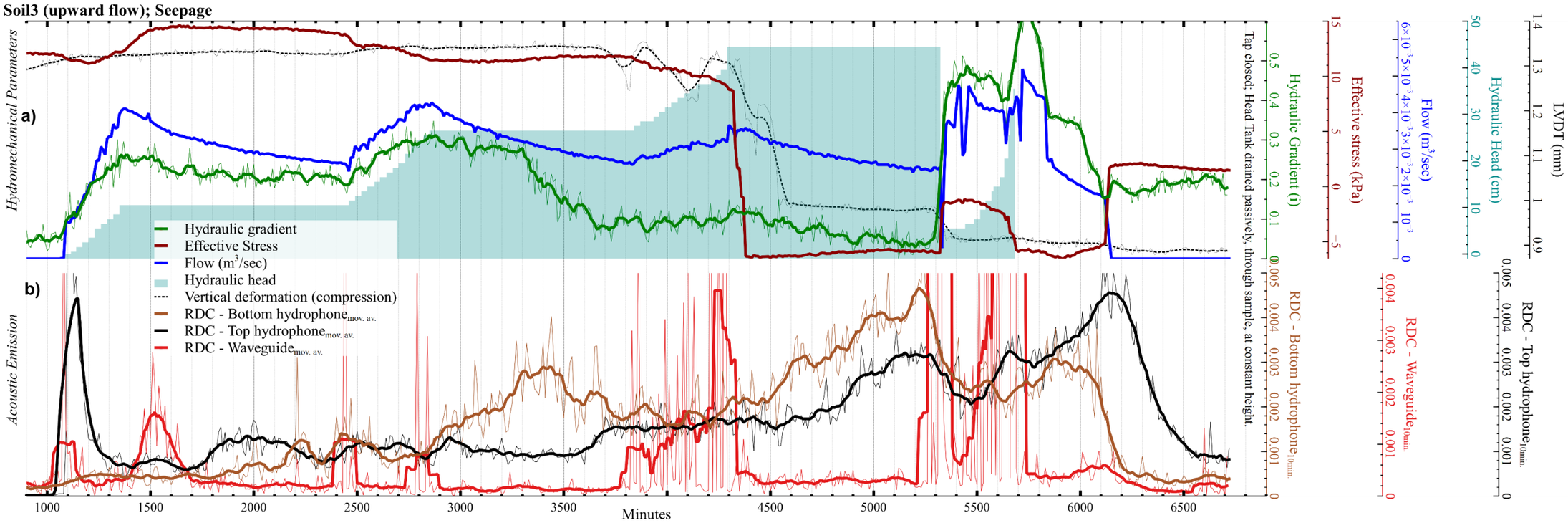


*Figure 4-10. Combined plot of the measured hydromechanical parameters (a) and AE (b) of S3T1 (post consolidation phase) in the time domain. Each parameter has an independent vertical axis with the same colour of the plotted curve (e.g. the blue line represents flow rate and corresponds to the blue vertical axis). The LVDT data indicates compression of the sample – a reduction of volume is reflected as an increased LVDT value (in millimetres). Thin lines represent raw data of variables shown with the same colour in thicker lines, which are moving averages.*

*Table 18. Summary of main general trends observed over time during the seepage test (post-consolidation) phase of test S3T1. Key to symbols in Table 35.*

S3T1 – Seepage test (post-consolidation)

| Time (minutes) | Hydraulic head | σ' | Q | i | LVDT (compression) | BH | WG | TH |
|---|---|---|---|---|---|---|---|---|
| 900-1400 | ↗ | ↘ | ↗ | ↗ | ↗ | ↗ | Λ | Λ |
| 1400-2400 | — | ⌒ | ↘ | ↘ | — | ↗ | Λ | ∿ |
| 2400-2900 | ↗ | ↘ | ↗ | ↗ | ↗ | ∿ | ∿ | Λ |
| 2900-3700 | — | — | ↘ | ↘ | — | ↗ | ↗ | — |
| 3700-4300 | ↗ | ↘ | ↗ | — | ∿ | ∿ | ↗ | ∿ |
| 4300-4600 | — | ↘ | ↘ | ↘ | ↘ | ↗ | ∿ | ∿ |
| 4300-5200 | — | ∿ | ↘ | ↘ | — | ↗ | ∿ | ↗ |
| 5200-5400 | ↘ | ↗ | ↗ | ↗ | ↘ | ↘ | Λ | ↘ |
| 5400-5700 | ↗ | ↘ | ∿ | ↗ | — | ∿ | Λ | ↗ |
| 5700-6700 | — | ↗ | ↘ | ↘ | ↘ | ↘ | ∿ | ↗ |

**S3T1 Consolidation phase**

In Figure 4-9 and Table 17 the consolidation phase of test S3T1 is shown. The hydromechanical variables showed an initial rise at about min. 10, corresponding to the [empty] lever beam touching the vertical loading rod. This affected the AE (Figure 4-9b) causing consecutive spikes on the sensors - noting that the moving average (the thicker lines; smoother signal) causes the apparent signal to be "broadened".

The *σ'* and LVDT rose in accordance with the vertical stress increase. By min. 80 these curves nearly flattened, although *σ'* and LVDT respectively formed slightly upward and downward slopes. On the AE, the vertical loading corresponded to spikes in all three sensors. After the loading ended, The AE drops, although TH and BH later (without external forcing) rise. From after loading until ca. min 1100, *Q* and *i* remained at baseline while the LVDT showed a constant upward trend and *σ'* stayed practically constant (with a slight downward trend, possibly related to wall friction, as will be explored in the Discussion section).

After adding the soil to the permeameter turbidity was observed in the water volume below the sample. The material in suspension (apparently mostly silt from the silica flour used in composing the sample) settled over time and seems to have caused the signal of the BH (and to a lesser extent, of the TH – less subject to this effect due to being at the top and in a smaller water volume above the sample) after the vertical loading.

**S3T1 Seepage test (post-consolidation)**

As seen in Figure 4-10 and Table 18, with the head rising at min. 1083, *Q* and *i* increased until the head rise ended, when they reverted to a downward slope. When the head rise began the LVDT interrupted the upward slope it was on and plateaued until the next head rise sequence, while the *σ'* dropped and by the middle of the head rise reverted into an increase that persisted until ca. min 1500. In this test *Q* stayed relatively low in comparison with other tests being discussed – in this test it reached a maximum of ca. $5*10^{-3}$ $m^3$/sec.

The WG spiked with the 1st head rise and again ca. 50 min. after the head stabilised – spikes at ca. min. 1100 and 1500. Particle movement (or early-stage internal erosion) was visually recognised at ca. min. 1100. The BH increased roughly with the head rise and then plateaued. The TH peaked with this head rise (to its highest values in this test; ca. min 1100) and dropped to a rough baseline, increasing again at min. 1800.

The 2nd head increase sequence of this test (min 2460 - 2850) had about the same effect on *Q* and *i* as the previous one, although less accentuated. The *σ'* decreased and flattened when the head rise stopped, while the LVDT slightly increased and flattened afterwards as well. The AE during the 2nd head rise correlated with a WG peak at its start and a second one at its end.

The hydrophones rose slightly. Once the head rise stopped the BH entered an upward slope that peak by min. 3450.

3rd head rise took place from min. 3840 to 4290, with the last step being of 5cm (while the other steps were of 1cm). In it, *Q* rose but less pronouncedly than in the previous head rise – a pattern of the flow rate increasing at progressively lesser extents with successive head rise cycles was observed. The *σ'* once again dropped, which became precipitous by the end of the head rise and bottomed until ca. min. 5300. The LVDT showed an oscillatory behaviour during the head rise that, once the head rise stopped, was replaced by a sharp drop that flattened at min 4550. The *i* during this head rise stayed practically flat and assumed a gentle downward slope once it ended.

On the AE, the 3rd head rise sequence did not noticeably affect the TH, but ca. 300 minutes after the head stabilised the TH entered an upward slope. The BH oscillated during this head rise and trended upwards when the head stabilised. The WG increased roughly in proportion to the head rise sequence and, when the head stopped being risen, dropped to a rough baseline – shape like the *σ'* but with a ca. 50 min. time offset.

The head drop at min 5322 was followed by a sharp rise in *σ'*, *i* and *Q*. The LVDT saw a drop that for the rest of the test gave place to a slight downward trend. When the head was quickly raised (min. 5442 to 5675), *i* increased and dropped again at the final head lowering, after which, when the head tank passively drained, it transitioned to a downward slope that stabilized by min. 6100. The *σ'* slightly dropped during the head rise and then, when the head was lowered, dropped sharply, slightly oscillated, and at ca. min 6100 vertically rose and met a plateau that was kept until data recording stopped. *Q* first rose at the tank drop of min. 5322, then remained relatively constant during the following head rise and, after the last head reduction, rose again and followed a trend like that of *i*.

With the head drop of min. 5322 the TH decreased, troughed, and with the next head rise reached a local peak; with the tank draining the TH trended upwards and peaked at ca. min. 6100. The WG showed two sharp peaks, at the head tank drop and over the head rise.

### *S4T1*

Test performed 05.11.2019 - 09.11.2019. During the sensor calibration phase of this test, noise reduction was attempted by re-building cable connectors. This operation did seem to improve the signal and minimise seemingly random voltage spikes. Both hydrophones showed a nearly identical and relatively low signal-to-noise ratio. This was an upward flow test.

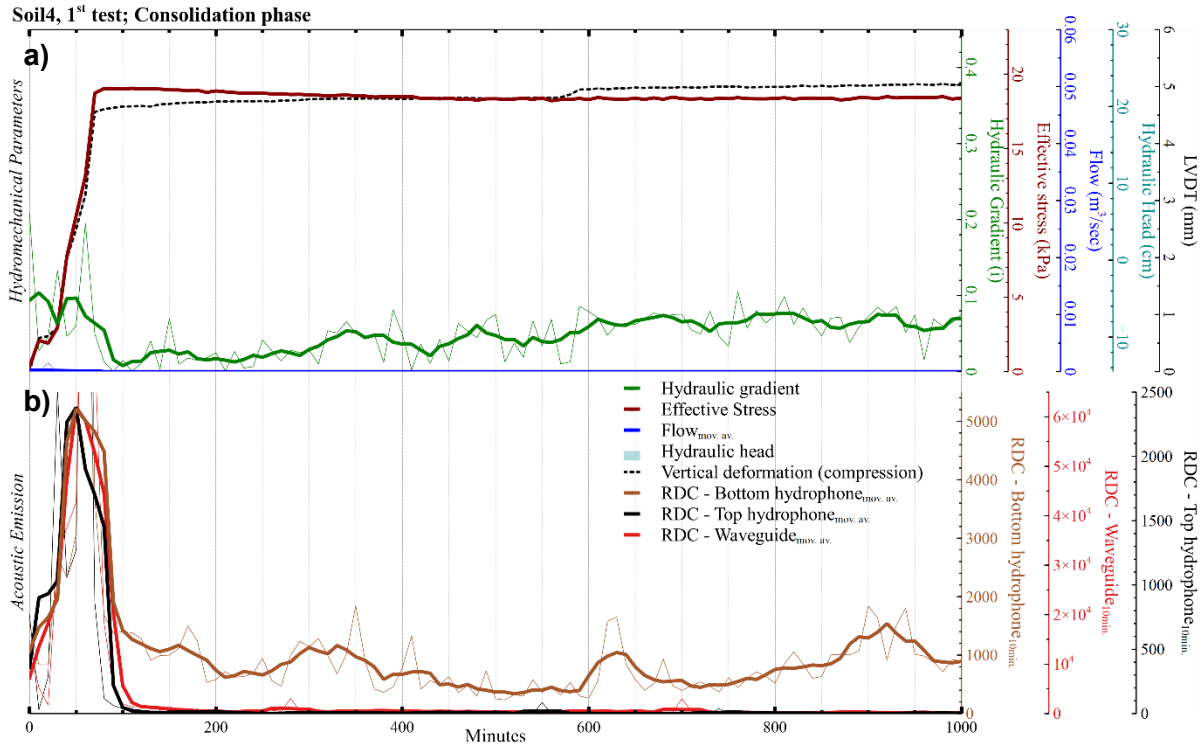


*Figure 4-11. Combined plot of the measured hydromechanical parameters (a) and AE (b) S4T1 (consolidation phase) in the time domain. Each parameter has an independent vertical axis with the same colour of the plotted curve (e.g. the blue line represents flow rate and corresponds to the blue vertical axis). The LVDT data indicates compression of the sample – a reduction of volume is reflected as an increased LVDT value (in millimetres). Thin lines represent raw data of variables shown with the same colour in thicker lines, which are moving averages.*

*Table 19. Summary of main general trends observed over time during the consolidation phase of test S4T1. Key to symbols in Table 35.*

S4T1 – Consolidation phase

| Time (minutes) | σ' | *i* | LVDT (compression) | BH | WG | TH |
|---|---|---|---|---|---|---|
| **0-200** | ↗ | ↘ | ↗ | Λ | Λ | Λ |
| **200-1000** | — | ↗ | ↗ | ∿ | ∿ | — |

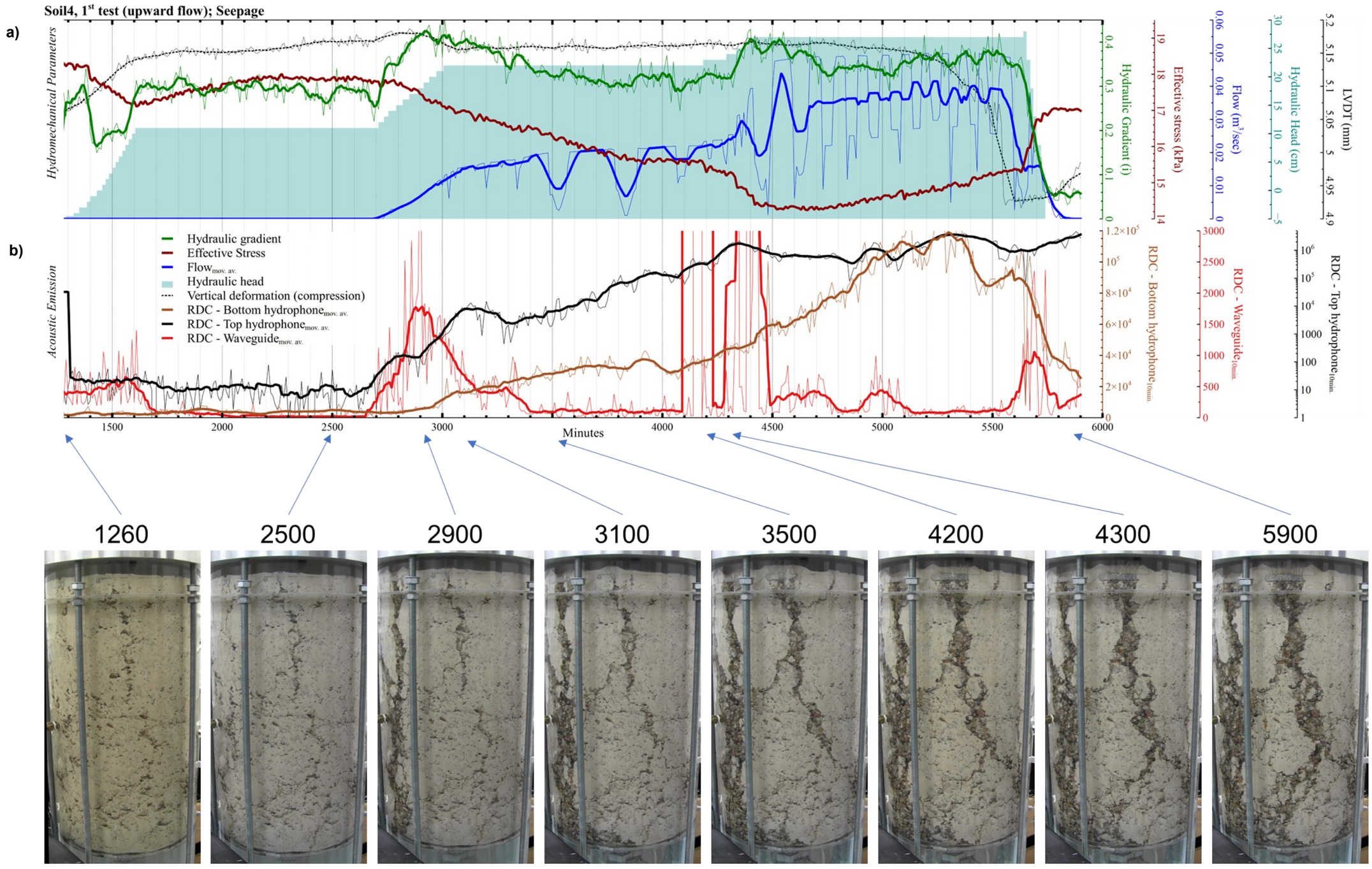


*Figure 4-12. Combined plot of the measured hydromechanical parameters (a) and AE (b) S4T1 (post consolidation phase) in the time domain. Each parameter has an independent vertical axis with the same colour of the plotted curve (e.g. the blue line represents flow rate and corresponds to the blue vertical axis). The LVDT data indicates compression of the sample – a reduction of volume is reflected as an increased LVDT value (in millimetres). Thin lines represent raw data of variables shown with the same colour in thicker lines, which are moving averages. Picture series below shows soil specimen at different points during the test (elapsed minutes indicated above each image).*

## S4T1 – Consolidation phase

In Figure 4-11 and Table 19 the consolidation phase of S4T1 is shown. Weight addition to the vertical loading system corresponded to steps LVDT and *σ'*. *Q* stayed unaltered (although with a small movement at min. 30) and *i* slightly trended downward until the loading ended. Spikes in all three AE sensors corresponded to the loading steps (Figure 4-11b), getting progressively higher. After the loading ended the WG and TH dropped to zero but the RDC while the BH oscillated.

## S4T1 – Seepage test (post- consolidation)

With the head increase, *σ'* dropped, LVDT rose, while *i* also rose but locally troughed between middle and end of the head rise. With the head constant, *σ'* formed an arch while the LVDT rose and *i* roughly stabilised (Figure 4-12, Table 20).

*Table 20. Summary of main general trends observed over time during the seepage test (post-consolidation) phase of test S4T1. Key to symbols in Table 35.*

S4T1 – Seepage test (post-consolidation)

| Time (minutes) | Hydraulic head | σ' | Q | i | LVDT (compression) | BH | WG | TH |
|---|---|---|---|---|---|---|---|---|
| 1300-1600 | ↗ | ↘ | — | ∿ | ↗ | ∿ | ∿ | — |
| 1600-2700 | — | ⌒ | — | ∿ | ↗ | ∿ | ∿ | — |
| 2700-3000 | ↗ | ↘ | ↗ | ↗ | ⌒ | ↗ | ↗ | ↗ |
| 3000-3800 | — | ↘ | ↗ | ↘ | ∿ | ↗ | ↘ | ∿ |
| 3800-4500 | ↗ | ↘ | ↗ | ↗ | ∿ | ↗ | ∧ | ∧ |
| 4500-5600 | — | ↗ | ∿ | ∿ | ↘ | ∧ | ∿ | ∧ |
| 5600-5900 | ↘ | ↗ | ↘ | ↘ | ↗ | ↘ | ∧ | ↘ |

During the 2nd head rise, the LVDT formed an arch, *σ'* decreased, *i* increased and *Q* showed a flow increase (its first non-null in this test). With the head constant, the LVDT stayed steady, *σ'* and *i* decreased and *Q* increased (although somewhat irregularly). In the 3rd head rise the hydromechanical parameters essentially repeated the seen in the 2nd head rise, except for the LVDT, which stayed about constant. Between the 3rd head rise and the head drop, *σ'* increased (opposite to the seen in the other constant-head intervals), *i* oscillated once (drop-rise), *Q* tended to a stable rate and the LVDT sloped downwards, which got accentuated by min 5200. When the head dropped, *σ'* and LVDT reverted to an increase while *Q* and *i* decreased and then plateaued.

On the AE (Figure 4-12b), the hydrophones essentially did not react until the second head rise (which was between min. 2710 – 3005) - coinciding with the first *Q* increase. At ca. min 2900 both hydrophones clearly started rising. Particle movement (or internal erosion) was noticed at ca. min. 2950. For the rest of the test both hydrophones basically showed continually

increased signals – the BH followed an upward slope that was accentuated by the 3rd head rise while the TH, after rising by the middle of the 2nd head rise, stayed roughly constant between this and the following head rise and by min 3900 also entered an upward slope (although more irregularly than the BH). When the head was dropped both hydrophones showed a signal decrease. The WG showed significant signals every time the head was manipulated, with some activity between the 2nd and 3rd head rises and after the final head drop.

### *S4T2*

Test performed between 06.12.2019 and 10.12.2019. After specimen composition and vertical loading, the effect of suspended particles settling and its change of intensity (amount of particles in suspension) over time influencing the AE of the BH was once again verified. Before the seepage test, the signal from both hydrophones was deemed quite stable (low noise). This test was intended as a repetition of test S4T1. This was an upward flow test.

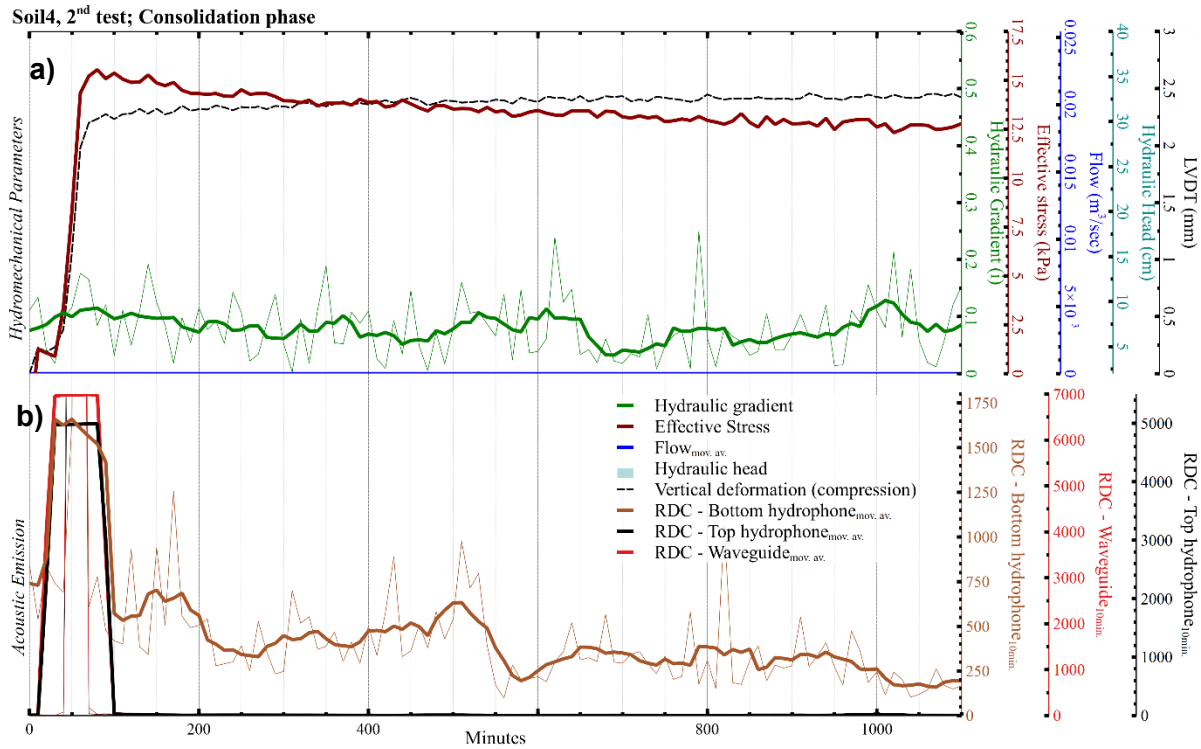


*Figure 4-13. Combined plot of the measured hydromechanical parameters (a) and AE (b) of S4T2 (consolidation phase) in the time domain. Each parameter has an independent vertical axis with the same colour of the plotted curve (e.g. the blue line represents flow rate and corresponds to the blue vertical axis). The LVDT data indicates compression of the sample – a reduction of volume is reflected as an increased LVDT value (in millimetres). Thin lines represent raw data of variables shown with the same colour in thicker lines, which are moving averages.*

*Table 21. Summary of main general trends observed over time during the consolidation phase of test S4T2. Key to symbols in Table 35.*

S4T2 – Consolidation phase

| Time (minutes) | σ' | *i* | LVDT (compression) | BH | WG | TH |
|---|---|---|---|---|---|---|
| **0-100** | ↗ | ∿ | ↗ | Λ | Λ | Λ |
| **100-1000** | ↘ | ∿ | ↗ | ∿ | — | — |

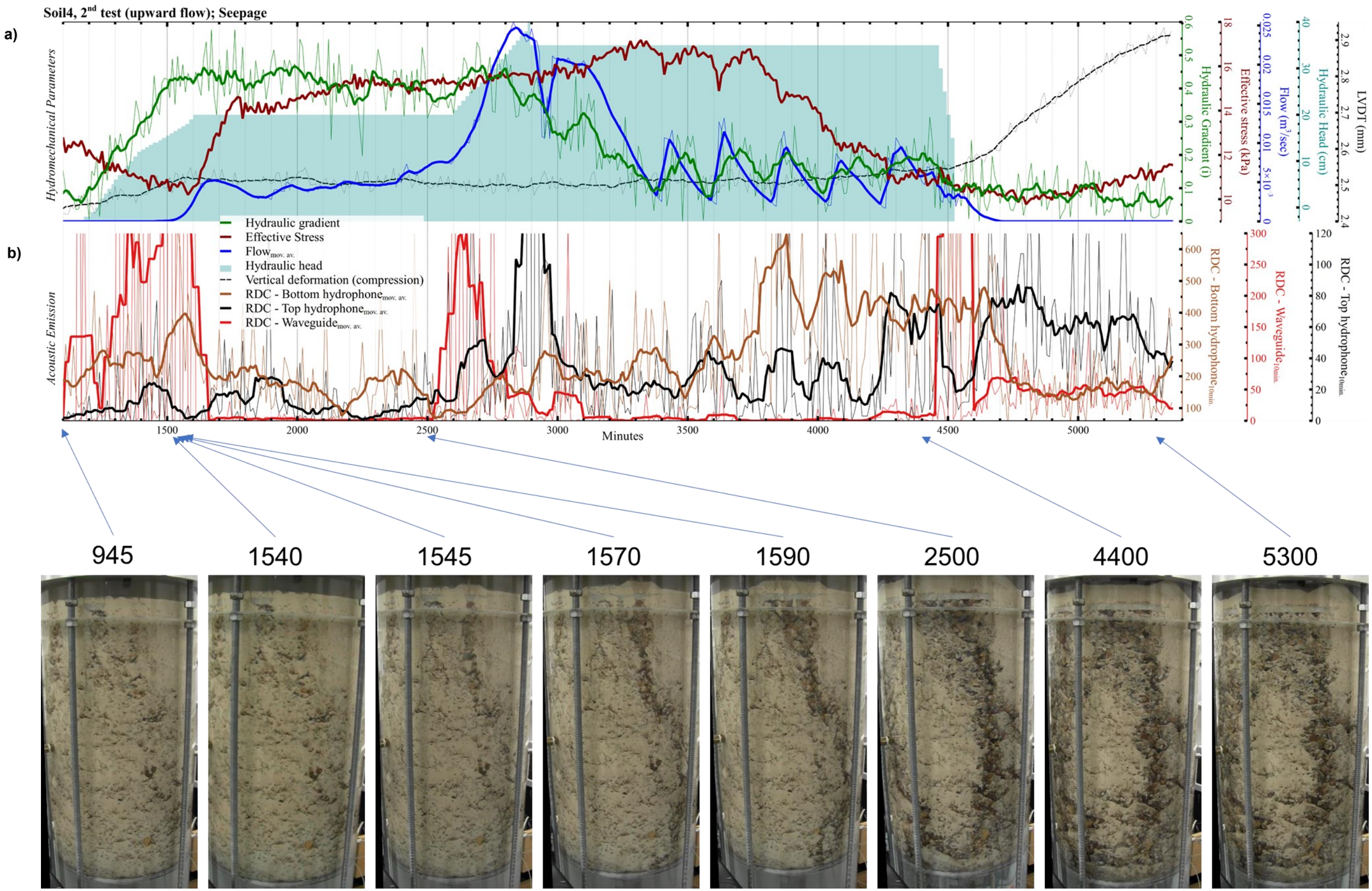


*Figure 4-14. Combined plot of the measured hydromechanical parameters (a) and AE (b) ofS4T2 (post consolidation phase) in the time domain. Each parameter has an independent vertical axis with the same colour of the plotted curve (e.g. the blue line represents flow rate and corresponds to the blue vertical axis). The LVDT data indicates compression of the sample – a reduction of volume is reflected as an increased LVDT value (in millimetres). Thin lines represent raw data of variables shown with the same colour in thicker lines, which are moving averages. Picture series below shows soil specimen at different points during the test (elapsed minutes indicated above each image).*

## S4T2 – Consolidation phase

In Figure 4-13 and Table 21 the consolidation phase of test S4T2 is shown. With vertical loading the LVDT and *σ'* increased. *Q* and *i* stayed unaltered, the latter with minor oscillations. Spikes in the AE of all three sensors corresponded to the loading (Figure 4-13b). After the loading ended the WG and TH dropped to baseline but the BH kept oscillating considerably.

The settling of material (silt) in suspension at the water volume below the sample was once again observed and seemed to produce the post-loading AE signal of the BH.

## S4T2 – Seepage test (post-consolidation)

With the 1st head rise, LVDT and *i* increased while *σ'* decreased. *Q* began rising by the end of the head rise. With the head constant, LVDT and *i* remained roughly stable (although with a slight downward trend and broad oscillations) and *Q* increased, with a rate that became less accentuated by min. 1700, which was also seen on the *σ'*.

On the AE, The WG, similarly to the seen in S4T1, peaked every time the head was manipulated, staying more active after the final head drop than between the head rises. The TH behaved analogously to the WG, but with a more irregular curve that denoted detection of more subtle phenomena while the head was constant – it notably showed an increase in almost exact correspondence with the initial rise in *Q*. Particle movement (or internal erosion) was noted at ca. min. 1460, which by ca. min. 1600 had evolved to an erosional pipe or preferential flow pathway. The BH also peaked during the 1st head rise and then dropped, oscillating roughly like *i* until the 2nd head rise, when it increased.

*Table 22. Summary of main general trends observed over time during the seepage test (post-consolidation) phase of test S4T2. Key to symbols in Table 35.*

S4T2 – Seepage test (post-consolidation)

| Time (minutes) | Hydraulic head | σ' | Q | i | LVDT (compression) | BH | WG | TH |
|---|---|---|---|---|---|---|---|---|
| 1100-1600 | ↗ | ↘ | ↗ | ↗ | ↗ | ↗ | ↗ | ↗ |
| 1600-2600 | — | ↗ | ↗ | ∿ | ∿ | ∿ | — | ∿ |
| 2600-2900 | ↗ | ∿ | ↗ | ↘ | ∿ | ↗ | Λ | Λ |
| 2900-3400 | — | ↗ | ↘ | ↘ | ↗ | ∿ | ↘ | ↘ |
| 3400-4400 | — | ↘ | ∿ | ∿ | ↗ | ↗ | ∿ | ∿ |
| 4400-5400 | ↘ | ∿ | ↘ | ↘ | ↗ | ↘ | Λ | ∿ |

With the 2nd head rise *Q* drastically increased and peaked, while *σ'* and the LVDT stayed practically unchanged and. By the middle of the head rise *i* began dropping. When the head got constant *Q* began dropping (as drastically as it had increased) and *σ'* sloped upward. Between ca. min 3300 and the head drop, *Q* and *i* showed a rather regular undulatory

behaviour, which was also seen on *σ'* with the difference of it sloping downward from ca. min 3800 until the head drop. With the head drop, *Q, σ'* and *i* decreased, while the LVDT notably increased until data recording stopped.

Between the 2nd head rise and the head drop the TH and BH showed an oscillatory behaviour comparable to the oscillations seen in *Q* and *i,* with the BH showing an amplitude increase by ca. min. 3800 (nearly parallel to the decrease in *σ'*); an equivalent amplitude increase was seen on the TH at ca. min. 4200 (nearly when *σ'* stopped decreasing). After the head drop (and after a WG peak) the BH and TH respectively decreased and increased.

### *S4T3*

This test was done between 13.12.2019 and 17.12.2019. It was a progression of the tests made with Soil 4 with the difference of having a higher vertical load (ca. 50% higher) than S4T1 and S4T2. In preparation for the test run and with the soil specimen already inside the permeameter, the amplifiers used for the load cells were damaged (i.e. water-induced electrical shortcut). The damaged devices were replaced. However, (re-)calibration of the load gauging system could not be done without removing the load cells from the apparatus (which by this point would require a near complete disassembly, including sample de-constitution). Hence, it was decided to run the test and calibrate the equipment afterwards – the gain/offset values from the calibration were [retroactively] applied to the collected data. This was an upward flow test.

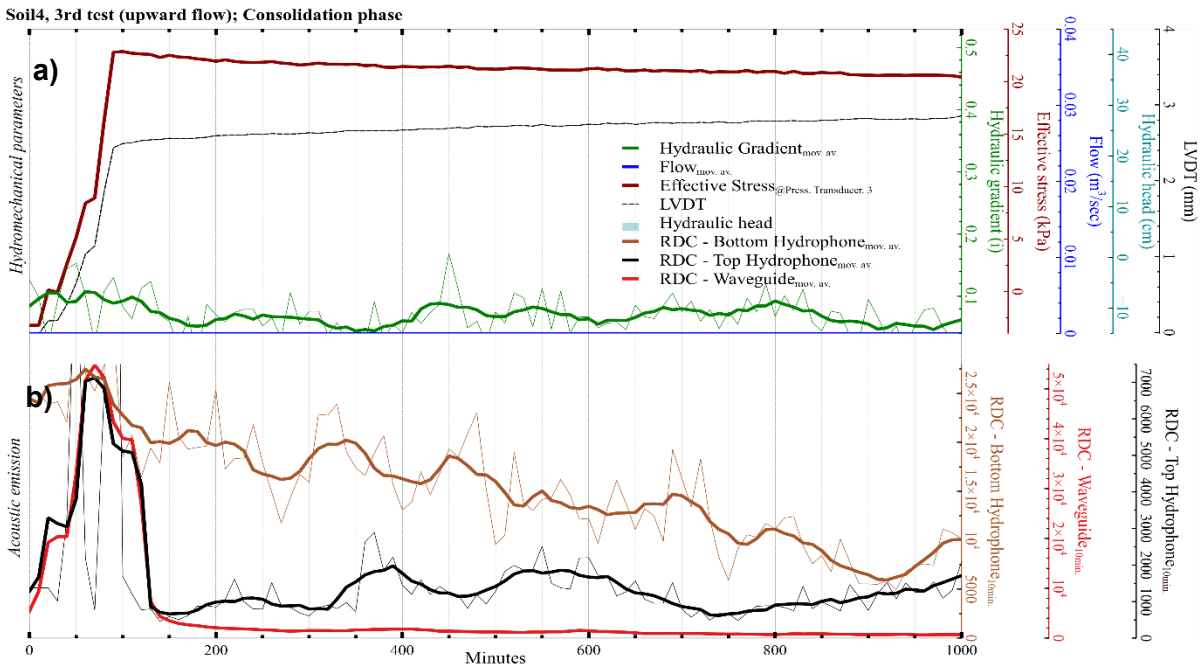


*Figure 4-15. Combined plot of the measured hydromechanical parameters (a) and AE (b) of S4T3 (consolidation phase) in the time domain. Each parameter has an independent vertical axis with the same colour of the plotted curve (e.g. the blue line represents flow rate and corresponds to the blue vertical axis). The LVDT data indicates compression of the sample – a reduction of volume is reflected as an increased LVDT value (in millimetres). Thin lines represent raw data of variables shown with the same colour in thicker lines, which are moving averages.*

*Table 23. Summary of main general trends observed over time during the consolidation phase of test S4T3. Key to symbols in Table 35.*

S4T3 – Consolidation phase

| Time (minutes) | σ' | *i* | LVDT (compression) | BH | WG | TH |
|---|---|---|---|---|---|---|
| 0-100 | ↗ | ↘ | ↗ | Λ | Λ | Λ |
| 100-1000 | ↘ | ∿ | ↗ | ↘ | — | ∿ |

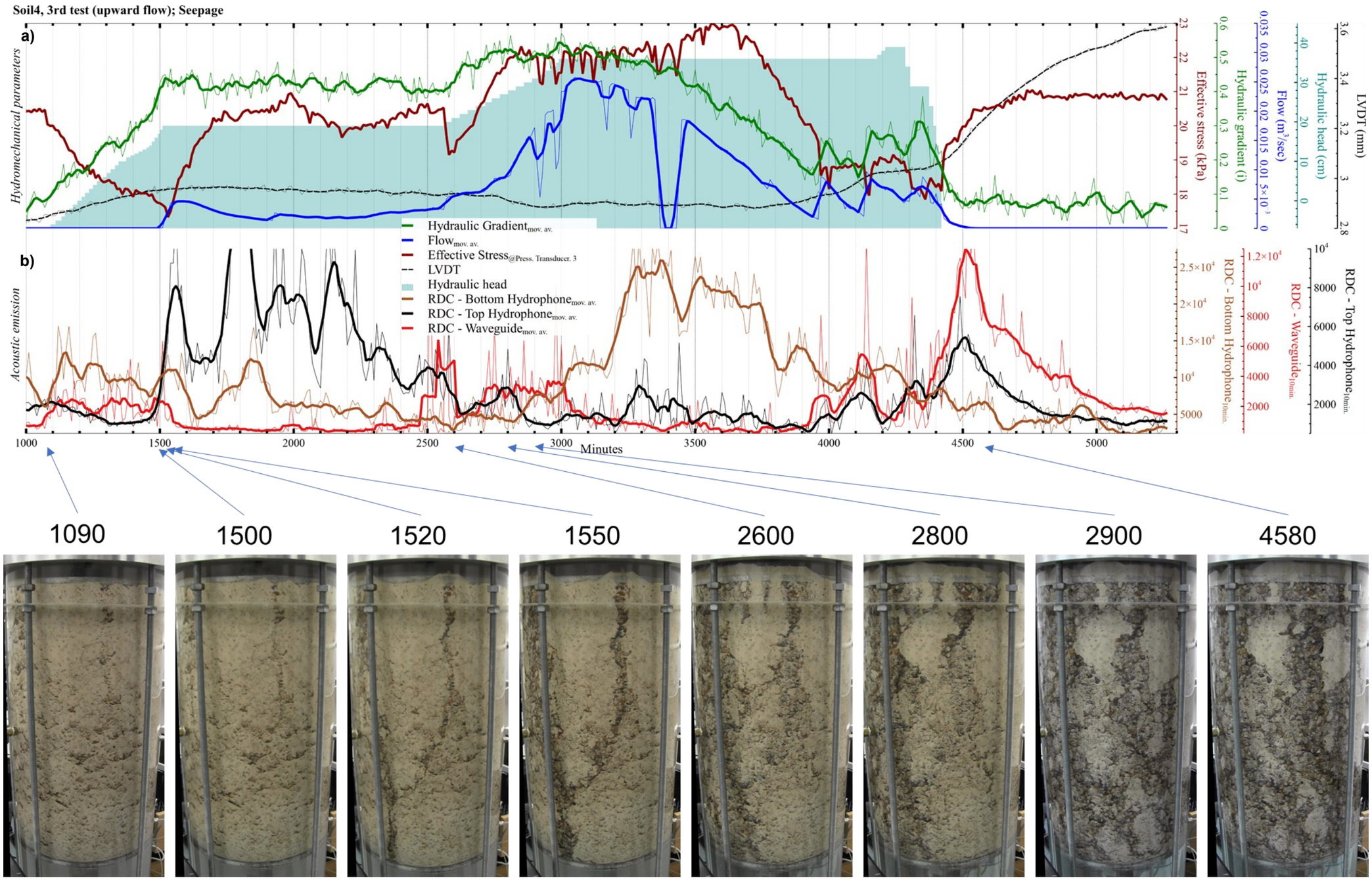


*Figure 4-16. Combined plot of the measured hydromechanical parameters (a) and AE (b) of S4T3 (post consolidation phase) in the time domain. Each parameter has an independent vertical axis with the same colour of the plotted curve (e.g. the blue line represents flow rate and corresponds to the blue vertical axis). The LVDT data indicates compression of the sample – a reduction of volume is reflected as an increased LVDT value (in millimetres). Thin lines represent raw data of variables shown with the same colour in thicker lines, which are moving averages. Picture series below shows soil specimen at different points during the test (elapsed minutes indicated above each image).*

## S4T3 – Consolidation phase

In Figure 4 18 and Table 23, the consolidation phase of S4T3 is represented. With addition of vertical load to the sample, *σ'* and LVDT showed marked increases. The *i* also slightly rose as pore-pressure dissipated/equalised through the sample. Once the vertical load ceased to increase, the LVDT entered a slight upward slope while the *σ'* sloped downward (essentially due to more stress being transferred to the bottom LC, partially overcoming wall friction).

The increase in vertical stress caused spikes in all three AE sensors. Turbidity and settling of silts in the water volume outside of the sample was once again observed and seemed to cause the signal observed in the BH and, to a lesser extent, the TH.

## S4T3 – Seepage test (post-consolidation)

As seen in Figure 4-16 and Table 24, the 1st head rise (ca. min 1091-1510) correlated with increases in the LVDT and *i* values and a decrease in *σ'*. When the head rise ceased, an initial *Q* increase was observed (locally peaking at ca. min. 1600), as well as an increase of *σ'* and a near stabilisation of *i* and the LVDT values – the LVDT formed a slight arch during the constant head interval. By ca. min 1700 and the following head rise *σ'* stopped rising and fluctuated (plateau, drop, rise).

*Table 24. Summary of main general trends observed over time during the seepage test (post-consolidation) phase of test S4T3. Key to symbols in Table 35.*

S4T3 – Seepage test (post-consolidation)

| Time (minutes) | Hydraulic head | σ' | Q | i | LVDT (compression) | BH | WG | TH |
|---|---|---|---|---|---|---|---|---|
| 1000-1500 | ↗ | ↘ | ↗ | ↗ | ↗ | ∿ | ∿ | ∿ |
| 1500-1600 | — | ↗ | ↗ | ∿ | — | Λ | Λ | Λ |
| 1600-2200 | — | ⌒ | ∿ | ∿ | — | ∿ | ∿ | ∿ |
| 2200-2550 | — | ↗ | ↗ | ∿ | — | ↘ | ↗ | ↘ |
| 2550-3000 | ↗ | ↗ | ↗ | ↗ | ↘ | ↗ | ∿ | Λ |
| 3000-3300 | — | ∿ | ↘ | ↘ | — | ↗ | ↘ | ↗ |
| 3300-3500 | — | ↗ | V | ↘ | — | V | V | ↘ |
| 3500-3900 | — | ↘ | ↘ | ↘ | ↗ | ↘ | ∿ | ↘ |
| 3900-4150 | — | ↘ | ∿ | ∿ | ↗ | ∿ | Λ | Λ |
| 4150-4350 | ∿ | ↘ | ∿ | ∿ | — | ↘ | ↗ | ↗ |
| 4350-5250 | ↘ | ↗ | ↘ | ↘ | ↗ | ↘ | Λ | Λ |

During this 1st head rise, hydrophones showed oscillations (especially the BH). Outstandingly, when *Q* showed its first measured increase, the TH spiked - this was also observed in the BH but less notably so. While the head was kept constant the TH signal spiked several times and sloped down from ca. min. 2150 onwards (parallel to a *σ'* trough). Particle movement (or early-

stage internal erosion) was noted by ca. min. 1490, which quickly (by ca. min. 1530) evolved an erosional pipe or preferential flow pathway.

The WG, once again (similarly to other tests, as described) showed elevated signals when the head was manipulated. It also became notably active from ca. min. 3900 onwards (correlating with an apparent clog-and-flow interval, as observed in the hydromechanical parameters – elaborated in the Discussion chapter) and slowly dropped after its peak following the head drop.

With the 2nd head rise (min. 2565 - 2990), *σ'*, *i* and *Q* increased – by ca. min. 2700 *σ'* and *i* roughly stabilised, correlating to an LVDT drop. On the AE, BH and TH showed an increase during this head rise. At ca. min 2700, the BH rise got accentuated while the TH showed a drop.

After the head was kept constant after the 2nd head rise, *Q* and *i* decreased while *σ'* increased – at ca. min. 3400 *Q* and *σ'* troughed locally (more accentuated on *Q*). By ca. min. 3650 the LVDT values started increasing and *σ'* decreasing. At min 3950 a sharp rise on *Q* and *i* and a sharp drop on *σ'* occurred, after which all these parameters entered a phase of periodic oscillations (*Q* and *i* with a nearly identical profile) that lasted until the next change in head.

On the AE, after the 2nd head rise the BH continued and accentuated the upward trend it was in, with a similar trend seen on the TH. The decrease in *Q* and *i* corresponded to a decrease in the TH and BH. The interval of periodic oscillations seen on *Q, i* and *σ'* corresponded to an overall TH increase and BH decrease (nonetheless with oscillations).

When the head was dropped, *Q* and *i* decreased while *σ'* increased, all three plateauing by min. 4550. After the head drop the LVDT entered an upward slope lasting until the end of data recording.

On the AE, the BH decreased with the head drop, roughly plateauing by min 4700. The TH increased in accordance with the head drop, notably peaking afterwards at about the same time as when the *σ'*, *Q* and *i* plateaued and in synchrony with a pronounced WG peak. From this point on WG and TH slowly decreased until data recording ended.

### *S4T4*

Test performed between 08.01.2020 and 12.01.2020. It was noticed and endorsed by the electronics technician that the behaviour of preamplifiers used with the AE sensors could change over time (e.g. due to temperature), causing the perceived background noise to oscillate. Hence, the detection thresholds have been constantly observed and adjusted accordingly. However, this phenomenon was not fully understood. One related effect was that interpretation of AE data should consider relative changes over time instead of absolute values. This test, which also induced seepage by upward water flow, was a progression of the tests made with Soil 4, having a higher vertical load (ca. 2x) than tests S4T1 and S4T2.

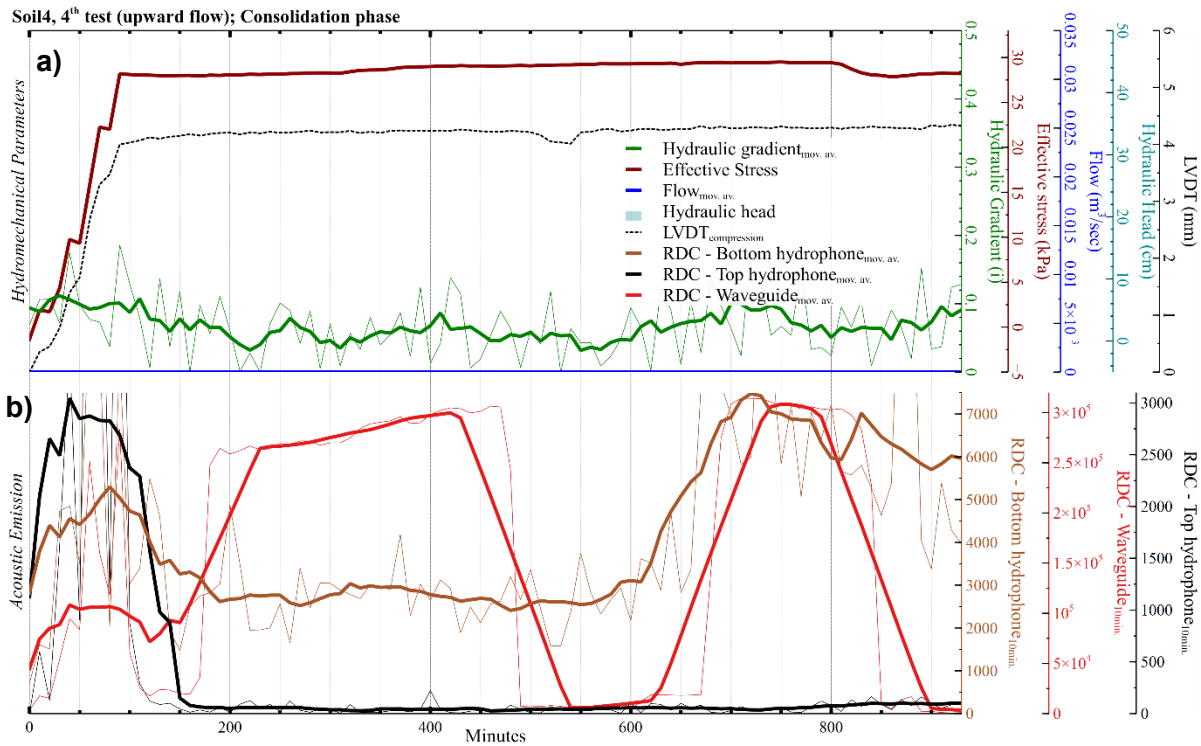


*Figure 4-17. Combined plot of the measured hydromechanical parameters (a) and AE (b) of S4T4 (consolidation phase) in the time domain. Each parameter has an independent vertical axis with the same colour of the plotted curve (e.g. the blue line represents flow rate and corresponds to the blue vertical axis). The LVDT data indicates compression of the sample – a reduction of volume is reflected as an increased LVDT value (in millimetres). Thin lines represent raw data of variables shown with the same colour in thicker lines, which are moving averages.*

*Table 25. Summary of main general trends observed over time during the consolidation phase of test S4T4. Key to symbols in Table 35.*

S4T4 – Consolidation phase

| Time (minutes) | σ' | *i* | LVDT (compression) | BH | WG | TH |
|---|---|---|---|---|---|---|
| **0-100** | ↗ | ∿ | ↗ | Λ | Λ | Λ |
| **100-450** | ↗ | ∿ | — | ↘ | ↗ | — |
| **450-700** | ↗ | ∿ | ∿ | ↗ | ↗ | ∿ |

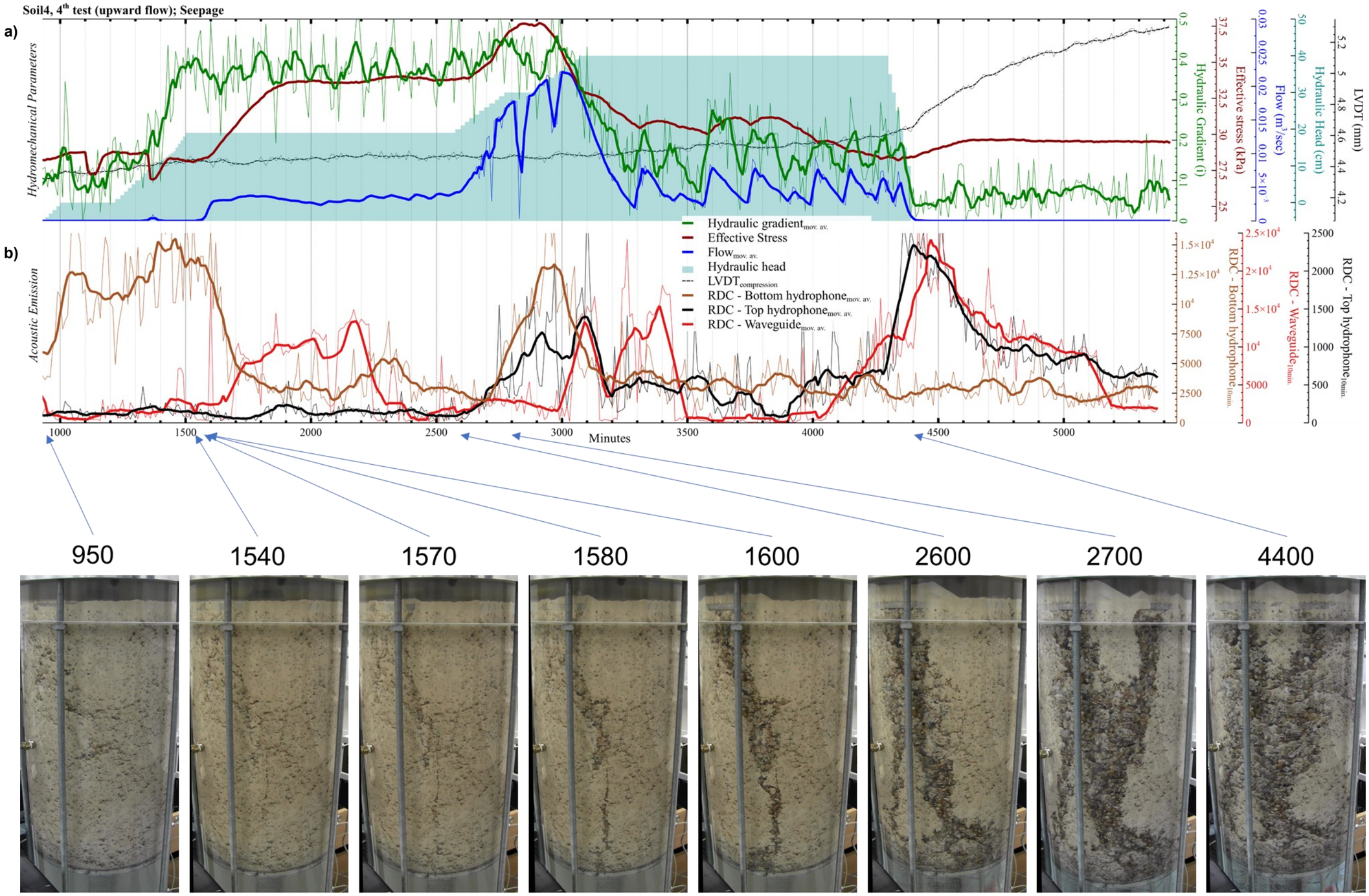


*Figure 4-18. Combined plot of the measured hydromechanical parameters (a) and AE (b) of S4T4 (post consolidation phase) in the time domain. Each parameter has an independent vertical axis with the same colour of the plotted curve (e.g. the blue line represents flow rate and corresponds to the blue vertical axis). The LVDT data indicates compression of the sample – a reduction of volume is reflected as an increased LVDT value (in millimetres). Thin lines represent raw data of variables shown with the same colour in thicker lines, which are moving averages. Picture series below shows soil specimen at different points during the test (elapsed minutes indicated above each image).*

**S4T4 - Consolidation phase**

As seen in Figure 4-17 and Table 25, the *σ'* and LVDT values increased in proportion to the loading steps and *i* slightly varied seemingly due to dissipation of excess pore pressure through the sample.

In the AE (Figure 4-17b), the hydrophones spiked in accordance with the loading, with the BH continuing with a significant signal (in accordance with the idea of settling of fines in suspension producing this AE signal). In the WG, two intervals of relatively high signal occurred at min. 170-490 and 670-850, the second of which corresponding to an increase in the BH. This WG behaviour seemingly related to the increased vertical stress used in this test being high enough to, with a time lag, overcome wall friction more effectively than in previous tests.

**S4T4 – Seepage test (post-consolidation)**

With the 1st head rises (Figure 4-18, Table 26) that ended by min. 1500, *i* and the LVDT showed increases (with *i* locally troughing when the head was momentarily fixed), while *σ'* stayed relatively unchanged (although with oscillations, including two troughs while the head was momentarily fixed). *Q* showed a small peak at ca. min 1360. When the head was made constant (min. 1500), *i* and LVDT roughly plateaued. By min. 1550 *σ'* and *Q* began rising, with the latter stabilising at ca. min. 1600 and the former at ca. min. 1950.

On the AE, this head rise ending by min. 1500 correlated with an elevated BH signal than subsidised by min. 1700. WG and TH showed minor oscillations – the largest of these on the TH corresponding to the small *Q* peak mentioned above. With the head constant, the WG showed a significant increase nearly synchronous with the *σ'* elevation, then decreasing by ca. min. 2250. The TH also increased (albeit comparatively modestly) in correspondence with the *σ'* plateauing. The BH showed a seemingly more irregular curve, with a local peak at ca. min. 2300.

In the following head rise interval (lasting between min. 2575 – 3070 and interrupted between min. 2770 – 2890), *Q* increased accordingly, with the same occurring with *σ'* but with a ca. 50 min. time offset. The LVDT stayed roughly constant and *i* increased during the head rise and decreasing during the head interruption. *σ'* peaked at ca. min. 2900 while *i* and *Q* peaked at ca. min. 3000.

On the AE, this head rise phase was reflected on both hydrophones as a marked rise that peaked at ca. min. 2950 and, on the TH, peaked again at ca. min. 3100 (which was also a WG peak). The start of the head rise was also reflected on the WG but in a less pronounced

manner. When the head was made constant, the WG increased once again (unlike the hydrophones, which kept dropping).

*Table 26. Summary of main general trends observed over time during the seepage test (post-consolidation) phase of test S4T4. Key to symbols in Table 35.*

S4T4 – Seepage test (post-consolidation)

| Time (minutes) | Hydraulic head | σ' | Q | i | LVDT (compression) | BH | WG | TH |
|---|---|---|---|---|---|---|---|---|
| 950-1500 | ↗ | ∿ | — | ↗ | ↗ | ↗ | ∿ | ∿ |
| 1500-2550 | — | ↗ | ↗ | ∿ | — | ↘ | ↗ | ↗ |
| 2500-3050 | ↗ | ∧ | ↗ | ∿ | — | ∧ | ⌒ | ↗ |
| 3050-3500 | — | ↗ | ↘ | ↘ | ↗ | ↘ | ∧ | ∧ |
| 3500-4000 | — | ⌒ | ∿ | ∿ | ↗ | ∿ | ∿ | ∿ |
| 4000-4300 | — | ↘ | ∿ | ∿ | ↗ | ∿ | ↗ | ∿ |
| 4300-4500 | ↘ | ↗ | ↘ | ↘ | ↗ | ∿ | ∧ | ∧ |
| 4500-5400 | — | — | — | ∿ | ↗ | ∿ | ↘ | ↘ |

Very subtle particle movement (or early-stage internal erosion) was observed at ca. min. 1350. This slowly evolved, until by min. 1600 evolved to an erosional pipe or preferential flow pathway, that at ca. min. 2650 gained much intensity.

The hydromechanical parameters (except for the LVDT) kept decreasing when the head was made constant. Between ca. min 3300 and the head drop, while the LVDT sloped upwards, *Q* and *i* enterer a phase of considerably regular/periodic oscillatory behaviour, with nearly synchronous peaks and throughs – analogous to a clog-and-flow regime, as is further elaborated in the Discussion section. The *σ'* also seemed to behave in such a periodic oscillatory way, but in a less well-defined manner. During this interval, the hydrophones also seemed to roughly show an equivalent periodic oscillatory behaviour, with the troughs in one sensor corresponding to peaks in the other and vice-versa.

After the head drop, *Q* and *i* decreased while *σ'* increased and the plateaued. The LVDT accentuated its upward slope and kept rising until end of data recording (which was quite like the observed in tests S4T2 and S4T3).

On the AE, the TH and WG increased with the head drop and peaked by its end, then decreased until data recording ended. The BH showed a less clear behaviour, with a considerably irregular set of undulations.

### *S4T5*

Test done between 22.01.2020 and 26.01.2020. In this experiment the water flow through the soil sample was directed downward. To allow for the passage of erodible particles through the downstream sample confinement (its bottom) there was no mesh between the soil and the specimen. This mesh essentially retained sand-sized particles. In the other tests the mesh was used to limit gravity-driven material expulsion especially during sample placement in the permeameter and the consolidation phase. The downward flow direction and consequent hydraulic arrangement made caused the hydraulic head to be controlled by lifting head tank and lowering the outflow tank outlet. The imposed vertical stress was like the one used in tests S4T1 and S4T2.

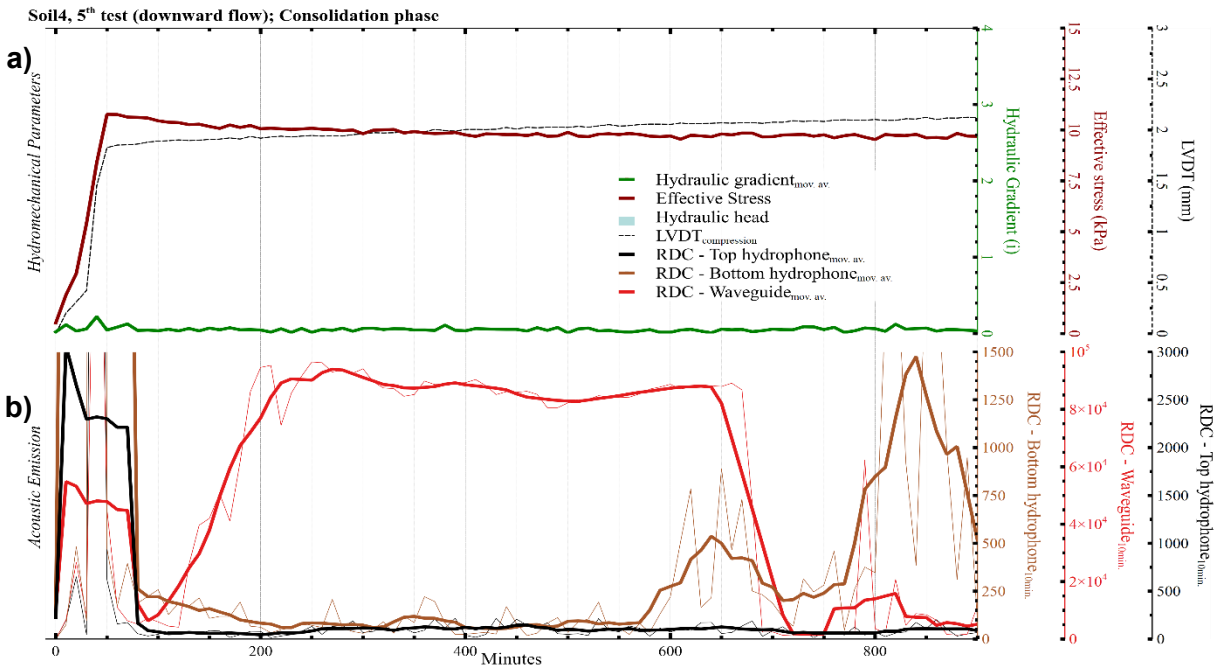


*Figure 4-19. Combined plot of the measured hydromechanical parameters (a) and AE (b) of test S4T5 (consolidation phase) in the time domain. Each parameter has an independent vertical axis with the same colour of the plotted curve (e.g. the blue line represents flow rate and corresponds to the blue vertical axis). The LVDT data indicates compression of the sample – a reduction of volume is reflected as an increased LVDT value (in millimetres). Thin lines represent raw data of variables shown with the same colour in thicker lines, which are moving averages.*

*Table 27. Summary of main general trends observed over time during the consolidation phase of test S4T5. Key to symbols in Table 35.*

S4T5 – Consolidation phase

| Time (minutes) | σ' | *i* | LVDT (compression) | BH | WG | TH |
|---|---|---|---|---|---|---|
| 0-100 | ↗ | — | ↗ | ∧ | ∧ | ∧ |
| 100-500 | ↘ | — | ↗ | ∿ | ∿ | ↗ |
| 500-900 | — | — | ↗ | ↗ | ↘ | ∿ |

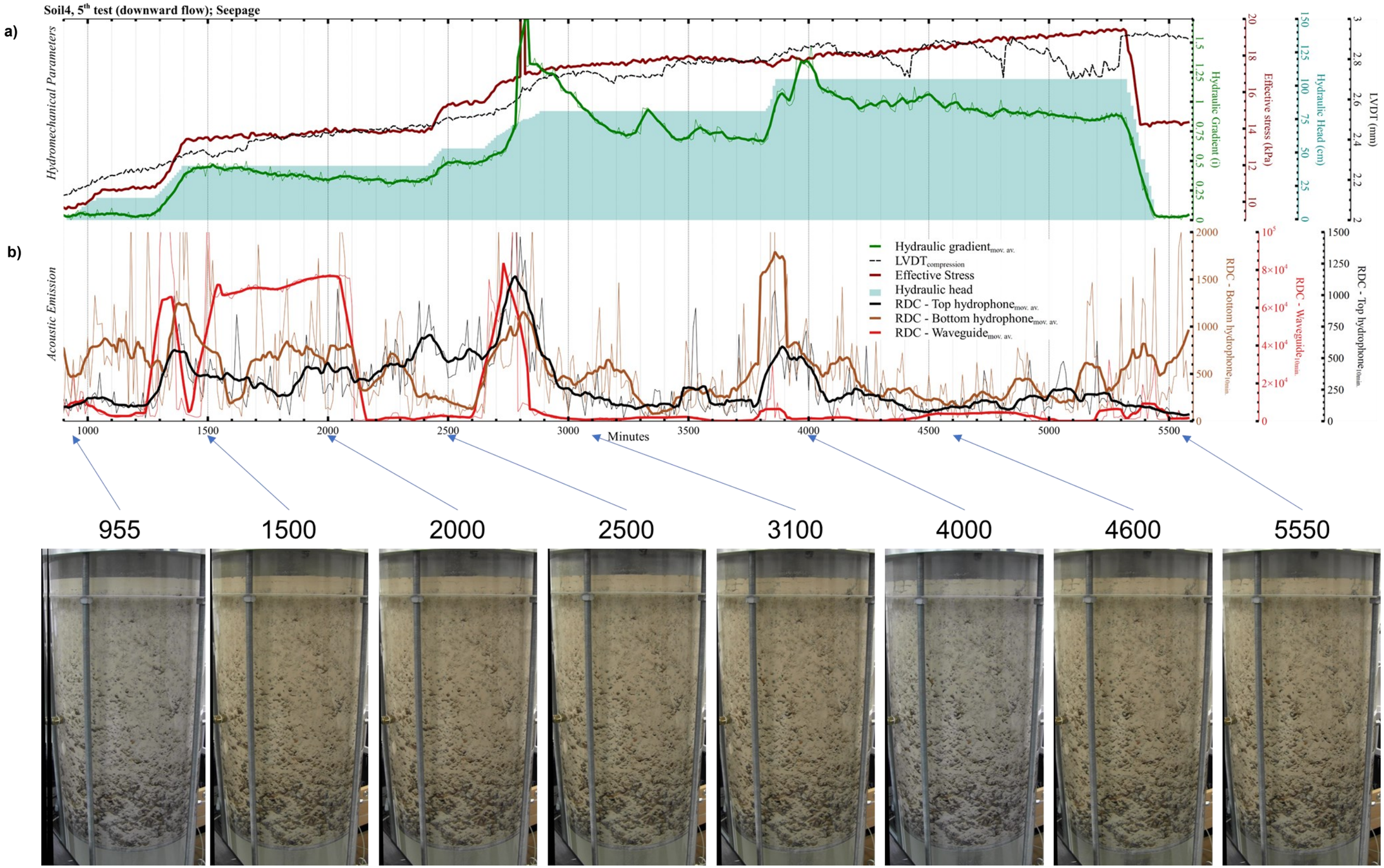


*Figure 4-20. Combined plot of the measured hydromechanical parameters (a) and AE (b) of S4T5 (post consolidation phase) in the time domain. Each parameter has an independent vertical axis with the same colour of the plotted curve (e.g. the blue line represents flow rate and corresponds to the blue vertical axis). The LVDT data indicates compression of the sample – a reduction of volume is reflected as an increased LVDT value (in millimetres). Thin lines represent raw data of variables shown with the same colour in thicker lines, which are moving averages. Picture series below shows soil specimen at different points during the test (elapsed minutes indicated above each image).*

**S4T5 – Consolidation phase**

As seen on Figure 4-19 and Table 27, *σ'* and LVDT rose in proportion to the loading steps and *Q* fluctuated just slightly. With a constant vertical load, *σ'* marginally sloped downward and the LVDT upward.

**S4T5 – Seepage test (post-consolidation)**

During this test the flow rate remained too low to be reliably measured, therefore *Q* is not shown in Figure 4-20. The downward flow direction resulted in a more stable relationship between the flow and how the particles settled – the induction of flow caused particles to reaccommodate, but the flow direction having the same direction as gravity seemingly caused particles to form conical structures that tended towards the natural rest angle of the material (dependant on flow energy) and relatively hydrodynamic, better dissipating/directing fluid flow around themselves.

*Table 28. Summary of main general trends observed over time during the seepage test (post-consolidation) phase of test S4T5. Key to symbols in Table 35.*

S4T5 – Seepage test (post-consolidation)

| Time (minutes) | Hydraulic head | σ' | *i* | LVDT (compression) | BH | WG | TH |
|---|---|---|---|---|---|---|---|
| 900-1500 | ↗ | ↗ | ↗ | ↗ | ↗ | ↗ | ↗ |
| 1500-2400 | — | — | ↗ | ↗ | ∿ | ⌒ | ∿ |
| 2400-2900 | ↗ | ↗ | ↗ | ↗ | ∧ | ∧ | ∧ |
| 2900-3800 | — | ⌒ | ↘ | ↗ | ∿ | — | ∿ |
| 3800-4000 | ↗ | ∿ | ↗ | ↗ | ∧ | ∧ | ∧ |
| 4000-5200 | — | ↗ | ↘ | ∿ | ∿ | ⌒ | ∿ |
| 5200-5600 | ↘ | ↘ | ↘ | ↗ | ↗ | ↘ | ↗ |

With each head rise sequence (Figure 4-20a), *σ'* increased. Its increase during the first head rise was smaller than at the second one, but from then on each successive *σ'* increase was less prominent than the preceding one. The hydraulic gradient (*i*) had a somewhat more complex behaviour (compared to *σ'*), showing an increase at every head rise sequence except the first one and the relative magnitude of that increase being more irregular as the test progressed. Also, *i* showed a slight decrease in the periods between each head rise sequence (additionally to a secondary increase at ca. min 3350) and, in this downward flow test, reached higher values than in other tests with Soil 4. When the head was dropped, both *σ'* and *i* dropped and then flattened (the former at a position higher than when the test started and the latter at the overall test baseline) until the test was terminated.

The LVDT rose during practically the entire test until the head was reduced, showing a few local depressions (min. 1480-1670, 3120-3410 and 5040-5300) and troughs (min. 4420 and

4810), momentarily increasing in slope during the 4th head rise sequence and, when the head was reduced, flattening at the highest value during the test. Slight particle movement (equivalent to early-stage internal erosion) was noted by ca. min. 1360, which intensified by ca. min 1520.

The AE of the BH was variable during the test, showing a series of peaks and troughs, but still the most protuberant of the peaks happening at the 2nd, 4th and 5th head rise sequences, all of which happening quite close in time to peaks in the TH and WG. The BH showed an upslope after the head tank was lowered. The TH signal was like the BH - relatively irregular -, but still, the 2nd, 4th and 5th head rise sequences correspond to its most prominent signals. With the head drop the TH entered a downslope. The WG behaved differently from the hydrophones in the sense that its high RDC points are more well defined in relation to its baseline. The WG had its highest points at the 2nd head rise (ca. 50 minutes before the other 2 sensors), min. 1500 - 2100 (its start coinciding with an LVDT drop) and ca. min. 2750. It also showed minor (nonetheless clear) elevations at min. 3850, 4400-4900, 5250 and 5400.

### *S5T1*

Test performed between 14.11.2019 and 19.11.2019. Some noise level drifting was observed in the AE and thresholds adjusted accordingly. Issue seemingly caused by preamplifiers.

There was a power outage while the equipment was being set-up, forcing the shutdown of the data acquisition system. Although it was not possible to confirm if this caused some sort of damage or change to the equipment, no such problem was observed. This was an upward flow test.

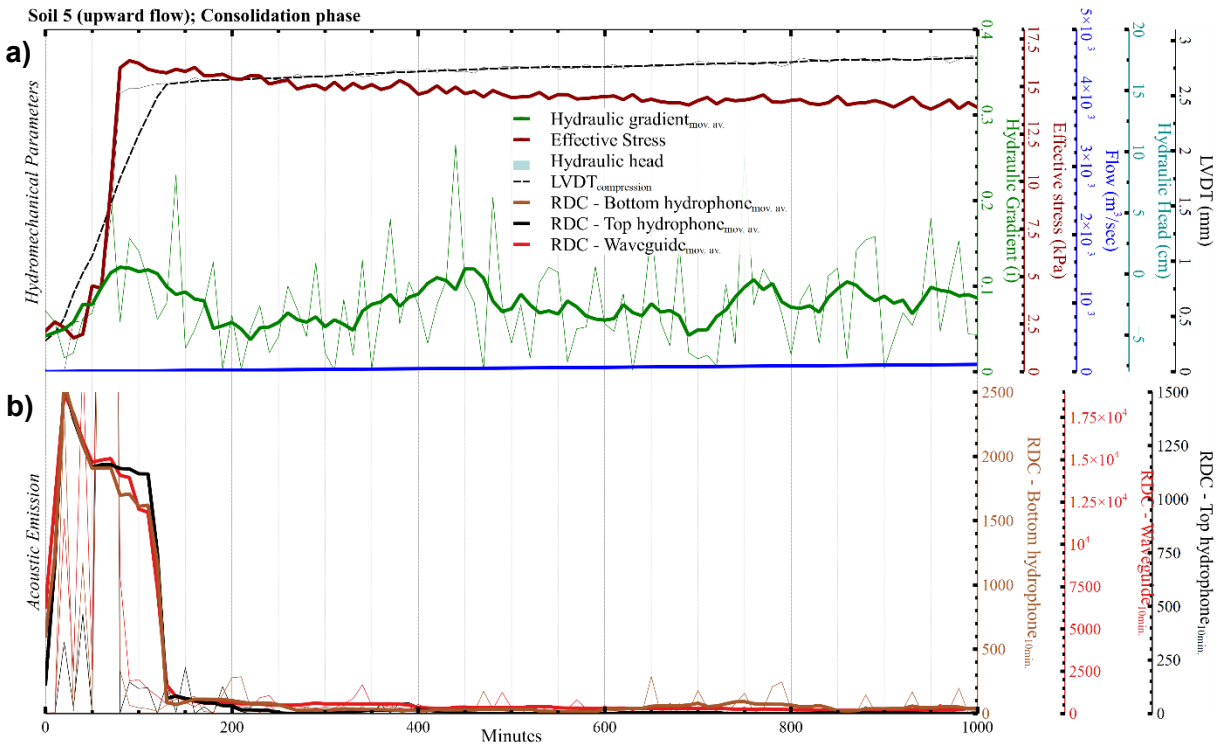


*Figure 4-21. Combined plot of the measured hydromechanical parameters (a) and AE (b) of S5T1 (consolidation phase) in the time domain. Each parameter has an independent vertical axis with the same colour of the plotted curve (e.g. the blue line represents flow rate and corresponds to the blue vertical axis). The LVDT data indicates compression of the sample – a reduction of volume is reflected as an increased LVDT value (in millimetres). Thin lines represent raw data of variables shown with the same colour in thicker lines, which are moving averages.*

*Table 29. Summary of main general trends observed over time during the consolidation phase of test S5T1. Key to symbols in Table 35.*

S5T1 – Consolidation phase

| Time (minutes) | σ' | *i* | LVDT (compression) | BH | WG | TH |
|---|---|---|---|---|---|---|
| **0-100** | ↗ | ↗ | ↗ | Λ | Λ | Λ |
| **100-1000** | ↘ | ∿ | ↗ | — | — | — |

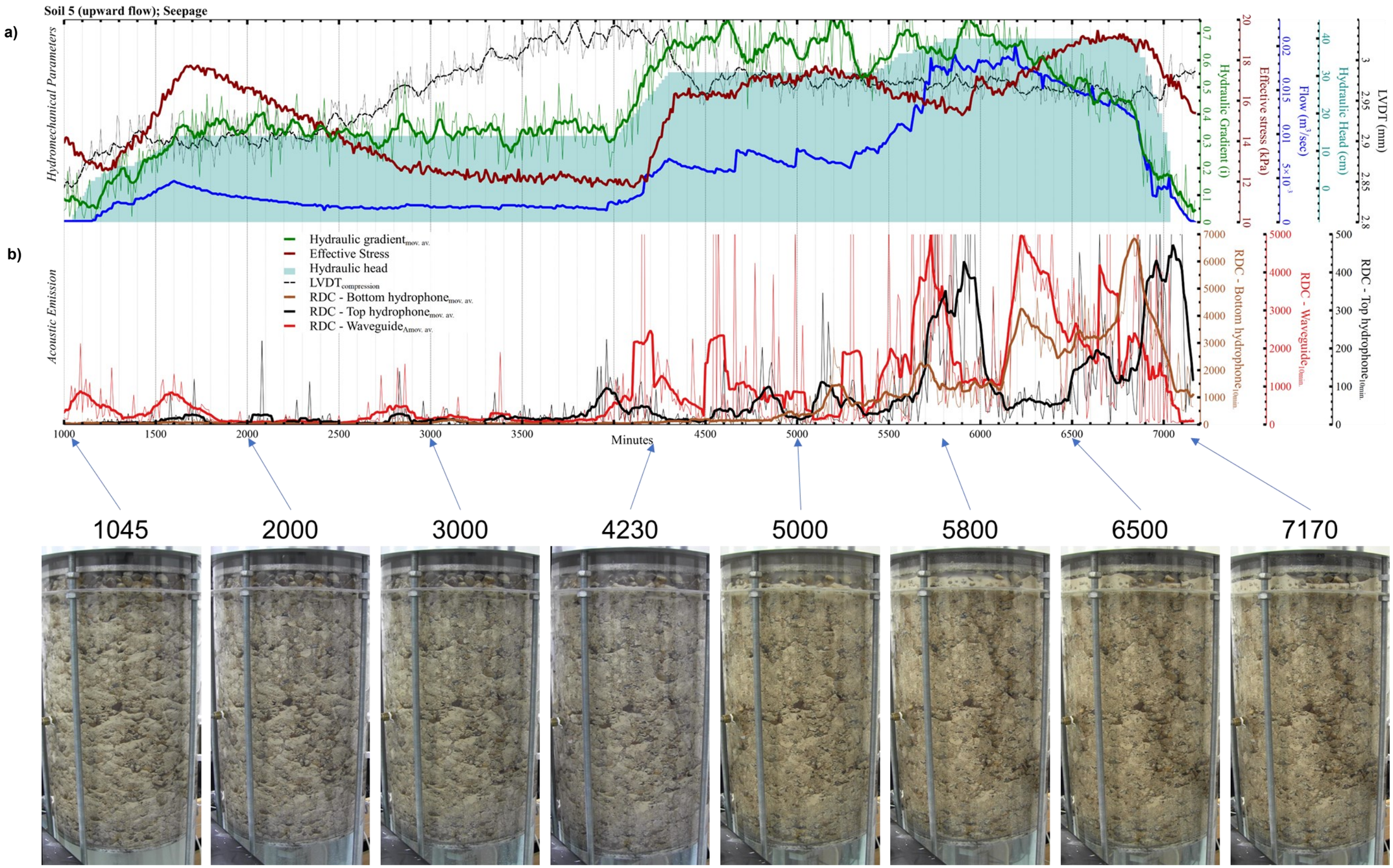


*Figure 4-22. Combined plot of the measured hydromechanical parameters (a) and AE (b) of S5T1 (post consolidation phase) in the time domain. Each parameter has an independent vertical axis with the same colour of the plotted curve (e.g. the blue line represents flow rate and corresponds to the blue vertical axis). The LVDT data indicates compression of the sample – a reduction of volume is reflected as an increased LVDT value (in millimetres). Thin lines represent raw data of variables shown with the same colour in thicker lines, which are moving averages. Picture series below shows soil specimen at different points during the test (elapsed minutes indicated above each image).*

## S5T1 – Consolidation phase

The consolidation phase of S5T1 is seen in Figure 4-21 and Table 29. *σ'* and LVDT show an upward trend corresponding to the vertical loading of the sample that, once the loading stops, give place to a downslope on the *σ'* and an upslope on the LVDT, all while *i* slightly oscillates. On the AE peaks corresponding to the vertical loading can be seen in the signal of all three sensors. Once the loading elds, all three sensors drop to baseline and stay so until the end of the plot.

## S5T1 – Seepage test (post-consolidation)

On Figure 4-22 and Table 30 the rest of the test can be seen. When the head tank began being risen, *σ'* began dropping until, by min. 1200, it increased until ca. min. 1700 (after the head was made constant), the, entering a downward slope that lasted until min. 4200 (decreasing slope at min. 2900). At ca. min. 4200 (when the head was elevated), *σ'* steeply increased before it flattened between min. 4300-4700 (after head was made constant). It then formed an arch that ended by min. 5900, began rising again (locally peaking at min 6000) until it reached its highest values in the plot. When the head was dropped, *σ'* entered a downslope that lasted until the end of the test.

*Table 30. Summary of main general trends observed over time during the seepage test (post-consolidation) phase of test S5T1. Key to symbols in Table 35.*

S5T1 – Seepage test (post-consolidation)

| Time (minutes) | Hydraulic head | σ' | *Q* | *i* | LVDT (compression) | BH | WG | TH |
|---|---|---|---|---|---|---|---|---|
| 1000-1700 | ↗ | ↗ | ↗ | ↗ | ↗ | — | ↗ | ↗ |
| 1700-3900 | — | ↘ | ↘ | ∿ | ↗ | — | ∿ | ∿ |
| 3900-4300 | ↗ | ↗ | ↗ | ↗ | ∿ | ↗ | Λ | Λ |
| 4300-5400 | — | ⌒ | ∿ | ∿ | ∿ | ↗ | ∿ | ↗ |
| 5400-5900 | ↗ | ↘ | ↗ | ∿ | ∿ | Λ | Λ | Λ |
| 5900-6800 | — | ↗ | ↘ | ↘ | ∿ | ↗ | Λ | ∿ |
| 6800-7900 | ↘ | ↘ | ↘ | ↘ | ↗ | Λ | ↘ | Λ |

At min. 1150, *Q* and *i* started rising. Both then increased with each head rise. However, in between the head rise sequences *Q* tended to show a slight downward trend while *i* tended to stay roughly constant or oscillate. Between ca. min. 4500-6000 *Q* and *i* behaved in a periodic, oscillatory way – with *Q* increasing between min. 4450-5700. This regular oscillation can also be seen, although less clearly, on [subtle] breaks in *σ'*. At ca. min. 6200 both *Q* and *i* entered a downward slope (which got steeper with the head drop) that lasted until the end of data recording.

The LVDT at first showed an increase that lasted until ca. min 4300 (with near-horizontal slope between min. 1400-2400. After a drop between ca. min. 4300-4500, the LVDT stayed roughly horizontal until the head was dropped, then sloping upward.

On the AE, all three sensors show an overall signal increase during the test, especially from min. 4000 onwards. Observing the data before min 4000 (Figure 4-23) with a zoomed AE vertical scale, it can be seen that the AE signal was correlated with changes in the hydromechanical parameters – as the head was risen between min. 1045-1261 and 1385-1627, peaks occurred in the WG and BH, while the TH increased during both intervals (peaking by the end of the 2nd one), and from then on the roughly corresponding to changes on *i*, *Q* and *σ'* (e.g. min. 2100, 2850, 3400, 3950). Particle movement (or early-stage internal erosion) was noted at ca. min 1500.

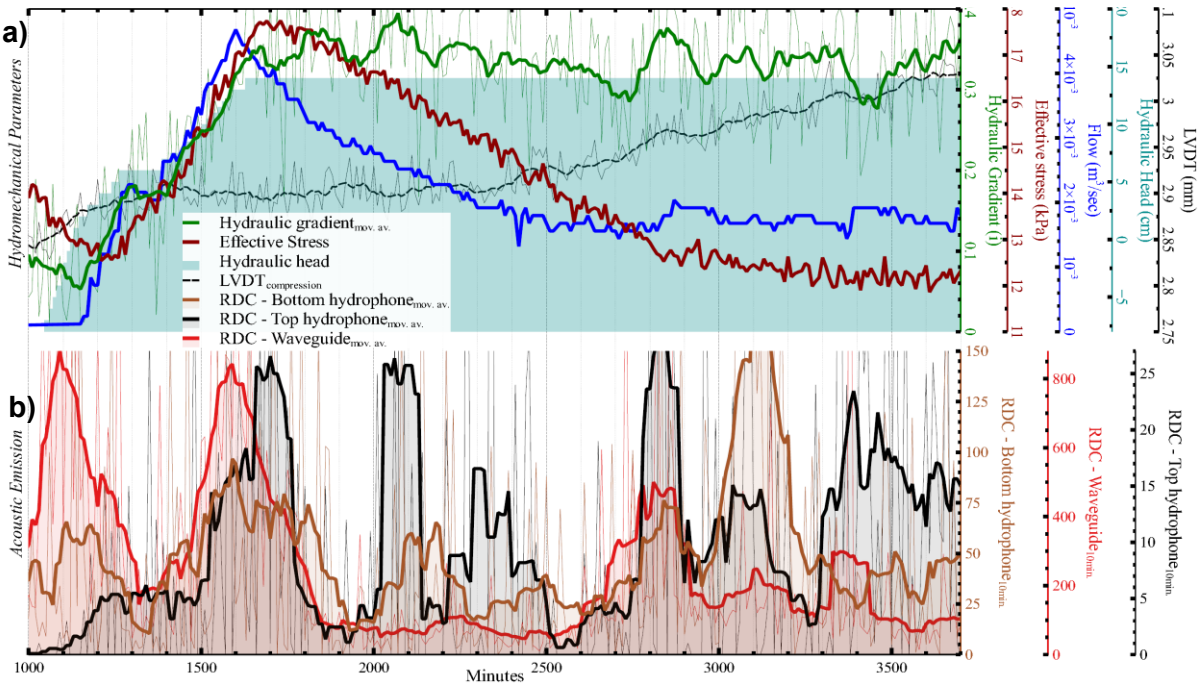


*Figure 4-23. Detail of Figure 4-22, from minute 1000 to 3700 with the vertical AE scales zoomed-in compared to the main picture.*

During the undulatory phase seen in *Q* and *i,* TH showed local peaks nearly parallel to the seen on *i* (min. 4850 and 5150). The TH then peaked between min 5200-6000 (when *Q* stopped rising and *σ'* troughed locally) and when the head tank was dropped. The WG peaked during every head rise, during the undulatory phase (min 4550, 5000 and 5300), ca. min. 6200 (when *Q* and *i* began dropping), min. 6700 (when *σ'* stopped rising) and decreased with the head lowering. The BH was slightly rising until at ca. min. 5200 it peaked locally (between TH and WG peaks), and kept on rising until the head was dropped, with more intermediate peaks (min. 5700 - near TH and WG peaks; min. 6700 - along with a WG peak), when it continually decreased until data recording interruption. An erosional pipe formed (in a rather abrupt, energetic way) at min. 5630 – clearly visible in the AE.

### *S6T1*

Test performed between 21.11.2019 and 25.11.2019. A ca. 1cm later of silt deposited on top of the top loading perforated plate, resulting from the settling of material that got in suspension following the insertion of the sample into the permeameter, possibly having effects on the flow rate at least during the start of the seepage test. This was an upward flow test.

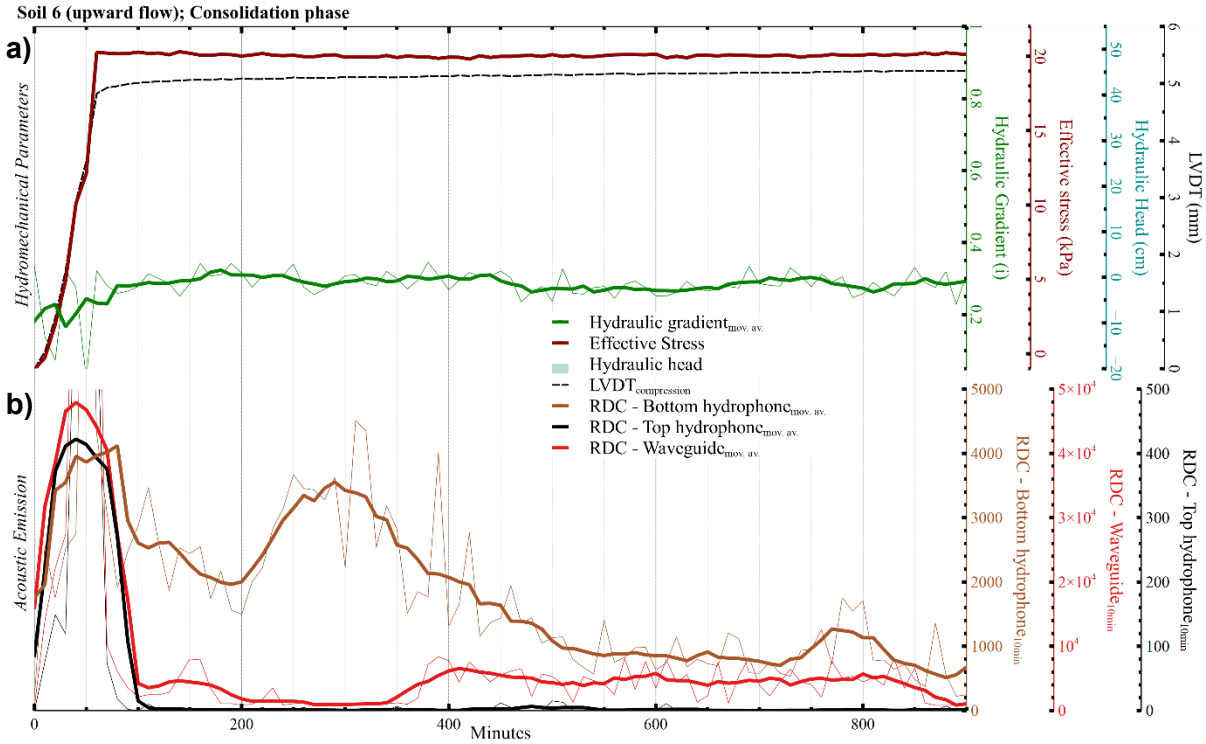


*Figure 4-24. Combined plot of the measured hydromechanical parameters (a) and AE (b) of S6T1 (consolidation phase) in the time domain. Each parameter has an independent vertical axis with the same colour of the plotted curve (e.g. the blue line represents flow rate and corresponds to the blue vertical axis). The LVDT data indicates compression of the sample – a reduction of volume is reflected as an increased LVDT value (in millimetres). Thin lines represent raw data of variables shown with the same colour in thicker lines, which are moving averages.*

*Table 31. Summary of main general trends observed over time during the consolidation phase of test S6T1. Key to symbols in Table 35.*

S6T1 – Consolidation phase

| Time (minutes) | σ' | i | LVDT (compression) | BH | WG | TH |
|---|---|---|---|---|---|---|
| 0-100 | ↗ | ↗ | ↗ | Λ | Λ | Λ |
| 100-900 | — | ∿ | ↗ | ↘ | ∿ | — |

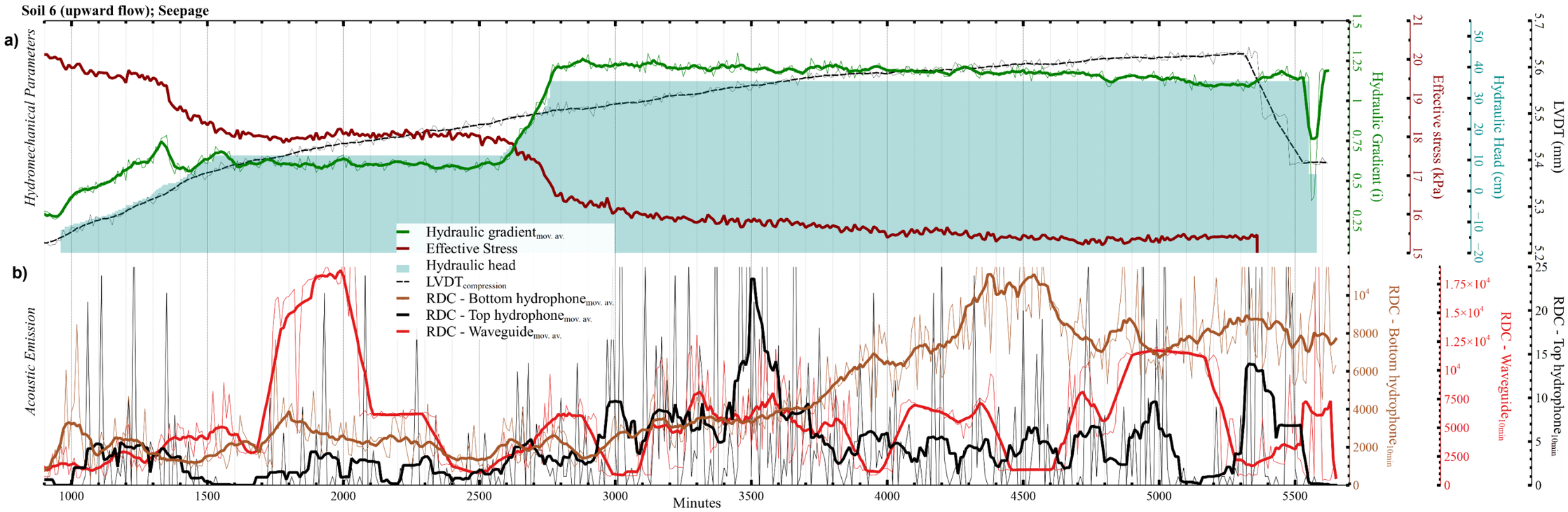


*Figure 4-25. Combined plot of the measured hydromechanical parameters (a) and AE (b) of S6T1 (post consolidation phase) in the time domain. Each parameter has an independent vertical axis with the same colour of the plotted curve (e.g. the blue line represents flow rate and corresponds to the blue vertical axis). The LVDT data indicates compression of the sample – a reduction of volume is reflected as an increased LVDT value (in millimetres). Thin lines represent raw data of variables shown with the same colour in thicker lines, which are moving averages.*

*Table 32. Summary of main general trends observed over time during the seepage test (post-consolidation) phase of test S6T1. Key to symbols in Table 35.*

S6T1 – Seepage test (post-consolidation)

| Time (minutes) | Hydraulic head | σ' | *i* | LVDT (compression) | BH | WG | TH |
|---|---|---|---|---|---|---|---|
| 900-1500 | ↗ | ↘ | ↗ | ↗ | Λ | ↗ | ⌒ |
| 1500-2600 | — | ∿ | ∿ | ↗ | ∿ | Λ | ∿ |
| 2600-2800 | ↗ | ↘ | ↗ | ↗ | ∿ | Λ | Λ |
| 2800-4000 | — | ↘ | ∿ | ↗ | ↗ | ⌒ | Λ |
| 4000-5400 | — | ∿ | ↘ | ↗ | ⌒ | ∿ | ∿ |
| 5400-5700 | ↘ | ↘ | ↘ | ↘ | ↗ | Λ | Λ |

**S6T1 – Consolidation phase**

During the consolidation phase of S6T1 (Figure 4-24 and Table 31), *σ'* and LVDT values increased according to the addition of vertical load, then staying constant until the end of this phase. The *i* stayed slightly oscillated.

In the AE of this consolidation phase, all the three sensors peaked in accordance with the vertical loading. After this loading, the TH dropped to baseline. The WG also dropped but still showed some oscillation. BH also dropped, but more gradually (with a peak at ca. min. 300) and with oscillations.

**S6T1 – Seepage test (post-consolidation)**

Throughout this phase (Figure 4-25 and Table 32) *σ'* and *i* practically mirrored each other, with *σ'* decreasing and *i* increasing every time the head was increased, except at the head drop by the end of the test, when both decreased. The LVDT increased throughout the plot, only dropping by the end of the test, when *σ'* also did so. During this test, the flow rate was too low to be reliably measured with the system in place – fluid mass increments below the sensitivity of the outflow tank balance.

On the AE (Figure 4-25b), the WG showed a seemingly irregular behaviour, with peaks at ca. min. 2000, 5000 and 5600 and troughs at ca. min. 2500, 3000, 3900, 4500 and 5300. The BH showed an irregular but progressive increase throughout the test, peaking by min. 4600 and forming a rough plateau lasting until the end of data recording. The TH increased with the head rises (except for peaks at ca min. 3500 and 5350, and a slight increase in scale between before and after the 2$^{nd}$ head rise), but the changes in its signal were not clearly distinguished from what might have been caused by noise - note that during this test the TH RDC was about one order of magnitude lower than in other tests and particle movement in this test was very subtle.

### 4.1.3 Summary of tests

The data produced by this test program revealed trends and recurrent behaviours of the measured variables. Some of the variability or discrepancy between tests may have been caused by inconsistencies in the testing procedure, equipment performance and/or even data processing. However, despite subtle imperfections, these results did achieve what they were intended for.

The principal observations were:

<u>Consolidation phase:</u>

- Addition of vertical stress to the sample caused it to compress (increase in LVDT values).
    - Noting that the displayed *σ'* was an interpolation between the measurements by the top and bottom load cells (and that wall friction and time influenced stress transmission to the bottom LC).
- Vertical stress increases and sample compression corresponded to AE spikes.
- Settling of fines (silt) in the water volume below the sample (at the bottom of which was the BH) tended to produce AE.

<u>Seepage test (post-consolidation):</u>

- The following variables tended to show proportionality at the start of a given test and then, as the system evolved (especially with formation of erosional pipes), became differently or less clearly correlated:
    - Effective stress and hydraulic head
    - Flow rate and hydraulic head
    - Flow rate and hydraulic gradient
- A constant hydraulic head often correlated with a decrease or oscillatory behaviour of the flow rate – seemingly related to [partial] clogging.
- Head decrease at the end of a given test, sometimes with a time lag, tended to correlate with:
    - Flow rate decrease
    - Hydraulic gradient decrease
    - Effective stress increase
    - AE increase
- The start of particle movement or onset of internal erosion tended to be reflected as an AE increase, especially on the TH.

# 5 Discussion

## 5.1 Introduction

This study intended to know to enhance understanding of AE generated by seepage-induced internal erosion and propose strategies for monitoring and interpretation. An interpretation of the results from the used approach is therefore pursued in this section.

In this interpretation the previously described experimental results are used to produce relevant correlations and, if possible, establish causal relationships between the hydromechanical parameters, the occurrence of seepage erosion and AE.

### a. Test phases

Each test can be subdivided in periods related to the main event or regime taking place. This subdivision intends to facilitate interpretation as it is perceived that the relevant phenomena focused on this thesis are likely to be qualitatively different among such phases. The selected phases are:

Consolidation: when the sample, after being placed in the permeameter, is subject to the addition of vertical stress and allowed to equilibrate with the higher stress condition (e.g. change in volume, have its particles rearranged, dissipate eventual pore overpressure). This was in every test done in drained conditions - the pore water can drain out from the soil matrix as the fluid in-/outlets are open. The vertical load is then kept constant during the rest of the test.

Head increase: when the hydraulic head was increased. This was done in a series of considerably small steps (0.5-10cm; mostly 1cm steps) and intended to cause either ain increase of hydraulic gradient and/or induce fluid flow through the sample, potentially promoting particle movement.

Ongoing flow: characterized by the occurrence of [measured] water flow through the sample while the hydraulic head is constant.

Head reduction: reversion of the head increase, ultimately leading to a neutral head condition and the cessation of water flow.

### 5.1.1 Consolidation

*Hydromechanics*

In the hydromechanical parameters during the consolidation phase of the different test plots in the Results section (chapter 4.1.2), the first and perhaps more obvious and expectable observation is that the effective stress (*σ'*) and LVDT (for which positive values represent a reduction in sample height, or compression) increased in proportion to the addition of vertical load. At the end of this phase the sample was considered normally consolidated.

Hydraulic gradient (*i*) was not significantly affected during this phase since the excess pore pressure could dissipate and the magnitude of volume change/compression of the sample (which, given the incompressibility of the fluid, could induce a compensatory pore-fluid expulsion) did not seem sufficient to strongly vary *i*.

In Figure 5-1 the vertical load applied to the sample is compared with the effect it had on sample deformation indicated by the LVDT compression - this vertical stress was of the stress applied to the top of the sample; S1T1 is excluded as the LVDT could not be installed by the time of the test. Also, the LVDT compression shown in Figure 5-1 is that of the second of the loading steps onward, since at the beginning of each test the level of soil compaction at the very surface of the soil was considered irregular simply due to the practical difficulty to lay the top loading plate on the sample in a precise and repeatable manner, which was practically eliminated after the initiation of the loading process.

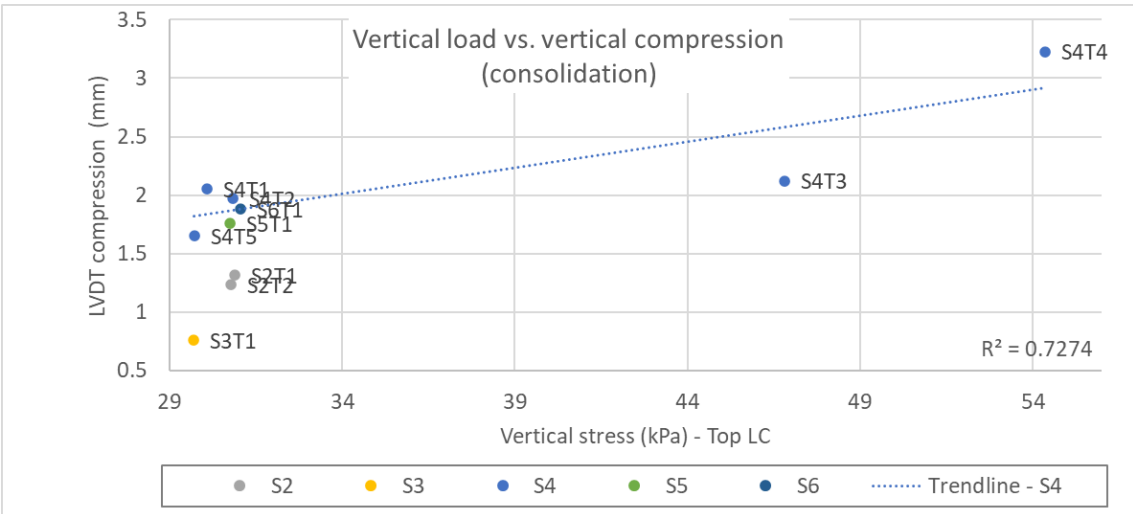


*Figure 5-1. Plot of sample vertical compression (LVDT) against applied vertical load as measured by the top LC during the consolidation phase. The trendline corresponds to the points of tests with Soil 4 (S4).*

The data points clustered at the left side of the plot (Figure 5-1) were expectedly so since the same load was applied to each of them (with the variability within the cluster being mainly accountable to the soils and their initial relative density being different). It could be observed that the two data points outside of the cluster (S4T3 and S4T4), despite having been subject

to higher loads than the other tests, reacted non-linearly to the increased load: S4T3 showed a level of deformation approximate to that of the other tests (nonetheless being at the upper end) while S4T4 clearly stood out by showing a much larger deformation. This effect is deemed to be because S4T4 had a vertical load sufficient to surpass a threshold of static friction (either of the soil or of the soil-wall interface) not overcome in the other tests. It can also be noted how the tests with a same soil grouped together in the plot, indicating consistency in their behaviour.

### *AE*

Acoustic emission during this phase exhibited RDC spikes during the application of vertical load. The main mechanism of AE generation was the inter-particle friction induced by the vertical load and the consequent soil compression, which, with sufficient force (accounting for the precedent level of soil compaction) forced the grains into a more compact arrangement/packing, sliding and rubbing against each other and producing the perceived sound (Dixon et al., 2015b; Uhlemann et al., 2016b; Smith and Dixon, 2019a).

However, the intensity of this AE activity (in terms of RDC) was non-linear with the progressive load increase - the AE activity correlated better with the magnitude of volumetric strain or particle re-accommodation (strain) than to the intensity of the vertical load. This can be caused by the overwhelming of the soil compaction-resistance static friction at certain (intermediate) loading steps, which, besides causing increased AE, also brings the soil skeleton to a more stable configuration that might not be overwhelmed by the following vertical load increase (and not affect the AE as much). Nonetheless, the stronger trend was that higher vertical loads caused more deformation and AE.

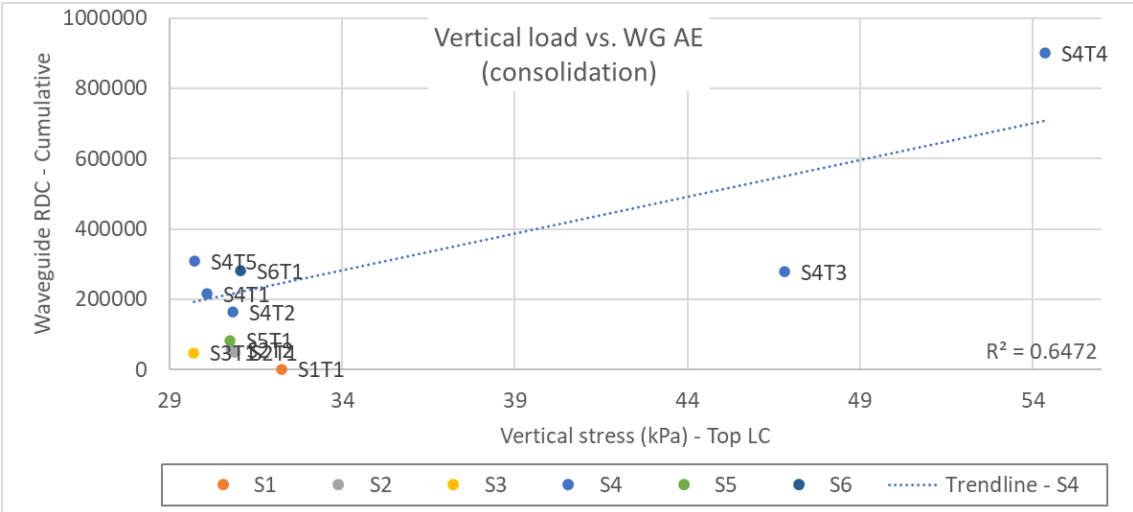


*Figure 5-2. AE cumulative RDC of the waveguide (WG) plotted against applied vertical stress during the consolidation phase. The trendline corresponds to the points of tests with Soil 4.*

In Figure 5-2 the vertical stress applied at the consolidation phase was plotted against the corresponding AE of the WG – the waveguide was selected for this plot because it was the acoustic sensor with the smallest amount of signal drift due to equipment issues between tests and because it has been reliably and precisely used by Smith et al. (Smith and Dixon, 2019a; Dixon et al., 2015b; Smith et al., 2014; Smith, 2015; Smith and Dixon, 2019c) for correlating AE with very subtle ground movements. In this plot the clear distinction in AE between the tests with a higher vertical load was deemed the most important aspect, followed by tests with a similar soil showing relatively similar values. This indicated a direct proportionality between stress application and AE. The reason for such behaviour appeared to be that higher stress produced a higher deformation (which might not be fully converted to vertical displacement as a portion of particle movement has an e.g. horizontal, rotational component) and therefore higher number of frictional particle interactions that are also more energetic, resulting in higher AE RDC counts.

It can be noticed that S4T3, despite having been subject to a higher vertical stress than S4T5, showed a less pronounced RDC. This is likely due to the fact that in S4T5, as it was a downward flow test, did not have a geomembrane/mesh between the sample and the bottom perforated plate, which allowed for a considerable amount of fines  to “fall through” during sample placement in the permeameter and left the bottom ca. 5-10 cm of the sample relatively deprived of fines, changing the sample properties and how it reacted to the consolidation. The equivalent can be also observed in Figure 5-4, where the

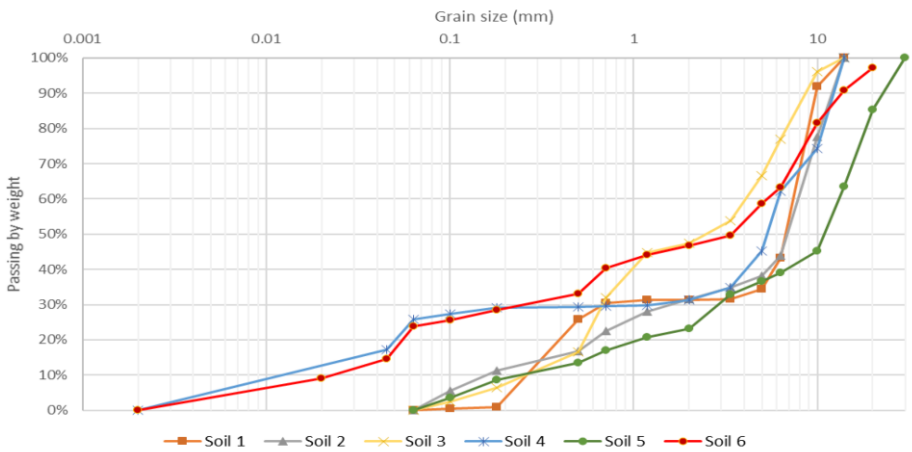


*Figure 5-3. Grain-size distribution of tested soils.*

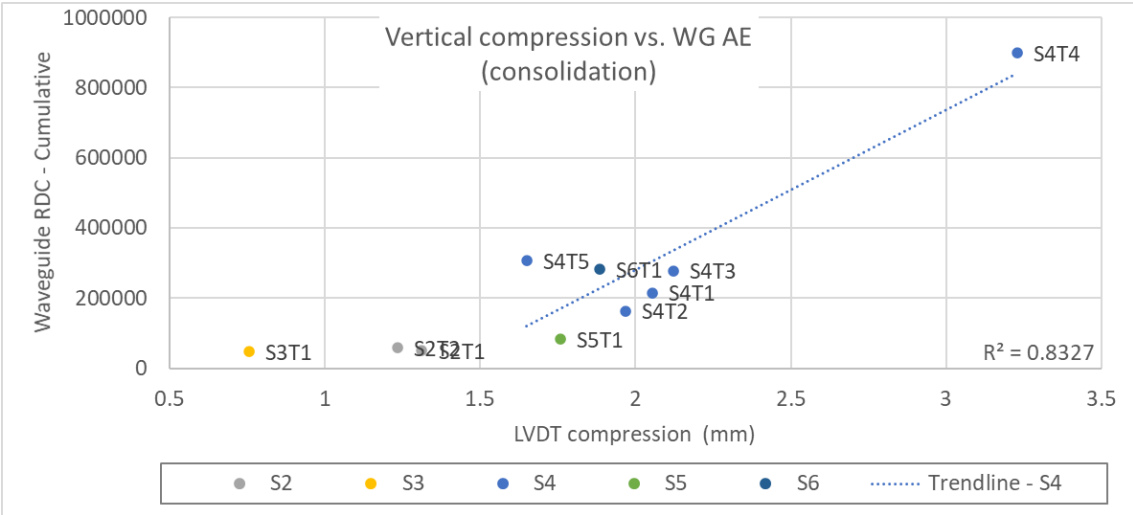


*Figure 5-4. AE cumulative RDC of the waveguide (WG) plotted against vertical compression (LVDT) during the consolidation phase. The trendline corresponds to the points of tests with Soil 4.*

The soil gradation also appeared to influence the detected AE since soils with a higher content of fines <0.1mm (i.e. Soil 4 and Soil 6; Soil 4 being the most gap-graded one; Figure 5-3) showed a stronger AE signal in proportion to the applied load. This appeared to stem from finer soil fractions being more susceptible to deformation as their stress-strain response tends to be more significant, producing more AE events (with a coefficient of proportionality not having been determined), at least for the explored levels of vertical stress and in comparison with soils that do not contain such finer fractions.

In Figure 5-4 the AE RDC from the WG was plotted against the vertical displacement (compaction) of the sample during the consolidation phase (with the LVDT compression being that of the second loading step onward, as in Figure 5-1). A broader and more homogenous horizontal (LVDT data) spread of the datapoints can be observed, which produced interesting results: vertical displacement (compression) showed a rather strong correlation with the measured AE. This gives further validity to the idea of AE corresponding to the amount of particle interactions during soil compaction as this compaction is due to particle re-accommodation and its intrinsic AE-generating frictional dynamics.

### 5.1.2 Head increase

This can be considered the actual start of the seepage erosion test. From the start of the application of a non-neutral hydraulic head the soil particles begin being subject to a force by the fluid and the test starts to better approximate the condition of a soil volume within a water-retaining earth structure.

### *Hydraulic gradient (i) and Flow rate (Q)*

An increase of hydraulic gradient (perhaps the most expected effect of the head increase; Hunter and Bowman, 2017a; Taylor et al., 2017; Rochim et al., 2017; Moffat and Herrera, 2015) was regularly noted in the beginning of the first head increase in the tests done – its magnitude depending on the applied head and the soil permeability (i.e. its capacity to dissipate the induced pressure gradient). Still, the hydraulic gradient (*i*) did not react in the same way at every head increase. As the tests evolved (with exception of S6T1) there is at least one moment when, either during or shortly after a head increase, a drop in *i* occurred.

While the increase in *i* did not always correspond to an increase in the measured AE rate (RDC/10min), a drop in *i* was usually either associated with or adjacent to an increase in AE. This suggested that, as the head was increased, the capacity of the soil to dissipate the beyond-hydrostatic pressure differential (and the consequent movement of the fluid through the soil pores) was put under stress; at some point, if the particle geometry allows, some of the grains (in principle the finer ones) began to be dislocated by the fluid flow. As was observed, random inhomogeneities in the soil matrix (e.g. a somewhat larger pore that might contain non-load-bearing [fine] particles) were reflected in also [slightly] localised inhomogeneous fluid flow and, intrinsically, the kinetic energy of the fluid was higher in certain points; in these points, the particles tended to be moved if the kinetic energy was sufficient, which tended to produce a region with higher porosity or hydraulic conductivity that could transmit the localised higher kinetic energy of the fluid to its immediate surroundings (especially but not exclusively in the direction of flow). If such a region of comparably (in relation to the rest of the sample) higher porosity or hydraulic conductivity was capable of significantly concentrating the fluid flow through the sample, this causes a relief in the overall pressure differential/releases overpressure and lowers the measured hydraulic gradient, as was observed. This might not increase the flow rate (which is one, overall value) as the local flow concentration did not necessarily signify an increase of global fluid flow. The mentioned particle movement (causing collisions and other frictional interactions) and its intensification were so reflected in the AE as higher RDC.

An increase in permeability must be separated from erosional pipe formation, at least in the early stages of the process. The re-accommodation of particles linked to the permeability increase can be slow and well distributed enough over the sample volume to keep *i* apparently proportional to the head increase; just once the flow is significantly concentrated for relative homogenisation of the pore pressure it occurs that *i* (which is one, overall value corresponding to the soil mass as a unit) saw a considerable drop.

The effect of head increases on flow rate (*Q*) was somewhat comparable to that observed with the hydraulic gradient, but with some differences.

In the tests with soil 2 (S2T1 and S2T2), *Q* and *i* followed comparable trends, but, especially in S2T2, the degree of their oscillations changed in proportionality during the tests. The main difference between these two tests is that in S2T1 the head was increased at a slower rate, indicating that the rate of head increase over time could have an effect on the way presumed flow-induced changes in the soil were reflected on *Q* and *i*. Nonetheless, in these two tests the changes in flow rate corresponded to the measured AE.

In the tests with Soil 4 (S4T1, S4T2, S4T3 and S4T4; excluding S4T5, which had downward flow), it was noted that the onset of [measured] flow just occurred at later steps of head rise, after *i* had already substantially increased; this was seemingly due to the lower permeability of this soil gradation – as the head is increased, the lower permeability caused the vertical pressure differential to be more slowly transmitted through the sample but it also, of course, limited the fluid flow. Once the abovementioned process of permeability increasing due to particle rearrangement evolved, the hydraulic conductivity could increase enough to allow the fluid flow to be measured.

In the same tests with soil 4 (S4T1, S4T2, S4T3 and S4T4), it was noticed that a head increase (about when a head of 20cm was reached) tended to cause an increase of *Q* disproportionally higher to the observed in the other head rise sequences and in a way that particularly de-coupled *Q* from *i*. This occurrence (which tends to be seen in the AE as a rise) suggested the formation of a preferential flow pathway (or erosional pipe). An occasional subsequent reduction in flow rate could be attributed to clogging on top of the sample (above the top perforated plate) by the accumulation of eroded/removed soil material, which tended to be seen at the end of preferential flow pathways/erosional pipes, and posed resistance to fluid flow. Such clogging was noted as a cause for reduction of flow (without reduction of head) in every test, to different degrees, except in S4T5, and S6T1.

Generally, the flow rates were a consequence of both the hydraulic head and the permeability of the soils; the former externally forced by the rise of the head tank and the latter resulting from the rearrangement of particles or internal erosion.

The downward-flow test with soil 4 (S4T5) produced flow rates that were too small to measure with the used system. These low flow rates were thought to have resulted from the lack of internal erosion; although in this test particle rearrangement was observed, this displacement tended to place the particles in local assemblages that were more resilient to seepage erosion: like in other tests with Soil 4, as the head was increased, a hydraulic gradient increase was induced and the relatively low initial soil permeability limited fluid flow; in this regime (with

continued head increase), the kinetic energy of the fluid was capable of dislocating particles, but the concordance between the downward flow and gravity seemingly caused the particles to form (or pile-up into) localised pyramidal/conical structures that, pointing upward, reached the equivalent of an angle of repose that, besides the characteristics of the material itself (e.g. interparticle friction) was correlated with the flow velocity. This made so that, to the applied heads, the soil seemed to become more stable as particles rearranged – it was noted that, shortly after head increase sequences, temporary local *i* spikes occurred, which was apparently when the soil got rearranged to the configuration stable for the newly reached hydraulic head/flow rate.

*Effective stress (σ')*

The effective stress (*σ'*) seemed to be predominantly controlled by the load measured by the bottom load cell: the top LC values, despite varying during a test, were mainly referent to the normal force applied by the vertical loading system, while the bottom LC reacted more to the load being transferred through the sample to the bottom loading plate (influenced by e.g. wall friction). Upward flow of the percolating water tended to counterbalance the force of gravity by the resistance or friction of the soil to this flow.

The effective stress (*σ'*) tended to be reduced when the head began being raised. With the soil in its most homogeneous configuration of a given test (before the possible effect of fluid flow or particle movement), the induced head tended to effectively push the soil upward in the case of this differential being applied from the bottom-up (i.e. upward flow tests). Also, the simple increase in pore pressure from the head increase reduced the effective stress, as can be expected from its definition.

When water flow occurred and went from acting relatively homogeneously in the overall soil mass to being sufficiently concentrated in preferential flow pathways (that developed due to particle re-accommodation/localised erosion), the measured σ' (which is one value, generalised for the whole sample, mostly regulated by the load perceived by the bottom loading plate) saw an increase as the upward (counter-gravity) push of the water flow was relieved from the overall soil mass.

In S4T4 the higher vertical stress faced with a similar hydraulic head range in comparison with the other tests seemingly made so that the lessening of the vertical load (perceived by the bottom LC due to the upward push of the applied head) was less significant than in these other tests – this was likely especially due to this higher vertical load having helped overcome the wall friction disproportionately (as in a threshold of static friction having been surpassed) to the seen in other tests.

In S4T5 (downward flow) the direction of flow reinforced/agreed/concorded the pull of gravity (despite the increase in pore pressure - the increase in pore pressure was much less significant than the kinetic energy of percolating fluid flow).

One particularity of the head increase phase is that the head rise itself could cause an amassing of the mentioned dynamics, such that their effect on the effective stress was exacerbated if energy (pore pressure, flow kinetic energy, particle motion) dissipation was overwhelmed by the rate of head increase. In other words, the added energy from the head increase may constantly be dissipated, but, if this addition of energy to the system was at a rate that surpassed the capacity of the soil to dissipate it, such energy built up.

*LVDT*

The LVDT measured the dislocation of the top perforated plate – if it moved up (away from the bottom perforated plate; equivalent to sample “expansion” or heave) the LVDT value decreased and if it moved down (towards the bottom perforated plate; sample compaction) the LVDT values increased.

The overall tendency in the permeameter tests was that the first head rise sequence corresponded to an increase in the LVDT values. In the tests with Soil 4 this occurred before the start of [measurable] water flow. The presumed cause of this was that this initial head rise caused a gradual increase in pore pressure (accompanied by a drop in effective stress) that reduced inter-particle friction and allowed the [constant] vertical load to gradually force the grains composing the soil skeleton into slight more compact arrangement. The effect of this mechanism seemed to depend on the soil not having suffered internal erosion (and especially formation of preferential flow paths) and having its permeability relatively low (in comparison with the rest of a given test) as a more efficient dissipation of pore overpressure made it less notable if not ineffective.

Reduction in LVDT values implied a vertical expansion of the volume containing the soil sample (i.e. upward movement of the top perforated plate). In upward flow the pressure or kinetic energy of the water might be capable of pushing the soil mass (and the top perforated plate) enough to cause upward vertical displacement. The hydraulic head would provide such energy and its capacity to push the soil mass would vary based on permeability, with more resistance to flow corresponding to a more effective push of the soil volume (and vice versa); the conditions could be such that an increase in hydraulic head did not incur in a proportional increase in flow rate and part of the head energy in effect heaved the soil (although the soil deformations due to this heave could be distributed over e.g. the soil height with varying degrees of homogeneity).

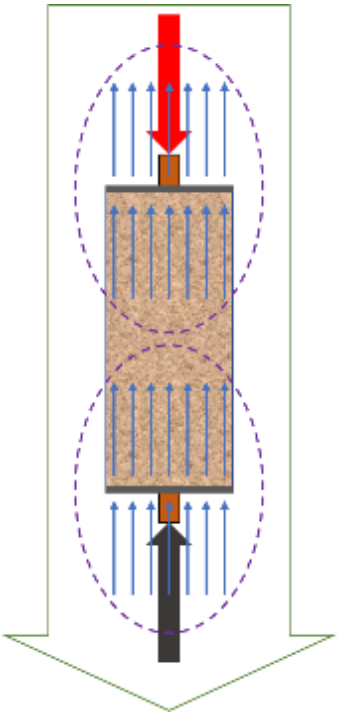

*Figure 5-5. Diagram of how the onset of upward flow (blue arrows) could affect the load cells (small orange squares) differently. Soil = brown pattern, dark; black arrow = normal force; red arrow = vertical load; outlining green arrow = gravitational force. Since the water flow would push the sample away from the BLC (decreasing its perceived load) and towards the TLC (increasing its perceived load), these measured forces would roughly cancel out in the calculation of an overall effective stress.*

A drop in effective stress could be seen in correlation with the onset/rise of water flow through the sample and with a rise in hydraulic gradient, as well as a decompression (increase in volume; top perforated plate "pushed" upwards). This could be caused by the upward water flow acting relatively homogenously on the whole soil mass and counteracting the pull of gravity, which could slightly heave the specimen (or at least a portion of it along with the top, loading plate) as witnessed by the LVDT.

This heaving effect may not be clearly reflected in the effective stress curve because the upward-flow kinetic energy caused the perceived load to be diminished at the bottom LC (since the soil, which acts as the "sail" being pushed the flow, was above it) and increased at the top LC. This different and opposite effect in the load cells tended to counterbalance. In other words, the calculated effective stress remained relatively uniform since the effect of upward flow in the top and bottom load cells cancelled out (at least partially), nonetheless causing an overall upward force and movement that was perceived by the LVDT (Figure 5-5).

### *Acoustic emission*

The AE-response from this phase was more subtle and complex than in the earlier phase. The raising of the head itself did not directly correspond to an increase in RDC/min. The dislocation of fluid through the sample appeared to trigger an AE response at first, but due to either lack of sensitivity of the acoustic sensors or the RDC threshold being set nearly or completely

above the signal produced by only fluid flow (which was the intention – this work focuses on suffusion, which includes particle movement), its measured AE signal was either minor or inexistent.

What seemed to produce more significant AE signals were dynamics involving particle or overall soil mass movement. Head rise intervals were moments when AE activity tended to be significant and depended on the kind of process taking place. In the initial head rise intervals, AE was mainly due to either movement of the soil mass as a whole (or involving a significant volume of it; quite slight movements) or the start of suffusive particle movement. The WG was more sensitive to the former since it implied friction of the mobilised soil against the WG – this effect was also witnessed by the LVDT if this movement also propagated to the top of the sample. As mentioned in talking about the hydromechanical parameters, the head rise phase was prone to inducing soil mass dislocations. Otherwise, particle movement (directly impacting the WG) within the sample was the cause of AE.

The susceptibility of particles in suspension (if present) to cause AE signals on the BH, as previously mentioned, was a complicating factor for identifying the start of suffusion. This tended to be the case at the earlier part of a given test since the wash-out of this turbidity (which was not instantaneous) was also induced by an occurrence that may also cause internal erosion: water flow (besides of course passive decantation). That is, if seepage-induced internal erosion was triggered while the water volume containing the BH still had a significant amount of suspended particles (which, being able to directly impact the WG may cause significant AE despite their small size) their AE may have been mixed. Nonetheless, even in this context, the BH AE would still mean particle transport and would be pertinent and meaningful when applied to field conditions.

The TH seems to have most faithfully detected seepage-induced internal erosion – the WG seemed limited to direct interactions and the BH may have been influenced by particles in suspension. Although the TH was also seemingly influenced by mass soil movements (witnessed by the LVDT; to a lesser degree than the WG since a significant portion of this acoustic energy is of a frequency below the hydrophone measurement window), its signal corresponded to observed particle movement that took place after the onset of fluid flow.

Over a test or monitoring period, the highest RDC rate may not have been the most meaningful. That because phase changes (e.g. start of particle movement or pipe formation) may be reflected in the AE as changes “hidden” or comparatively concealed by higher RDC values that could correspond to the simple continuation of a process. This meant that interpretation should be done by observing the data at with the nuance of different scales and relative changes instead of simply focusing on AE peaks. This regards data from the tests

here discussed, including their limitations, which is likely to be improved upon and allow for a more precise and mathematic/algorithmic oriented analysis.

### 5.1.3 Ongoing flow (constant head)

This portion of the different tests was when the head tank remained at a constant height while water flow through the soil sample took place. As this water flow occurred, the soil particles might (or not) have reorganised, changing the soil in terms of e.g. permeability, homogeneity of water flow over its volume, grain-size distribution (overall or locally). Some of the perceived effects could result from the evolution or exacerbation of small-scale dynamics (e.g. single-pore-scale particle movements that initially influenced just their immediately neighbourhood; from soil grain or pore-size inhomogeneities) that might have been triggered before any [measurable] impression in the sensors of the test rig, including having been triggered in a previous test phase such as the head increase sequences.

This ongoing flow phase was particularly important because it in principle represented how the soil erosional dynamics could evolve (and become drastic) in the absence of changes to test conditions, or spontaneously.

*Hydraulic gradient (i) and Flow rate (Q)*

Hydraulic gradient (*i*) and Flow rate (*Q*) had varied behaviours during this ongoing flow phase of tests. The mechanisms responsible for the behaviour of these variables in this phase, excluding remaining constant (which implies the lack of relevant mechanisms; possibly applicable also to the head increase phase), seem to be the following:

- A reduction of *Q* denoted reduction of permeability due to partial clogging.
- Increase in *Q* meant an increase in permeability.
- Such a reduction might or not have had a corresponding effect on *i*.
- A correspondent drop in *i* implied no significant concentration of flow ("well-distributed" partial clogging for a rise in *Q*).
- A rise in *i* implied concentration of flow (overall hydraulic conductivity might vary but with concentration of flow) or simply a more drastic overall erosion.

There might be a time lag between the effects noted in these variables and they can be affected at different proportions or magnitudes in face of the causal soil dynamics.

*Effective stress (σ')*

The behaviour of the effective stress (*σ'*) while under constant head flow mainly differed from the condition where the head was being increased in that there is no scaling of the energy added to the system by the head rise. This meant that the soil and its hydraulic conditions

(e.g. particle distribution, flow rate, pore pressure) tended to either an equilibrium (perhaps a dynamic one) or a progressive condition (where properties of the system continually accumulate or degrade).

Essentially, all three kinds of simplified trends (rise, drop and [near-]steadiness) were observed with the *σ'* during this phase of the test. Differently from the rising head condition (where the head rise played a substantial role), the state with flow under constant head had appeared to be mostly affected by changes to the structure of the soil sample – which clarified its relevance to the evolution of internal erosion.

A drop in *σ'* during this phase of upward flow tests seemed to have been due to particle migration resulting in permeability reduction ([partial] clogging) that, in turn, caused the kinetic energy of the flow to counteract gravity. A rise in *σ'* is thought to have been due to an increase in permeability that allowed the kinetic energy of flow to be better dissipated – which was more significantly effected if fluid flow became [to some extent] concentrated. A constant *σ'* appeared to correspond to practically no change to the soil. In the case of downward flow, a static head (in the absence of particle transport or internal erosion) corresponded to a near-constant effective stress.

It should be noted that, effects of the head rise phase often have the arguably equivalent of inertia, in the sense of requiring time for the added energy (head rise) to the system to be dissipated or absorbed by e.g. the soil, pore-pressure, consequently "overspilling" into the following test phase. Concomitantly, the end of the head rise phase (thus halting the rate of head energy addition and allowing the system to [quasi] balance) could be reflected in a marked reversal of hydromechanical trends when the head was kept constant.

#### *5.1.3.1 Clog-and-flow*

The persistence of flow might cause particle reorganisation with two main effects (which, if at all occurring, can be consecutive, alternate in time or interact in various ways):

- Erosion proceeded to make the soil continually more permeable (e.g. by forming preferential pathways or simply overall removal of fines)

- Particles might have accumulated downstream possibly causing partial blockage to flow, reducing overall permeability.

If the soil (or its hydromechanical conditions, e.g. particle distribution, flow rate, pore pressure) showed a tendency to dynamically equilibrate, this was here called clog-and-flow. Clog-and-flow was here by and large defined as when particle transport by fluid flow caused particle deposits to form downstream of the soil sample and these deposits eventually offer a [partial]

barrier to fluid flow; this obstruction to flow was then partly or fully undone by the flow energy itself and cycles back to being formed (clog/flow reduction) and wiped out (flow increase). A way in which this might occur (and was observed in upward flow tests) is illustrated in Figure 5-6.

The observed in Figure 5-6 can be described as follows:

a) Material removed from the soil sample is deposited downstream of a preferential flow pathway, adjacent to it.
b) This deposit grows until its angle of repose is reached.
c) More material is added to the deposit but now directly above the preferential flow path (increasing resistance to flow, or clogging).
d) The amount of material above the flow path builds up (further increasing resistance to flow - further clogging).
e) The increased resistance to flow caused a rise in fluid pressure between inside the soil sample and the volume above it sufficient to provoke the expulsion of material from the top of the flow path (relief of clog; return to the equivalent of (c) or (d)). If more material is added to the deposit, the cycle may repeat.

It should be noted that the mentioned soil deposits responsible for the clogging tended to be quite loose and belong to the grain fraction that is fine enough to be transported by the flow but coarse enough to just be transported for a short distance (especially upwards), in the range necessary for the deposit to form and grow. Therefore, the characteristics of the formed deposits did not only depend on the soil properties but also on the kinetic energy of the fluid flow (which, as mentioned, might be unequally distributed over the sample). In the performed tests the grain size of such deposits tended to be from silt to fine sand.

One other note is that the fluid pressure difference (between within the soil sample and the volume above it, argued to increase as clogging proceeds) was not the measured hydraulic gradient of the sample, although they might behave similarly (which was observed in the tests described in this thesis).

Naturally, this effect could be considered an artifact of the used test equipment and methodology. However, it is thought that the discussed in this sub-section can be analogised to the formation and progression of sand boils (Bridle, 2017; ICOLD, 2016; USBR, 2015)

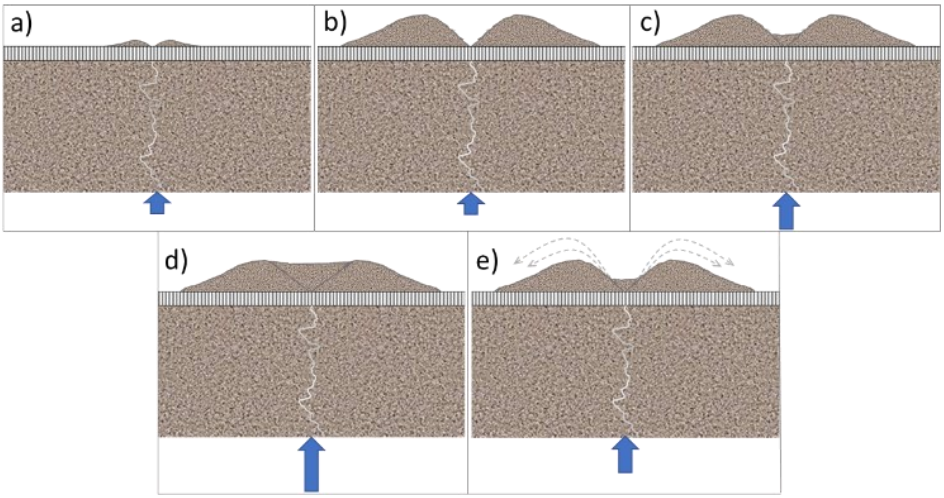


*Figure 5-6. Illustration of one clog-and-flow progression driven by seepage erosion in upward flow permeameter test - side view. Horizontal band with vertical line pattern represents perforated plate, volume below it is the soil sample, clear irregular line a preferential flow path and blue arrow indicates fluid pressure difference between within the soil sample and above it. The shapes above the perforated plate represent material removed from the soil sample and the grey dashed arrows show the ejection of material.*

Note that the abovementioned mode of clogging is one way in which it could happen. Another such way is when particles are transported downstream and, within the sample, become more concentrated in a portion of the soil volume (i.e. particles moved from the upstream to the downstream side of the sample) and there is no significant formation of preferential flow paths (the soil gradation and flow rate are, in effect, homogeneous for any given slice of the sample perpendicular to flow direction). Hence, the permeability of the sample becomes roughly proportional to the concentration of fines (or particles passive of suffusion) over itself – the upstream portion becomes more permeable and the downstream less so. This makes the hydraulic conductivity of the sample as a whole lower (the less permeable portion being the restraint) and, depending on the capacity of this lower hydraulic conductivity to block fluid flow, a [partial] clog may form. As this case relies on preferential flow paths not forming and once/if the clogging gets eroded the re-occurrence of well-distributed particle accumulations (perpendicularly to flow direction) is unlikely, it tends to not produce clog-and-flow cycles but tends to be a “one of” clogging during an experiment or progression of internal erosion.

### 5.1.4 Onset of erosion

Arguably, the highest interest of studying AE for monitoring seepage-induced internal erosion is in detecting the start of the erosional process, or the moment when the permeating fluid begins transporting particles. The attainment of this early detection carries the opportunity to make decisions and act with the highest likelihood of successful remediation, which is supposedly second-best only to predicting the process altogether.

Figure 5-7 shows a series of plots in which $Q$, $i$ and $\sigma'$ were overlayed with the AE RDC/10min of the TH, represented in relative terms by the size of circles on each curve. The TH was

focused because it was deemed to be the AE sensor with the more reliable signal – the BH seemed significantly influenced by the presence of particles in suspension (especially at this initial phase of tests) and the WG seemed exclusively sensitive to direct interactions with moving soil particles, both of which are still significant but deemed less so than the TH.

The observed AE signal was susceptible to hardware responsiveness and threshold setting (done at each test by observing apparent noise band and electing the voltages produced above it as valid). This made so that a) associating a voltage response of the sensor to a certain amount of internal erosion – or making one quantifiable by the other – was not considered reliably doable and b) the defined filters may have excluded signal. Therefore, signal interpretation was partly qualitative. However, it so happened that the AE signal was still quite clear and useful.

In the plots of Figure 5-7 the onset of internal erosion (or at least particle movement) was interpreted as a large and clear rise in the RDC of the sensor (made graphically obvious in the plots by increases in circle sizes). The correlation between this onset and the displayed hydromechanical parameters considered strongest was with the flow rate ($Q$), where a certain flow rate (thus the kinetic energy of the fluid) being achieved seemed to trigger the erosional process. There was an apparent non-linearity to this correlation since it was possible that the AE showed an increase when $Q$ reached a certain value for a second time or AE decreased over time despite an increase in $Q$. Possible causes of such behaviour are: a) particle movement was detected just when the set voltage threshold was met (but had already started, however slightly), b) particle movement just needed time to begin or become significant (i.e. particle dynamics needed time to evolve) and/or c) as erosion evolved there was a “clearing” of pores with initially active particle movement as some of the mobilised particles were removed/pushed out of these proto-preferential flow paths, reducing the amount of particle collisions.

About the qualitative aspect of this interpretation: a quantifiable proportionality between the observed phenomena and the recorded signal was strongly implied (and simply could not be irrefutably asserted), meaning that improvements to the hardware/processing are very likely to make such a quantification genuinely doable.

If the fines that may be transported by the fluid flow were not load bearing, that is, if the stress (load) was supported by a skeleton that excludes the fines, a load increase that did not overcome the static friction of this skeleton seemed to not influence the occurrence of suffusion.

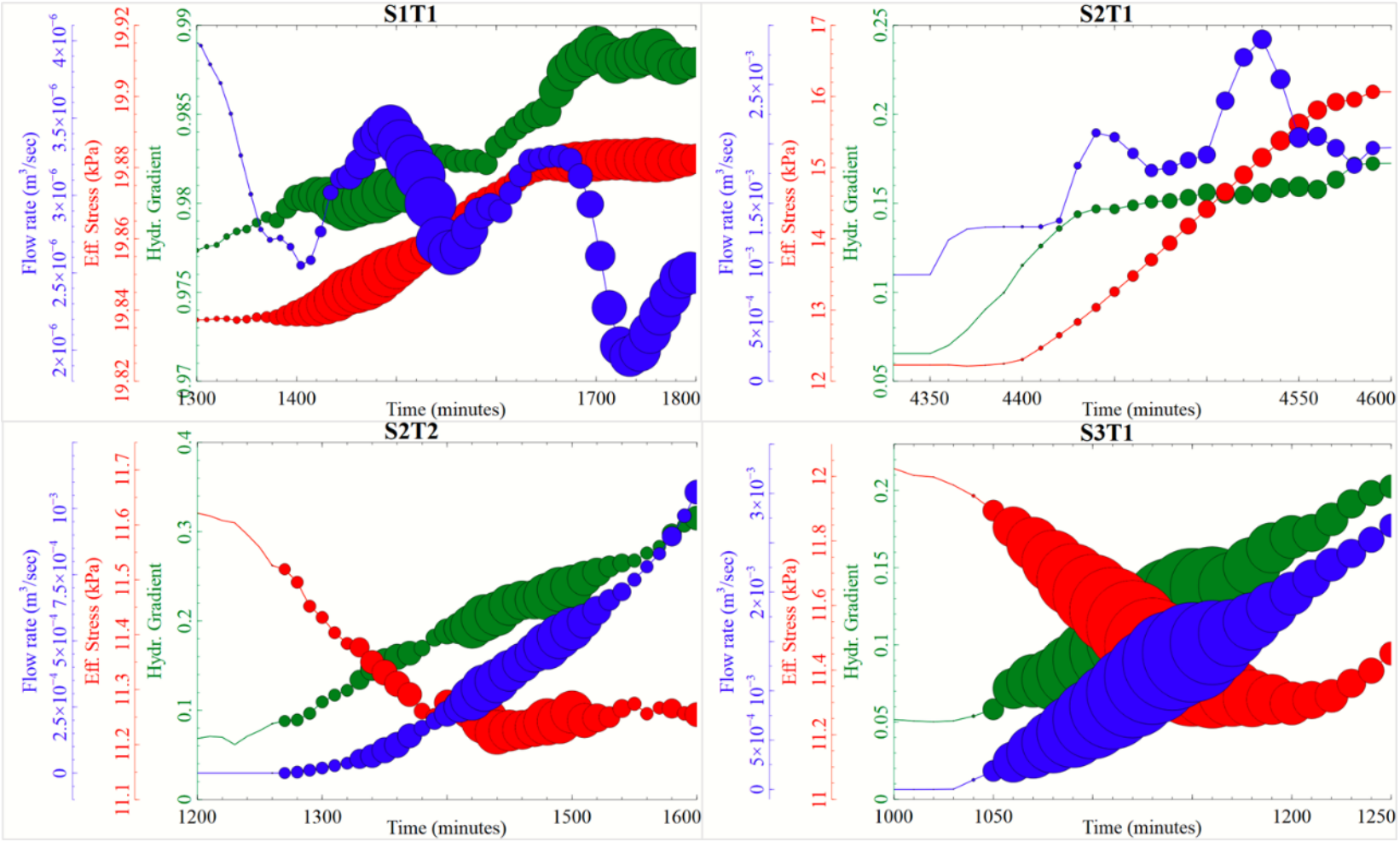


*Figure 5-7. Time-domain plots of internal erosion onset as detected by the top hydrophone (TH). The colours of the plots and y-axes correspond respectively to effective stress (red), hydraulic gradient (green) and flow rate (blue). The circle sizes indicate the comparative AE RDC/10min over time – these do not correspond to absolute values (e.g. when confronting plots) but intend to show how the AE grew over time. In each plot the circle sizes in all the curves (Q, i and σ') are the same at any given time. 1 of 3.*

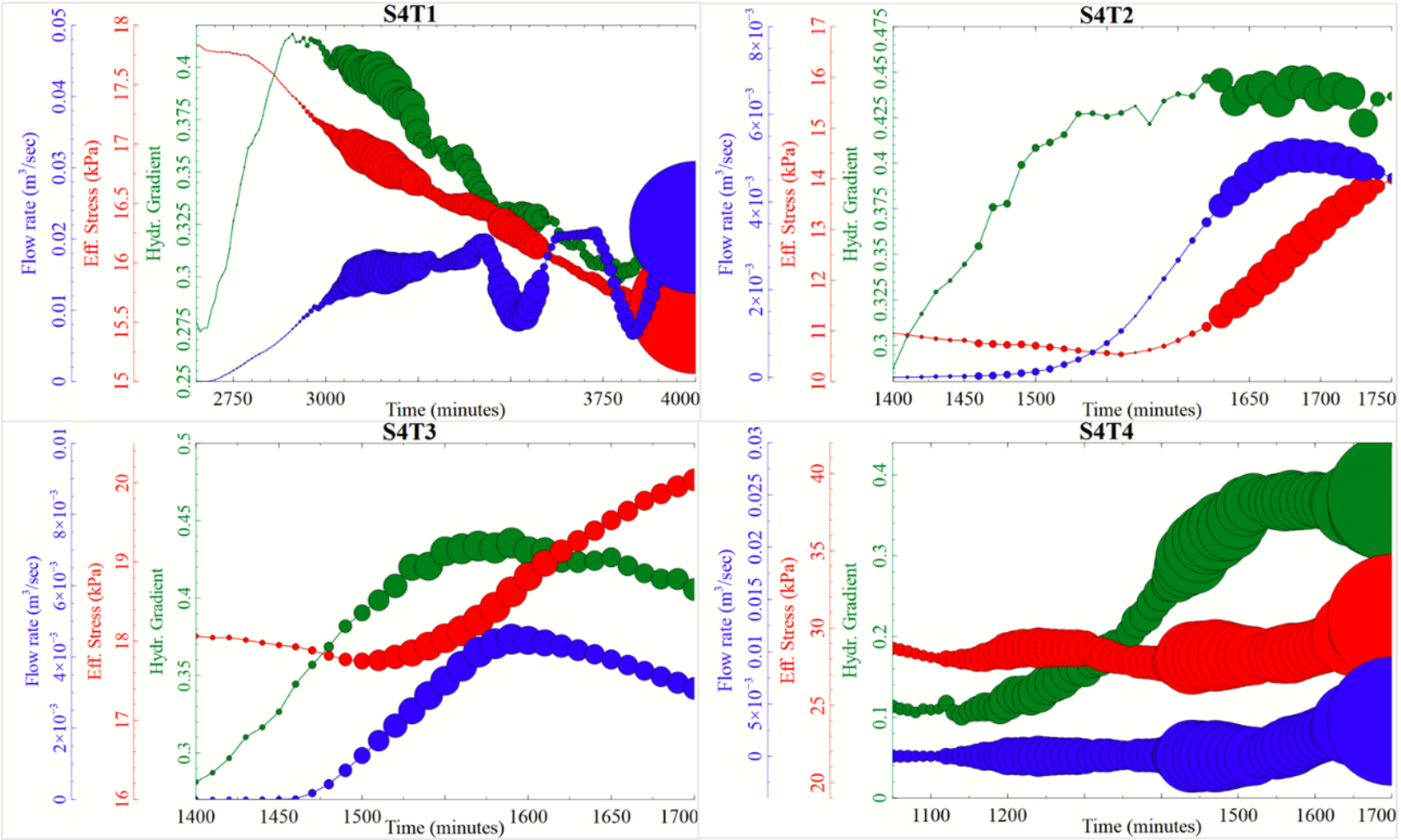


*Figure 5-8. Time-domain plots of internal erosion onset as detected by the top hydrophone (TH). The colours of the plots and y-axes correspond respectively to effective stress (red), hydraulic gradient (green) and flow rate (blue). The circle sizes indicate the comparative AE RDC/10min over time – these do not correspond to absolute values (e.g. when confronting plots) but intend to show how the AE grew over time. In each plot the circle sizes in all the curves (Q, i and σ') are the same at any given time.*
*2 of 3.*

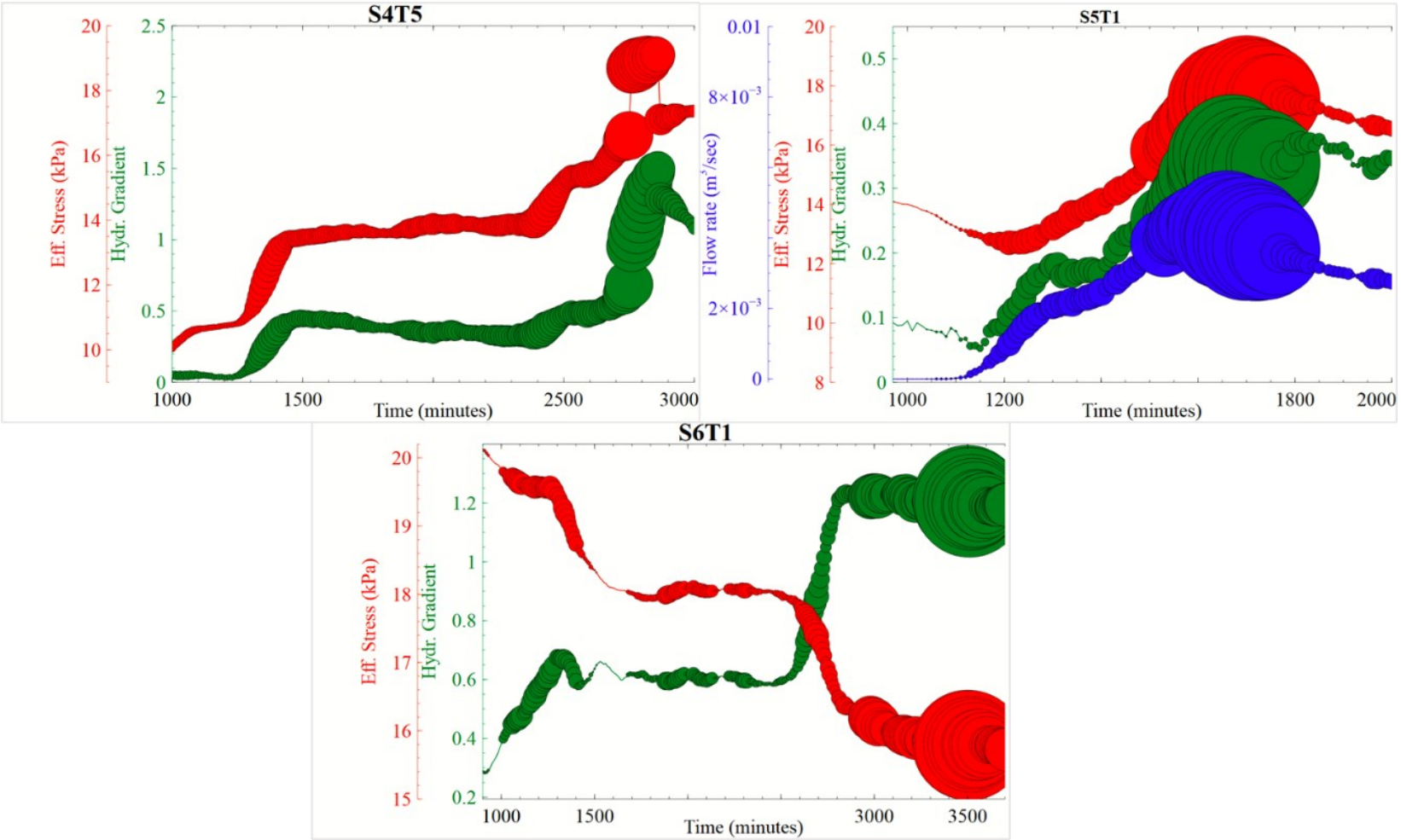


*Figure 5-9. Time-domain plots of internal erosion onset as detected by the top hydrophone (TH). The colours of the plots and y-axes correspond respectively to effective stress (red), hydraulic gradient (green) and flow rate (blue). The circle sizes indicate the comparative AE RDC/10min over time – these do not correspond to absolute values (e.g. when confronting plots) but intend to show how the AE grew over time. In each plot the circle sizes in all the curves (Q, i and σ') are the same at any given time. 3 of 3.*

*Note on seepage velocity:*

Seepage velocities considered in geotechnical engineering are generally area-averaged flow rates and their relation to the actual fluid velocity at the pore scale was unclear; existing models for estimating hydraulic conductivity fail to explain the governing variables, which relate to the micro- scale properties of the void space (Taylor et al., 2017). There is a tendency to consider the soil as a homogeneous mass and that the onset of erosion corresponds to a generalized change of the measured properties (e.g. hydraulic gradient), ignoring that instability (or at least initiation of particle movement) can occur in localized portions of the soil mass in a way that the measured variables do not reflect due to the scale of their measurements (including that an effect in the measurements may simply be of low magnitude and marginal in proportion to the measured scale). Figure 5-10 illustrates how the fluid properties under seepage flow can vary at the (sub-)particle scale and is corroborated by the observations made in the experiments of this study.

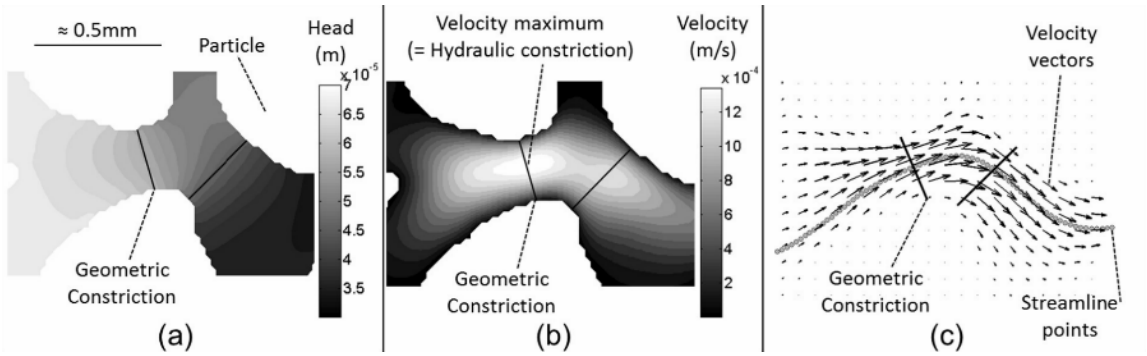


*Figure 5-10. CFD simulation of how preferential flow paths and local flow velocities can vary significantly even within a single void constriction. (a) Head contours, (b) velocity contours, and (c) velocity vectors and streamline. (Taylor et al., 2017).*

Increases in flow velocity may produce the equivalent of different phases of internal erosion, since the increased kinetic energy may be able to mobilise a different portion of the soil (e.g. non-load-bearing coarser grains that fit through pores). This could be induced e.g. by the head being further increased or by particle transport reorganising the soil in a way that flow becomes more concentrated.

## 5.2 Comparison with other studies

Comparison between the results of this research and other studies in the available literature shows that this work offers new insights, partly because other authors have not yet addressed the matter at hand in a similar way. Such studies tend to have the following comparative faults:

- Just address the hydromechanics of the issue by simulating it without exploring new ways of remediation or detection (no AE).

- Observe AE produced by seepage only (no induction or distinction with internal erosion)
- Observing internal erosion through AE but in overly susceptible or otherwise unrealistic conditions.

These often consider the occurrence of internal erosion in considerably advanced stages or under acute forcing. For instance, the use of eroded particles (ejected from the soil specimen confinement) as indicator of internal erosion is seemingly flawed because it may correspond to a relatively advanced portion of the erosional process – in the experiments of this study it was observed that, when [localised; Figure 5-10] flow kinetic energy sufficient to move particles in a susceptible soil is achieved, the overall hydraulic gradient might remain effectively unchanged. This effect is deemed only visible if the hydraulic head is changed slowly enough and give small changes in the sample time to develop, as a quick or acute change in such conditions may simply cause internal erosion in an obvious but extreme way.

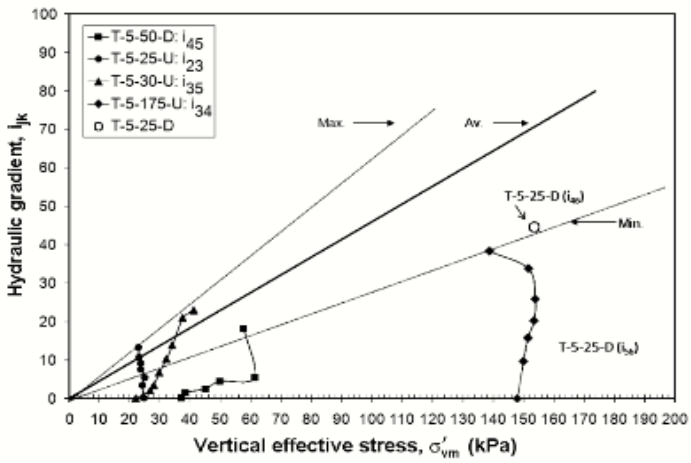


*Figure 5-11. Hydromechanical boundary to internal instability for a given soil gradation as reflected by the relationship between effective stress and hydraulic gradient (Moffat and Fannin, 2011)*

Compared to the seen in Figure 5-11 (Moffat and Fannin, 2011) and other work, the tests, results and interpretations in this thesis:

- Showed longer and more complex development of soil dynamics, with tests lasting several days and with respective cycles of head rise, constant head, and return of the head to neutral.
- Used a more moderate and more slowly applied range of hydraulic heads/gradients, allowing the soil dynamics to progress in a way marginal to its stabilisation (e.g. internal erosion was not induced due to hyperbolic surmounting of its stability boundaries)
- Considered nuances of seepage erosion, inhomogeneities of particle distribution, localised differences in hydromechanics as relevant (regardless of their measurability)

The table below (Table 33) lists particularities and specifications of other studies.

*Table 33. Comparison with comparable studies.*

| Characteristics / Study | Type of study | Target issue (summarized) | Water flow direction | Test duration (~minutes) | Stress induction | Hydraulic gradient | Sample dimensions; height×width (mm) | Grain-size range (mm) | Notes |
|---|---|---|---|---|---|---|---|---|---|
| *Ferdos et al., 2018* | Experimental (permeameter) | Creation of constitutive law for the onset of internal erosion. | Upward | 1530-5800 | Vertical; rigid wall. 0-59.8kPa | 0.2-4.1 | 350×200×150 | 0.01-10 | Original erosion apparatus capable of applying hydraulic and mechanical loading while observing the erosion process |
| *Moffat et al., 2011* | Experimental (permeameter) | Susceptibility to internal erosion of widely graded cohesionless soils. Novel insight into the spatial and temporal progression of seepage-induced internal instability | Up- and downward | 820-11570 | Vertical; rigid wall. 25-175kPa | 0-31 (average) | 325-550×279 | 0.03-80 | Internal erosion identified visually (through rig wall), from post-test observations, changes in hydraulic gradient and from axial displacement. |
| *Robbins et al., 2017* | Experimental (permeameter) | Measure hydraulic conditions in backward erosion piping. | Horizontal to vertical | 60-130 | Self-weight | 0.2-1 | 25.4; 75.6;152.4×1000 | 0.2 ($d_{10}$) – 0.65 ($d_{60}$) | Induced erosional pipe at the top of the sample and measurement of pressure, pipe flow velocity and pipe geometry in time. |
| *Slangen and Fannin, 2017* | Experimental (permeameter) | Description of a flexible wall permeameter for investigating seepage-induced internal instability. | Upward | 60-370 | Triaxial; flexible wall. 50-100kPa | ----- | 100×100 | 0.1-2 | Describes need to measure volume change during multistage seepage flow to avoid misinterpretation of seepage flow effects. |
| *Marot et al., 2016* | Experimental (permeameter) | Energy-based experimental method for estimating the susceptibility to suffusion and backward erosion. | Downward | 30-300 | Triaxial; flexible wall. 0, 15 and 100kPa | 0.1-18 | 100×50 | 0.0005-10 | Method can be used for cohesionless soils and clayey sand. |
| *Douglas et al., 2019* | Experimental (permeameter) | Development of method for predicting the amount of erosion and the erosion mechanism based on the gradation of the soil. | Downward | 15-235000 | Self-weight | 1-10 | 470×500 | 0.08-70 | Test showed global backward erosion, suffusion, and internal instability without erosion from the sample. |
| *Liang et al., 2019* | Experimental (permeameter) | Suffusion induction increasing hydraulic gradients under isotropic and anisotropic stress conditions. Proposition of formula to estimate critical hydraulic gradients. | Upward | 300-400 (estimated) | Triaxial; flexible wall. 10-116kPa | 0.1-0.8 | 200×100 | 0.08-10 | Suffusion identified by eroded mass and changes in hydraulic gradient. |
| *Taylor et al., 2017* | Experimental (permeameter) and CFD | Pore-scale understanding of water flow in soil; proposition of first principles simulation approach for modelling flow in the void space. | Upward | ----- | Self-weight | ----- | 150×75 (permeameter) 9×6×6 (CFD modelling) | 0.05-20 | Void geometry obtained by MicroCT scan and used for CFD simulations. |
| *Flammer et al., 2001* | Experimental (saturation chamber) | Acoustic assessment of flow patterns in unsaturated soil | ----- | 11400 | Self-weight | ----- | 800×300 | <1 (loess) | Absorption of acoustic energy seen to increase and sound velocity to decrease during water infiltration and re- distribution in soil. |
| *Hung et al., 2009* | Experimental (permeameter) | Detection of seepage by monitoring acoustic emission | Upward | ----- | Self-weight | 0.11-0.92 | 276.2×114.3 | 2.8-7.1 (median) | Development of methodology for detecting excessive seepage using AE intensity. |
| *Lin et al., 2020* | Experimental (triaxial cell) | Use of AE for characterizing drained triaxial compression tests with dry sands. | ----- | 60-180 | Triaxial; flexible wall. 100-600kPa | ----- | 100×50 | 0.07-5 | Correlation between AE hit rate and strain under different stress conditions observed. |
| *Lu and Wilson, 2012* | Experimental (flume) | Use of active and passive acoustic techniques to monitor and assess soil pipeflow and internal erosion. | Horizontal (5%slope) | 30 | Self-weight | ----- | 250×1000×1400 | Providence silt loam. | Link between effective stress and its relationship with the P-wave velocity to erosional processes (active acoustics) and pipeflow detection from time and freuqncy-domain analysis (passive acoustics). |
| <u>This study</u> | Permeameter; gap-graded soils | Internal erosion detection with AE | Up- and downward | 4000-10000 | Vertical; rigid wall. 30-54.3kPa | 0-4.5 | 500×280 (cylinder) | 0.002-14 | Yes (hydrophones, waveguide) |

*Effective stress vs. hydraulic gradient:*

A common assessment of internal erosion based on hydromechanical parameters has been done by confronting effective stress and hydraulic gradient (Moffat and Fannin, 2011; Chang and Zhang, 2013; Li, 2008). Two examples of this approach from the experimental results of this thesis can be seen in Figure 5-12, Figure 5-13 and Figure 5-14. Other such plots can be found in the Appendix.

The occurrence of particle movement/suffusion triggered by seepage can be noted by the relative increase in the size of the circles on the plot, which correspond to the AE RDC from the top hydrophone. This directly meets the central purpose of this research.

The plotted relationships between *i* and *σ'* formed paths that varied from one test to another due to random inhomogeneities in the sample. This influenced e.g. localised flow rates (Figure 5-10) and the predisposition to formation of preferential flow pathways. In turn, the eventual dominance of such local differences in relation to the properties of the overall soil volume could be determined, which may vary in degree. In other words, the apparatus outputted single/global *i* and *σ'* values that considered the sample as a whole, but localised/nuanced dynamics (which could partially influence or dominate the measurements) had to be taken into account in interpreting the results, despite not being quantified or even quantifiable.

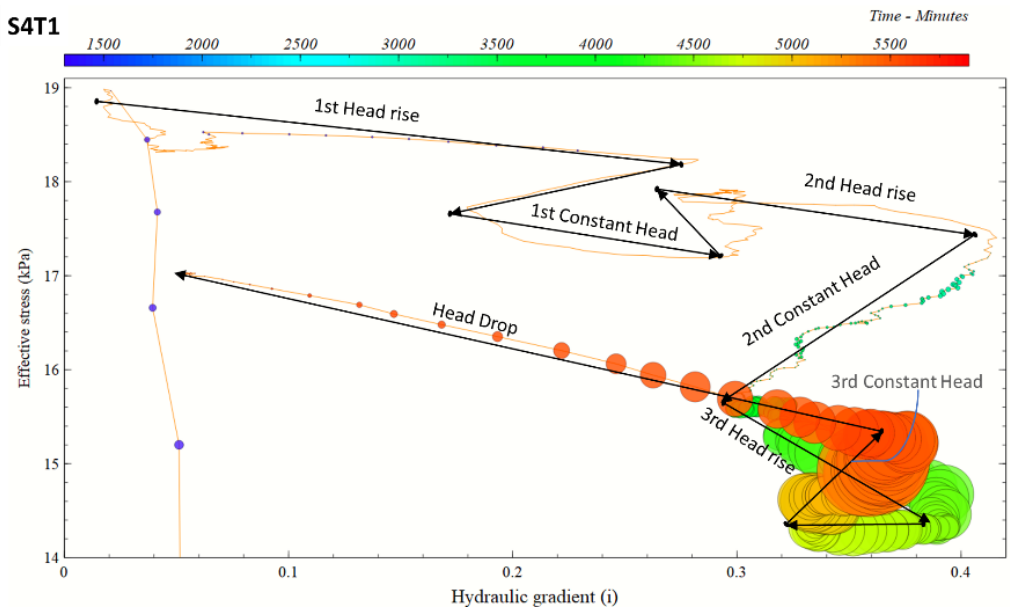


*Figure 5-12. Effective stress vs. hydraulic gradient of S4T1. Colour coding represents passage of time (legend on top - minutes) and the size of circles represents relative RDC magnitude (counts/10min). Black arrows and corresponding/parallel text inform consecutive test phases.*

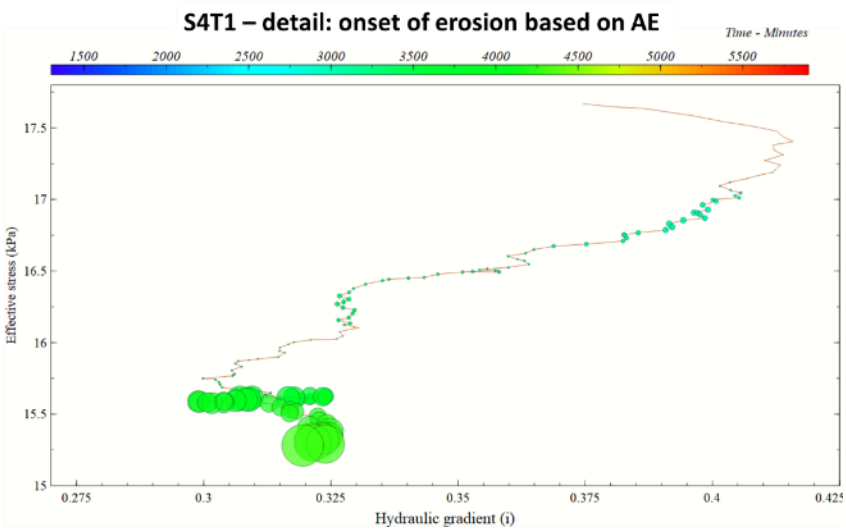


*Figure 5-13. Portion of plot shown in Figure 5-12, between minutes 2800 and 4300. During this interval the onset of internal erosion has been inferred as witnessed by the increase in circle sizes (indicating relative RDC/10min), in the passage between the 2nd constant head to the 3rd head increase moments (indicated in Figure 5-12).*

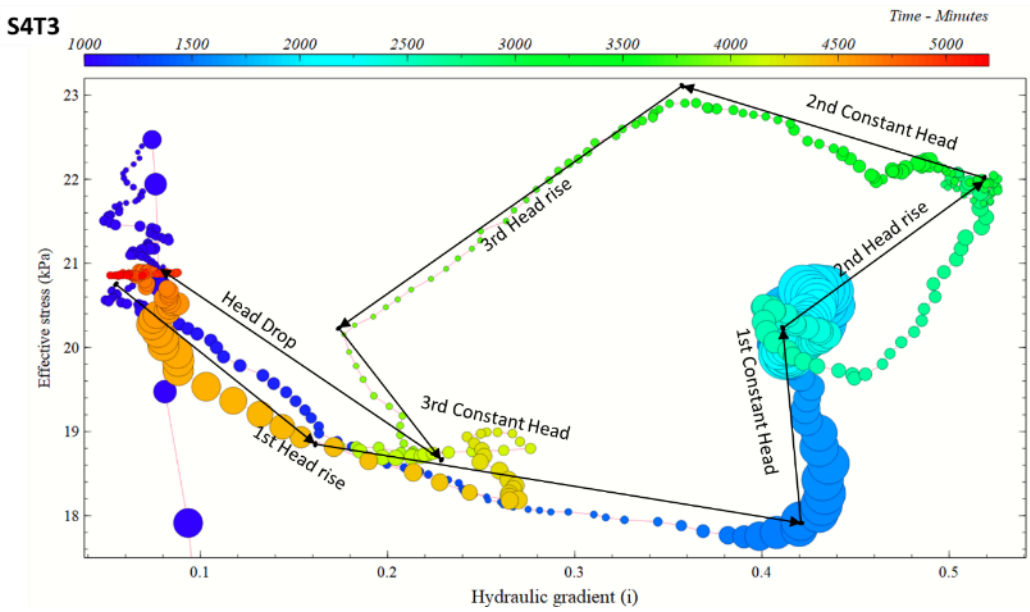


*Figure 5-14. Effective stress vs. hydraulic gradient of S4T3. Colour coding represents passage of time (legend on top - minutes) and the size of circles represents relative RDC magnitude (counts/10min). Black arrows and corresponding/parallel text inform consecutive test phases. Onset of internal erosion interpreted during the passage between the 1st head rise and the following constant head interval (when circle sizes show notable increase; ca. min 1500).*

### *Note on de-aired water not having been used:*

The use of de-aired was considered unnecessary for the following reasons:

- In real-world/field conditions dissolved air in water is rather ubiquitous.

- This project was centred on the detectionf internal erosion using AE and the interaction of air [bubbles] with sound propagation in not negligible (Raichel, 2006; Lurton, 2010; Kadam

and Nayak, 2016). Therefore, considering the point mentioned above, using de-aired water was likely to make the AE results from laboratory testing less realistic and reduce their potential applicability of the technique where it matters – the real world.

- The piping/tubing of the permeameter was designed not to trap air bubbles, especially in the upward flow configuration. Air bubble entrapment would be limited to the soil itself, in a way that would possibly also occur in nature.

- A series of peer-reviewed published studies do not use or do not mention the use of de-aired water in their permeameter tests - e.g.: USACE 1953, Adel et al. 1988, Skempton and Brogan 1994, Wann and Fell 2004, Mao 2005, Liu 2005, Sibille et al 2015, Yang 2019, Zhang 2019. See .Table 34. In the case of authors that do not mention using de-aired water, given the extra effort in producing it, it is strongly implied that they did not use it.

*Table 34. Test conditions of studies investigating the occurrence of internal erosion* (Li, 2008).

| Year | Author | Specimen Size (cm) | Surcharge (kPa) | Water Quality | Hydraulic gradient | Flow direction | Vibration | Criteria |
|---|---|---|---|---|---|---|---|---|
| 1953 | USACE | 25.4 | 0 | Tap water | 0.5 – 16 | downward | Vibration | Geometric |
| 1985 | Kenney and Lau | h=20 – 50<br>d=24.5 or 58 | 10 | Re-circulated water | Re > 10 | Downward | Manual tapping | Geometric |
| 1988 | Adel et al. | l = 105 | 0 | Not mentioned | 0 – 1 | Horizontal | No | Hydraulic |
| 1994 | Skempton and Brogan | h = 15.5<br>d = 13.9 | 0 | Not mentioned | 0 – 1 | Upward | No | Hydraulic |
| 1996 | Honjo et al. | h = 10<br>d=15 or 30 | 0.9 | Tap water | 2.5 – 19 | Downward | Tapping | Geometric |
| 2004 | Wan and Fell | h = 25 - 30<br>d = 30 | 0 | Not mentioned | 10 – 20 | Downward/ Upward | No | Geometric/ Hydraulic |
| 2005 | Moffat | h = 30 – 50<br>d = 28 | 25-175 | Distilled and de-aired | 1.0 – 65 | Downward/ Upward | No | Hydromechanical |
| 2005 | Mao | h = 20 – 30 | 0 | Not mentioned | 0 – 1 | Upward | No | Geometric/ Hydraulic |
| 2005 | Liu | h = 20 – 30 | 0 | Not mentioned | 0 – 1 | Upward | No | Geometric/ Hydraulic |
| 2006 | Fannin and Moffat | h = 10<br>d = 10 | 25 | Distilled and de-aired | 0.1 – 15 | Downward | Automatic vibration | Geometric |

- Producing the necessary amounts of de-aired water for the performed tests would severely increase the necessary experimental setup in an arguably unnecessary way.

- It is not denied that the presence of air in water may have in important factors concerning seepage. But, although the use of de-aired water may produce "cleaner" results, the trade-off regarding realism and other factors such as mentioned above led to the decision of not using it.

- The focus of this project was the use of AE for the detection of internal erosion. Roughly speaking, the specific conditions (e.g. hydraulic gradient, flow rate, permeability, effective stress) at which internal erosion occurred during the performed tests was secondary: if internal

erosion occurred, the capacity of using AE for detecting particle transport by fluid seepage was the central point being examined. The parallel analysis of the hydromechanical parameters (which may have been relevantly influenced by the presence of air in the used water or not) served to better assert the occurrence of internal erosion and investigate the AE signal as internal erosion developed.

- The observation of and results from the performed tests indicate that the produced outcomes satisfied the purposes of this research.

## 5.3 Factors influencing the onset of instability.

Beyond the geometric criteria governing the feasibility of grains mobilised by internal erosion to be transported/fit through the pore spaces of the soil, the onset of seepage-induced internal instability was interpreted as a result of the following criteria being met:

*a) Internal instability*

Existence of pore spaces large enough for the passage of grains transported by fluid seepage as well as a grading that has the finer portion of the grain-size distribution subject to different hydromechanic conditions than the rest of the soil. The overall effective stress seemed unimportant if the soil fraction passive of suffusion is not load-bearing.

*b) Sufficient pore-scale flow velocity*

Seepage velocity with enough kinetic energy to transport soil particles of the fraction satisfying the conditions described above. Noting that the seepage velocity to be considered is that at the pore-scale (Figure 5-10).

Note that these criteria may be met just locally within a given soil volume – intrinsic, incidental, or random heterogeneities within the soil, which can be of the particles themselves or of their hydromechanic circumstances, can trigger or somehow influence the process.

*Note on the influence of other processes:*

It is possible that slow and progressive (bio-)chemical or mechanical degradation (e.g. mineral dissolution, hydraulic or cryogenic erosion) of soil grains over long time periods may have effects in soil properties such as grain-size distribution, permeability, and particle shape. Allied to a sufficient time scale (reminding that several dams, levees are quite old), a series of variables like pH of the fluid, seepage, biological activity, temperature, cyclicity, fluid viscosity,

flow regime within pores (linear, turbulent), and so on could play a role (Kump et al., 2000; Luquot and Gouze, 2009; Maher and Chamberlain, 2014; Anbeek et al., 1994; Anbeek, 1993; Reeves and Rothman, 2013; Jung and Navarre-Sitchler, 2018; Beckingham et al., 2016; Brantley, 2010). This could eventually change the soil enough to make it transition from a condition of internal stability to one of internal instability and can be considered a candidate explanation (or at least an additional one) for why some structures eventually show signs of integrity loss/damage/ many years after their construction. (Kump et al., 2000; Luquot and Gouze, 2009; Maher and Chamberlain, 2014; Anbeek, 1993; Reeves and Rothman, 2013; Jung and Navarre-Sitchler, 2018; Beckingham et al., 2016; Brantley, 2010). Such arguments reiterate the importance of real-time, continuous, and non-invasive structural monitoring.

## 5.4 Influence of test equipment

Intrinsic to the use of laboratory testing for studying field/real-world phenomena is how much the used equipment influences the produced outcomes as well as how aptly the experiments represent the targeted matter. This issue is here treated in relation to the present study and with focus on the following points.

### *Stress application and wall friction*

Although there seemed to be no significant problem with the way in which vertical stress is produced and applied to the top of the soil sample, the transmission of this stress over the length of the sample was hindered by the friction between the soil and the permeameter wall. A time lag between the application of vertical stress (as the static friction slowly gives in) as well and deformation as well as a slow transmission of vertical stress through the sample (from top to bottom; due to wall friction) could not be excluded as cause of post-loading AE.

Specifying how much (e.g. soil-permeameter coefficient of friction) and with what geometry (where in the sample, at what gradient, linearly or not) the vertical stress transmission was affected by wall friction was not accomplished. It was nonetheless observed that this was a partial effect (the addition of vertical load was reflected in the bottom LC) and varied during a given test (due to e.g. soil erosion, flow rate, hydraulic head), as described in the Results and Discussion sections – naturally, this fact was taken into account when interpreting the data.

### *Boundary effects*

Intrinsic to the use of a tube as sample container, is how the interface between the specimen and internal wall of the tube may have different properties compared to its inside/core, especially in terms of porosity, permeability, and stress conditions. Aside for being legitimised

by published work done by other authors who use similar approaches (Moffat et al., 2011; Li, 2008; Hunter and Bowman, 2017a; Moffat and Fannin, 2006), the formation of e.g. preferential flow paths at the soil-wall boundary did not appear to occur at the initial stages of the erosional process as at the top of the sample small particle movements were observed near the centre of its diameter.

In advanced stages (e.g. well-developed erosional pipes), erosion did seem to concentrate at the permeameter wall, but this seems to be more likely because this (acrylic) wall is in effect not erodible and, when soil erosion reaches it, particles are restrained to move within the soil and, with erosion progressing, the wall-soil discontinuity does become a preferential pathway. In fact, this is a reason why only vertical flow (down- or upward) tests were done: despite the likelihood of boundary effects at the wall-soil interface, a vertical positioning of the permeameter tube keeps all points of a given horizontal slice of the specimen (including its perimeter) radially symmetric – any part of the sample near the wall (given that it's cylindrical) is equivalent to any other such part. Conversely, with a permeameter tube positioned non-horizontally, the top and bottom half of the tube (notably the top and bottom extremes) will tend to be under fundamentally different circumstances considering e.g. gravity and fluid flow in terms of how particle movement will tend to preferentially accumulate particles at the lower side (e.g. increasing its permeability) while emptying the higher portion (making it a nearly unescapable preferential flow pathway), which, arguably, only exacerbates boundary effects.

Compared to the expected in a real circumstance in which a surface equivalent to the permeameter wall (i.e. a solid anthropogenic or geologic structure) is absent, the geometry of the erosional process, especially pipe formation, is thought to proceed in a less predictable way and perhaps more slowly (as lateral dislocation of proto-preferential pathways is more likely) but would still be delimited by either preestablished inhomogeneities in the soil mass (e.g. anisotropies (load or deformation driven), [depositional] artifacts of the building process, layering, etc) and/or by the sort of fluid dynamics illustrated by flow nets (see section 2.3.2, Influential factors for internal erosion).

### *Confining plates*

The use of perforated plates containing the top and bottom of the sample can be criticised for, at the downstream of upward flow, allowing the accumulation of eroded particles on the plate and in the "open water" volume above it. This might induce the kind of clogging described previously (Figure 5-6) in a way that may, arguably, not be represented by real/field processes – for instance, in a real earth structure the filter would likely transition from a high to a low stress condition gradually and not at one well-defined surface such as simulated by the perforated plate. However, the soil skeleton is assumed to be effectively immobile even at

relatively low stresses and a transition such as in the used permeameter could be expected at the surface of a given structure below which seepage may occur (e.g. dam toe)

Furthermore, the design of the perforated plates respects the geometric distinction (corroborated by observation) between coarser grains passive of being eroded and the finer ones subject to it by having properly sized orifices/perforations that allow the passage of the latter while containing the former.

*Particle ejection from permeameter*

In case of particle transport in the sample and especially in upward flow, soil particles can be removed/eroded from the sample but the kinetic energy of the water flow [on the downstream] might not be sufficient to effectively eject this material (or a fraction of it) from the permeameter (towards the outflow tank). This can result in particles accumulating downstream (on top of the sample for upward flow) and at least partially clogging/creating resistance to the flow itself. Despite being an artifact of equipment design, this is in effect analogous to real/field situations such as the formation of a sand boil (Technical Advisory Committee on Flood Defences, 1999)

*AE sensors*

One relevant question is why the different AE sensors responded differently. Besides issues with their calibration and correspondent quantification of their signal, two main aspects seemed to be the source of this difference: a) their operational mechanisms and b) their position within the permeameter relative to the soil sample (leading to the capture of meaningfully different signals):

a) The waveguide seemed to only detect signals caused by its direct interaction with the soil (friction, particle collisions) while the hydrophones detected signals from compressional waves transmitted by the fluid (caused by particle interactions at a distance or simply fluid movements/flow) without excluding the detection of direct particle interactions with themselves (collisions; as the hydrophones are outside of the sample, friction by movement of the soil matrix was excluded).
b) The TH was above the sample (ca. 5cm from the top perforated plate), the WG inserted into the soil sample (at about its centre; perpendicular to the permeameter length/height and overall fluid direction) and the BH below the soil sample (ca. 40cm below the bottom perforated plate).

The difference in operational mechanisms (a) helps explain the signal difference between the WG and the hydrophones – if the region of the sample adjacent to the WG moved, this would be detected, while the signal of the hydrophones reflects the more general behaviour if the

sample. This of course fails to explain the difference of detection between the hydrophones – departing from the idea that the signal these two devices should be similar.

A clue about the different signals of the hydrophones is given by their positions. After positioning the soil in the permeameter it was noted that the water volume below the perforated plate became turbid with fines (from the soil mixture) that inadvertently passed through the bottom perforated plate and diffusely stayed in suspension. The particles responsible for this turbidity (primarily silica flour, the finest base material used to form the intended soil gradations) slowly fell to the bottom of this water volume– where the BH was located (b) – by decantation and a portion of these fine grains made direct contact with the BH, which would not happen with the TH by virtue of its opposite position (b). The preferential direction of this movement implies that the number of particles hitting the BH could vary over time. This would explain why the signal of the BH during vertical loading is in some tests seems less pronounced than the signal of the other AE sensors: the “background signal” of the BH (ring-down counts per 10 minutes) caused by decantation of fines can rival that of the vertical loading (“moderating” its relative RDC spikes), besides lasting for a longer period of time. Also, based this idea, the onset of water flow would “flush out” this turbidity, reducing the signal of the BH – this, with the applicable particularities, was observed in the subsequent phases of the performed tests. This seems to agree with the observations by Koerner et al. (1981), Figure 2 18.

Attenuation is another possible cause for the difference between the hydrophones, in the sense that acoustic events reaching one of these sensors might not be able to travel [through the sample] and reach the other one. This possible issue could not be verified because of the preceding difficulties with calibrating and establishing proportionality of their output.

It should also be noted that the used 10kHz-100kHz frequency filtering, even with or at the cost of less environmental noise and clearer signal, can cause the omission of acoustic signals corresponding to real soil interactions that happen to be outside of this frequency range.

### 5.4.1 Justification of faults and deficiencies

Much more and better had been planned to be done in this research. Although the plans were realistically within the possibilities, problems along the way forced compromises to be made. These problems were not sufficient to spoil the research but did lessen its achievements in face of what could have been done. This may be taken as cautionary for future research. The main issues faced are described below.

*Time*

The time it took to build the designed test apparatus was drastically extended by the less-than-ideal availability of technicians and specialised machinery (e.g. machining and welding of parts, installation of fittings, etc). This made time for testing and possibly modifying the equipment as well as fixing other problems scarce – in fact, this experience implied that this should be avoided due to the project restraints. Therefore, although improvements were identified and desirable, it was decided that the program had to move forward.

It should be mentioned that this PhD candidate had not been trained in some of the performed tasks such as equipment design and operation of some of the equipment – my know-how was mostly in understanding the data and scientific principles involved. But nonetheless, these were studied and attempted, with results that are considered satisfiable given the circumstances.

*Apparent equipment defects*

Ancillary equipment (e.g. preamplifiers for the load cells and acoustic sensors) appeared not to work as consistently and accurately as expected. This had effects such as the absolute values (or at least their margin of error) of some of the sensors being debateable, particularly when comparing different tests. Solving this issue was of course attempted, including by consulting apt colleagues and technicians, but the specifics of this problem (which was itself deduced) were not identified and no solution was found. Uncertainties in this regard rendered even measures like equipment acquisition/replacement questionable as this lack of technical understanding made it hard to justify new funding allocation (which had already been generous and entrusting).

However, despite such issues, the produced measurements turned out to be quite useful and interesting, being chiefly applied for understanding the evolution of the studied processes by observing relative changes over time.

*Frequency domain analysis*

The intention to study the acoustic data in the frequency domain had been intended since the preliminary phases of this research and had even been prepared in the newly commissioned test rig. However, during the first tests lasting longer than ca. 500 minutes, a problem with the data storage system made this unfeasible. The storage of the data required for this type of analysis (at least in the considered format and compatible with the available software) seemed to overwhelm the capacity of the used computer and network set-up, repeatedly crashing it. Therefore, the simpler and more manageable data discussed in this thesis were used, which turned out to be nonetheless quite valuable.

## 5.5 Implications

This research was attempted to address the problem of monitoring the occurrence of seepage-induced internal erosion in water-retaining earth structures. Some of these implications are described below.

### 5.5.1 Monitoring of seepage-induced internal erosion with AE

This study demonstrated that AE can be used for detecting seepage-induced internal erosion. The most conclusive indication of that is shown in Figure 5-7, where a clear AE signal corresponding to particle movement being triggered by fluid seepage was observed, especially in a way that differentiated it from simple fluid seepage without particle transport.

A practical methodology for AE-monitoring implementation in real structures is a gap in knowledge still exists that needs addressing. One issue is the propagation of (or the capacity to detect) AE over distances from its source that render the approach feasible (both technically and economically). In other words, it was not possible to assertively determine how far from the acoustic source an acoustic sensor has to be to be able to detect it (which was a function of equipment sensitivity as well of the physics of sound propagation itself). The next phase of work should focus on quantifying attenuation such that sensor distribution and spacings can be determined for field deployment.

To be noted that the issue of environmental noise/signal filtering was considerably overcome – the test conditions were such that noise in the laboratory (e.g. people walking/talking (in- and outside), door opening/closing, light vehicle traffic (less than 30m away), electrical pumps (outflow tank), chain hoist (head tank), etc) was quite common. Despite modestly trying to reduce such environmental noise, not eliminating (or even drastically reducing) it served as a test in its own right, one that revealed positive for the practicality of this methodology as AE detection remained seemingly undisturbed.

Although the translation of the observed AE signal into details such as the degree of erosion, the specific association with soil type, or inference to the behaviour of particular hydromechanical parameters was not achieved, the observation of how significant changes to the erosional process (especially its onset but also its intensification) are reflected in the AE is in itself seen as a valuable advancement of this approach.

The described laboratory testing was considered a crucial step for promoting the usage of acoustic emission for the detection of seepage-induced internal erosion. However, it may not be sufficient for allowing this technique to be applied in real circumstances. For that, testing in scale models and in real structures is considered important.

The use of AE for detection of internal erosion offers the capacity to recognise the initiation of particle transport by seepage flow, which allows remediation measures (e.g. basin drainage, installation of reinforcements, evacuations) to be taken before the structure has suffered severe/critical/hazardous damage. This is a result of this technique being able to detect processes occurring within the structure and hidden from observations of its exterior. AE detection is a technique with advantages compared to other monitoring methods, most significantly in its capacity to identify particle transport (and not only e.g. the presence of water within the structure). One way in which this detection can be made is by inspecting the pertinent acoustic signal and, having examined the materials composing the structure and other local characteristics, identifying significant changes in its normal signature or acceleration/progression of its magnitude.

*Suggested Implementation*

Monitoring in real assets could be done by placing hydrophones in a water-saturated region portion near or within the structure, with the water volume between the sensors and the area subject internal erosion being contiguous. Sensor spacing should be done based on equipment sensitivity and sound attenuation through the medium (soil-fluid mixture, considering anisotropy and relevant variables). For example, with the filtered median signal intensity observed in this study (ca. -90dB) an attenuation of 30dB/m (Robb et al., 2006), and the sensitivity of the used hydrophones given by the manufacturer (-207dB), sensors could be [conservatively] placed at a distance of ca. 4m from the signal source or from one another for full coverage – equivalent to one sensor per 268m$^3$ or per 50m$^2$ over a surface.

Waveguide-based detection could also be used, where acoustic sensors may be attached to structural elements (e.g. pipes, sheet-piles) that would serve as waveguides or simply to elements installed for this purpose. This mode of detection is deemed to only detect phenomena directly interacting (e.g. impacting, shearing) with the waveguide.

The produced data would then be observed and analysed by an operator trained in the pertinent principles such as the onset and evolution of internal erosion and analogous processes and how such processes can be reflected in the acoustic signal.

This suggestion is simply conjectural; further knowledge acquisition as well as the use of superior equipment may allow for different approaches or extend the capacity of this proposition.

The list below represents a step-by-step for implementing AE monitoring:

***Suggested AE monitoring scheme for seepage-induced internal erosion in water-retaining structures***

**A)**

**Laboratory testing of constituents/materials**

- Sample of material(s) (including interfaces/boundaries) to be tested for internal erosion susceptibility in permeameter apparatus (e.g. bespoke permeameter used in this project)

**B)**

**Equipment installation**

- Hydrophones to be positioned within region(s) with potential for internal erosion, within contiguous water saturated volume, considering their detection capabilities.
- Piezoceramic transducers to be attached to waveguides reaching into susceptible region(s)

**C)**

**Calibration**

- Instrument configuration to provide neutral values within suitable range

**D)**

**Identification of [known] noise or irrelevant signal**

- Observation of effect cycles and known gradual environmental changes (e.g. seasons, climate)
- Equipment noise (e.g. intrinsic to apparatus, electric oscillations)
- Environmental noise (anthropogenic and natural)

**E)**

**Monitoring**

- Regular examination of data by trained professional

⟶ AE occurrence non-attributable to phenomena characterized in previous steps indicates potential <u>hazard</u>.

## 6 Conclusions

This research was set out to develop an approach to interpret seepage-induced internal erosion using AE measurements. Its outcomes and achievements in relation to the predefined objectives can be described as follows:

Objective 1)

A newly designed, bespoke test apparatus capable of simulating seepage-induced internal erosion in a controlled manner while detecting AE and measuring hydromechanical parameters has been successfully commissioned.

- Laboratory experiments with the constructed test device have been performed in soil samples representative of materials used in the construction of water-retaining earth structures, and the onset and progression of seepage-induced internal erosion replicated and analysed.

Objective 2)

Datasets of AE generated by seepage-induced internal erosion in a series of internally unstable soils have been produced.

- Very significant amounts of data from AE as well as hydromechanical parameters were generated and processed.
- This information was made comprehensible and suitable for interpretation.

Objective 3)

The understanding of AE generated by seepage-induced internal erosion by analysing the produced datasets has been advanced. Insights about the mechanisms governing the occurrence and evolution of such erosional processes have also been offered.

- It was possible to determine the occurrence of seepage-induced internal erosion using AE detection.
    - Seepage flow without the transport of soil particles could be differentiated from seepage flow with the transport of soil particles using AE.
    - The AE produced during soil compaction/consolidation was also evident.
- AE was ascertained as useful to determine the occurrence of seepage-induced internal erosion by observing how its signal varies over time in terms of RDC.
- Seepage-induced internal erosion is likely to be a non-linear process.
    - As soil dynamics evolve, changes in hydromechanical variables incur pattern changes, possibly invalidating extrapolations based their preceding behaviour.
- The factor considered critical for the occurrence of internal erosion was flow velocity at the pore scale.
    - If the velocity of flow at the pore scale has enough kinetic energy to transport the finer soil fraction through the pore spaces, granted the satisfaction of grain-

pore geometrical criteria (transported grains must fit through the spaces), internal erosion is to be expected.

- The AE rate was not necessarily proportional to the stage of internal erosion as the erosion itself may form areas of preferential flow that become clearer of particles being transported and therefore less prone to particle interactions that produce AE.
- Changes to the hydromechanical parameters at the scale of the full sample may not be noticeable during the early stages of internal erosion.
    - Due to non-homogeneities, the conditions for the initiation of seepage-induced internal erosion (especially pore-scale flow velocity) as well as the primary phases of the erosional process may only be found in a small portion of the sample and produce negligible changes to the overall hydromechanical conditions.
- As it stands from this work at the time of its conclusion, the diagnosis of internal erosion based on AE should require the analysis of a trained professional observing the dataset as a whole and at different scales – improvements as proposed in this thesis are expected to make a framework for algorithmically interpreting the related AE possible.

Objective 4)

A generalised strategy for the use of AE monitoring to detect and interpret seepage and seepage erosion behaviour has been described. (See section 5.5).

- The use of hydrophones for detecting AE within a water-saturated medium (i.e. using water as sound propagator) is a viable and effective way to detect suffusive/frictional dynamics in soil.
    - Hydrophones have the advantage of monitoring a soil volume without the need of waveguides (as the fluid behaves as such).
    - Waveguide-based systems are also effective but have their detection range limited to phenomena directly contacting them.

*Newly found understanding:*

- AE can be used for detecting seepage-induced internal erosion
- Localised deviations of variables such as flow rate (e.g. at the pore-scale), effective stress and soil fabric (e.g. GSD inhomogeneities) are crucial – considering a soil volume as uniform can be misleading.
- Hydrophones are a practicable instruments for detecting AE within a water-saturated medium.
- A soil volume in an advanced stage of internal erosion (e.g. a fully formed erosional pipe) may have a weaker AE signal than in earlier erosional phases – displacement of soil particles may be more intense while the pipe is being formed.
- Soil dynamics progression can cause non-linearities in the related hydromechanical parameters.

## 6.1 Recommendations for future work

The following suggestions are made to support future research. These may reflect insufficiencies, faults or simply address matters beyond the scope of this study, which are elaborated if pertinent.

- Since AE quantification in response to physical changes to the tested specimens was not as successful as intended due to limitations of either the used sensors (incl. accessories or support equipment like amplifiers and connectors) or the capacity to manipulate them, it is suggested that improving this issue would substantially improve test results. Addressing this matter should also improve test comparability, which was also a problem and was reflected in equipment responding somewhat differently from one test to another.
- The time it took to design and, especially, build the new permeameter added to the relatively long duration of tests consumed a large fraction of the time prescribed for this project and reduced the amount of testing done. Hence, future work would benefit of a larger number of tests with different soil gradations and under different conditions as it is thought that some of the questions left unanswered by this project because of this limitation.
- The use of a triaxial cell – adapted, especially in terms of size - could also benefit future work since the rigid wall of the used permeameter seemed to cause uncertainties

related to stress distribution. This was considered during the equipment design phase of this work but hurdles such as how to install equipment through the kind of membrane usually employed in triaxial cells were deemed difficult to solve given the available time, resources and expertise.

- The length of the test performed (thousands of minutes) made data storage and processing possible issues that were bypassed by reducing the type(s) and time resolution of the recorded data – for instance, analysing the signal waveforms and constructing spectrograms were desired but not accomplished for this reason, resorting instead to the simpler RDC approach. Hence, future studies could benefit of addressing this issue since a richer data analysis is expected to clarify the use of this methodology for the purposes here pursued.
- As it is intrinsic to most laboratory-scale experimentation, the translation of the results from this work to field conditions still cannot be specified – issues such as AE detectability, process velocities (e.g. time for development of seepage, internal erosion, pace of particle travel), variability within volume of targeted structure, influence of geometries (e.g. structural design, composition), or simply unexpected effects of scale may play crucial roles. Therefore, in addition to improved laboratory testing, field experiments are considered essential to inform or at least verify practical implementation.

# References


Aldrich, J.E. (2007) Basic physics of ultrasound imaging. *Critical Care Medicine*, 35 (Suppl): S131–S137. doi:10.1097/01.CCM.0000260624.99430.22.

Anbeek, C. (1993) The effect of natural weathering on dissolution rates. *Geochimica et Cosmochimica Acta*, 57 (21–22): 4963–4975. doi:10.1016/S0016-7037(05)80002-X.

Anbeek, C., Van Breemen, N., Meijer, E.L., et al. (1994) The dissolution of naturally weathered feldspar and quartz. *Geochimica et Cosmochimica Acta*, 58 (21): 4601–4613. doi:10.1016/0016-7037(94)90194-5.

Ardalan, A.A. and Jafari, M. (2012) Multi-sensor approach to settlement analysis of earth dams. *Computational Geosciences*, 16 (1): 123–138. doi:10.1007/s10596-011-9258-y.

Artese, G., Perrelli, M., Artese, S., et al. (2015) Geomatics activities for monitoring the large landslide of Maierato, Italy. *Applied Geomatics*, 7 (3): 171–188. doi:10.1007/s12518-014-0146-8.

Bai, Q., Wang, Q., Wang, D., et al. (2019) Recent advances in brillouin optical time domain reflectometry. *Sensors (Switzerland)*, 19 (8). doi:10.3390/s19081862.

Bar, N., Kostadinovski, M., Tucker, M., et al. (2020) Rapid and robust slope failure appraisal using aerial photogrammetry and 3D slope stability models. *International Journal of Mining Science and Technology*. doi:10.1016/j.ijmst.2020.05.013.

Bardet, J.P. and Sayed, H. (1993) Velocity and attenuation of compressional waves in nearly saturated soils. *Soil Dynamics and Earthquake Engineering*, 12 (7): 391–401. doi:10.1016/0267-7261(93)90002-9.

Barzaghi, R., Cazzaniga, N.E., De Gaetani, C.I., et al. (2018) Estimating and comparing dam deformation using classical and gnss techniques. *Sensors (Switzerland)*, 18 (3). doi:10.3390/s18030756.

Bashan, G., Diamandi, H.H., London, Y., et al. (2018) Optomechanical time-domain reflectometry. *Nature Communications*, 9 (1). doi:10.1038/s41467-018-05404-0.

Bayoumi, A. (2011) On the Evaluation of Settlement Measurements Using Borehole Extensometers. *Geotechnical and Geological Engineering*, 29 (1): 75–90. doi:10.1007/s10706-010-9352-2.

Beckingham, L.E., Mitnick, E.H., Steefel, C.I., et al. (2016) Evaluation of mineral reactive surface area estimates for prediction of reactivity of a multi-mineral sediment. *Geochimica et Cosmochimica Acta*, 188: 310–329. doi:10.1016/j.gca.2016.05.040.

Beemer, R.D., Murali, M., Biscontin, G., et al. (2018) Use of a MEMS accelerometer to measure orientation in a geotechnical centrifuge. *International Journal of Physical Modelling in Geotechnics*, 18 (5): 253–265. doi:10.1680/jphmg.16.00077.

Berryman, J.G. (1981) Elastic wave propagation in fluid-saturated porous media. *The Journal of the Acoustical Society of America*, 69 (2): 416–424. doi:10.1121/1.385457.

Biller, T., Smith, A. and Dixon, N. (2019) Monitoring seepage-induced internal erosion using acoustic emission. *European Working Group on Internal Erosion*, pp. 18–21. doi:10.1016/J.SANDF.2013.06.008.

Biot, M.A. (1955) Theory of Propagation of Elastic Waves in a Fluid-Saturated Porous Solid. II. Higher Frequency Range. *The Journal of the Acoustical Society of America*, 28 (2): 179–191. doi:10.1121/1.1908241.

Biot, M.A. (1956) Theory of Propagation of Elastic Waves in a Fluid-Saturated Porous Solid. I. Low-Frequency Range. *The Journal of the Acoustical Society of America*, 28 (2): 168–178. doi:10.1121/1.1908239.

Biot, M.A. (1962) Mechanics of deformation and acoustic propagation in porous media. *Journal of Applied Physics*, 33 (4): 1482–1498. doi:10.1063/1.1728759ï.

Bolton Seed, H. and Duncan, J.M. (1987) The failure of Teton dam. *Engineering Geology, Elsevier Science Publishers B.V*, 24: 173–205. Available at: https://ac.els-cdn.com/0013795287900603/1-s2.0-0013795287900603-main.pdf?_tid=d997a624-0014-49b6-8abb-006ccce208c2&acdnat=1530186005_d4100c06c94cf2475dac2ad94895f082 (Accessed: 28 June 2018).

Borragan, V. and Vazquez, M.A. (2014) *Modelling Internal Erosion Within An Embankment Dam Prior To Breaching*. KTH Royal Institute of Technology, Stockholm, SWEDEN. Available at: http://kth.diva-portal.org/smash/get/diva2:783478/FULLTEXT01.pdf.

Bowles, F.A. (1997) Observations on attenuation and shear-wave velocity in fine-grained, marine sediments. *J. Acoust. Soc. Am.*, 6 (December): 3385–3397. doi:10.1121/1.419374.

Brantley, S.L. (2010) Weathering: Rock to regolith. *Nature Geoscience*, 3 (5): 305–306. doi:10.1038/ngeo858.

Bridle, R. (2017) "Internal Erosion Mechanics and Risk Estimation Based on ICOLD Bulletin 164." In *Geo-Risk 2017*. Reston, VA, June 2017. American Society of Civil Engineers. pp. 137–146. doi:10.1061/9780784480724.013.

Brown, G.O. (2002) Henry Darcy and the making of a law. *Water Resources Research*, 38 (7): 11-1-11–12. doi:10.1029/2001WR000727.

Buckingham, M.J. (1997) Theory of acoustic attenuation, dispersion, and pulse propagation in unconsolidated granular materials including marine sediments. *The Journal of the Acoustical Society of America*, 102 (5): 2579. doi:10.1121/1.420313.

Camici, S., Barbetta, S. and Moramarco, T. (2017) Levee body vulnerability to seepage: the case study of the levee failure along the Foenna stream on 1 January 2006 (central Italy). *Journal of Flood Risk Management*, 10 (3): 314–325. doi:10.1111/jfr3.12137.

Campora, M., Palla, A., Gnecco, I., et al. (2019) The laboratory calibration of a soil moisture capacitance probe in sandy soils. *Soil and Water Research*, 15 (2): 75–84. doi:10.17221/227/2018-SWR.

Cedergren, H.R. (1989) *Seepage, drainage, and flow nets*. Wiley.

Chang, D., Zhang, L. and Cheuk, J. (2014) Mechanical consequences of internal soil erosion. *HKIE Transactions*, 21 (4): 198–208. doi:10.1080/1023697X.2014.970746.

Chang, D.S. and Zhang, L.M. (2013a) Critical Hydraulic Gradients of Internal Erosion under Complex Stress States. *Journal of Geotechnical and Geoenvironmental Engineering*, 139 (9): 1454–1467. doi:10.1061/(ASCE)GT.1943-5606.0000871.

Chang, D.S. and Zhang, L.M. (2013b) Extended internal stability criteria for soils under seepage. *Soils and Foundations*, 53 (4): 569–583. doi:10.1016/J.SANDF.2013.06.008.

Chanson, H. (2004) *The hydraulics of open channel flow : an introduction ; basic principles, sediment motion, hydraulic modelling, design of hydraulic structures*. Elsevier Butterworth Heinemann.

Chapuis, R.P., Contant, A. and Baass, K.A. (1996) Migration of fines in 0–20 mm crushed base during placement, compaction, and seepage under laboratory conditions. *Canadian Geotechnical Journal*, 33 (1): 168–176. doi:10.1139/t96-032.

Chaunsali, R., Li, F. and Yang, J. (2016) Stress wave isolation by purely mechanical topological phononic crystals article. *Scientific Reports*, 6 (1): 1–10. doi:10.1038/srep30662.

Chen, C., Zhang, L.M. and Chang, D.S. (2016) Stress-Strain Behavior of Granular Soils Subjected to Internal Erosion. *Journal of Geotechnical and Geoenvironmental Engineering*, 142 (12): 06016014. doi:10.1061/(ASCE)GT.1943-5606.0001561.

Chikahisa, H., Matsumoto, K., Kumagai, K., et al. (2004) "Measurement of ground displacement during tunnel excavation by the optical measurement system for ground displacement." In Ohnishi, Y and Aoki, K (ed.). *Contribution of Rock Mechanics to the New Century, Vols 1 and 2*. 2004. pp. 617–622.

Chou, H. Ter, Lee, C.F., Huang, C.H., et al. (2013) The monitoring and flow dynamics of gravelly debris flows. *Journal of Chinese Soil and Water Conservation*, 44 (2): 144–157.

Christie, M.D., Sun, S., Deng, L., et al. (2019) A variable resonance magnetorheological-fluid-based pendulum tuned mass damper for seismic vibration suppression. *Mechanical Systems and Signal Processing*, 116: 530–544. doi:10.1016/j.ymssp.2018.07.007.

Cita Sari, U., Prabandiyani Retno Wardani, S. and Partono, W. (n.d.) *Influence of pore water pressure to seepage and stability of embankment dam (case study of Sermo Dam Yogyakarta, Indonesia)*. Available at: https://www.matec-conferences.org/articles/matecconf/pdf/2017/15/matecconf_sicest2017_05007.pdf.

Colomina, I. and Molina, P. (2014) Unmanned aerial systems for photogrammetry and remote sensing: A review. *ISPRS Journal of Photogrammetry and Remote Sensing*. 92 pp. 79–97. doi:10.1016/j.isprsjprs.2014.02.013.

Colque Espinoza, B. and Brylawski, E. (2007) "Structural & geotechnical instrumentation of the Pichi Picún Leufú Hydroelectric Dam, Argentina: A 54-m (177-ft) compacted gravel embankment dam with an upstream concrete slab and cutoff wall." In *Geotechnical Special Publication*. 2007. p. 58. doi:10.1061/40940(307)58.

Crawford-Flett, K.A. (2014) *An improved hydromechanical understanding of seepage-induced instability phenomena in soil*. doi:10.14288/1.0167453.

Crosta, G. and Prisco, C. di (1999) On slope instability induced by seepage erosion. *Canadian Geotechnical Journal*, 36 (6): 1056–1073. doi:10.1139/t99-062.

Curioni, G., Chapman, D.N., Royal, A.C.D., et al. (2019) Time domain reflectometry (TDR) potential for soil condition monitoring of geotechnical assets. *Canadian Geotechnical Journal*, 56 (7): 942–955. doi:10.1139/cgj-2017-0618.

Dallo, Y.A.H., Wang, Y. and Ahmed, O.Y. (2013) Assessment of the internal stability of granular soils against suffusion. *European Journal of Environmental and Civil Engineering*, 17 (4): 219–230. doi:10.1080/19648189.2013.770613.

Davis, J.L. and Annan, A.P. (1989) Ground-penetrating radar for high-resolution mapping of soil and rock stratigraphy. *Geophysical Prospecting*, 37 (5): 531–551. doi:10.1111/j.1365-2478.1989.tb02221.x.

Devlin, J.F. (2015) HydrogeoSieveXL: an Excel-based tool to estimate hydraulic conductivity from grain size analysis. *Hydrogeology Journal*. doi:10.1007/s10040-015-1255-0.

Dixon, N., Hill, R. and Kavanagh, J. (2003) Acoustic emission monitoring of slope instability: development of an active waveguide system. *Proceedings of the Institution of Civil Engineers - Geotechnical Engineering*, 156 (2): 83–95. doi:10.1680/geng.2003.156.2.83.

Dixon, N., Smith, A., Meldrum, P., et al. (2014) Quantification of reactivated landslide behaviour using acoustic emission monitoring. *Landslides*, 12 (3): 549–560. doi:10.1007/s10346-014-0491-z.

Dixon, N., Smith, A., Spriggs, M., et al. (2015a) Stability monitoring of a rail slope using acoustic emission. *Proceedings of the Institution of Civil Engineers-Geotechnical Engineering*, 168 (GE5): 373–384. doi:10.1680/geng.14.00152.

Dixon, N. and Spriggs, M. (2007) Quantification of slope displacement rates using acoustic emission monitoring. *Canadian Geotechnical Journal*, 44 (8): 966–976. doi:10.1139/T07-046.

Dixon, N., Spriggs, M.P., Meldrum, P., et al. (2010) Development of a low cost acoustic emission early warning system for slope instability. *Proceedings of the 11th IAEG Congress. Auckland, new Zealand*, pp. 1803–1810.

Dixon, N., Spriggs, M.P., Smith, A., et al. (2015b) Quantification of reactivated landslide behaviour using acoustic emission monitoring. *Landslides*, 12 (3): 549–560. doi:10.1007/s10346-014-0491-z.

Dondurur, D. (2018) *Acquisition and Processing of Marine Seismic Data*. Elsevier. doi:10.1016/C2016-0-01591-7.

Doughty, M., Eyles, N., Eyles, C.H., et al. (2014) Lake sediments as natural seismographs: Earthquake-related deformations (seismites) in central Canadian lakes. *Sedimentary Geology*, 313: 45–67. doi:10.1016/j.sedgeo.2014.09.001.

Douglas, K.J., Fell, R., Peirson, W.L., et al. (2019) Experimental investigation of global backward erosion and suffusion of soils in embankment dams. *Canadian Geotechnical Journal*, 56 (6): 789–807. doi:10.1139/cgj-2018-0088.

Dutta, N.C. and Ode, H. (1983) Seismic reflections from a gas-water contact. *Geophysics*, 48 (2): 148–162. doi:10.1190/1.1441454.

Fannin, R.J. and Slangen, P. (2014) On the distinct phenomena of suffusion and suffosion. *Géotechnique Letters*, 4 (4): 289–294. doi:10.1680/geolett.14.00051.

Fannin, R.J., Slangen, P., Mehdizadeh, A., et al. (2015) Discussion: On the distinct phenomena of suffusion and suffosion. *Géotechnique Letters*, 5 (3): 129–130. doi:10.1680/jgele.15.00017.

Fathi, E. and Golestani, M. (2017) Considering of Instrumentation Performance Results in Soil Dams and comparing with Numerical Analysis: a case study on Doosti soil dam in Iran. *Electronic Journal of Geotechnical Engineering*, 22 (7): 271–292. Available at: https://www.researchgate.net/profile/Eiman_Fathi/publication/323545257_Considering_of_Instrumentation_Performance_Results_in_Soil_Dams_and_comparing_with_Numerical_Analysis_a_case_study_on_Doosti_soil_dam_in_Iran/links/5a9b970445851586a2ac3e4f/Considering.

Fell, R., Chi, ;, Wan, F., et al. (2003) Time for Development of Internal Erosion and Piping in Embankment Dams. *Journal of Geotechnical and Geoenvironmental Engineering*, 129 (4): 307–314. doi:10.1061/(ASCE)1090-0241(2003)129:4(307).

Ferdos, F. (2016) *Internal erosion phenomena in embankment dams*. KTH Royal Institute of Technology TRITA-HYD.

Ferdos, F., Dargahi, B. and Solari, L. (2018) Mechanism of Suffusion Erosion Phenomenon In Porous Media. *J Geol Geosci*, 2 (1): 2018–1.

Flammer, I., Blum, A., Leiser, A., et al. (2001) *Acoustic assessment of flow patterns in unsaturated soil*. Available at: www.elsevier.nlrlocaterjappgeo (Accessed: 29 August 2018).

Fonseca, J., Sim, W.W., Shire, T., et al. (2014) Microstructural analysis of sands with varying degrees of internal stability. *Géotechnique*, 64 (5): 405–411. doi:10.1680/geot.13.T.014.

Foster, M., Fell, R. and Spannagle, M. (2000) The statistics of embankment dam failures and accidents. *Canadian Geotechnical Journal*, 37 (5): 1000–1024. doi:10.1139/t00-030.

Foster, M.A. (1999) *The probability of failure of embankment dams by internal erosion and piping*. The University of New South Wales.

Fraden, J. (2010) *Handbook of Modern Sensors*. Fourth Edi. Springer New York. doi:10.1007/978-1-4419-6466-3.

Freidman, B.L., Camenzuli, D. and Lackie, M. (2014) Locating an ice-covered Antarctic landfill using ground magnetometry. *Antarctic Science*, 26 (4): 361–368. doi:10.1017/S0954102013000953.

Gelb, A. and Van der Velde, W.. (1968) *Multiple input describing functions and nonlinear system design*.

Ghasemzadeh, H. and Abounouri, A.A. (2013) Compressional and shear wave intrinsic attenuation and velocity in partially saturated soils. *Soil Dynamics and Earthquake Engineering*, 51: 1–8. doi:10.1016/J.SOILDYN.2013.03.011.

Gong, H., Kizil, M.S., Chen, Z., et al. (2019) Advances in fibre optic based geotechnical monitoring systems for underground excavations. *International Journal of Mining Science and Technology*, 29 (2): 229–238. doi:10.1016/j.ijmst.2018.06.007.

Hardie, M., Lisson, S., Doyle, R., et al. (2013) Determining the frequency, depth and velocity of preferential flow by high frequency soil moisture monitoring. *Journal of Contaminant Hydrology*, 144 (1): 66–77. doi:10.1016/j.jconhyd.2012.10.008.

Heather-Smith, H. (2020) *Generation and propagation of acoustic emissions in buried steel infrastructure for monitoring soil-structure interactions*. Loughborough University. doi:10.26174/THESIS.LBORO.12652409.V1.

Heck, M., Hammer, C., van Herwijnen, A., et al. (2018) Automatic detection of snow avalanches in continuous seismic data using hidden Markov models. *Natural Hazards and Earth System Sciences*, 18 (1): 383–396. doi:10.5194/nhess-18-383-2018.

Heckmann, T., Bimböse, M., Krautblatter, M., et al. (2012) From geotechnical analysis to quantification and modelling using LiDAR data: a study on rockfall in the Reintal catchment, Bavarian Alps, Germany. *Earth Surface Processes and Landforms*, 37 (1): 119–133. doi:10.1002/esp.2250.

Hellman, K., Ronczka, M., Günther, T., et al. (2017) Structurally coupled inversion of ERT and refraction seismic data combined with cluster-based model integration. *Journal of Applied Geophysics*, 143: 169–181. doi:10.1016/j.jappgeo.2017.06.008.

Hewlett Packard (1981) *The Fundamentals of Signal Analysis Application [Note 243]*. Palo Alto, California: Hewlett Packard Company. doi:Publication Number 5952-8898.

Hiep, H. and Chung, S.G. (2018) Back-analysis of geotechnical parameters on PVD-improved ground in the Mekong Delta. *Geotextiles and Geomembranes*, 46 (4): 402–413. doi:10.1016/j.geotexmem.2018.03.005.

Hobbs, P. (2008) Coastal cliff monitoring. *Geo-connection UK*, 6 (3): 16–17. Available at: http://www.geoconnexion.com/geoconnexionuk.php.

Holmes, J.D., Carey, W.M., Dediu, S.M., et al. (2007) Nonlinear frequency-dependent attenuation in sandy sediments. *The Journal of the Acoustical Society of America*, 121 (5): EL218–EL222. doi:10.1121/1.2720937.

Horikoshi, K. and Takahashi, A. (2015) Suffusion-induced change in spatial distribution of fine fractions in embankment subjected to seepage flow. *Soils and Foundations*, 55 (5): 1293–1304. doi:10.1016/j.sandf.2015.09.027.

Hung, M.H., Lauchle, G.C. and Wang, M.C. (2009) Seepage-induced acoustic emission in granular soils. *Journal of Geotechnical and Geoenvironmental Engineering*, 135 (4): 566–572. doi:10.1061/ASCE1090-0241(2009)135:4(566).

Hunter, R.P. and Bowman, E.T. (2017a) Visualisation of seepage-induced suffusion and suffosion within internally erodible granular media. *Géotechnique*, pp. 1–13. doi:10.1680/jgeot.17.P.161.

Hunter, R.P. and Bowman, E.T. (2017b) Visualisation of seepage induced suffusion and suffosion within internally erodible granular media. *Géotechnique*, pp. 1–48. doi:10.1680/jgeot.17.p.161.

Ibrahim, M.R., Jaafar, J., Yahya, Z., et al. (2010) *A feasibility study of building structural deformation monitoring using Global Positioning System (GPS), terrestrial surveying technique (TST) and crack gauge measurement (CGM)*. In 10 August 2010. Institute of Electrical and Electronics Engineers (IEEE). pp. 8–8. doi:10.1109/cspa.2010.5545342.

ICOLD (2016) "Internal erosion of existing dams, levees and dikes, and their foundations, Volume 2: Case histories, investigations, testing, remediation and surveillance." In *International Commission on Large Dams, Paris*. 2016.

Indraratna, B., Israr, J. and Li, M. (2018) Inception of geohydraulic failures in granular soils-an experimental and theoretical treatment. *Géotechnique*, 68 (3): 233–248. doi:10.1680/jgeot.16.P.227.

*ISO TS 17892-11.2004* (2004). Geneva: International Organization for Standardization. Available at: https://www.iso.org/standard/38524.html.

Israr, J. and Indraratna, B. (2018) Mechanical Response and Pore Pressure Generation in Granular Filters subjected to Uniaxial Cyclic Loading. *Canadian Geotechnical Journal*, p. cgj-2017-0393. doi:10.1139/cgj-2017-0393.

Israr, J. and Israr, J. (2018) Experimental Investigation and Assessment of Internal Stability of Granular Filters under One-Dimensional Static and Cyclic Loading. *Geotechnical Testing Journal*, 41 (1): 103–116. doi:10.1520/GTJ20170027.

James, M.R., Chandler, J.H., Eltner, A., et al. (2019) Guidelines on the use of structure-from-motion photogrammetry in geomorphic research. *Earth Surface Processes and Landforms*, 44 (10): 2081–

2084. doi:10.1002/esp.4637.

Jayawardana, D., Kharkovsky, S., Liyanapathirana, R., et al. (2016) Measurement System with Accelerometer Integrated RFID Tag for Infrastructure Health Monitoring. *IEEE Transactions on Instrumentation and Measurement*, 65 (5): 1163–1171. doi:10.1109/TIM.2015.2507406.

Ju, M., Li, J., Yao, Q., et al. (2019) Rate effect on crack propagation measurement results with crack propagation gauge, digital image correlation, and visual methods. *Engineering Fracture Mechanics*, 219. doi:10.1016/j.engfracmech.2019.106537.

Jung, H. and Navarre-Sitchler, A. (2018) Scale effect on the time dependence of mineral dissolution rates in physically heterogeneous porous media. *Geochimica et Cosmochimica Acta*, 234: 70–83. doi:10.1016/j.gca.2018.05.009.

Kadam, V. V. and Nayak, R. (2016) Basics of Acoustic Science. *Acoustic Textiles*, pp. 33–42. doi:10.1007/978-981-10-1476-5_2.

Kammann, F., Marx, B., Hill, W., et al. (2017) "Intelligent pipelines with integrated fibre-optics for single-ended distributed strain sensing." In *SHMII 2017 - 8th International Conference on Structural Health Monitoring of Intelligent Infrastructure, Proceedings*. 2017. International Society for Structural Health Monitoring of Intelligent Infrastructure, ISHMII. pp. 90–95.

Kasireddy, V., Ergan, S., Akinci, B., et al. (2015) Visualization requirements of engineers for risk assessment of embankment dams. *Visualization in Engineering*, 3 (1). doi:10.1186/s40327-014-0014-y.

Ke, L. and Takahashi, A. (2012) Strength reduction of cohesionless soil due to internal erosion induced by one-dimensional upward seepage flow. *Soils and Foundations*, 52 (4): 698–711. doi:10.1016/j.sandf.2012.07.010.

Ke, L. and Takahashi, A. (2014) Experimental investigations on suffusion characteristics and its mechanical consequences on saturated cohesionless soil. *Soils and Foundations*, 54 (4): 713–730. doi:10.1016/j.sandf.2014.06.024.

Keaton, J.R. (2018) "Noncohesive Soils." In *Bobrowsky P.T., Marker B. (eds) Encyclopedia of Engineering Geology. Encyclopedia of Earth Sciences Series*. Springer, Cham. pp. 689–690. doi:10.1007/978-3-319-73568-9_212.

Kenney, T.C. and Lau, D. (1985) Internal stability of granular filters. *Canadian Geotechnical Journal*, 22 (2): 215–225. doi:10.1139/t85-029.

Kibblewhite, A.C. (1989) Attenuation of sound in marine sediments: A review with emphasis on new low-frequency data. *Journal of the Acoustical Society of America*, 86 (2): 716–738. doi:10.1121/1.398195.

Kim, K., Choi, J., Chung, J., et al. (2018) Structural displacement estimation through multi-rate fusion of accelerometer and RTK-GPS displacement and velocity measurements. *Measurement: Journal of the International Measurement Confederation*, 130: 223–235. doi:10.1016/j.measurement.2018.07.090.

Kim, S.W. and Won, J.S. (2003) Measurements of Soil Compaction Rate by Using JERS-1 SAR and a Prediction Model. *IEEE Transactions on Geoscience and Remote Sensing*, 41 (11 PART II): 2683–2686. doi:10.1109/TGRS.2003.817185.

King, M.S. (2009) Recent developments in seismic rock physics. *International Journal of Rock Mechanics and Mining Sciences*, 46 (8): 1341–1348. doi:10.1016/j.ijrmms.2009.04.008.

Koerner, R.M., McCabe, W.M. and Lord Jr, A.E. (1981) *Acoustic Emission Behavior and Monitoring of Soils*. ASTM STP 750. Gray, R.E. and Drnevich, V.P. (eds.). West Conshohocken, PA, USA: ASTM International.

Kojima, Y., Shigeta, R., Miyamoto, N., et al. (2016) Low-cost soil moisture profile probe using thin-film capacitors and a capacitive touch sensor. *Sensors (Switzerland)*, 16 (8). doi:10.3390/s16081292.

Koo, M.H. and Suh, M.C. (2001) Geotechnical and hydrogeological approaches towards conservation

of the Muryong Royal Tomb in Korea. *Environmental Geology*. 41 (3–4) pp. 470–479. doi:10.1007/s002540100417.

Kossoff, D., Dubbin, W.E., Alfredsson, M., et al. (2014) Mine tailings dams: Characteristics, failure, environmental impacts, and remediation. *Applied Geochemistry*, 51: 229–245. doi:10.1016/J.APGEOCHEM.2014.09.010.

Kovács, G. (1981) *Seepage hydraulics*. Elsevier Scientific Pub. Co.

Krutov, D.A. (2019) Repairing earth dam drainage systems. *Vestnik MGSU*, (7): 901–911. doi:10.22227/1997-0935.2019.7.901-911.

Kump, L.R., Brantley, S.L. and Arthur, M.A. (2000) Chemical weathering, atmospheric CO2, and climate. *Annual Review of Earth and Planetary Sciences*, 28: 611–667. doi:10.1146/annurev.earth.28.1.611.

Kuranchie, F.A. (2015) *Characterisation and applications of iron ore tailings in building and construction projects*. Edith Cowan University. Available at: http://ro.ecu.edu.au/theses/1623.

Kwee, J. (2018) "Sub-bottom pipeline and cable detection using automated contact recognition." In *EAGE Near Surface Geoscience 2018*. 2018.

Langroudi, F., Soroush, M., Shourijeh, A., et al. (2015) A comparison of micromechanical assessments with internal stability/instability criteria for soils. *Powder Technology*, 276: 66–79. doi:10.1016/j.powtec.2015.02.014.

Li, M. (2008) *Seepage Induced Instability in Widely Graded Soils*., (May): 319. doi:10.14288/1.0063080.

Li, M. and Fannin, R.J. (2008) Comparison of two criteria for internal stability of granular soil. *Canadian Geotechnical Journal*, 45 (9): 1303–1309. doi:10.1139/T08-046.

Li, M. and Fannin, R.J. (2012) A theoretical envelope for internal instability of cohesionless soil. *Géotechnique*, 62 (1): 77–80. doi:10.1680/geot.10.T.019.

Li, X. and Pyrak-Nolte, L.J. (1998) Acoustic monitoring of sediment-pore fluid interaction. *Geophysical Research Letters*, 25 (20): 3899. doi:10.1029/1998GL900028.

Liang, Y., Yeh, T.-C.J., Wang, J., et al. (2019) Onset of suffusion in upward seepage under isotropic and anisotropic stress conditions. *European Journal of Environmental and Civil Engineering*, 23 (12): 1520–1534. doi:10.1080/19648189.2017.1359110.

Liang, Y., Yeh, T.-C.J., Zha, Y., et al. (2017) Onset of suffusion in gap-graded soils under upward seepage. *Soils and Foundations*, 57 (5): 849–860. doi:10.1016/J.SANDF.2017.08.017.

Lin, C.P. and Tang, S.H. (2005) Development and calibration of a TDR extensometer for geotechnical monitoring. *Geotechnical Testing Journal*, 28 (5): 464–471. doi:10.1520/gtj12188.

Lin, W., Liu, A., Mao, W., et al. (2020) Acoustic emission characteristics of a dry sandy soil subjected to drained triaxial compression. *Acta Geotechnica*, 15 (9): 2493–2506. doi:10.1007/s11440-020-00932-w.

Lipták, M. (2011) Analysis of Bridge Structure Deformation Measured by Total Station. *INGEO 2011 – 5th International Conference on Engineering Surveying* , pp. 99–104. Available at: http://www.geof.unizg.hr/pluginfile.php/7399/mod_book/chapter/166/TS03_3.pdf.

Liu, X., Su, S., Ma, J., et al. (2019a) Deformation activity analysis of a ground fissure based on instantaneous total energy. *Sensors (Switzerland)*, 19 (11). doi:10.3390/s19112607.

Liu, Y., Li, J. and Fang, Z.N. (2019b) Groundwater level change management on control of land subsidence supported by borehole extensometer compaction measurements in the houston-galveston region, Texas. *Geosciences (Switzerland)*, 9 (5). doi:10.3390/geosciences9050223.

Lovisa, J., Asce, M., Sivakugan, N., et al. (2014) Tall Oedometer Testing: Method to Account for Wall Friction. *Int. J. Geomech*, 15 (2). doi:10.1061/(ASCE)GM.1943-5622.0000359.

Lu, P., Lalam, N., Badar, M., et al. (2019) Distributed optical fiber sensing: Review and perspective.

*Applied Physics Reviews*. 6 (4). doi:10.1063/1.5113955.

Lu, Z. and Wilson, G. V. (2012) Acoustic Measurements of Soil Pipeflow and Internal Erosion. *Soil Science Society of America Journal*, 76 (3): 853. doi:10.2136/sssaj2011.0308.

Luquot, L. and Gouze, P. (2009) Experimental determination of porosity and permeability changes induced by injection of CO2 into carbonate rocks. *Chemical Geology*, 265 (1–2): 148–159. doi:10.1016/j.chemgeo.2009.03.028.

Lurton, X. (2010) "Underwater acoustic wave propagation." In *An Introduction to Underwater Acoustics. Principles and Applications*. Springer. p. 680.

Maher, K. and Chamberlain, C.P. (2014) Hydrologic regulation of chemical weathering and the geologic. *Science*, 343 (6178): 1502–1504. doi:10.1126/science.1250770.

Mao, W., Yang, Y. and Lin, W. (2019) An acoustic emission characterization of the failure process of shallow foundation resting on sandy soils. *Ultrasonics*, 93: 107–111. doi:10.1016/j.ultras.2018.11.007.

Marcello, A., Frigerio, A. and Mazzà, G. (2009) *Case histories: a worldwide view*. In pp. 273–334. doi:10.2495/978-1-84564-142-9/08.

Marchamalo, M., Galán, D., Sánchez, J.A., et al. (2011) DGPS technology in construction: Movement control in large structures. *Informes de la Construccion*, 63 (522): 93–102. doi:10.3989/ic.10.008.

Marot, D., Rochim, A., Nguyen, H.-H., et al. (2016) Assessing the susceptibility of gap-graded soils to internal erosion: proposition of a new experimental methodology. *Natural Hazards*, 83 (1): 365–388. doi:10.1007/s11069-016-2319-8.

Marsella, M., Nardinocchi, C., Paoli, A., et al. (2020) Geodetic measurements to control a large research infrastructure: The Virgo detector at the European Gravitational Observatory. *Measurement: Journal of the International Measurement Confederation*, 151. doi:10.1016/j.measurement.2019.107154.

Martínez-Moreno, F.J., Delgado-Ramos, F., Galindo-Zaldívar, J., et al. (2018) Identification of leakage and potential areas for internal erosion combining ERT and IP techniques at the Negratín Dam left abutment (Granada, southern Spain). *Engineering Geology*. doi:10.1016/J.ENGGEO.2018.04.012.

Martínez-Rincón, J., Mullarkey, C.A., Viza, G.I., et al. (2017) Ultrasensitive inverse weak-value tilt meter. *Optics Letters*, 42 (13): 2479. doi:10.1364/ol.42.002479.

Mewis, J. and Wagner, N.J. (2009) Thixotropy. *Advances in Colloid and Interface Science*. 147–148 (C) pp. 214–227. doi:10.1016/j.cis.2008.09.005.

Michlmayr, G., Cohen, D. and Or, D. (2012) Sources and characteristics of acoustic emissions from mechanically stressed geologic granular media - A review. *Earth-Science Reviews*. 112 (3–4) pp. 97–114. doi:10.1016/j.earscirev.2012.02.009.

Moebius, F., Canone, D. and Or, D. (2012) Characteristics of acoustic emissions induced by fluid front displacement in porous media. *Water Resources Research*, 48 (11): 1–12. doi:10.1029/2012WR012525.

Moffat, R. (2005) *Experiments on the internal stability of widely graded cohesionless soils*. University of British Columbia. doi:10.14288/1.0063322.

Moffat, R. and Fannin, R.J. (2011) A hydromechanical relation governing internal stability of cohesionless soil. *Canadian Geotechnical Journal*, 48 (3): 413–424. doi:10.1139/T10-070.

Moffat, R., Fannin, R.J. and Garner, S.J. (2011) Spatial and temporal progression of internal erosion in cohesionless soil. *Canadian Geotechnical Journal*, 48 (3): 399–412. doi:10.1139/T10-071.

Moffat, R. and Herrera, P. (2015) Hydromechanical model for internal erosion and its relationship with the stress transmitted by the finer soil fraction. *Acta Geotechnica*, 10 (5): 643–650. doi:10.1007/s11440-014-0326-z.

Moffat, R.A. and Fannin, J. (2006) A Large Permeameter for Study of Internal Stability in Cohesionless Soils. *Geotechnical Testing Journal*, 29 (4): 273–280.

Moraci, N., Mandaglio, M.C. and Ielo, D. (2014) Analysis of the internal stability of granular soils using different methods. *Canadian Geotechnical Journal*, 51 (9): 1063–1072. doi:10.1139/cgj-2014-0006.

Moreira, A., Prats-Iraola, P., Younis, M., et al. (2013) A tutorial on synthetic aperture radar. *IEEE Geoscience and Remote Sensing Magazine*, 1 (1): 6–43. doi:10.1109/MGRS.2013.2248301.

Mori, K. (2007) Monitoring Small Amount of Seepage Water of Earth Dam by Tippingbucket Rain Gauge. *Journal of the Japan Society of Engineering Geology*, 48 (4): 203–206. doi:10.5110/jjseg.48.203.

Moriyama, T., Nishiyama, K., Izumi, S., et al. (2016) "Smart Rainwater Tanks as a Rainguage Network and Dam for Flood Control." In *Procedia Engineering*. 2016. Elsevier Ltd. pp. 243–246. doi:10.1016/j.proeng.2016.07.466.

Mulley, R. (2004) *Flow of industrial fluids : theory and equations*. CRC Press.

Nagendran, S.K., Ismail, M.A.M. and Tung, W.Y. (2019) Integration of UAV photogrammetry and kinematic analysis for rock slope stability assessment. *Bulletin of the Geological Society of Malaysia*, 2019 (67): 117–123. doi:10.7186/bgsm67201913.

Narita, K. (2000) *Design and Construction of Embankment Dams*. Available at: http://aitech.ac.jp/~narita/tembankmentdam1.pdf.

Nguyen, C.D., Benahmed, N., Philippe, P., et al. (2017) Experimental study of erosion by suffusion at the micro-macro scale Radjai, F., Nezamabadi, S., Luding, S., et al. (eds.). *EPJ Web of Conferences*, 140: 09024. doi:10.1051/epjconf/201714009024.

Ni, K.C. and Gao, W.S. (2014) Application of shape acceleration array technology to shaking table model test of soil-structure system. *Yantu Lixue/Rock and Soil Mechanics*, 35: 278–283.

O'Brien, W.D., Darmondy, R.G.J. and Munson, D.C.J. (1996) *Acoustic Characterization of Soil*.

Oelze, M.L., O 'brien, W.D. and Darmody, R.G. (2002) Measurement of Attenuation and Speed of Sound in Soils. *Soil Sci. Soc. Am. J.*, (66): 788–796. Available at: http://www.brl.uiuc.edu/Publications/2002/Oelze-SSAJ-7882002.pdf.

Okeke, A.C.-U. and Wang, F. (2016) Hydromechanical constraints on piping failure of landslide dams: an experimental investigation. *Geoenvironmental Disasters*, 3 (1): 4. doi:10.1186/s40677-016-0038-9.

Omofunmi, O.E., Kolo, J.G., Oladipo, A.S., et al. (2017) *A Review on Effects and Control of Seepage through Earth-fill Dam*., 22 (5): 1–11. doi:10.9734/CJAST/2017/28538.

Oskay, C. and Zeghal, M. (2011) A survey of geotechnical system identification techniques. *Soil Dynamics and Earthquake Engineering*. 31 (4) pp. 568–582. doi:10.1016/j.soildyn.2010.11.011.

Ouyang, M. and Takahashi, A. (2016) Influence of initial fines content on fabric of soils subjected to internal erosion. *Canadian Geotechnical Journal*, 53 (2): 299–313. doi:10.1139/cgj-2014-0344.

Pehme, P.E. (2011) Groundwater Geophysics: A Tool for Hydrogeology. *Environmental and Engineering Geoscience*, 17 (1): 96–98. doi:10.2113/gseegeosci.17.1.96.

Perrone, A., Lapenna, V. and Piscitelli, S. (2014) Electrical resistivity tomography technique for landslide investigation: A review. *Earth-Science Reviews*. 135 pp. 65–82. doi:10.1016/j.earscirev.2014.04.002.

Prasad, M., Zimmer, M.A., Berge, P.A., et al. (2004) *Laboratory Measurements of Velocity and Attenuation in Sediments*.

Pride, S.R. and Berryman, J.G. (2003) Linear dynamics of double-porosity dual-permeability materials. II. Fluid transport equations. *Physical Review E - Statistical Physics, Plasmas, Fluids, and Related Interdisciplinary Topics*, 68 (3): 10. doi:10.1103/PhysRevE.68.036604.

Radzicki, K. (2016) The concept of quasi-3D monitoring of seepage and erosion processes and deformations in dams and dikes, considering in particular linear measurement sensors. *Czasopismo Techniczne*, 0 (0). Available at: http://ejournals.eu/sj/index.php/Cz/article/view/6103.

Raichel, D.R. (2006) *The science and applications of acoustics*. 2nd ed. Springer. doi:10.1121/1.1582438.

Rasskazov, L.N., Yadgorov, E.K. and Nikolaev, V.B. (2018) Field Observations of Soil Settlements, Displacements, and Pore Pressure in Dams. *Power Technology and Engineering*, 51 (6): 611–620. doi:10.1007/s10749-018-0881-9.

Reeves, D. and Rothman, D.H. (2013) Age dependence of mineral dissolution and precipitation rates. *Global Biogeochemical Cycles*, 27 (3): 906–919. doi:10.1002/gbc.20082.

Richards, K.S. and Reddy, K.R. (2014) Kinetic energy method for predicting initiation of backward erosion in earthen dams and levees. *Environmental and Engineering Geoscience*, 20 (1): 85–97. doi:10.2113/gseegeosci.20.1.85.

Rico, M., Benito, G., Salgueiro, A.R., et al. (2007) *Reported tailings dam failures A review of the European incidents in the worldwide context*. doi:10.1016/j.jhazmat.2007.07.050.

Riley, F.S. (1969) Analysis of Borehole Extensometer Data from Central California. *Land Subsidence, Volume 2*, pp. 423–431.

Rinehart, R. V, Parekh, M.L., Rittgers, J.B., et al. (2012) *Preliminary Implementation of Geophysical Techniques to Monitor Embankment Dam Filter Cracking at the Laboratory Scale*., pp. 1401–1408.

Robb, G.B.N., Best, A.I., Dix, J.K., et al. (2006) The frequency dependence of compressional wave velocity and attenuation coefficient of intertidal marine sediments. *The Journal of the Acoustical Society of America*, 120. doi:10.1121/1.2345908.

Robbins, B.A., van Beek, V.M., López-Soto, J.F., et al. (2017) A novel laboratory test for backward erosion piping. *International Journal of Physical Modelling in Geotechnics*, pp. 1–14. doi:10.1680/jphmg.17.00016.

Rochim, A., Marot, D., Sibille, L., et al. (2017) Effects of Hydraulic Loading History on Suffusion Susceptibility of Cohesionless Soils. *Journal of Geotechnical and Geoenvironmental Engineering*, 143 (7): 04017025. doi:10.1061/(ASCE)GT.1943-5606.0001673.

Rönnqvist, H. and Viklander, P. (2014) On the Kenney-Lau Approach to Internal Stability Evaluation of Soils. *Geomaterials*, 04 (04): 129–140. doi:10.4236/gm.2014.44013.

Rönnqvist, H. and Viklander, P. (2015) Applying Empirical Methods to Assess the Internal Stability of Embankment Dam Cores of Glacial Till. *Geomaterials*, (January): 1–18. doi:10.4236/gm.2015.51001.

Rönnqvist, H. and Viklander, P. (2018) Effects of Suffusion in Dam Core Soils with Varying Degrees of Internal Instability. *Electronic Journal of Geotechnical Engineering*, 23: 141–152.

Rönnqvist, H., Viklander, P. and Knutsson, S. (2017) Experimental Investigation of Suffusion in Dam Core Soils of Glacial Till. *Geotechnical Testing Journal*, 40 (3): 426–439. doi:10.1520/GTJ20150298.

Rosen, P.A., Hensley, S., Joughin, I.R., et al. (2000) Synthetic aperture radar interferometry. *Proceedings of the IEEE*, 88 (3): 333–382. doi:10.1109/5.838084.

Rosenblum, S. and Brownfield, I.K. (n.d.) *Magnetic Susceptibilities of Minerals*.

Rosenbrand, E. (2011) *Investigation into quantitative visualisation of suffusion*.

Rouse, C., Styles, P. and Wilson, S.A. (1991) Microseismic emissions from flowslide-type movements in South Wales. *Engineering Geology*, 31 (1): 91–110. doi:10.1016/0013-7952(91)90059-T.

de Rubertis, K. (ed.) (2018) *Monitoring Dam Performance*. Reston, VA: American Society of Civil Engineers. doi:10.1061/9780784414828.

Sasaki, T., Shioya, R., Sakai, T., et al. (2020) Position and posture measurements using laser projection markers for infrastructure inspection. *Electronics (Switzerland)*, 9 (5). doi:10.3390/electronics9050807.

Sato, M. and Kuwano, R. (2015) Suffusion and clogging by one-dimensional seepage tests on cohesive soil. *Soils and Foundations*, 55 (6): 1427–1440. doi:10.1016/j.sandf.2015.10.008.

Schlaeger, S., Huebner, C. and Becker, R. (2005) Simple soil moisture probe for low-cost measurement

applications. *Proceedings of the 6th Conference on Electromagnetic Wave Interaction with Water and Moist Substances ISEMA*, pp. 258–265. Available at: http://bbs.ednchina.com/uploadedn/Blog/2008/4/15/d3a9ca1a-d25c-4788-8d56-e0b1f78d7e7f.pdf.

Sessler, G.M. (1991) Acoustic sensors. *Sensors and Actuators: A. Physical*, 26 (1–3): 323–330. doi:10.1016/0924-4247(91)87011-Q.

Shire, T. and O'Sullivan, C. (2017) A network model to assess base-filter combinations. *Computers and Geotechnics*, 84: 117–128. doi:10.1016/J.COMPGEO.2016.11.014.

Shire, T., O'Sullivan, C., Hanley, K.J., et al. (2014) Fabric and Effective Stress Distribution in Internally Unstable Soils. *Journal of Geotechnical and Geoenvironmental Engineering*, 140 (12): 04014072. doi:10.1061/(ASCE)GT.1943-5606.0001184.

Sibille, L., Marot, D. and Sail, Y. (2015a) A description of internal erosion by suffusion and induced settlements on cohesionless granular matter. *Acta Geotechnica*, 10 (6): 735–748. doi:10.1007/s11440-015-0388-6.

Sibille, L., Marot, D. and Sail, Y. (2015b) A description of internal erosion by suffusion and induced settlements on cohesionless granular matter. *Acta Geotechnica*, 10 (6): 735–748. doi:10.1007/s11440-015-0388-6.

Skempton, A.W. and Brogan, J.M. (1994) Experiments on piping in sandy gravels. *Géotechnique*, 44 (3): 449–460. doi:10.1680/geot.1994.44.3.449.

Slangen, P. (2015) *On the influence of effective stress and micro-structure on suffusion and suffosion*., (June).

Slangen, P. and Fannin, R.J. (2017a) A Flexible Wall Permeameter for Investigating Suffusion and Suffosion. *Geotechnical Testing Journal*, 40 (1): 20150287. doi:10.1520/GTJ20150287.

Slangen, P. and Fannin, R.J. (2017b) The role of particle type on suffusion and suffosion. *Géotechnique Letters*, 7 (1): 1–5. doi:10.1680/jgele.16.00099.

Smalley, I.J. and Dijkstra, T.A. (1991) The Teton Dam (Idaho, U.S.A.) failure: problems with the use of loess material in earth dam structures. *Engineering Geology*, 31 (2): 197–203. doi:10.1016/0013-7952(91)90006-7.

Smethurst, J.A., Smith, A., Uhlemann, S., et al. (2017) Current and future role of instrumentation and monitoring in the performance of transport infrastructure slopes. *Quarterly Journal of Engineering Geology and Hydrogeology*, 50 (3): 271–286. doi:10.1144/qjegh2016-080.

Smith, A. (2015) *Quantification of slope deformation behaviour using acoustic emission monitoring*. Available at: https://dspace.lboro.ac.uk/2134/18593.

Smith, A., Biller, T., Dixon, N., et al. (2019a) "Acoustic emission monitoring in geotechnical element tests." In *XVII ECSMGE-2019*. Reyjavik, 2019.

Smith, A. and Dixon, N. (2014) Quantification of landslide velocity from active waveguide-generated acoustic emission. *Canadian Geotechnical Journal*, 52 (4): 413–425. doi:10.1139/cgj-2014-0226.

Smith, A. and Dixon, N. (2019a) Acoustic emission behaviour of dense sands. *Géotechnique*, pp. 1–45. doi:10.1680/jgeot.18.p.209.

Smith, A. and Dixon, N. (2019b) Acoustic emission behaviour of dense sands. *Géotechnique*, pp. 1–16. doi:10.1680/jgeot.18.P.209.

Smith, A. and Dixon, N. (2019c) Acoustic emission generated by glass beads in compression and shearing. *Granular Matter*, 21 (4): 1–16. doi:10.1007/s10035-019-0944-0.

Smith, A., Dixon, N. and Fowmes, G.J. (2017) Early detection of first-time slope failures using acoustic emission measurements: large-scale physical modelling. *Géotechnique*, 67 (2): 138–152. doi:10.1680/jgeot.15.P.200.

Smith, A., Dixon, N., Meldrum, P., et al. (2014) Acoustic emission monitoring of a soil slope: Comparisons with continuous deformation measurements. *Géotechnique Letters*, 4 (4): 255–261.

doi:10.1680/geolett.14.00053.

Smith, A., Moore, I.D. and Dixon, N. (2019b) “Acoustic Emission Sensing of Pipe-Soil Interaction: Development of an Early Warning System for Buried Pipe Deformation.” In *International Conference on Smart Infrastructure and Construction 2019 (ICSIC)*. January 2019. ICE Publishing. pp. 463–468. doi:10.1680/icsic.64669.463.

Smith, S.W. (1999) *Digital Signal Processing*. 2nd ed. San Diego, California: California Technical Publishing.

Soga, K. and Schooling, J. (2016) Infrastructure sensing. *Interface Focus*. 6 (4). doi:10.1098/rsfs.2016.0023.

Stark, T.D. and Choi, H. (2008) Slope inclinometers for landslides. *Landslides*, 5 (3): 339–350. doi:10.1007/s10346-008-0126-3.

Szabo, T.L. (1995) Causal theories and data for acoustic attenuation obeying a frequency power law. *The Journal of the Acoustical Society of America*, 97 (1): 14–24. doi:10.1121/1.412332.

Take, W.A. and Valsangkar, A.J. (2001) Earth pressures on unyielding retaining walls of narrow backfill width. *Can. Geotech. J.*, 38: 1220–1230. doi:10.1139/cgj-38-6-1220.

Taylor, H.F., O’Sullivan, C., Sim, W.W., et al. (2017) Sub-particle-scale investigation of seepage in sands. *Soils and Foundations*. doi:10.1016/j.sandf.2017.05.010.

Technical Advisory Committee on Flood Defences (1999) *Technical report on sand boils (piping)*. Delft: Technical Advisory Committee on Flood Defences. Available at: https://repository.tudelft.nl/islandora/object/uuid%3Af6d03006-7744-452e-8ff2-a4914f118184?collection=research.

Telford, W.M., Geldart, L.P. and Sheriff, R.E. (1990) *Applied Geophysics*. Cambridge University Press. doi:10.1017/CBO9781139167932.

Terzaghi, K. (1925) *Erdbaumechanik auf bodenphysikalischer Grundlage*. Leipzig : Deuticke, 1925.

Terzaghi, K. (1939) 45th James Forrest Lecture, 1939. Soil Mechanics - A New Chapter in Engineering Science. *Journal of the Institution of Civil Engineers*, 12 (7): 106–142. doi:10.1680/ijoti.1939.14534.

Terzaghi, K. and Peck, R.B. (1948) *Soil mechanics in engineering practice*. Chapman & Hall (ed.). New York: J. Wiley & Sons.

To, H.D., Scheuermann, A. and Galindo-Torres, S.A. (2016) Probability of Transportation of Loose Particles in Suffusion Assessment by Self-Filtration Criteria. *Journal of Geotechnical and Geoenvironmental Engineering*, 142(2): 04. doi:10.1061/(ASCE)GT.1943-5606.0001403.

Tohyama, M. (Mikio) and Koike, T. (1998) *Fundamentals of acoustic signal processing*. San Diego, California: Academic Press. doi:10.1016/B978-0-12-692660-6.X5000-6.

Tole, N.M. (2005) *Basic physics of ultrasonographic imaging*. Ostensen, H. (ed.). Geneva, Switzerland: World Health Organization.

Tomlinson, S.S. and Vaid, Y.P. (2000) *Seepage forces and confining pressure effects on piping erosion*. Available at: http://www.nrcresearchpress.com/doi/pdf/10.1139/t99-116.

Torisu, S.S., Faustin, N.E., Elshafie, M.Z.E.B., et al. (2019) *Monitoring of Shaft Excavations in Clay*. In January 2019. Thomas Telford Ltd. pp. 655–664. doi:10.1680/icsic.64669.655.

U. S. Society on Dams (2011) *Materials for embankment dams*. doi:10.1016/0148-9062(85)92801-3.

U.S. Department of the Interior (2012) *Embankment Dams*. Design Sta. U.S. Department of the Interior Bureau of Reclamation.

Uhlemann, S., Smith, A., Chambers, J., et al. (2016a) Assessment of ground-based monitoring techniques applied to landslide investigations. *Geomorphology*, 253: 438–451. doi:10.1016/J.Geomorph.2015.10.027.

Uhlemann, S., Smith, A., Chambers, J., et al. (2016b) Assessment of ground-based monitoring

techniques applied to landslide investigations. *Geomorphology*, 253: 438–451. doi:10.1016/j.geomorph.2015.10.027.

Uicker, J., Pennock, G. and Shigley, J. (2010) *Theory Of Machines and Mechanisms*. 4th ed. Oxford University Press.

USBR (2015) "Internal Erosion Risks for Embankments and Foundations." In *Best Practices in Dam and Levee Safety Risk Analysis*. United States Department of Interior, Bureau of Reclamations. pp. 1–134.

Usher, A.P. (1929) *A History of Mechanical Inventions: Revised Edition - Abbott Payson Usher - Google Books*. New York: Harvard University Press (reprinted by Dover Publications 1988).

Wan, C.F. (2006) *Experimental Investigations of Piping Erosion and Suffusion of Soils in Embankment Dams and their Foundations*. The University of New South Wales. Available at: http://unsworks.unsw.edu.au/fapi/datastream/unsworks:40033/SOURCE01?view=true.

Wan, C.F. and Fell, R. (2008) Assessing the Potential of Internal Instability and Suffusion in Embankment Dams and Their Foundations. *Journal of Geotechnical and Geoenvironmental Engineering*. doi:10.1061/ASCE1090-0241(2008)134:3(401).

Wang, G., Yu, J., Kearns, T.J., et al. (2014) Assessing the accuracy of long-term subsidence derived from borehole extensometer data using GPS observations: Case study in Houston, Texas. *Journal of Surveying Engineering*, 140 (3). doi:10.1061/(ASCE)SU.1943-5428.0000133.

White, A.B., Colman, B., Carter, G.M., et al. (2012) NOAA's rapid response to the Howard A. Hanson Dam flood risk management crisis. *Bulletin of the American Meteorological Society*, 93 (2): 189–207. doi:10.1175/BAMS-D-11-00103.1.

Wightman, E., Jalinoos, F., Sirles, P., et al. (2003) *Application of Geophysical Methods to Highway Related Problems*.

Witten, A.J. (2017) *Handbook of geophysics and archaeology*. Taylor and Francis. doi:10.4324/9781315093260.

Yaacob, R. and Mustapa, M.Z. (2010) Grain-size distribution and subsurface mapping at the Setiu wetlands, Setiu, Terengganu. *Environmental Earth Sciences*, 60 (5): 975–984. doi:10.1007/s12665-009-0236-9.

Yang, J., Yin, Z.Y., Laouafa, F., et al. (2019) Analysis of suffusion in cohesionless soils with randomly distributed porosity and fines content. *Computers and Geotechnics*, 111: 157–171. doi:10.1016/j.compgeo.2019.03.011.

Yastika, P.E., Shimizu, N. and Abidin, H.Z. (2019) Monitoring of long-term land subsidence from 2003 to 2017 in coastal area of Semarang, Indonesia by SBAS DInSAR analyses using Envisat-ASAR, ALOS-PALSAR, and Sentinel-1A SAR data. *Advances in Space Research*, 63 (5): 1719–1736. doi:10.1016/j.asr.2018.11.008.

Yeboah-Forson, A., Comas, X. and Whitman, D. (2014) Integration of electrical resistivity imaging and ground penetrating radar to investigate solution features in the Biscayne Aquifer. *Journal of Hydrology*, 515: 129–138. doi:10.1016/j.jhydrol.2014.04.045.

Zalesky, J., Capova, K. and Zalesky, M. (2014) "Concept of fibre optics geotechnical deformation monitoring and in-situ deployment in open cast mine." In *International Multidisciplinary Scientific GeoConference Surveying Geology and Mining Ecology Management, SGEM*. 2014. International Multidisciplinary Scientific Geoconference. pp. 179–186.

Zhang, Y.F., Gao, J.C., Zhang, W., et al. (2017) Model Test Study on Steel Pipe Pile Foundation Based on Shape Acceleration Array. *Zhongbei Daxue Xuebao (Ziran Kexue Ban)/Journal of North University of China (Natural Science Edition)*, 38 (4). doi:10.3969/j.issn.1673-3193.2017.04.010.

Zhi, M., Shang, Y., Zhao, Y., et al. (2016) Investigation and monitoring on a rainfall-induced deep-seated landslide. *Arabian Journal of Geosciences*, 9 (3). doi:10.1007/s12517-015-2206-8.

Zhou, Z.Q., Ranjith, P.G. and Li, S.C. (2018) An experimental testing apparatus for study of suffusion

of granular soils in geological structures. *Tunnelling and Underground Space Technology*, 78: 222–230. doi:10.1016/J.TUST.2018.05.003.

Zhu, Y., Irmak, S., Jhala, A.J., et al. (2019) Time-domain and frequency-domain reflectometry type soil moisture sensor performance and soil temperature effects in fine- And coarse-textured soils. *Applied Engineering in Agriculture*, 35 (2): 117–134. doi:10.13031/aea.12908.

# Appendix

## Transferrable skills training

| Event/Activity | Date | #Hours |
|---|---|---|
| Essential Teaching Skills training course | February 2018 | 6 |
| Landslide tsunamis: large scale physical modelling of landslide-reservoir interaction; Andy Take; Department of Civil Engineering at Queen University (Canada) | December 2017 | 2 |
| Research Seminar | May 1st 2018 | 3 |
| The contribution of non-destructive testing in the development of innovative materials; Dimitrios G. Aggelis, MEMC, Vrije Universiteit Brussel | May 1st 2018 | 1.5 |
| Concrete characterization and quality control through the modelling and application of wave dispersion and attenuation; Sokratis Iliopoulos MEMC, Vrije Universiteit Brussel | May 1st 2018 | 1.5 |
| IAS Lecture 'Migration in Science - implications for post-Brexit Britain; Venki Ramakrishnan, President of the Royal Society; Recipient of th Prize in Chemistry | May 18th 2018 | 2 |
| Assessing Output Quality; Malcolm Cook, Kevin Lomas, Neil Dixon, Ginny Franklin | June 11th 2018 | 1 |
| 15th BGA Young Geotechnical Engineers Symposium | July 2nd and 3rd 2018 | 16 |
| Invigilation training | June 2018 | 2 |
| Data analysis in R with Tidyverse | March 28th 2018 | 2 |
| Research methodologies |  | 2 |
| A Reference Architecture for a Resilient UK Water Supply System | May 2nd 2018 | 5 |
| High performance computing / Hydra | February 15th 2018 | 2 |
| Other Brown Bag seminars |  | 6 |
| Doctoral Seminar | 12 September 2018, 09.00 12.00am. RT025 | 3 |
| Enterprise Workshop - An insight into Knowledge Transfer Partnerships | 20 September 2018, 12.00 2.00pm. RT025 | 2 |
| Brown Bag Seminar on Assessing journal papers | 02 October 2018, 01.00-02.00pm. RT040 | 1 |
| Fundamentals of NVivo | 04 October 2018, 10.00am 04.00pm, N004 | 6 |
| Association for Project Management (APM) research talk | November 19th 2018 , 01:30-02:30 p.m.; RT 0.25 | 1 |
| LaTeX Workshop | November 20th 2018, 01:00-02:00 p.m.; RT 0.25 | 1 |
| Water Group Seminar: The dynamics of turbulence through the lens of the velocity gradient tensor | November 29th 2018, 01:00-02:00 p.m.; RT 0.25 | 1 |
| Water Group Seminar: Disaster risk reduction | December 13th 2018, 01:00-02:00 p.m.; RT 0.29 | 1 |
| 7ÅÌÃÏÍÅ ÓÅÍÉÎÁÒ ÆÏÒ .ÉÃË 3ÁÒÔÁÉÎ ȷ(ÅÁÄ ÏÆ 'ÅÏÔÅÃÈÎÉÃÁÌ %ÎÇÉÎÅ %ÎÇÉÎÅÅÒÉÎÇõ ÁÎÄ ÐÒÅÓÅÎÔÁÔÉÏÎ ÏÎ (3φ ȷ5+õÓ ÌÁÔÅÓÔ ÈÉÇÈ ÓÐÅÅÄ | December 14th 2018, 01:00-02:00 p.m.; RT 0.29 | 1 |
| Visit from the R&D manager of Severn Trent water, Keiron Maher (Speakers: Lesley Parker and Keiron Maher) | February 7th 2019, 01:00-02:30 p.m.; RT 0.25 | 1.5 |
| Simulink (Mathworks) online course | March 19th-22nd 2019, [online] | 5 |
| Brown Bag Seminar - Applying Successfully for Funding and Fellowships; Dr. Bianca Howard and Dr. Alister Smith | March 26th 2019, 01:00-02:00 p.m.; RT 0.37 | 1 |
| Brown Bag Seminar: Using Design to Disseminate Research; Design for data visualisation. Dr. Nils Jaeger and Nicholas Johnson | April 30th 2019, 01:00-02:00 p.m.; RT 0.25 | 1 |
| %7'ʐ)% φüÔÈ !ÎÎÕÁÌ -ÅÅÔÉÎÇ ȷ%ÕÒÏÐÅÁÎ 7ÏÒËÉÎÇ 'ÒÏÕÐ ÏÎ )ÎÔÅÒÎÁ | 18-21 June 2019, University of British Columbia | 40 |
| Technical Seminar: Trenchless Pipe Installation, Repair and Replacement; Prof Ian D. Moore (Canada Research Chair in Infrastructure %ÎÇÉÎÅÅÒÉÎÇη 1ÕÅÅÎõÓ 5ÎÉÖÅÒÓÉÔÙň #ÁÎÁÄÁɋ | July 8th 2019, 11-12:30 | 1.5 |
| 7ÏÒËÓÈÏÐ ×ÉÔÈ 0ÒÏÆÅÓÓÏÒ )ÁÎ $8 -ÏÏÒÅ ȷ#ÁÎÁÄÁ 2ÅÓÅÁÒÃÈ #ÈÁÉÒ É | July 8th 2019, 14-16:00 | 2 |
| Performance-based design of critical infrastructure considering soil-structure interaction effects - Anastasios Sextos, Professor of Earthqua Engineering Director, University of Bristol | *ÕÌÙ ύÔÈ φτυ 15:00 | 1.5 |
| )!3 ,ÅÃÔÕÒÅɖ 3ÕÐÅÒÓÉÚÅ ÔÈÁÔ ,ÁÒÇÅ ÓÃÁÌÅ ÔÅÓÔÉÎÇ ÁÔ ÔÈÅ 'ÅÏ%Î Canada) | July 10th 2019 16:00-18:00 | 2 |
| "ÌÁÓÔ ÅÆÆÅÃÔÓ ÆÒÏÍ ÖÅÒÙ ÌÁÒÇÅ ÅØÐÌÏÓÉÏÎÓ ʐ ÒÅÓÅÁÒÃÈ ÁÎÄ ÁÐÐÌÉ | July 12th 2019, 12:30-13:30 | 1 |
| Support of undergraduate students with laboratory experimentation | November 6th 2019, 9-12am | 3 |
| Laboratory tutoring - Water seepage through soil; Bernoulli's principle. | November 12th to December 3rd 2019 (Tuesdays and Fridays From ca. 3 to 5pm). | 14 |
| SPSS (IBM) statistical analisys training online course | February 5th-7th 2020 | 5 |
| Brown Bag Seminar: Career experiences in academia (Dr. Eleonora Brembilla, RA; Dr. Tom Djikstra, Senior Lecturer in Engineering Geolo Professor Andy Dainty, the Dean and Professor of Construction Sociology) | February 19th 2020, 12:30 13:30 | 1 |
| Trip to UBC, Vancouver (Canada) - Broadcast of research, prospection of future collaborations, discussion with experts in Internal Erosion | March 21st-28th 2020 | 40 |
| "ÒÏ×Î "ÁÇ 3ÅÍÉÎÁÒ ʐ 4ÈÅ ȭ0Èõ ÉÎ ÔÈÅ 0È$ɖ Á ÄÉÖÅ ÉÎÔÏ ÒÅÓÅÁÒÃÈ Stokoe (Professor of Social Interaction) | 27th of April 12.30 - 2pm on Microsoft Teams | 1.5 |
| "ÒÏ×Î "ÁÇ 3ÅÍÉÎÁÒɖ 4ÒÁÃËÉÎÇ ÔÈÅ ÉÍÐÁÃÔ ÏÆ ÙÏÕÒ ÐÕÂÌÉÃÁÔÉÏÎÓ ʐ Franklin (Academic Librarian of ABCE) | υυÔÈ ÏÆ -ÁÙ on Microsoft Teams | 1 |
| Total hours |  | 191 |
| Days equivalent |  | 32 |

## Results of test with Soil 1

S1T1: commissioning test realised between 31.08.2019 and 04.09.2019. This test was performed with the new apparatus but there were technical difficulties that caused imprecisions regarding especially the flow rate and effective stress as well as having caused the registry of the hydraulic head to be lost, which made the pore pressure be used instead. It also did not have an LVDT installed. Hence, this can be considered a commissioning test that nonetheless produced useful data. This was an upward flow test.

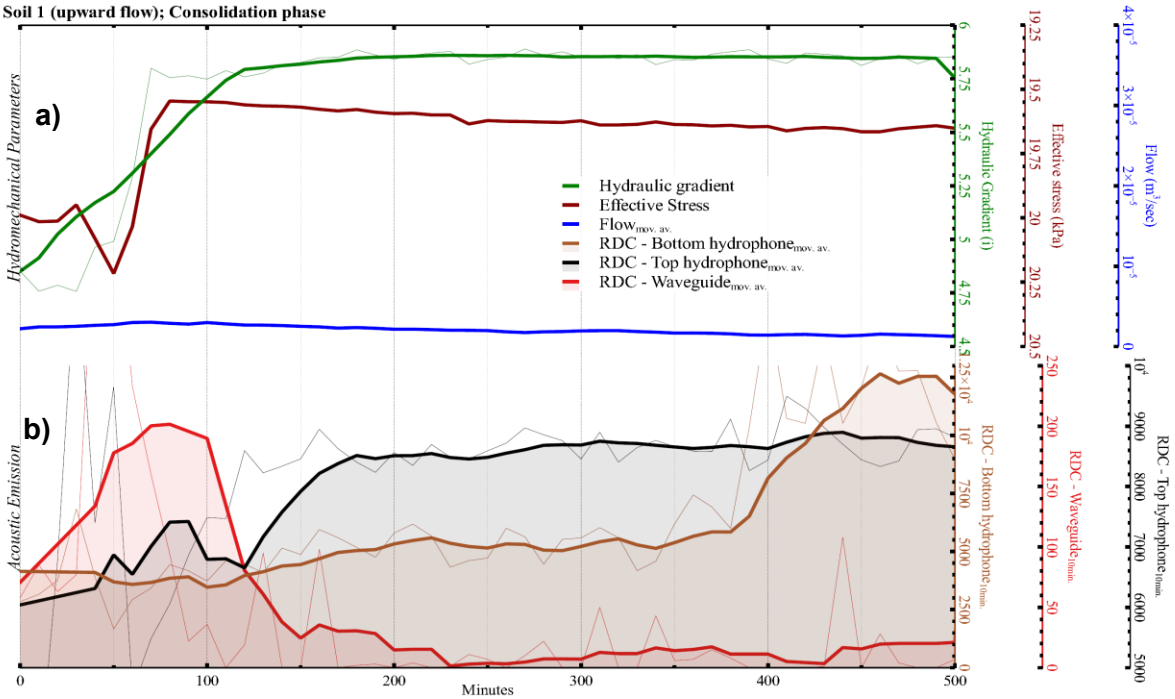


*Figure 0-1. Combined plot of the measured hydromechanical parameters (a) and AE (b) of test S1T1 (consolidation phase) in the time domain. Each parameter has an independent vertical axis with the same colour of the plotted curve (e.g. the blue line represents flow rate and corresponds to the blue vertical axis). Thin lines represent raw data of variables shown with the same colour in thicker lines, which are moving averages.*

*Table 35. Description of symbols used in summary tables of general plot trends of permeameter tests.*

| Key | |
|---|---|
| Rise | ↗ |
| Drop | ↘ |
| Plateau | — |
| Fluctuating | ∿ |
| Peak (local) | Λ |
| Trough (local) | V |
| Arc | ⌒ |

*Table 36. Summary of main general trends observed over time during the consolidation phase of test S1T1. Key to symbols in Table 35.*

S1T1 – Consolidation phase

| Time (minutes) | σ' | i | BH | WG | TH |
|---|---|---|---|---|---|
| 0-100 | ↗ | — | ∧ | ∧ | ∧ |
| 100-180 | — | — | ↗ | ↗ | ↘ |
| 180-300 | — | — | — | — | — |
| 300-500 | — | — | — | — | ↗ |

## S1T1 Consolidation

The hydromechanical parameters of the consolidation phase of test S1T1 are shown in Figure 0-1a and Table 36. During this phase (from min. 30 to 80), the effective stress (*σ'*) showed a rise (momentarily interrupted by a local trough) proportional to the addition of vertical load to the sample that by min. 80 reached a plateau (with a slight downward slope) that lasted until the end of this test phase. The hydraulic gradient (*i*) showed an analogous trend – presumably due to the fluid movement, as will be explored in the Discussion section. The amount of fluid exiting the sample was negligible.

The AE measured during the consolidation phase of this test is seen on Figure 0-1b. The RDC of the waveguide (WG) showed an accentuated peak corresponding to the vertical loading, then gradually decreasing until a baseline apparently corresponding to the dissipation of excess pore-water pressure was found. A peak equivalent to the vertical loading was also seen on the top hydrophone (TH), but, after the RDC of this sensor troughed with the end of the loading, a further increase was observed, which formed a plateau lasting until the end of the plot. The Bottom hydrophone (BH) also showed a peak during the vertical loading but a more modest one when compared to the RDC values it reached by the end of the plot, which happened after a slight upward slope by the BH.

After inserting the sample in the permeameter it was noted that the water volume below the bottom confining plate (at the bottom of which was the BH) had become turbid (e.g. with silt). As this material settled it seemed to impact the BH and at least partially cause the signal observed after the vertical loading phase. This turned was observed in several tests – with its detected intensity varying with soil composition (i.e. fines/silt content) and sensitivity of the acoustic sensors (caused by issues with the sensors themselves or accessory equipment like amplifiers and connectors).

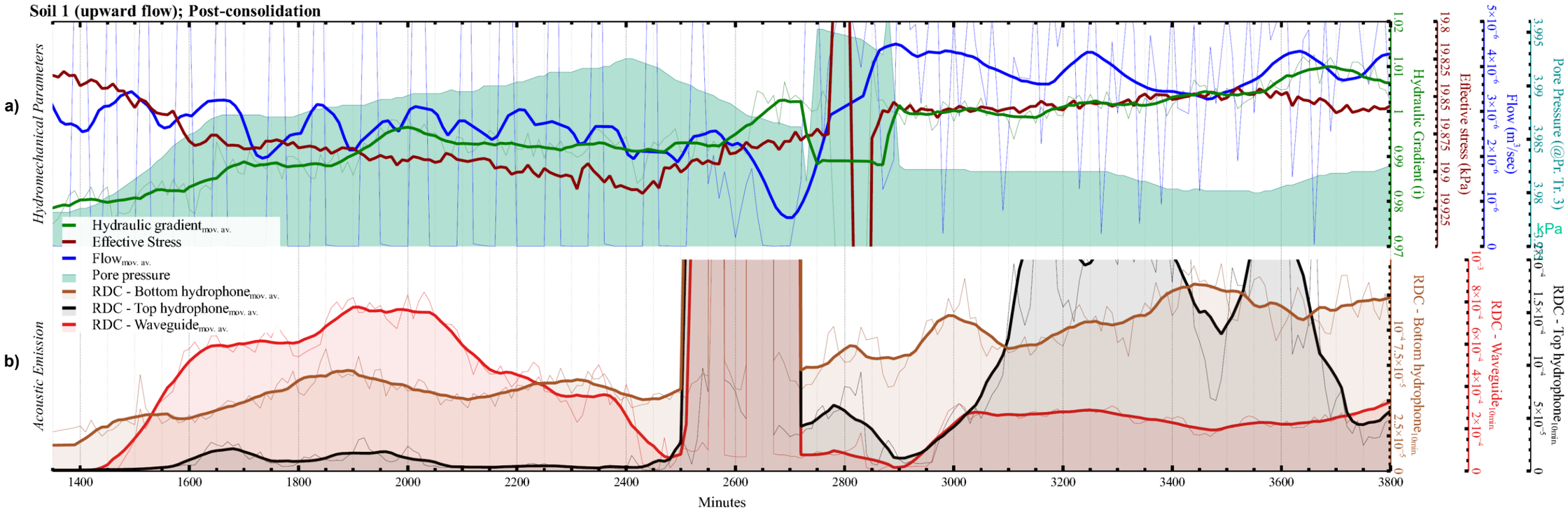


*Figure 0-2. Combined plot of the measured hydromechanical parameters (a) and AE (b) of test S1T1 (post consolidation phase) in the time domain. Each parameter has an independent vertical axis with the same colour of the plotted curve (e.g. the blue line represents flow rate and corresponds to the blue vertical axis). The LVDT data indicates compression of the sample – a reduction of volume is reflected as an increased LVDT value (in millimetres). Thin lines represent raw data of variables shown with the same colour in thicker lines, which are moving averages. Apparent instability of Flow measurement was due to equipment issues.*

*Table 37. Summary of main general trends observed over time during the seepage test (post-consolidation) phase of test S1T1. Key to symbols in Table 35.*

S1T1 – Seepage test (post-consolidation)

| Time (minutes) | Hydraulic head | σ' | Q | i | BH | WG | TH |
|---|---|---|---|---|---|---|---|
| 1300-1650 | ↗ | ↘ | ∿ | ↗ | ↗ | ↗ | ↗ |
| 1650-2000 | ↗ | ↘ | ∿ | ↗ | ↗ | ↗ | ∿ |
| 2000-2400 | ↗ | ↘ | ∿ | — | ∿ | ↘ | — |
| 2400-2750 | ↘ | ↗ | ↘ | ↗ | Λ | Λ | Λ |
| 2750-2900 | ↗ | ∿ | ↗ | ↗ | ↗ | ↘ | ↘ |
| 2900-3300 | — | — | ∿ | — | ↗ | — | Λ |
| 3300-3550 | ↘ | ↗ | ↘ | ↗ | ↗ | ↘ | V |
| 3550-3800 | ↗ | ↘ | ∿ | ⌒ | — | ↗ | ↘ |

**S1T1 Seepage test (post-consolidation)**

The hydromechanical parameters of the rest of the test are found in Figure 0-2a and Table 37. As the head was manipulated, the flow rate (*Q*) stayed relatively constant until ca. min 2600, when it swung once down-and-up, and by ca. min 2900 became relatively stable. The *σ'* showed an overall trend that mirrored the pore pressure; it at first dropped while the pore pressure was being increased (the rate of pore pressure increase slowed by min. 1650, which also made the downslope of the *σ'* become less steep), which happened until ca. min. 2400. By this point, parallel to the pore pressure reverting to a decrease, the *σ'* began increasing, showed a significant up-down swing between ca. min. 2750 and 2850 (roughly parallel to a similarly anomalous movement of the other hydromechanical parameters). Accordingly, when the pore pressure at first plateaued (until ca. min 3300), formed a slight upward concavity (min. 3300-3650) and then continued a gentle rise until the end of the test, the *σ'* replicated the plateau and then formed a slight arch followed by a gentle drop in parallel.

The hydraulic gradient (*i*) at first increased until ca. min 2000, stayed relatively constant until ca. min. 2550 (although with a slight downward trend until ca, min 2300), swung in rough opposition to the flow rate (up-down) and, by min 2900, stabilized. From ca. min 3150 onwards *i* entered an overall upward trend that lasted until the end of the plot. On the AE (Figure 0-2b), the RDC of all three sensors began by showing an increase. However, this increase initiated at different times for each sensor: the BH at ca. min. 1400. WG ca. min. 1450 and TH ca. min. 1550. Movement of soil particles (or early-stage internal erosion) was noticed by min. 1450. This initial signal of the TH and WG then subsidised, respectively by ca. min. 2100 and 2450, while the BH stayed relatively constant (although in an oscillatory way) from ca. min. 1900 to min. 2500.

At min 2500 the signal of the three acoustic sensors drastically increased (reaching their highest values of the test). By min. 2720 the RDC of the three sensors dropped in a similarly drastic way, although the TH did not meet its baseline (where it was before the drastic increase). After this point the BH followed a rough overall upward trend until the end of the plot. The WG stayed at ca. baseline (slightly sloping down) until min 2900, when in increased, reached a plateau by min. 3025 and remained so (with slight oscillations) until the end of the plot. The TH between min 2720 and 2850 increased, formed a local trough at ca. min. 2900, rose, and stayed considerably elevated between min. 3100 and 3700 (interrupted by a local trough at min. 3470) and, after a decrease ending at in. 3750, stabilized until the end of the plot. An erosional pipe or preferential flow pathway was noted at ca. min. 2600.

## Hydrophone specifications

*AS-1, Aquarian Scientific Broadband Measurement Hydrophone*

Further details:

- Passive piezo device
- Linear range: 1Hz to 100kHz ±2dB
- Receiving Sensitivity: -208dBV re 1µPa (40µV / Pascal)
- Transmitting Sensitivity: 140dB SPL re 1µPa, 1Vrms input at 1meter, 90kHz
- Maximum Input Voltage: 30V p-p (continuous); 150V p-p (<10% duty cycle, <100KHz)
- Horizontal Directivity(20kHz): ±0.2dB
- Horizontal Directivity (100kHz): ±1dB
- Vertical Directivity (20kHz): ±1dB
- Vertical Directivity (100kHz): +6dB -11dB
- Operating depth: 200m
- Survival depth: 350m
- Operating temperature range: -10°C to +80°C
- Nominal capacitance: 5nF +/- 15% (plus cable @ 118pF/m)
- Output connection: BNC (standard)
- Size: 12mm D x 40mm L
- Weight (in air): 8g (plus cable @ 28g/m)
- Cable length: 9 meters standard. Any length on request.
- Cable Jacket: Polyurethane, OD: 4.5mm
- Encapsulant: Polyurethane

Free Field Voltage Sensitivity

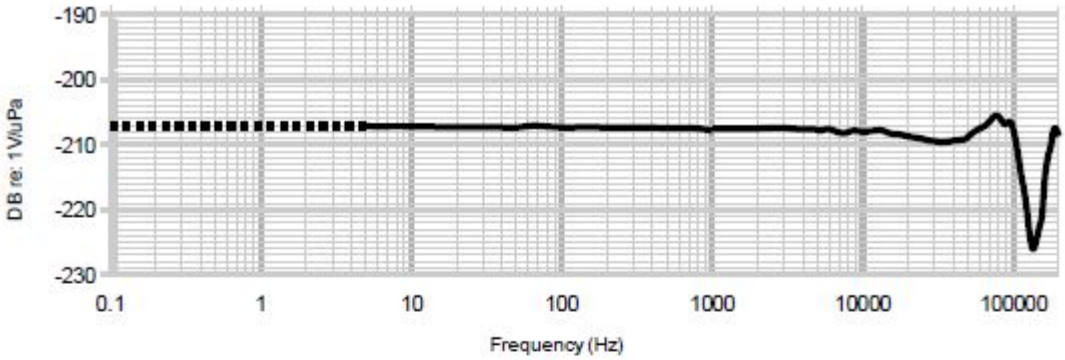


Transmitting Voltage Response

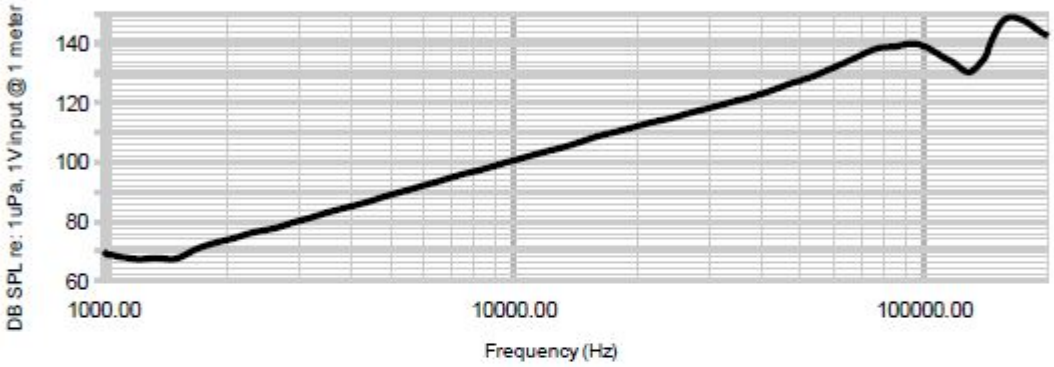


Impedance Phase

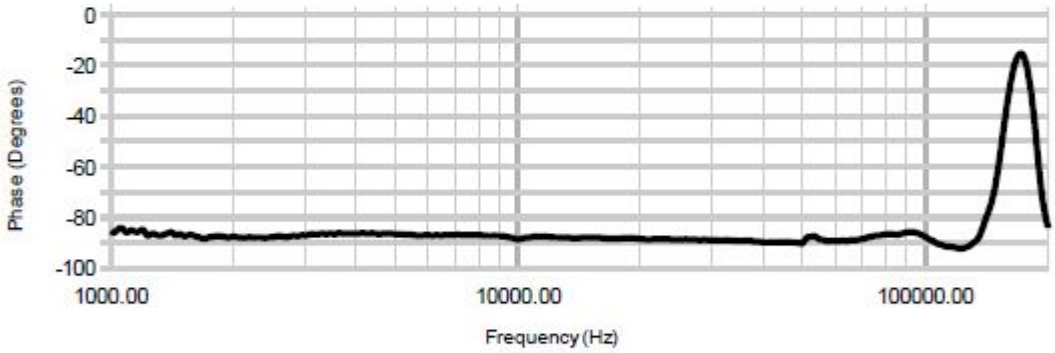


Impedance Magnitude

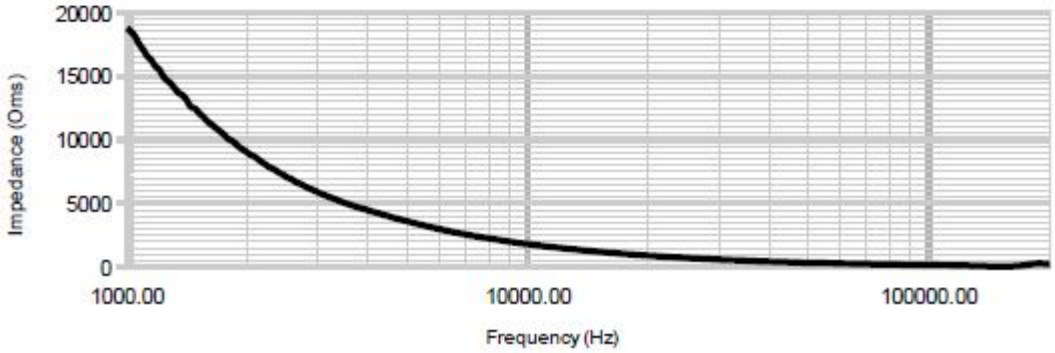


FFVS: Nominal 5Hz – 100KHz, -207.6 (+2.1 / -2.0) dB re: 1V/uPa. Not tested (theoretical) below 5Hz.

Aquarian Scientific
1004 Commercial Ave. #225
Anacortes, WA 98221 USA
www.aquarianscientific.com

AS-1 hydrophone

SN#: (typical)

Directional Response, 20KHz XY (Horizontal)

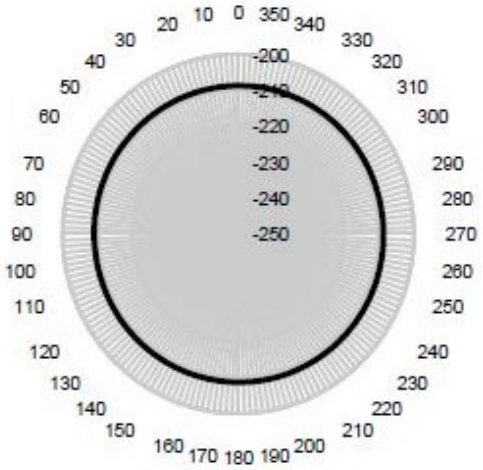


Directional Response, 20KHz XZ (Vertical)

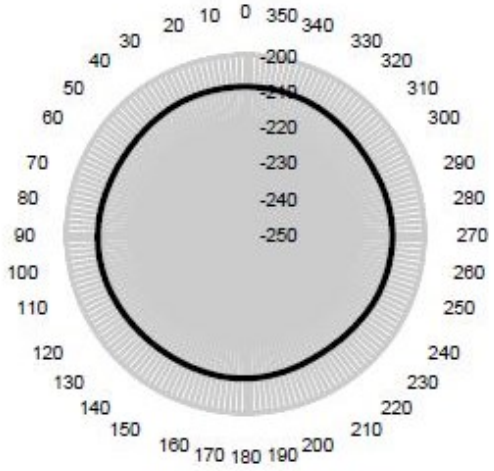


Directional Response, 100KHz XY (Horizontal)

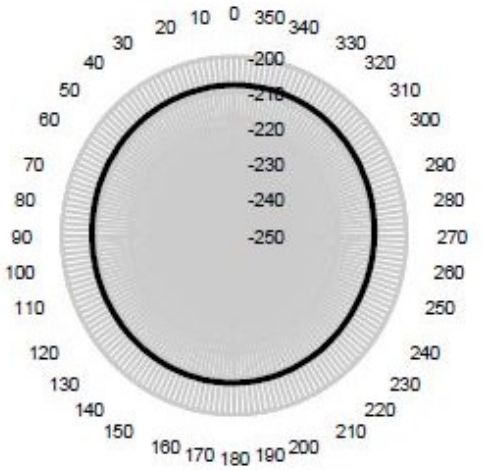


Directional Response, 100KHz XZ (Vertical)

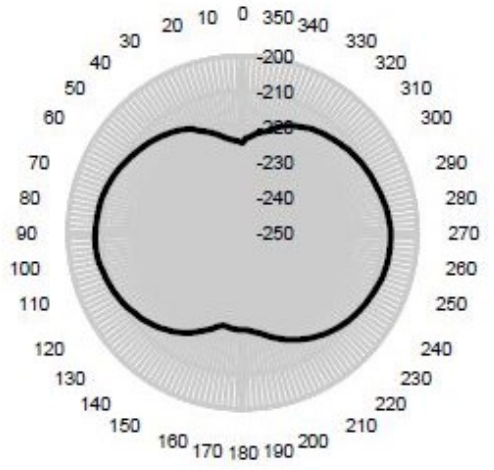


**NOTES:**
Data obtained from US Navy, Underwater Sound Reference Division, Newport. Average of three samples measured, June 2013.

Measurements taken at end of 9-meter cable

FFVS Low frequency response is limited by amplifier input impedance. Fc= 1/4.71e-8(amplifier input impedance) – Approximately 1Mohm for 20Hz cutoff; 22Mohm for 1Hz; 220Mohm for 0.1Hz.

Directional Response: Hydrophone rotated on same axis as the cable for XY measurements. XZ measurements are made with rotation perpendicular to the cable and with origin (0 degrees) facing end opposite the cable.

## Specifications of load cells

| **LC101 stainless steel “S” beam load cells (OMEGA)**<br>*Specifications:* | | |
|---|---|---|
| Excitation | | 10 Vdc, 15 Vdc maximum |
| Output | | 3 mV/V ±0.0075 mV/V |
| Linearity | | ±0.03% FSO (0.1% 40 K) |
| Hysteresis | | ±0.02% FSO (0.1% 40 K) |
| Repeatability | | ±0.01% FSO (0.05% 40 K) |
| Zero Balance | | ±1% FSO |
| Operating Temp Range | | -40 to 93°C (-40 to 200°F) |
| Compensated Temp Range | | 17 to 71°C (60 to 160°F) |
| Thermal Effects | Zero | 0.002% FSO/°C |
| | Span | 0.002% FSO/°C |
| Safe Overload | | 150% of capacity |
| Ultimate Overload | | 300% of capacity |
| Input Resistance | | 350 ±10 Ω |
| Output Resistance | | 350 ±10 Ω |
| Full Scale Deflection | | 0.010 to 0.020" |
| Construction | | 17-4 PH stainless steel |
| Electrical (4-Conductor Shielded Cable) | | 9 m (30') 20 AWG |

## Specifications of pressure transducers

| **PXM309 Series Pressure Transducers**<br>*Specifications:* | | |
|---|---|---|
| Supply Voltage | | Reverse polarity and over voltage protected |
| 0 to 10 Vdc Output | | 15 to 30 Vdc at 10 mA |
| 4 to 20 mA | | 9 to 30 Vdc |
| Static Accuracy 350 mB to 700 bar | | ±0.25% FS BSL at 25ºC (includes linearity, hysteresis and repeatability) |
| Long Term Stability (1 yr) | | ±0.25% FS |
| Total Error Band | | 70 mB ±4.5% gage |
| | | 140 mB ±3% gage |
| | | 350 mB ±1.5% gage and absolute |
| | | 1 to 20 bar ±1% absolute |
| | | 1 to 700 bar ±1% gage |
| Note: total error band includes all accuracy errors, thermal errors, span and zero tolerances. | | |
| Isolation (Body to Any Lead) | | 1 M Ω at 25 Vdc |
| Pressure Cycles | | 1 x 107 full scale cycles |
| Pressure Overload | | 3 x rated pressure or 1.38 bar whichever is greater |
| Burst Pressure | | 5 x rated pressure or 1.72 bar whichever is greater |
| Operating Temperature | | -40 to 85ºC |
| Response Time | | 1 mS |
| Bandwidth | | DC to 1 kHz type |
| Pressure Connection | | G 1⁄4 Male |
| Wetted Parts | | 316 SS |
| CE Compliant | | EC55022, EC55011, Emissions Class A&B |
| IEC | | 61000 -2, -3, -4, -5, -6, & -9 |
| Shock | | 50 g 11 mSec half sine shock |
| Vibration | | ± 20 g |
| Electrical Connections | PXM309 | 1.5 m (5') 2 or 3-conductor cable, mA or 10V outputs |
| | PXM319 | mini DIN connector with mating connector included |
| | PXM359 | M12 4-pin connector |
| ROHS Compliant | | Yes |
| Weight | | Typical 150 g depending upon configuration |

## Logging scale specifications

| **KERN DE35K5D Platform scale**<br>*Specifications:* | |
|---|---|
| Adjustment options | External calibration |
| Linearity | 15 g \| 30 g |
| Readability [d] | 5 g \| 10 g |
| Recommended adjusting weight | 30 kg (M1) |
| Repeatability | 5 g \| 10 g |
| Resolution | 3 3.500 |
| Stabilisation time under laboratory conditions | 2,500 s |
| Tare range | 35 kg |
| Warm up time | 10 min \| 10 min |
| Weighing capacity [Max] | 15 kg \| 35 kg |
| Weighing system | Strain gauge |
| Counting resolution | 3500 |
| Mininum piece weight at piece counting (Laboratory | 10 g |
| Maximum humidity | 80% |
| Maximum operating temperature | 35 °C |
| Minimum ambient temperature | 5 °C |
| Input voltage | 220 V - 240 V AC 50 Hz |
| Dimensions housing (WxDxH) | 318 x 305 x 75 mm |
| Dimensions of display device (WxDxH) | 225 x 110 x 55 mm |
| Dimensions of weighing plate (WxDxH) | 318 x 308 x 75 mm |
| Material weighing plate | stainless steel |
| Weighing surface (WxD) | 315 x 305 mm |

## Load on top and bottom load cells

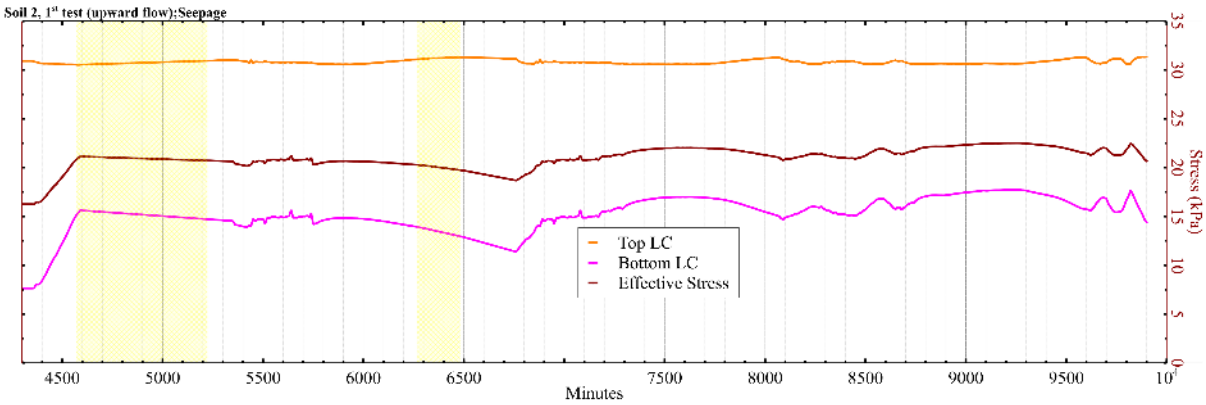


*Figure 0-3. Stress measured independently on top and bottom load cells (orange and magenta lines) as well as interpolated effective stress at the position of pressure transducer 3 (red line). Yellow areas represent data gaps. S2T1.*

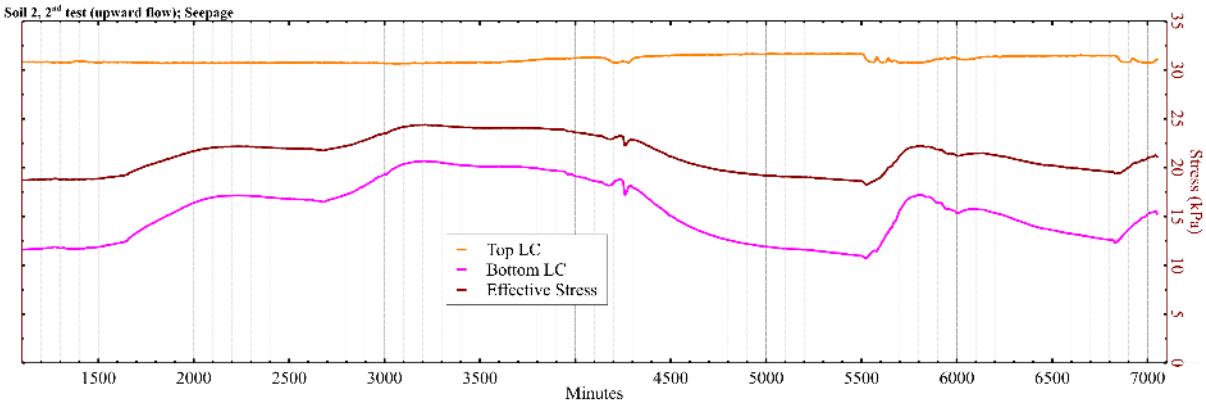


*Figure 0-4. Stress measured independently on top and bottom load cells (orange and magenta lines) as well as interpolated effective stress at the position of pressure transducer 3 (red line). S2T2.*

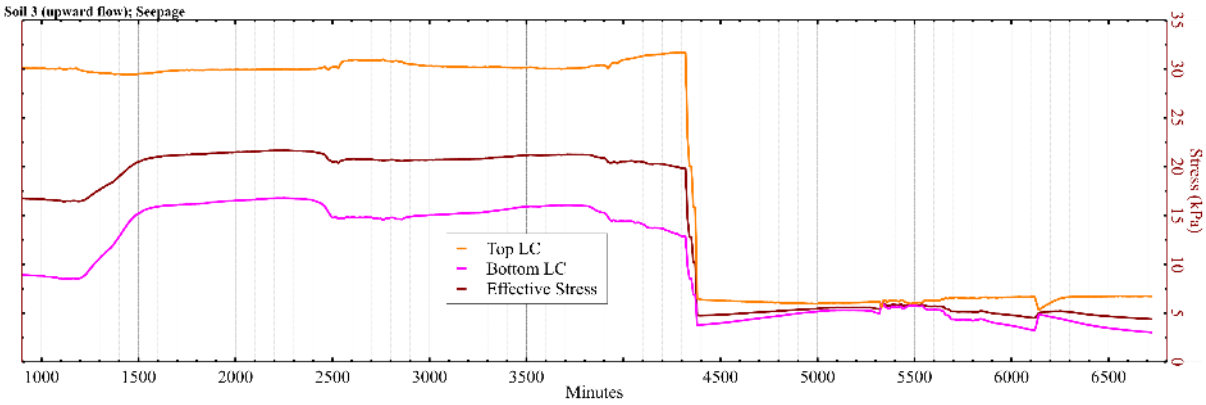


*Figure 0-5. Stress measured independently on top and bottom load cells (orange and magenta lines) as well as interpolated effective stress at the position of pressure transducer 3 (red line). S3T1.*

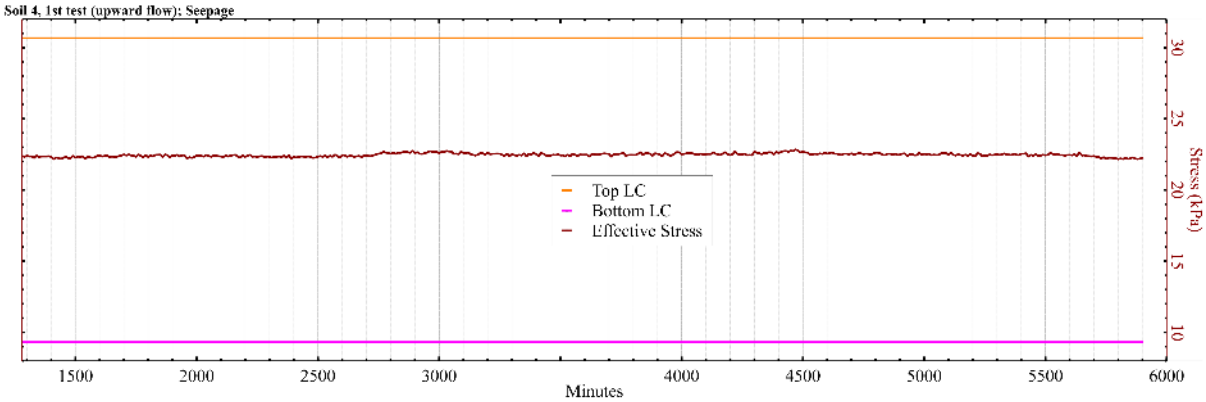


*Figure 0-6. Stress measured independently on top and bottom load cells (orange and magenta lines) as well as interpolated effective stress at the position of pressure transducer 3 (red line). S4T1.*

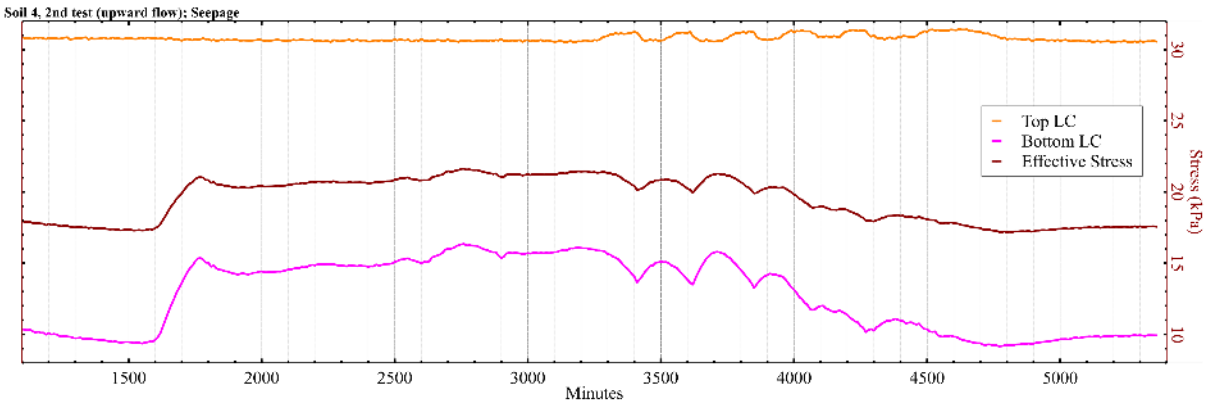


*Figure 0-7. Stress measured independently on top and bottom load cells (orange and magenta lines) as well as interpolated effective stress at the position of pressure transducer 3 (red line). S4T2.*

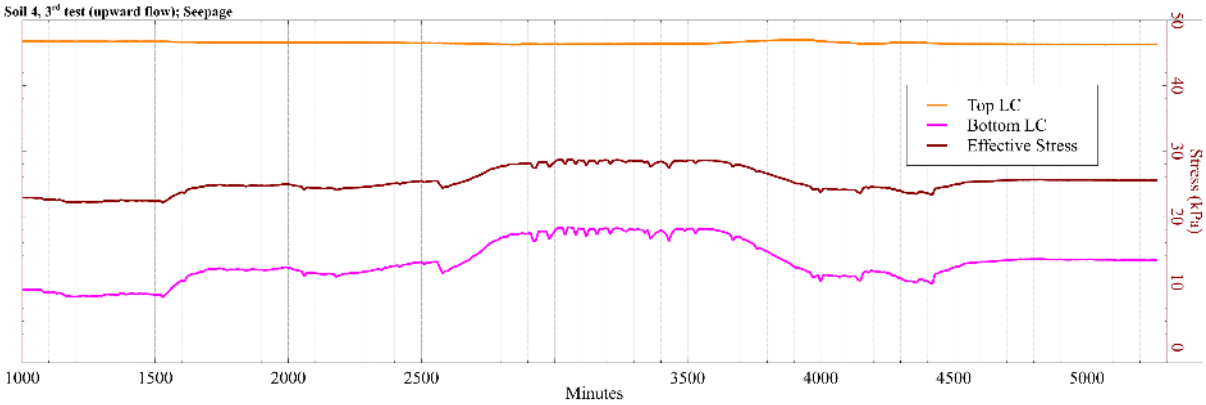


*Figure 0-8. Stress measured independently on top and bottom load cells (orange and magenta lines) as well as interpolated effective stress at the position of pressure transducer 3 (red line). S4T3.*

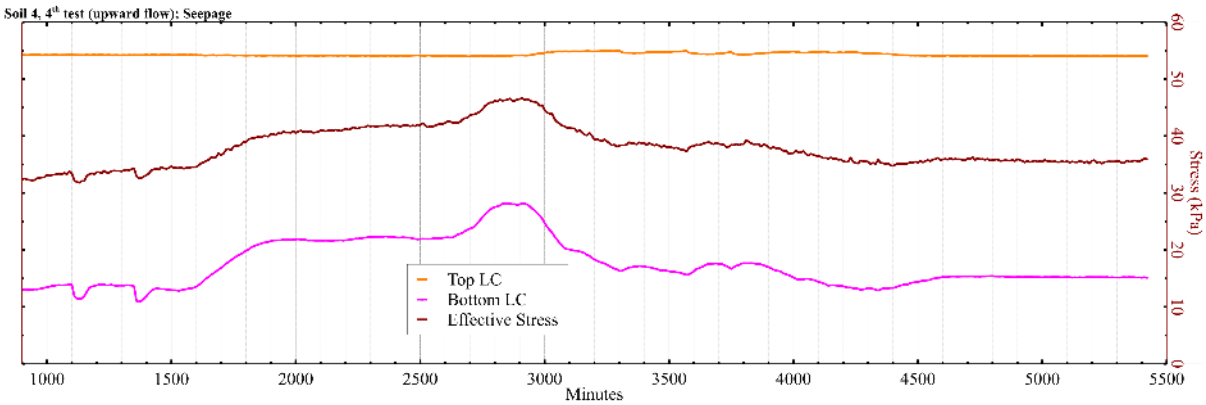


*Figure 0-9. Stress measured independently on top and bottom load cells (orange and magenta lines) as well as interpolated effective stress at the position of pressure transducer 3 (red line). S4T4.*

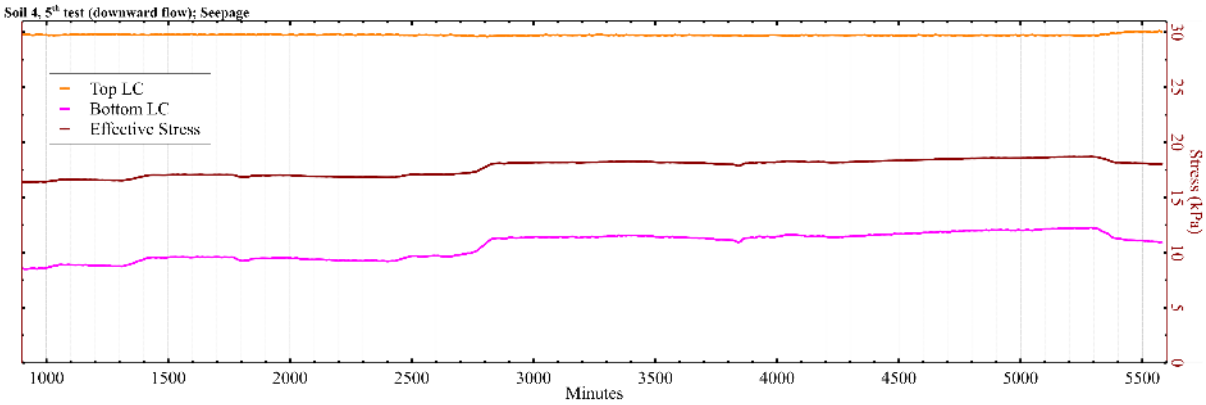


*Figure 0-10. Stress measured independently on top and bottom load cells (orange and magenta lines) as well as interpolated effective stress at the position of pressure transducer 3 (red line). S4T5.*

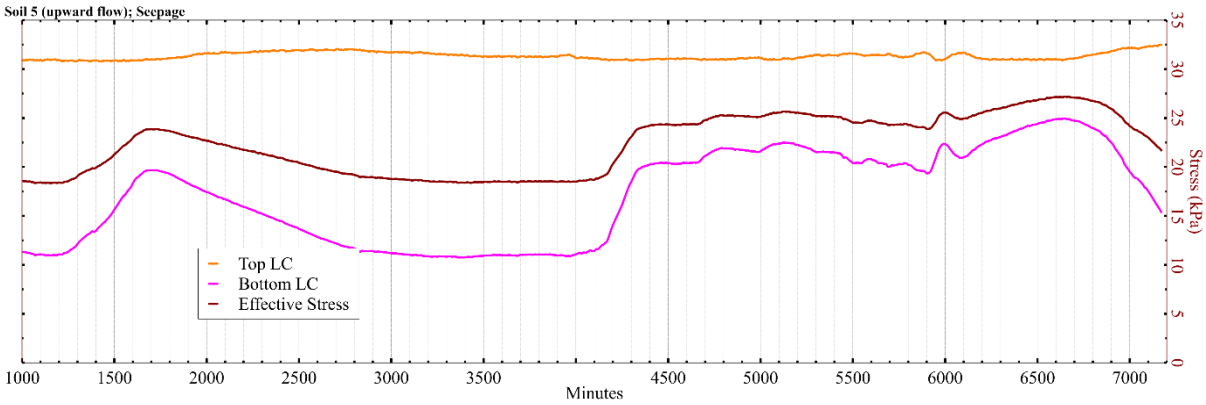


*Figure 0-11. Stress measured independently on top and bottom load cells (orange and magenta lines) as well as interpolated effective stress at the position of pressure transducer 3 (red line). S5T1.*

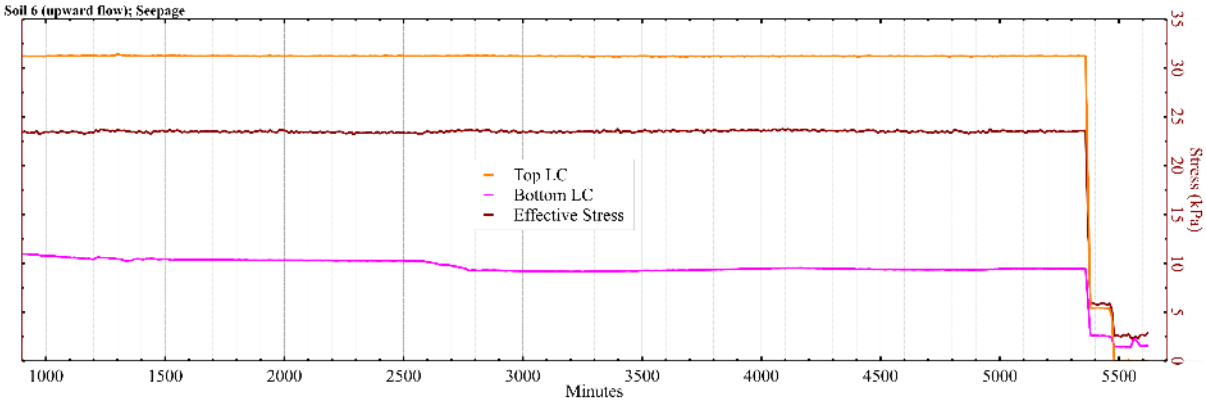


*Figure 0-12. Stress measured independently on top and bottom load cells (orange and magenta lines) as well as interpolated effective stress at the position of pressure transducer 3 (red line). S6T1.*

## Permeability

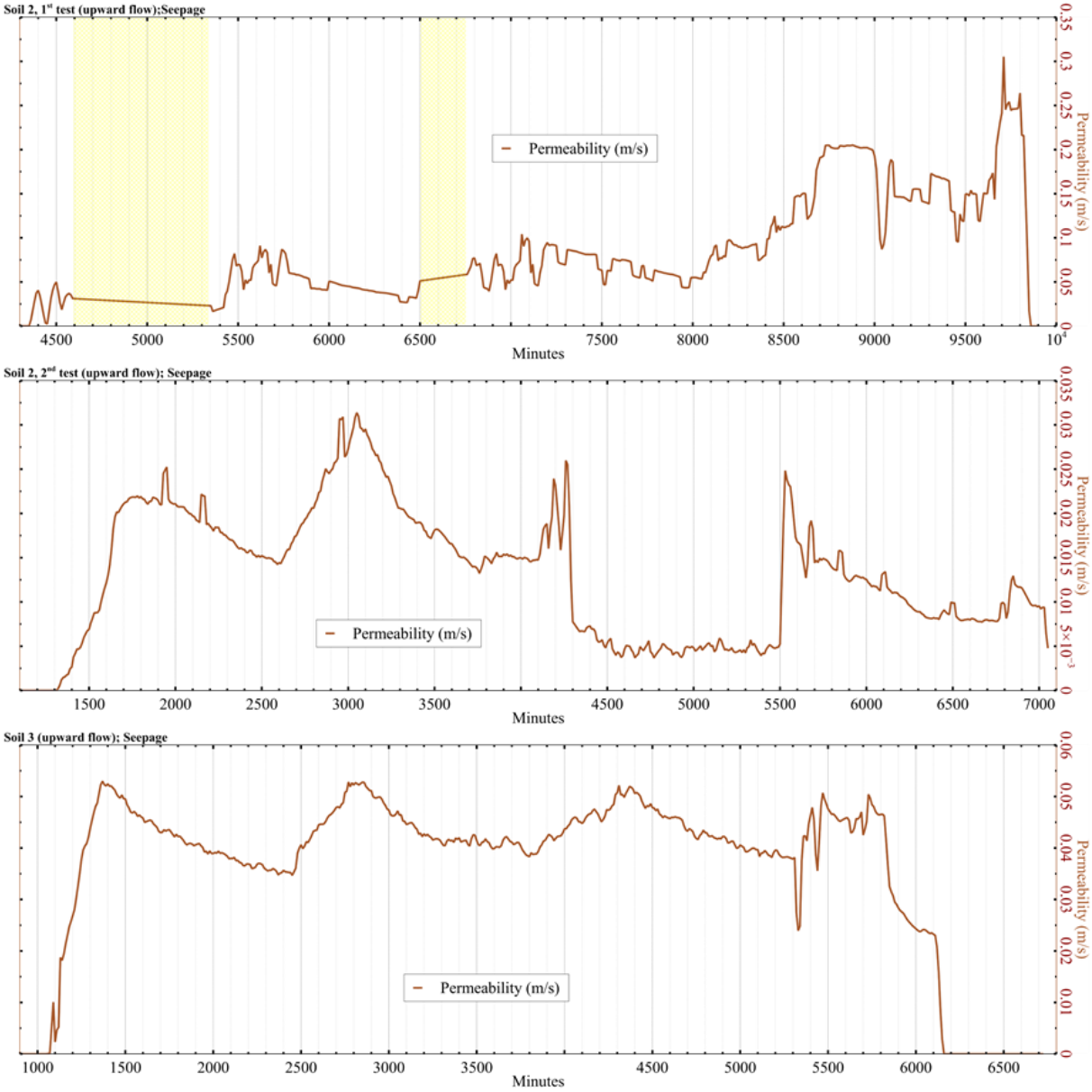


*Figure 0-13. Plots of permeability (m/s) during the seepage phase of permeameter tests S2T1, S2T2 and S3T1 – yellow areas in test S2T1 represent data gaps.*

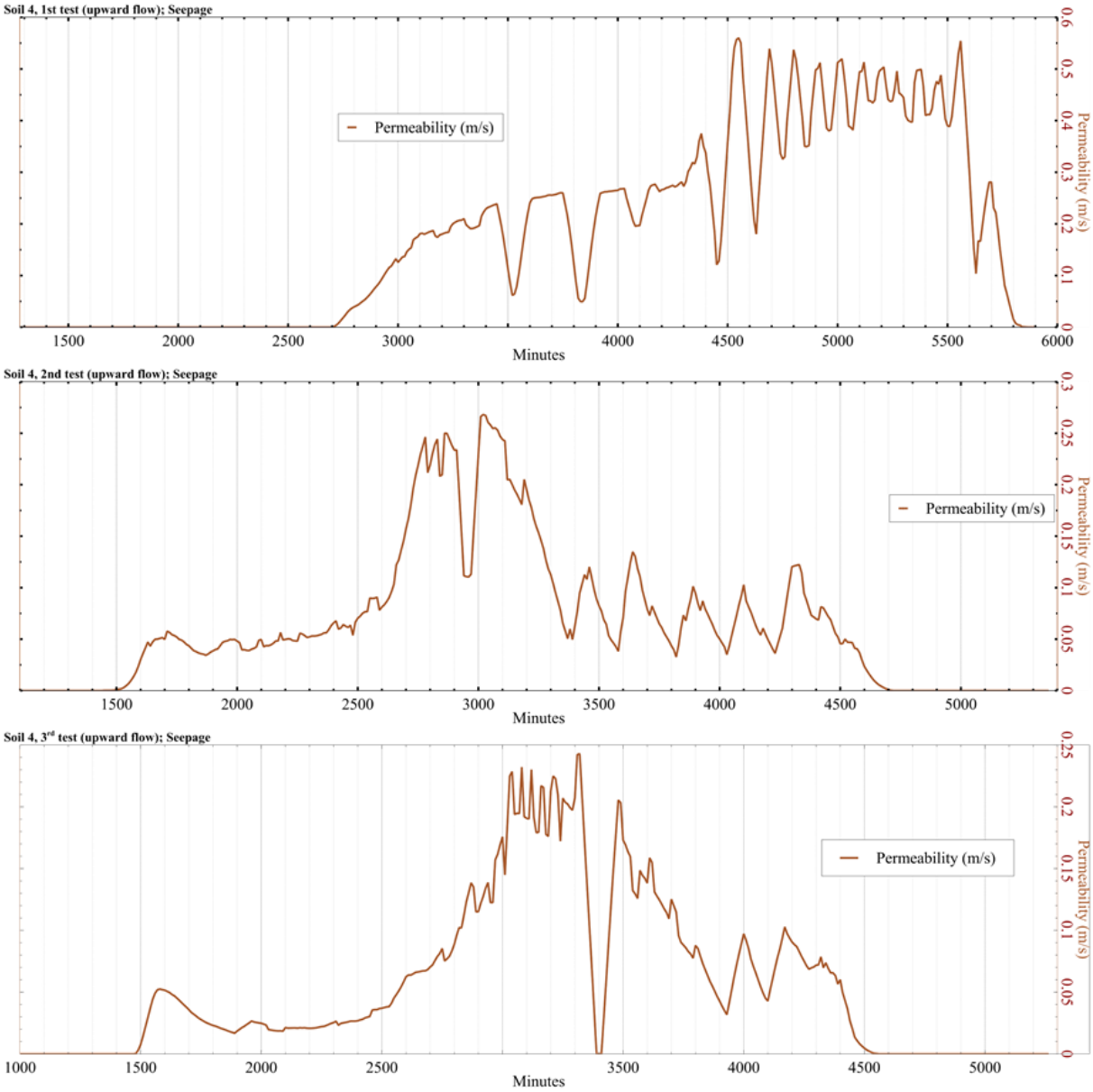


*Figure 0-14. Plots of permeability (m/s) during the seepage phase of permeameter tests S4T1, S4T2 and S4T3.*

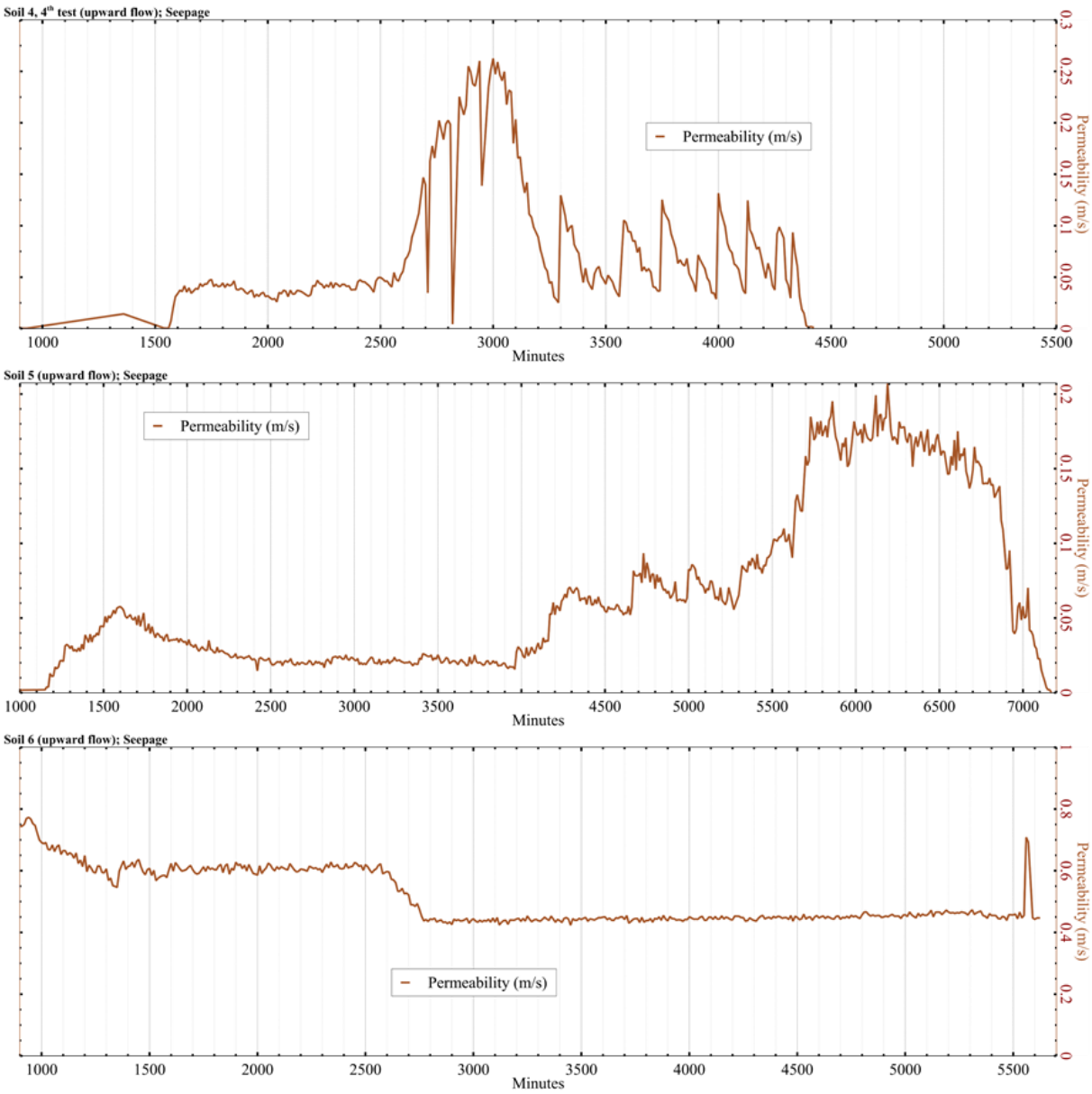


*Figure 0-15. Plots of permeability (m/s) during the seepage phase of permeameter tests S4T4, S5T1 and S6T1.*

## Pore pressures

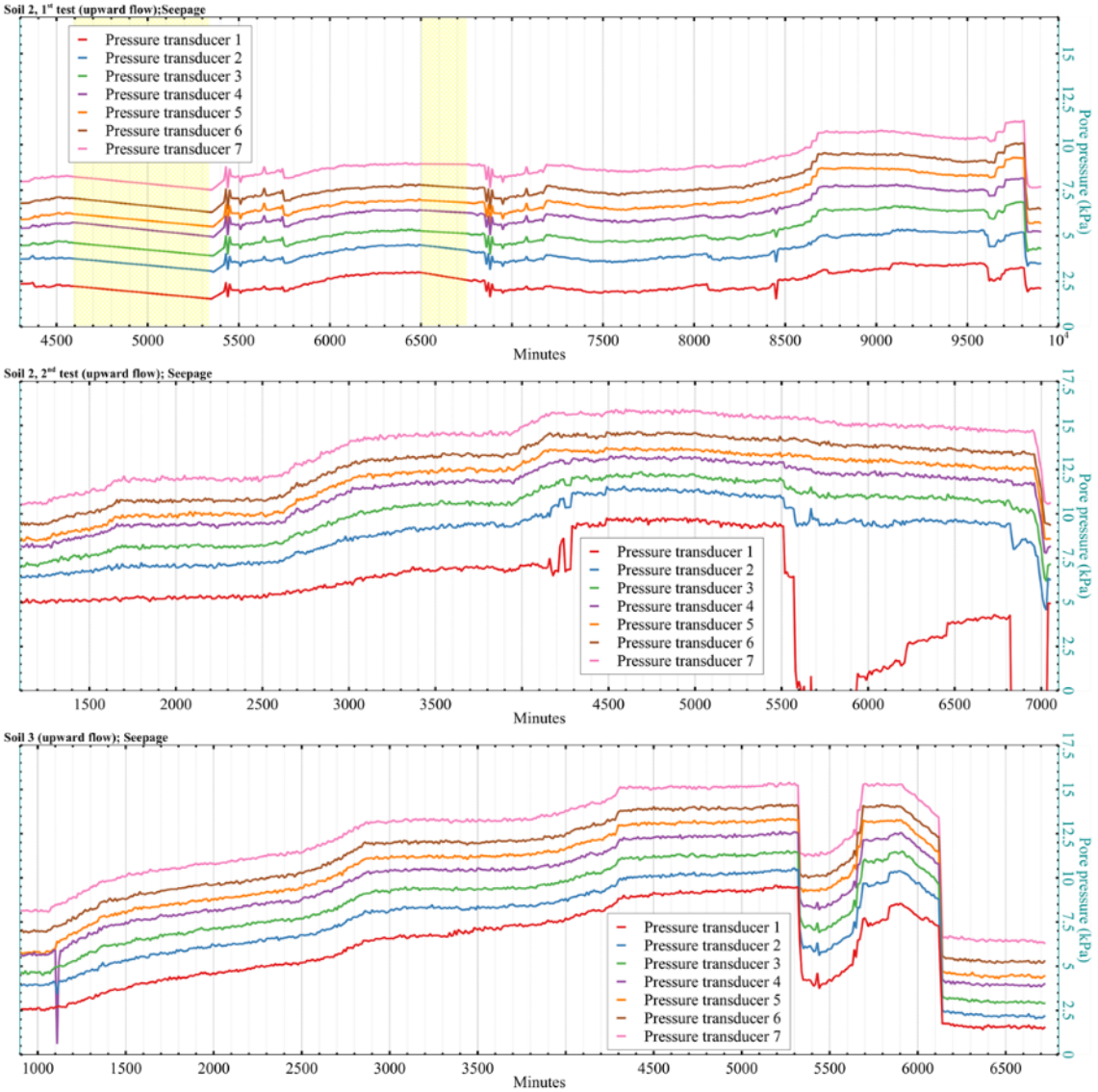


*Figure 0-16. Data from all individual pressure transducers during the seepage phase of tests S2T1, S2T2 and S3T1.*

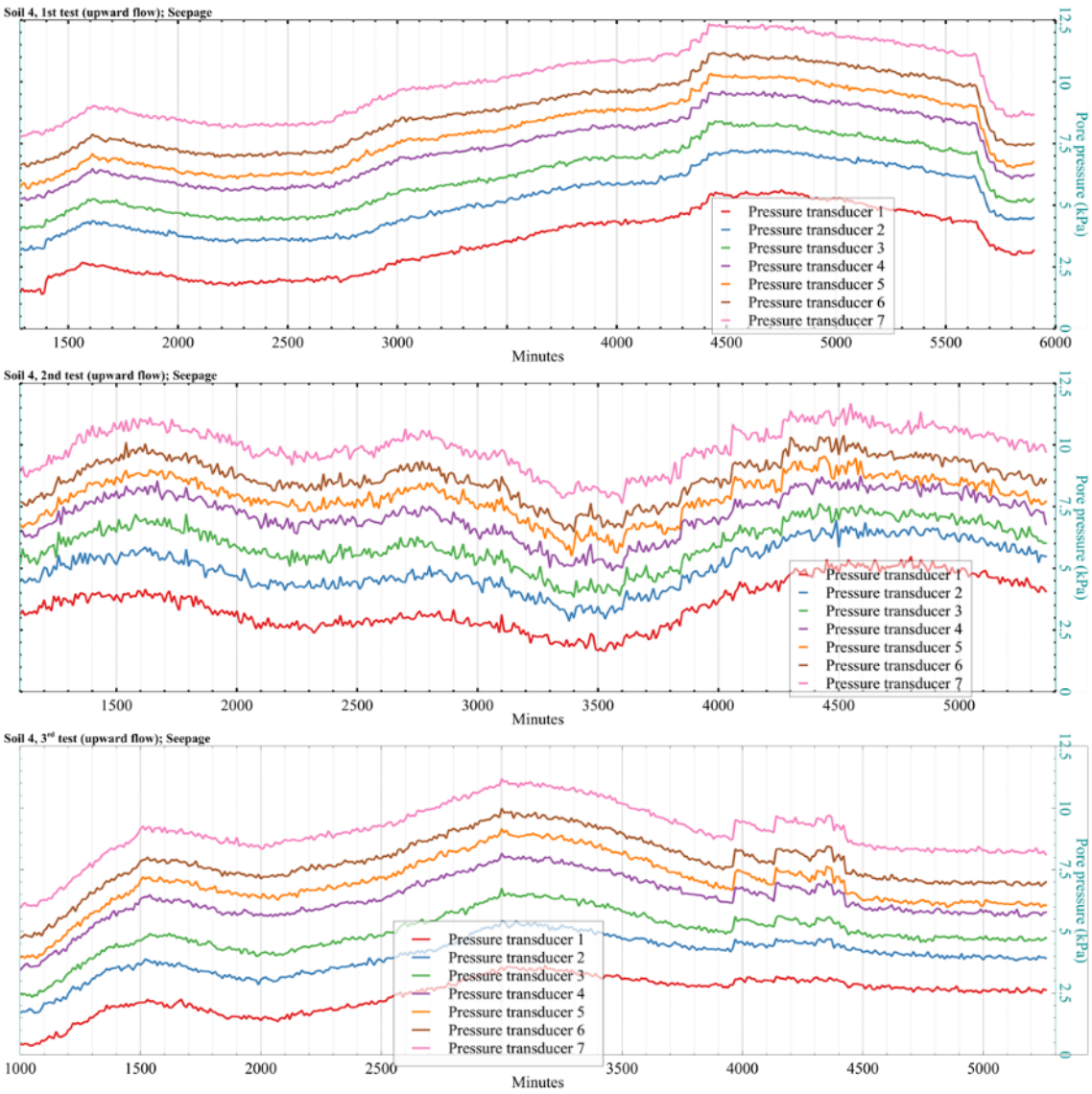


*Figure 0-17. Data from all individual pressure transducers during the seepage phase of tests S4T1, S4T2 and S4T3.*

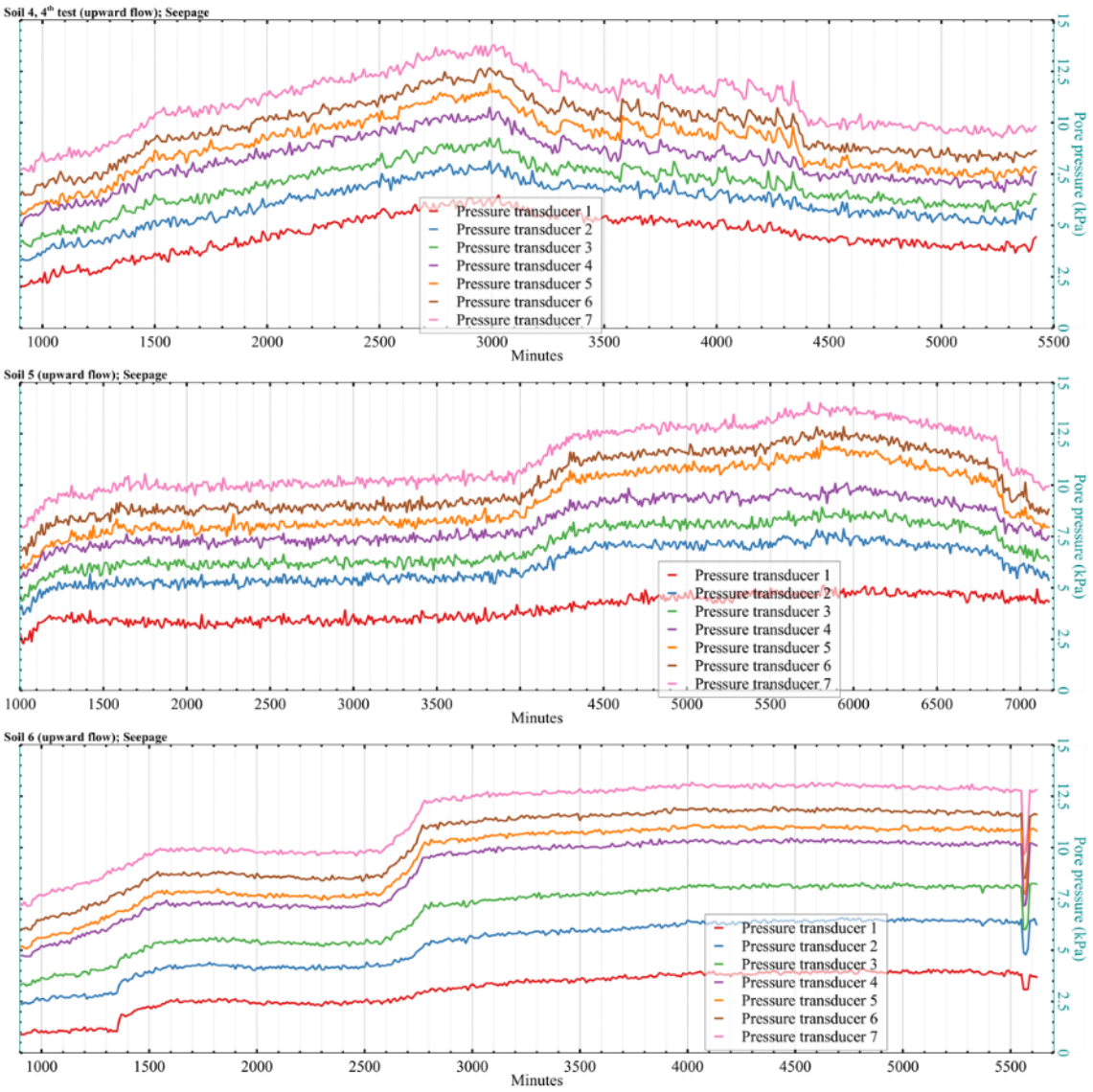


*Figure 0-18. Data from all individual pressure transducers during the seepage phase of tests S4T4, S5T1 and S5T1.*

## Estimated critical hydraulic gradients

Critical hydraulic gradients estimations for tested soil gradations calculated using the equation:

$$i_{cr} = \frac{G_S - 1}{1 + e}$$ (Terzaghi and Peck, 1948)

Where $i_{cr}$=critical hydraulic gradient, $G_s$=specific gravity of soil and $e$=void ratio of soil.

| | **Soil 1** | **Soil2** | **Soil 3** | **Soil 4** | **Soil 5** | **Soil 6** |
|---|---|---|---|---|---|---|
| **$i_{cr}$** | 1.05 | 0.961 | 0.970 | 0.928 | 1.122 | 0.969 |

## Calibration values used in tests.

*Table 38. Calibration values applied to data acquisition software (LabView) for the different sensors and gauges.*

| *Instrument* | | *Parameter* | | *Value* | | | | | | | | |
|---|---|---|---|---|---|---|---|---|---|---|---|---|
| | | | ***S2T1*** | ***S2T2*** | ***S3T1*** | ***S4T1*** | ***S4T2*** | ***S4T3*** | ***S4T4*** | ***S4T5*** | ***S5T1*** | ***S6T1*** |
| Bottom hydrophone | | RDC 1st threshold (V) | 0.005 | 0.00025 | 0.00023 | 0.00025 | 0.00025 | 0.00025 | 0.00025 | 0.00025 | 0.00025 | 0.00025 |
| | | RDC 2nd threshold (V) | ----- | 0.0006 | 0.008 | 0.0006 | 0.0006 | 0.0006 | 0.0006 | 0.0006 | 0.0006 | 0.0006 |
| | | Amplification (dB) | 20 | 40 | 40 | 40 | 40 | 40 | 40 | 40 | 40 | 40 |
| Top hydrophone | | RDC 1st threshold (V) | 0.004 | 0.0012 | 0.0008 | 0.00025 | 0.00025 | 0.00025 | 0.00025 | 0.00025 | 0.0012 | 0.0012 |
| | | RDC 2nd threshold (V) | ----- | 0.002 | 0.004 | 0.0006 | 0.0006 | 0.0006 | 0.0006 | 0.0006 | 0.002 | 0.002 |
| | | Amplification (dB) | 20 | 40 | 40 | 40 | 40 | 40 | 40 | 40 | 40 | 40 |
| Waveguide | | RDC Threshold (V) | 0.03 | 0.006 | 0.006 | 0.006 | 0.006 | 0.006 | 0.004 | 0.004 | 0.006 | 0.006 |
| | | Amplification (dB) | 9+40 | 9+40 | 9+40 | 9+40 | 9+40 | 9+40 | 9+40 | 9+40 | 9+40 | 9+40 |
| Pressure transducers (top to bottom) | 1 | Offset | 1.43 | 1.43 | 1.43 | 1.43 | 1.43 | 1.43 | 1.43 | 1.43 | 1.43 | 1.43 |
| | | Gain | 0.7 | 0.7 | 0.7 | 0.7 | 0.7 | 0.7 | 0.7 | 0.7 | 0.7 | 0.7 |
| | 2 | Offset | 1.43 | 1.43 | 1.43 | 1.43 | 1.43 | 1.43 | 1.43 | 1.43 | 1.43 | 1.43 |
| | | Gain | 0.73 | 0.73 | 0.73 | 0.73 | 0.73 | 0.73 | 0.73 | 0.73 | 0.73 | 0.73 |
| | 3 | Offset | 1.43 | 1.43 | 1.43 | 1.43 | 1.43 | 1.43 | 1.43 | 1.43 | 1.43 | 1.43 |
| | | Gain | 0.7 | 0.7 | 0.7 | 0.7 | 0.7 | 0.7 | 0.7 | 0.7 | 0.7 | 0.7 |
| | 4 | Offset | 1.43 | 1.43 | 1.43 | 1.43 | 1.43 | 1.43 | 1.43 | 1.43 | 1.43 | 1.43 |
| | | Gain | 0.7 | 0.7 | 0.7 | 0.7 | 0.7 | 0.7 | 0.7 | 0.7 | 0.7 | 0.7 |
| | 5 | Offset | 1.43 | 1.43 | 1.43 | 1.43 | 1.43 | 1.43 | 1.43 | 1.43 | 1.43 | 1.43 |
| | | Gain | 0.7 | 0.7 | 0.7 | 0.7 | 0.7 | 0.7 | 0.7 | 0.7 | 0.7 | 0.7 |
| | 6 | Offset | 1.44 | 1.44 | 1.44 | 1.44 | 1.44 | 1.44 | 1.44 | 1.44 | 1.44 | 1.44 |
| | | Gain | 0.7 | 0.7 | 0.7 | 0.7 | 0.7 | 0.7 | 0.7 | 0.7 | 0.7 | 0.7 |

| | | | | | | | | | | | | |
|---|---|---|---|---|---|---|---|---|---|---|---|---|
| | 7 | Offset | 1.43 | 1.43 | 1.43 | 1.43 | 1.43 | 1.43 | 1.43 | 1.43 | 1.43 | 1.43 |
| | | Gain | 0.7 | 0.7 | 0.7 | 0.7 | 0.7 | 0.7 | 0.7 | 0.7 | 0.7 | 0.7 |
| Load cells | Bottom | Offset | 0.179 | 0.179 | 0.179 | 0.179 | 0 | 0 | 0 | 0.179 | 0.179 | 0.179 |
| | | Gain | 85 | 85 | 85 | 85 | 1 | 1 | 1 | 85 | 85 | 85 |
| | Top | Offset | -0.012 | -0.012 | -0.012 | -0.012 | 0 | 0 | 0 | -0.012 | -0.012 | -0.012 |
| | | Gain | 90 | 90 | 90 | 90 | 1 | 1 | 1 | 90 | 90 | 90 |
| LVDT | | Offset | -7.07 | -7.07 | -7.07 | -7.07 | -7.07 | -7.07 | -7.07 | -7.07 | -7.07 | -7.07 |
| | | Gain | 3.75 | 3.75 | 3.75 | 3.75 | 3.75 | 3.75 | 3.75 | 3.75 | 3.75 | 3.75 |

## Additional permeameter drawings

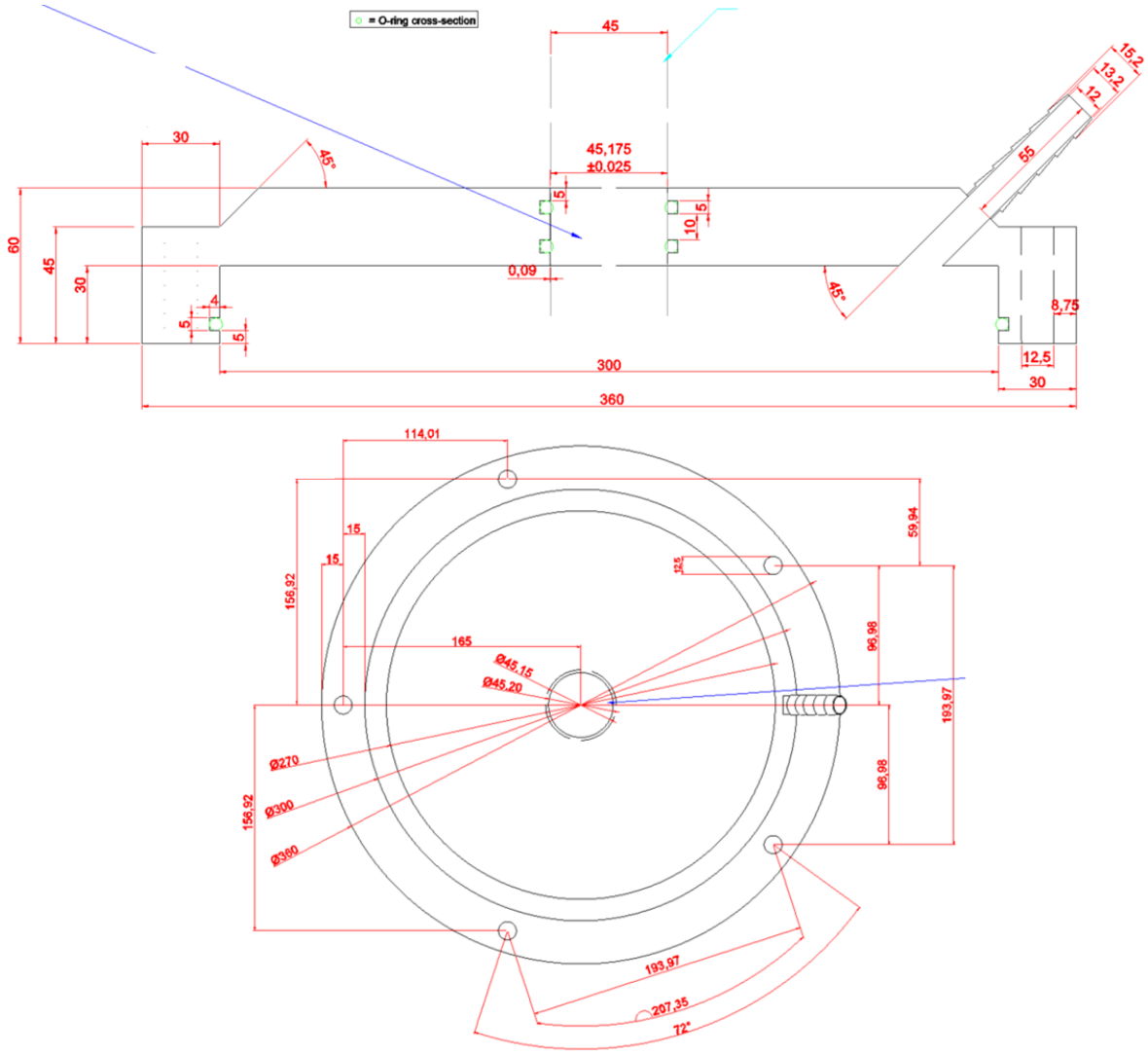


*Figure 0-19. Side and top views of drawings used to manufacture top cap of the permeameter cell. The dark blue arrow indicates the orifice through which the vertical loading shaft is placed. Besides having the connection between the vertical loading system and the soil itself, it serves as top cover for the permeameter and has a water in-/outlet. The five radially distributed orifices on its outer limits (top view; same observed on bottom cap) are for the placement of studs connecting the top and bottom caps and assuring the proper assembly of the cell. The shown dimensions (red) are in millimetres.*

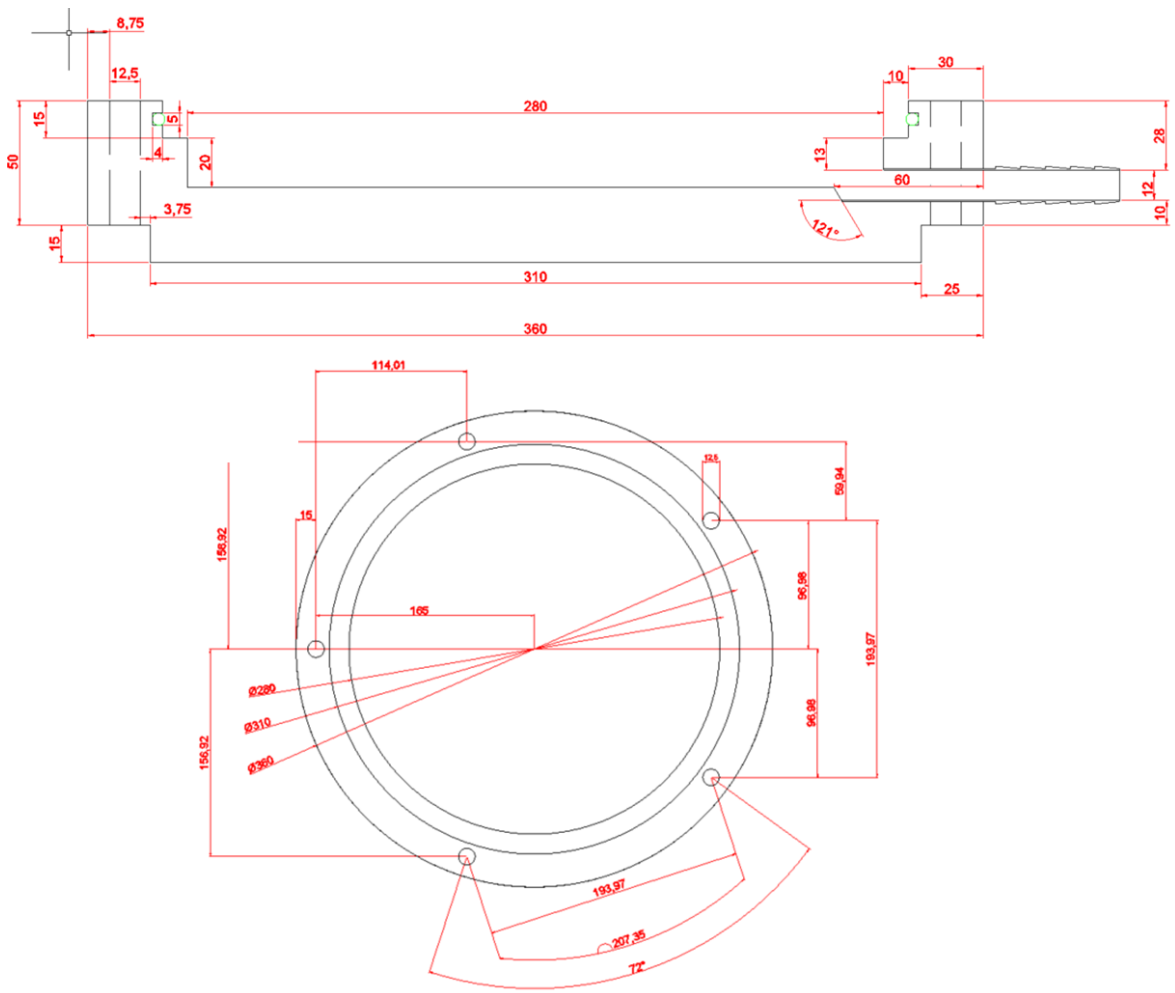


*Figure 0-20. Side and top views of drawings used to manufacture bottom cap of the permeameter cell. It is the bottom cover for the permeameter, has a water in-/outlet and serves as base for the bottom load cell. The shown dimensions (red) are in millimetres.*

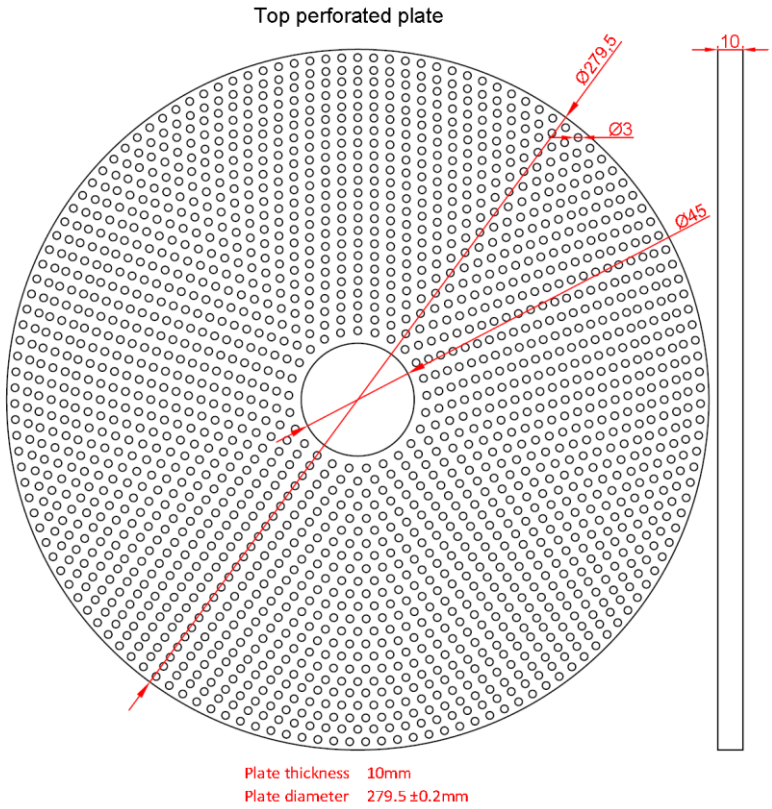


*Figure 0-21. Production drawing for top/loading plate (1840 3mm holes; displayed dimensions are in millimetres). The central gap (45mm) is where the vertical loading rod is attached.*

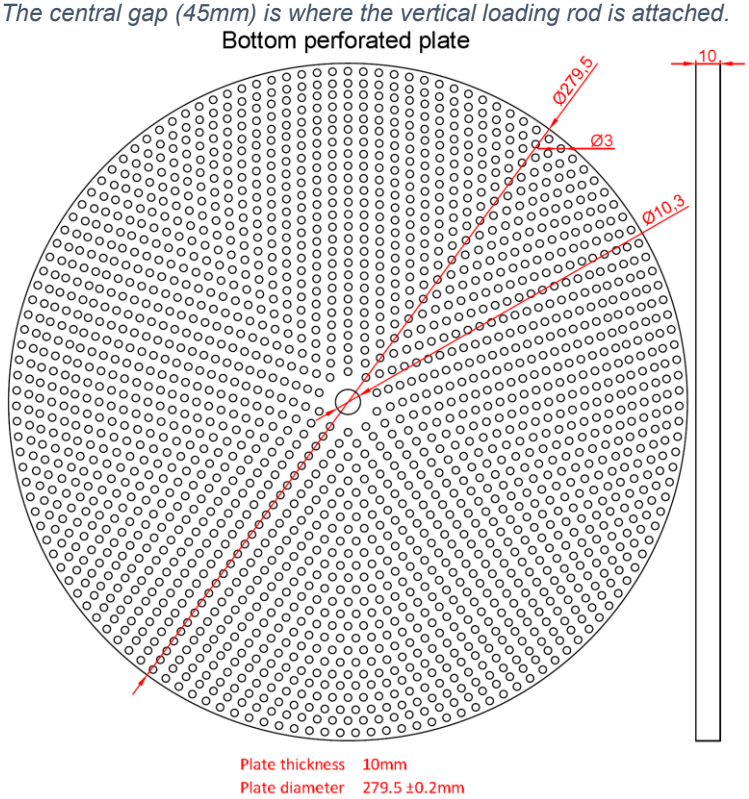


*Figure 0-22. Production drawing for top/loading plate (1885 3mm holes; displayed dimensions are in millimetres). The central orifice is where the bottom load cell is attached.*

## Additional plots of hydraulic gradient vs effective stress

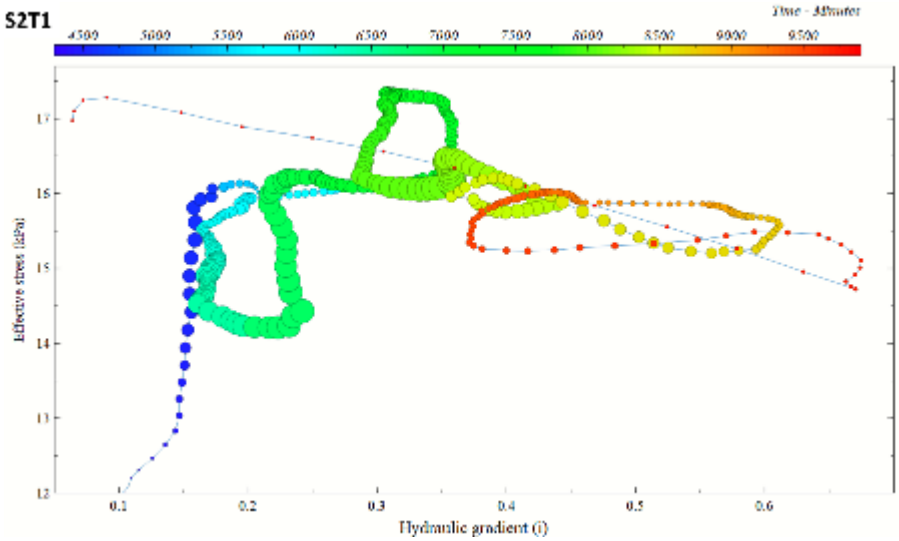


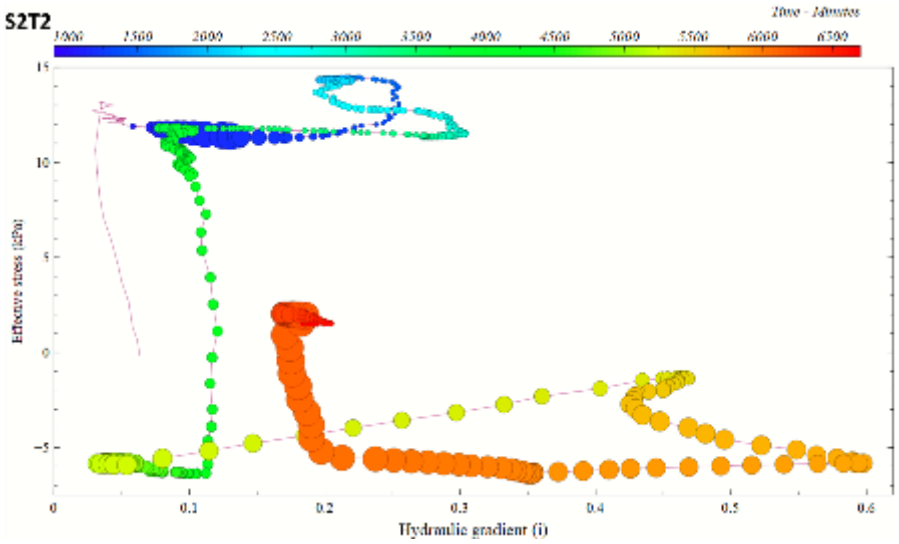


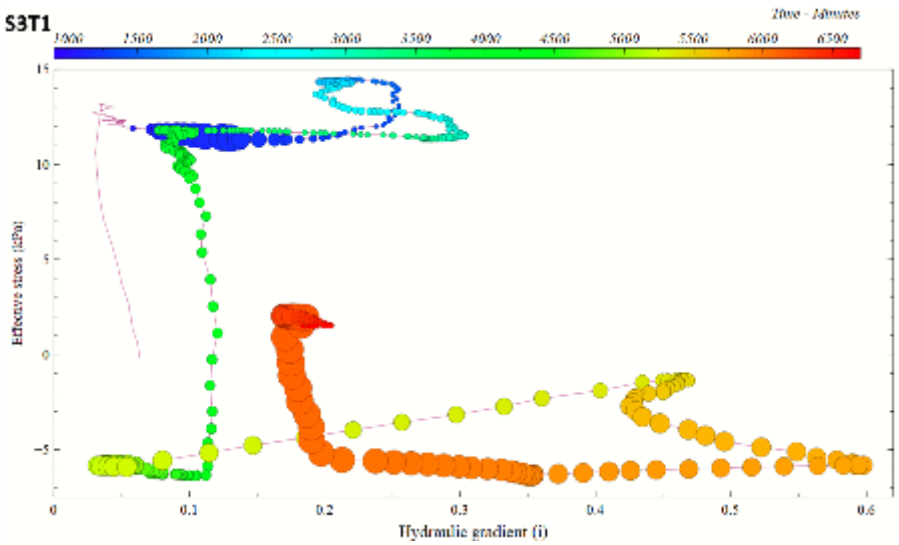

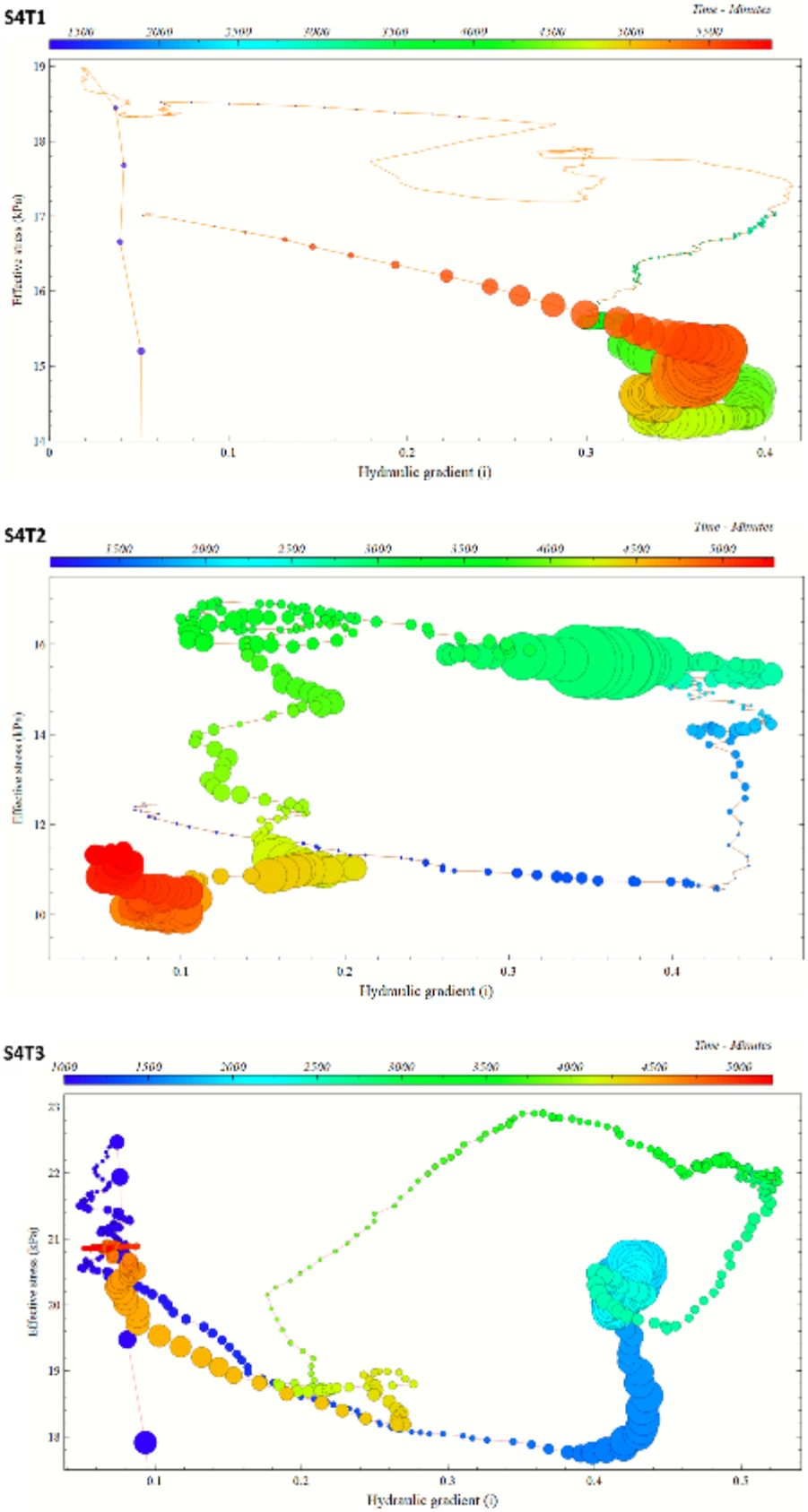
S4T1
Time - Minutes
Effective stress (kPa)
Hydraulic gradient (i)
S4T2
Time - Minutes
Effective stress (kPa)
Hydraulic gradient (i)
S4T3
Time - Minutes
Effective stress (kPa)
Hydraulic gradient (i)

**S4T4**

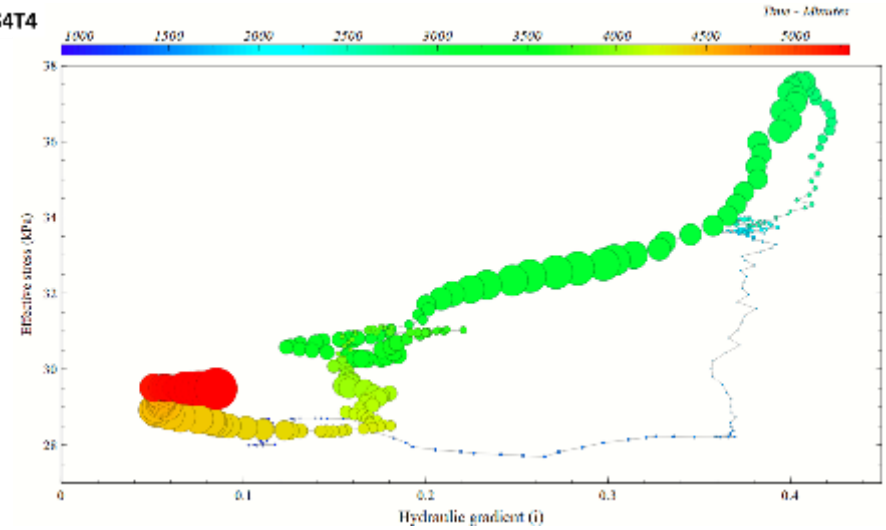


**S4T5**

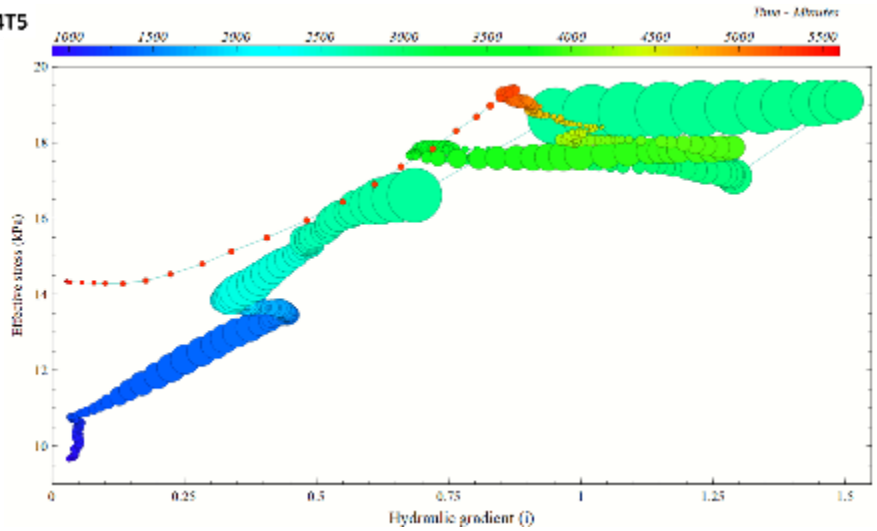


**S5T1**